University of Tennessee, Knoxville
Trace: Tennessee Research and Creative Exchange

Doctoral Dissertations | Graduate School

8-2011

Challenges for the Accurate Determination of the Surface Thermal Condition via In-Depth Sensor Data

Bryan Scott Elkins
belkins1@utk.edu

Recommended Citation

Elkins, Bryan Scott, "Challenges for the Accurate Determination of the Surface Thermal Condition via In-Depth Sensor Data. " PhD diss., University of Tennessee, 2011.
https://trace.tennessee.edu/utk_graddiss/1075

This Dissertation is brought to you for free and open access by the Graduate School at Trace: Tennessee Research and Creative Exchange. It has been accepted for inclusion in Doctoral Dissertations by an authorized administrator of Trace: Tennessee Research and Creative Exchange. For more information, please contact trace@utk.edu.

To the Graduate Council:

I am submitting herewith a dissertation written by Bryan Scott Elkins entitled "Challenges for the Accurate Determination of the Surface Thermal Condition via In-Depth Sensor Data." I have examined the final electronic copy of this dissertation for form and content and recommend that it be accepted in partial fulfillment of the requirements for the degree of Doctor of Philosophy, with a major in Aerospace Engineering.

Majid Keyhani, Major Professor

We have read this dissertation and recommend its acceptance:

Jay I. Frankel, Rao V. Arimilli, Jayne Wu

Accepted for the Council:
Dixie L. Thompson

Vice Provost and Dean of the Graduate School

(Original signatures are on file with official student records.)

Challenges for the Accurate Determination of the Surface Thermal Condition via In-Depth Sensor Data

A Dissertation Presented for
the Doctor of Philosophy Degree
The University of Tennessee, Knoxville

Bryan Scott Elkins
August 2011

Acknowledgements

I would like to acknowledge the many people who have facilitated the completion of this work. I am grateful to my co-advisors, Dr. Majid Keyhani and Dr. Jay Frankel, for their support and direction. Their encouragement and mentorship have been essential throughout my graduate career and to the completion of this dissertation. I would also like to express my sincere gratitude to my committee members, Dr. Rao Arimilli and Dr. Jayne Wu, for their insightful suggestions in the development of this work.

I would like to acknowledge Mr. Dennis Higdon for his software and hardware expertise, as well as for the many hours of troubleshooting assistance he provided. I am also grateful for the assistance and advice of Mr. Danny Graham in the fabrication of my dissertation project.

I would also like to thank my fellow graduate students, Mr. Jake Plewa and Mr. Andrew Stubblefield, as well as undergraduate research assistant Aaron Myers for their assistance in this project, and for their friendship. I am also grateful for the collaboration and assistance of Ms. Manguo Huang and Mr. Xuejun Zhou during their time at the University of Tennessee.

Financial support throughout my graduate career has been provided through many avenues. I am especially grateful to Drs. Keyhani and Frankel for their assistance in securing consistent support for my work. I would like to thank the Mechanical, Aerospace, and Biomedical Engineering Department for supporting me through Graduate Teaching Assistantships for many semesters. I am also thankful to Dr. Joseph Sheeley for providing one year of support through a contract with Aerospace Testing Alliance (09-16-FRANKEL). I am grateful to the National Science Foundation (CBET-0601236) and to NASA (EPSCoR-NNX10AN35A) for their financial support of my doctoral work.

Abstract

The overall goal of this work is to provide a systematic methodology by which the difficulties associated with the inverse heat conduction problem (IHCP) can be resolved. To this end, two inverse heat conduction methods are presented. First, a space-marching IHCP method (discrete space, discrete time) utilizing a Gaussian low-pass filter for regularization is studied. The stability and accuracy of this inverse prediction is demonstrated to be more sensitive to the temporal mesh than the spatial mesh. The second inverse heat conduction method presented aims to eliminate this feature by employing a global time, discrete space inverse solution methodology. The novel treatment of the temporal derivative in the heat equation, combined with the global time Gaussian low-pass filter provides the regularization required for stable, accurate results.

A physical experiment used as a test bed for validation of the numerical methods described herein is also presented. The physics of installed thermocouple sensors are outlined, and loop-current step response (LCSR) is employed to measure and correct for the delay and attenuation characteristics of the sensors. A new technique for the analysis of LCSR data is presented, and excellent agreement is observed between this model and the data.

The space-marching method, global time method, and a new calibration integral method are employed to analyze the experimental data. First, data from only one probe is used which limits the results to the case of a semi-infinite medium. Next, data from two probes at different depths are used in the inverse analysis which enables generalization of the results to domains of finite width. For both one- and two-probe analyses, excellent agreement is found between the actual surface heat flux and the inverse predictions. The most accurate inverse technique is

shown to be the calibration integral method, which is presently restricted to one-probe analysis. It is postulated that the accuracy of the global time method could be improved if the required higher-time derivatives of temperature data could be more accurately measured. Some preliminary work in obtaining these higher-time derivatives of temperature from a voltage-rate interface used in conjunction with the thermocouple calibration curve is also presented.

Table of Contents

Chapter 1: Introduction 1

1.1 Literature Review 4

1.2 Scope of Dissertation 16

Chapter 2: Space-Marching Method for Inverse Heat Conduction Problem 18

2.1 Space-Marching Method Introduction 18

2.2 Problem Description 19

2.3 Penetration Time 21

2.4 Inverse Method 25

2.5 Stability and Accuracy Investigation of the Inverse Method 30

2.6 Digital Filtering – Regularization with Physical Meaning 36

2.7 Results with Measurement Error 42

2.8 Heat flux Evaluation via Heating Rate 47

2.9 Transient Surface Heat flux With Measurement Error 50

2.10 Chapter Summary 52

Chapter 3: Global Time Method for Inverse Heat Conduction Problem 54

3.1 Global Time Method Introduction 54

3.2 Problem Description and Inverse Technique 55

3.3 Regularization via Digital Filtering 58

3.4 Errorless Data 60

3.5 Noisy Data 65

3.6 Chapter Summary 75

Chapter 4: In-Situ Higher-Time Derivative of Temperature Sensors for Aerospace Heat Transfer 76

4.1 Motivation for Higher-Time Derivatives of Temperature Sensor 76
4.3 Time Derivatives of Temperature Sensor 82
4.4 Heat Transfer Experiment 94
4.5 Results 99
4.6 Chapter Summary 105
Chapter 5: Sandwich Experiment 107
5.1 Experimental Setup 107
5.2 Electrical Wiring 114
5.3 Sandwich Experimental Procedure 118
5.4 Direct Model 120
Chapter 6: Characterization of In-Depth Probes 123
6.1 Thermocouple model 127
6.2 Loop-Current Step Response 129
6.3 Two-Probe Taylor Series Method 146
6.4 Recommended Characterization for Sandwich Experiment 155
Chapter 7: Experimental Results with One-Probe Analysis 157
7.1 Data Analysis 157
7.2 Experimental Validation of Inverse Techniques 165
7.3 Chapter Summary 201
Chapter 8: Experimental Results with Two-Probe Analysis 203
8.1 Two-Probe Data Analysis Procedure 203
8.2 Two-Probe Analysis of Experimental Data 204
8.3 Chapter Summary 223
Chapter 9: Conclusions and Future Work 224

9.1 Conclusions 224
9.2 Future Work 227
List of References 230
Appendix 236
A.1 Uncertainty in Actual Surface Heat Flux 237
A.2 Uncertainty in Global Time Inverse Method 241
Vita 251

List of Figures

Figure 2.1: Illustration of lead data to capture background noise ($0 \le t \le 15$s) and experimental penetration time. Temperatures measured from a back face thermocouple resulting from a surface heat flux of 4.3 W/cm^2 switched on at 15s. 24

Figure 2.2: Inverse surface temperature and heat flux solution using "perfect," discrete data ($\varepsilon = 0\%$) from the exact solution for test case 1. Mesh parameters used are $t_p/\Delta t = 30$ and $d/\Delta x = 9$..... 28

Figure 2.3: Comparison of inverse results for test case 1 using the exact solution as input data with varying mesh parameters: coarse mesh: $t_p/\Delta t = 1$, $d/\Delta x = 2$; fine mesh: $t_p/\Delta t = 40$, $d/\Delta x = 30$; and optimized mesh: $t_p/\Delta t = 30$, $d/\Delta x = 9$..... 31

Figure 2.4: Inverse prediction RMS error for test case 1 over the interval $5 < t/t_p < 15$ for the dimensionless surface temperature and heat flux values using exact data for (a) fixed nodal spacing and (b) fixed temporal mesh. 33

Figure 2.5: Optimization of mesh for test case 1. (a) Stability correlation relating the spatial mesh size ($d/\Delta x$) to the temporal mesh size ($t_p/\Delta t$) and (b) optimum mesh for both stability and accuracy. 35

Figure 2.6: Choice of cutoff frequency by tangent line method. 39

Figure 2.7: Effectiveness of filter at eliminating unwanted noise. (a) Noisy, filtered temperature and heat flux input data ($\eta = 1$) used to predict (b) surface ($\eta = 0$) conditions. Parameters used were $\bar{f}_c = 2.0$, $d/\Delta x = 9$ and $t_p/\Delta t = 30$ for test case 1. 41

Figure 2.8: Effect of input error, ε on the surface temperature and heat flux error histories. The RMS error was calculated over the interval $5 < t/t_p < 15$ for test case 1..... 43

Figure 2.9: Effect of Δt using noisy ($\varepsilon = 10\%$), filtered data on the inverse-predicted surface (a) temperature error and (b) heat flux error histories. The RMS error was calculated over the interval $5 < t/t_p < 15$ for test case 1. 45

Figure 2.10: Effect of Δx using noisy ($\varepsilon = 10\%$), filtered data on the inverse-predicted surface (a) temperature error and (b) heat flux error histories. The RMS error was calculated over the interval $5 < t/t_p < 15$ for test case 1. 46

Figure 2.11: Half-space application: (a) input heat flux data obtained via the heat flux-heating rate integral relationship at sensor site ($\eta = 1$), (b) the resultant surface temperature ($\eta = 0$) and (c) the resultant surface heat flux ($\eta = 0$). Parameters used were $\varepsilon = 10\%$, $\bar{f}_c = 2.0$, $d/\Delta x = 9$ and $t_p/\Delta t = 30$, respectively for test case 1..... 48

Figure 2.12: Inverse results with a transient surface boundary condition and 10% measurement error: (a) pulse flux (test case 2) and (b) triangular flux (test case 3). Both results used the parameters $\varepsilon = 10\%$, $\bar{f}_c = 2.0$, $d/\Delta x = 9$ and $t_p/\Delta t = 30$. 51

Figure 3.1: Inverse results using N=4 using errorless, discrete data. (a) temperature and (b) heat flux inverse predictions. 63

Figure 3.2: Effect of the sampling rate on the inverse heat flux prediction with N=7 using errorless data. (a) $\bar{f}_s = 265$ and (b) $\bar{f}_s = 400$. 64

Figure 3.3: Technique for estimating the noise present in the data: (a) first order fit to data (b) least squares fit to residual and (c) actual and estimated noise. 66

Figure 3.4: Gaussian low-pass filter exploration. (a) optimum cutoff frequency range and (b) insensitivity of Gaussian filter to a small change in cutoff frequency. 68

Figure 3.5: Inverse results using a normal distribution, with a standard deviation of 0.01 and a dimensionless cutoff frequency of 2.6. (a) Noisy data used as input to the inverse code, (b) inverse temperature results and (c) inverse heat flux results. 69

Figure 3.6: Temperature data for Beck triangle problem (a) raw data with $\sigma = 0.01$ and $\bar{f}_s = 1200$ (b) insensitivity of Gaussian filter to change in cutoff frequency..... 71

Figure 3.7: Inverse results for the classical Beck triangle problem for (a) surface temperature prediction and (b) surface heat flux prediction. Noise was simulated using a normal distribution, $\sigma = 0.01$ and $\bar{f}_c = 3.5$ used for regularization. 72

Figure 4.1: Schematic of probe placement (below surface) for surface flux jump location simulation..... 79

Figure 4.2: (a) Temperature and (b) heating rate histories at indicated embedded sites. Boundary condition is shown in Figure 4.1 with $q_s = 10^6$ W/m^2. 80

Figure 4.3: (a) Second and (b) third time derivatives of temperature histories at indicated embedded sites. Boundary condition is shown in Figure 4.1 with $q_s = 10^6$ W/m^2. 81

Figure 4.4: Schematic of concept for acquiring necessary voltage rates with minimal high frequency content and minimal time lag. Here, e_m, m=1,2.. are voltage outputs from differentiator that are mathematically related to the thermocouple voltage, V_i. 85

Figure 4.5: (a) Basic differentiating circuit used in practice (m=1,2,…) and (b) symbolic element as expressed in Figure 4.4. 85

Figure 4.6: Typical power spectra from DFT for a thermocouple drop test. The physical cut-off frequency is estimated as $f_{c,p}$=35 Hz. 88

Figure 4.7: Filtering effect in the designed differentiator as a function of frequency for two sample cut-off frequencies. 89

Figure 4.8: Lag times as a function of frequency to demonstrate that increasing the differentiator cut-off frequency produces a corresponding decrease in circuit component delay times. 90

Figure 4.9: 2-Stage Low-Pass filter (Butterworth) designed to remove signal frequency content $f>f_{c,p}$. (a) Circuit schematic and (b) symbolic element for use in Figure 4.4..... 92

Figure 4.10: Butterworth filter characteristics as a function of frequency for each stage and as a cascaded filter indicating $f_{fil} = f_{c,p}$=35 Hz as designed. 93

Figure 4.11: Isothermal hot bath used for experimentally verifying sensor along with a schematic diagram. (a) Picture of setup and (b) labeled sketch of setup. 96

Figure 4.12: Experimentally acquired thermocouple data, Gaussian filter, and analytic model results. 100

Figure 4.13: Analytic model results, Gaussian filter and sensor output results for first-time derivative of temperature. 102

Figure 4.14: Analytic model results, Gaussian filter and sensor output for second-time derivative of temperature. 103

Figure 4.15: Analytic continuation, as defined with the aid of Eq. (4.2), indicates that future temperatures can be estimated based on using rate-based sensors. 104

Figure 5.1: Sandwich electrical heating experimental setup shown with (a) side view and (b) planview. Line of symmetry exists along the centerline of the heater. 108

Figure 5.2: Dimensioned sketch (not to scale) of custom heater. The heater was machined from a 0.125mm thick nichrome foil..... 109

Figure 5.3: Electrical wiring diagram of sandwich experiment. 115

Figure 5.4: Discretization sketch for three layer finite difference model of sandwich experiment..... 121

Figure 6.1: Temperature and heat flux data uncorrected for response time. (a) Raw and filtered temperature data and (b) resulting semi-infinite heat flux. Data for probe A0 from run qRHIt5f200. 124

Figure 6.2: Inverse predicted surface temperature and heat flux using sandwich experiment data from run qRHIt5f200, uncorrected for response time. (a) Surface temperature with uncertainty band and (b) surface heat flux with uncertainty band. Data used can be seen in Figure 6.1. 125

Figure 6.3: Effect of thermocouple wire orientation on lead losses. 126

Figure 6.4: LCSR test circuit setup using AC current for heating. DIO SSR1 closes when DIO SSR2a and DIO SSR2b open to prevent damage to the data acquisition board. 130

Figure 6.5: LCSR data for probe A0 for V_{RMS} = 16.3V, Δt_{heat} = 0.25s, ΔT = 12.7 °C, and f_s = 200 Hz.. Time regions where parameters have the strongest influence are shown. 133

Figure 6.6: Model 1 results for LCSR testing of probe A0. (a) Sensitivity coefficient and (b) comparison of model with raw data. Testing parameters were V_{RMS} = 16.3V, Δt_{heat} = 0.25s, ΔT = 12.7 °C, and f_s = 200 Hz. 135

Figure 6.7: Model 2 results for LCSR testing of probe A0. (a) Sensitivity coefficients and (b) comparison of model with raw data. Testing parameters were V_{RMS} = 16.3V, Δt_{heat} = 0.25s, ΔT = 12.7 °C, and f_s = 200 Hz. 137

Figure 6.8: Model 3 results for LCSR testing of probe A0. (a) Sensitivity coefficient and (b) comparison of model with raw data. Testing parameters were V_{RMS} = 16.3V, Δt_{heat} = 0.25s, ΔT = 12.7 °C, and f_s = 200 Hz. 139

Figure 6.9: Model 4 results for LCSR testing of probe A0. (a) Sensitivity coefficient and (b) comparison of model with raw data. Testing parameters were V_{RMS} = 16.3V, Δt_{heat} = 0.25s, ΔT = 12.7 °C, and f_s = 200 Hz. 141

Figure 6.10: (a) Temperature and (b) heat flux for probe A0 showing the effect of shifting for LCSR characterization values. One-probe analysis used as detailed in Chapter 7. 144

Figure 6.11: Inverse predicted surface temperature and heat flux using data corrected for response time. (a) Surface temperature prediction with uncertainty band and (b) Surface heat flux with uncertainty band. Data used for prediction can be seen in Figure 6.10 with one-probe analysis as detailed in Chapter 7. 145

Figure 6.12: Two-Probe Taylor Series method results with simulated data. (a) Input dimensionless data and (b) resulting time constant prediction with N = 9, $\bar{f}_s$ = 1000. 152

Figure 6.13: Effect of varying (a) number of derivatives used and (b) sampling rate on the resulting Two-Probe Taylor series results using simulated data. 153

Figure 6.14: Two-Probe Taylor Series results using sandwich experiment data from run qCHIt10f1200 with $N = 9$. 154

Figure 7.1: Penetration time of back surface with run qCHIt10f60 where $t_{p'} = t_{on} + t_p$..... 161

Figure 7.2: Comparison of surface flux obtained direct measured power history (q_{s1}) and direct FD model which accounts for heater capacitance and mica layer (q_{s2}). Heater voltage was sampled at 7500 Hz. 164

Figure 7.3: Flow chart for preprocessing of data for use in one-probe inverse analysis. 166

Figure 7.4: (a) Imposed surface flux and (b) back face thermocouple histories for run qCLOt3f200. Maximum difference between TChalf1 and TChalf2 was 0.02°C. 168

Figure 7.5: Details of post-processing the data for run qCLOt3f200. (a) Raw and LCSR-shifted experimental A0 data and (b) optimum cutoff frequency range. 169

Figure 7.6: (a) Direct FD model temperature history at probe A0 depth compared with LCSR-shifted experimental A0 data and (b) resulting local heat flux using semi-infinite medium integral equation. Experimental data was regularized with f_c = 0.9 Hz. 170

Figure 7.7: Space-marching inverse results for run qCLOt3f200 for (a) surface temperature and (b) surface heat flux. Parameters used were $d/\Delta x = 21$, $t_p/\Delta t$ = 21.5, and $f_c = 0.9$ Hz. The error norms were calculated over $12\text{s} \le t \le 22\text{s}$. 172

Figure 7.8: (a) Raw and LCSR-shifted experimental A0 data for run qCLOt3f1200 and (b) resulting local heat flux for probe A0. 175

Figure 7.9: Space-marching inverse results for run qCLOt3f1200 for (a) surface temperature and (b) surface heat flux. Parameters used were $d/\Delta x = 9$, $t_p/\Delta t = 30$, and $f_c = 0.9$ Hz. The error norms were calculated over $12\text{s} \le t \le 22\text{s}$. 176

Figure 7.10: (a) Raw and LCSR-shifted experimental A0 data for run qCHIt3f200 and (b) resulting local heat flux for probe A0. 178

Figure 7.11: Space-marching inverse results for run qCHIt3f200 for (a) surface temperature and (b) surface heat flux. Parameters used were $d/\Delta x = 21$, $t_p/\Delta t$ = 21.5, and $f_c = 0.9$ Hz. The error norms were calculated over $12\text{s} \le t \le 22\text{s}$. 179

Figure 7.12: (a) Raw and LCSR-shifted experimental A0 data for run qRHIt5f200 and (b) resulting local heat flux for probe A0. 180

Figure 7.13: Space-marching inverse results for run qRHIt5f200 for (a) surface temperature and (b) surface heat flux. Parameters used were $d/\Delta x = 21$, $t_p/\Delta t = 21.5$, and $f_c = 1.5$ Hz. The error norms were calculated over $12s \leq t \leq 22s$. 181

Figure 7.14: (a) First and (b) fifth time derivative of shifted temperature data from run qCLOt3f200 with $f_c = 0.9$ Hz. 183

Figure 7.15: Global time inverse (a) temperature and (b) heat flux results using global time inverse method with $N = 4$ and $f_c = 0.9$ Hz for run qCLOt3f200. Discontinuity seen when single filter method of obtaining time derivatives is employed. The error norms were calculated over $12s \leq t \leq 22s$. 184

Figure 7.16: Effect of increased sampling rate on global time inverse method. Inverse (a) temperature and (b) heat flux results for run qCLOt3f1200 using global time inverse method with $N = 4$ and $f_c = 0.9$ Hz. The error norms were calculated over $12s \leq t \leq 22s$. 185

Figure 7.17: Global time inverse (a) temperature and (b) heat flux results using global time inverse method with $N = 4$ and $f_c = 0.9$ Hz for run qCHIt3f200. The error norms were calculated over $12s \leq t \leq 22s$. 186

Figure 7.18: Global time inverse results for (a) temperature and (b) heat flux using data from run qRHIt3f200 with $N = 4$ and $f_c = 1.5$ Hz. The error norms were calculated over $12s \leq t \leq 22s$ 187

Figure 7.19: Uncertainty in global time inverse results for (a) temperature and (b) heat flux using data from run qRHIt3f200 with $N = 4$ and $f_c = 1.5$ Hz. The error norms were calculated over $12s \leq t \leq 22s$. 190

Figure 7.20: Calibration integral method data for calibration qCHIt10f200 and real run qCLOt3f200. (a) Actual calibration and real run heat flux and (b) calibration and real run temperature histories 194

Figure 7.21: (a) First and (b) second temporal derivative of temperature data from calibration run qCHIt10f200 and real run qCLOt3f200. Derivatives were taken using Gaussian filter function. 195

Figure 7.22: Calibration integral method inverse results for (a) temperature and (b) heat flux using calibration run qCHIt10f200 ($f_c = 1.1$ Hz) and real run qCLOt3f200 ($f_c = 0.9$ Hz). The error norms were calculated over $12s \leq t \leq 22s$ 197

Figure 7.23: Calibration integral method inverse results for (a) temperature and (b) heat flux using calibration run qCHIt10f1200 ($f_c = 0.9$ Hz) and real run qCLOt3f1200 ($f_c = 0.9$ Hz). The error norms were calculated over $12s \leq t \leq 22s$. 198

Figure 7.24: Calibration integral method inverse results for (a) temperature and (b) heat flux using calibration run qCHIt10f200 (f_c = 1.1 Hz) and real run qCHIt3f200 (f_c = 0.9 Hz). The error norms were calculated over 12s ≤ t ≤ 22s..... 199

Figure 7.25: Calibration integral method inverse results for (a) temperature and (b) heat flux using calibration run qCHIt10f200 (f_c = 1.1 Hz) and real run qCHIt3f200 (f_c = 1.5 Hz). The error norms were calculated over 12s ≤ t ≤ 22s..... 200

Figure 8.1: Flow chart for preprocessing of data for use in two-probe inverse analysis..... 205

Figure 8.2: Inputs for inverse problem using data from run qCHIt3f200. (a) Raw, filtered, and shifted temperature data for both probes and (b) local heat flux at both probe sites using the single- and two-probe approach. Cutoff frequencies used were $f_{c,A0}$ = 0.9 Hz and $f_{c,B0}$ = 1.1 Hz..... 206

Figure 8.3: Two-probe inverse results for surface (a) temperature and (b) heat flux. Data used from run qCHIt3f200 seen in Figure 8.2..... 208

Figure 8.4: Inputs for inverse problem using data from run qRHIt5f200. (a) Raw, filtered, and shifted temperature data for both probes and (b) local heat flux at both probe sites using the single- and two-probe approach. Cutoff frequencies used were $f_{c,A0}$ = 1.5 Hz and $f_{c,B0}$ = 1.1 Hz..... 209

Figure 8.5: Two-probe inverse results for surface (a) temperature and (b) heat flux. Data used from run qRHIt5f200 seen in Figure 8.4..... 210

Figure 8.6: Comparison of two-probe inverse results with single-probe global time and calibration integral method for surface (a) temperature and (b) heat flux. Data used from run qCHIt3f200 seen in Figure 8.2..... 212

Figure 8.7: Comparison of two-probe inverse results with single-probe global time and calibration integral method for surface (a) temperature and (b) heat flux. Data used from run qRHIt3f200 seen in Figure 8.4..... 213

Figure 8.8: Inputs for inverse problem using data from run qCHIt10f200. (a) Raw, filtered, and shifted temperature data for both probes and (b) local heat flux at both probe sites using the single- and two-probe approach. Cutoff frequencies used were $f_{c,A0}$ = 1.1 Hz and $f_{c,B0}$ = 1.3 Hz. Note semi-infinite medium condition is violated at t = 22s..... 217

Figure 8.9: Two-probe inverse results for surface (a) temperature and (b) heat flux. Data used from run qCHIt10f200 seen in Figure 8.8. Note semi-infinite medium condition is violated at t = 22s..... 218

Figure 8.10: Inputs for inverse problem using data from run qCH10t10f1200. (a) Raw, filtered, and shifted temperature data for both probes and (b) local heat flux at

both probe sites using the single- and two-probe approach. Cutoff frequencies used were $f_{c,A0}$ = 1.0 Hz and $f_{c,B0}$ = 1.3 Hz. 220

Figure 8.11: Effect of increasing the data density on the two-probe global time inverse results for surface (a) temperature and (b) heat flux. Data used from run qCHIt10f1200 seen in Figure 8.10..... 221

Figure 8.12: Uncertainty bands for actual and inverse predicted surface (a) temperature and (b) heat flux. Data used from run qCHIt10f200 seen in Figure 8.8. 222

Figure A.1: Sketch of drilled hole geometry and uncertainty of hole depth..... 246

List of Tables

Table 3.1: Predicted heat flux RMS error as a function of the sampling rate, $\bar{f}_s$, projection order, *N*, and choice of cutoff frequency, $\bar{f}_c$; $\bar{f}_{c,mean}$ and $q_{RMS,mean}$ are average values resulting from five independent noise distributions. 74

Table 4.1: Properties of Copper Bronze. 79

Table 4.2: Differentiator components used in generating results displayed in Figure 4.10 where $\left\|\tau_{lag}\right\|_{\infty} = \max_{f\in[0,f_{c,dif})}\left|\tau_{lag}\right|$ 88

Table 4.3: Components used in constructing the low-pass filter displayed in Figure 4.12. 95

Table 4.4: List of test equipment used in generating all displayed electronic data. 95

Table 4.5: Type T thermocouple calibration data T [20.3°C, 46.6°C]. Calibration performed after amplification. 97

Table 4.6: Descriptive times for the thermocouple drop tower run. 106

Table 5.1: Thermophysical and electrical properties of materials used. 110

Table 5.2: Measured distances for the sandwich experiment. 110

Table 5.3: Probe distance and resistance measurements. 112

Table 5.4: List of equipment and material used in sandwich experiment. 113

Table 5.5: Experimental details of the 9 sandwich experiment runs performed. 119

Table 6.1: LCSR results for all installed sandwich experiment probes. 143

Table 7.1: Inverse error norms for temperature and heat flux calculated over $12s \le t \le 22s$. Global time method uses the double filter for derivatives. Calibration Integral uses the thermocouple temperature as the kernel (rather than the heating rate). 174

Table 7.2: Global time inverse method error norms for run qCLOt3f200 189

Table 8.1: Inverse error norms for temperature and heat flux using both the one- and two-probe approaches. Calibration Integral uses the thermocouple temperature as the kernel (rather than the heating rate). The time range indicates the domain used to calculate the error norms. 214

Table A.1: Uncertainty parameters for actual surface heat flux calculation..... 239

Table A.2: Contribution of uncertainty in k, ρ, C, and d to the overall uncertainty in the inverse predicted surface temperature and heat flux for different values of N. Temperature uncertainty is in °C and heat flux uncertainty is in W/cm^2. Data used from run qCHIt3f200..... 248

Table A.3: Contribution of uncertainty in temperature data and its temporal derivatives to the overall uncertainty in the inverse predicted surface temperature for different values of N in °C. Data used from run qCHIt3f200..... 248

Table A.4: Contribution of uncertainty in heat flux data and its temporal derivatives to the overall uncertainty in the inverse predicted surface temperature for different values of N in °C. Data used from run qCHIt3f200..... 248

Table A.5: Contribution of uncertainty in temperature data and its temporal derivatives to the overall uncertainty in the inverse predicted surface heat flux for different values of N in W/cm^2. Data used from run qCHIt3f200..... 249

Table A.6: Contribution of uncertainty in heat flux data and its temporal derivatives to the overall uncertainty in the inverse predicted surface heat flux for different values of N in W/cm^2. Data used from run qCHIt3f200..... 249

List of Symbols

Symbols

a_P finite difference coefficient, subscripts E, W also used, W/(m^2•K)

a_P^0 finite difference storage coefficient, W/(m^2•K)

C specific heat capacity, J/(kg•K)

d x-distance from the surface to the embedded sensors, m

f frequency, Hz

f_c cutoff frequency used in digital filter, Hz

f_n discrete value of frequency, Hz

f_s sampling rate, Hz

F linear operator for global time inverse method

Fo Fourier number (dimensionless time), $\alpha t/d^2$

Fo_{cv} nodal Fourier number, $\alpha\Delta t/\Delta x^2$

Fo_p dimensionless penetration time $\alpha t_p/d^2$

k thermal conductivity, W/(m•K)

L width of finite domain, m

N number of computational nodes in the x-direction

n a certain node in the x-direction

$\overline{q}$ dimensionless heat flux, q/q_s

q_d heat flux at sensor site, W/m^2

q_s maximum surface heat flux, W/m^2

q heat flux in the x-direction, W/m^2

P number of samples in time

R residual

T temperature variable, °C

T_d temperature data at sensor site, °C

T_i initial temperature, °C

t time variable, s

t_{max} maximum time in sampled data, s

t_{on} time at which the surface source is turned on, s

t_p penetration time, s

t_{ref} reference time value, d^2/α

U_ψ uncertainty in variable ψ

x spatial variable in the x-direction, m

x_n discrete value of x in space, m

z exponential power used in penetration time estimation

α thermal diffusivity, m^2/s

Δt time step for the finite difference method, s

Δx distance between nodes in the x-direction, m

ε measurement error

η dimensionless spatial variable, x/d

θ dimensionless temperature response, $\theta = \dfrac{T(\eta\, d, Fo\, d^2/\alpha) - T_i}{q_s d/k} = \theta(\eta, Fo)$

λ sensor characteristic, $s^{1/2}$

ρ density, kg/m^3

σ standard deviation

τ sensor characteristic, sometimes time constant, s

ϕ_1 first minimization function for determination of cutoff frequency

ϕ_2 second minimization function for determination of cutoff frequency

Accents

$(\hat{\ })$ filtered

$(\tilde{\ })$ noisy

$(\bar{\ })$ dimensionless

$(\dot{\ })$ time derivative

Subscripts

est estimated

exact exact value

inv result from inverse projection

mean mean of function or variable

num numerical simulation

RMS root mean square

TC thermocouple

Chapter 1: Introduction

The inverse heat conduction problem (IHCP) involves estimating the surface thermal condition without the use of surface-mounted sensors. Although the goal of the IHCP can be to resolve a variety of surface conditions – i.e., convection heat transfer coefficient, radiation heat transfer, surface heat flux, and temperature – the prediction techniques are generally identical. Resolution of the surface condition always involves projecting interior data (an ill-conditioned procedure) to the surface. Temperature and heat flux measurements are taken below the surface, and the surface thermal condition is projected using the interior data. IHCPs are of particular interest when the surface is under a harsh thermal environment, such as high temperatures and/or high heat fluxes, which precludes the use of sensors on the surface. Applications of the IHCP include atmospheric reentry, solid rockets, nozzles, hypersonic flow, quenching, and fire research.

There are several difficulties that arise when attempting to resolve the inverse heat conduction problem. These issues will be briefly introduced here, discussed further in the Literature Review, and expanded upon in subsequent chapters.

The IHCP is well-known to be ill-posed – i.e., noise in the data will be magnified in the surface projection [1, 2]. The physics of conduction provide a venue for the explanation of this phenomenon. In the forward (or direct) problem, diffusion damps out high frequency oscillation as the thermal front passes from the surface through the body. In the opposite direction (inverse), any high frequency oscillations present in the data (i.e., noise) are amplified as the surface condition is projected from the sensor site [1, 2]. Therefore, all inverse techniques must employ some form of regularization of the data which is a nontrivial task.

Another difficulty encountered when dealing with the IHCP is that temperature data are required from embedded sensors. Often these sensors are thermocouples which are characterized by the first order model – i.e., the temperature reported by a thermocouple is not the temperature of the medium. This is due to the probe's sensor characteristics (size, thermal capacitance, contact resistance, or lead losses effects). As the effect of the sensor characteristics increases, the difference between thermocouple temperature and medium temperature also increases. Therefore, it is essential to quantify and account for sensor characteristics before inverse projections are made.

Also tantamount to the resolution of the surface condition with in-situ data is an understanding of the penetration time. An embedded sensor will require a finite amount of time to feel a change in the surface condition[3]. We call this amount of time the penetration time. Therefore, transient inverse predictions will not be capable of resolving changes in the surface condition that occur more rapidly than the signal can penetrate through the medium.

Once an understanding of the physics encompassed by the inverse heat conduction problem is achieved, one must select a projection technique whereby the data from embedded sensors will be used to predict the surface thermal condition. There are several methods available to resolve the IHCP including "exact solutions," space-marching, sequential function specification, control volume techniques, non-integer system identification (NISI) methods and others (see [1]). Complexity of the inverse solution schemes can range from a few lines of code, to highly involved. Regularization can be incorporated into the projection scheme itself, or it can be used as an external process.

Coupled with the projection scheme is the treatment of the time. Beck et al. [1] classify three approaches to the time domain. In the first approach, the projection scheme incorporates all time data up to the current time. The second approach requires use of all time up to the current, plus a few future time steps of data. The third domain utilizes all time data (i.e., global time). Global time methods are highly appealing as they allow the smallest time steps in the inverse estimation. However, they require the resolution of higher order time derivatives of temperature, which can be problematic when dealing with noisy data.

After selecting a projection method, a test case using errorless data should be used. Analysis of the IHCP projection algorithm for the case of errorless data provides two distinct advantages. First, an inverse result based on errorless data will demonstrate the method's maximum attainable stability and accuracy – that is, the addition of noise will only worsen the inverse projection. Second, since IHCP projection methods are numerical and, therefore, subject to round-off error, the scenario under which round-off error should be studied is the case of errorless data. Despite the fact that few researchers address this issue explicitly, round-off errors do play an important role in the stability and accuracy of the inverse projection.

The final IHCP method then consists of a projection technique, regularization and sensor characterization. It is important for an IHCP technique to be experimentally validated. Oftentimes, noisy data is simulated as either a uniform or Gaussian distribution, having a zero mean, by way of a random number generator. The simulated noise is added to an exact solution and is supplied to the inverse scheme as "data." This approach has merit, and is especially convenient when no experimental data are available. However, in order for an inverse method to be truly validated, it should use real data from a physical experiment.

1.1 Literature Review

Projection Methods

The surface condition for an IHCP can be resolved using a variety of techniques. It would be impossible to document all IHCP methods. Therefore, the intent of this literature search is to provide a sampling of the most commonly used techniques. These include exact solutions, function specification, space-marching and finite difference, calibration methods and others.

One of the early inverse projection schemes was proposed by Burgraff [4] and used an exact solution for the transient one-dimensional IHCP with provided temperature and heat flux data at an embedded sensor site. An infinite series involving time derivatives of the temperature and heat flux data was truncated to two terms, and the surface heat flux was found. The time derivatives of temperature and heat flux were found by differentiating a polynomial representation of the simulated input data. While this method provided a clear investigation using errorless data, measurement error analysis was not included. Additionally, accuracy was limited since only two terms of the infinite series were used. Greater accuracy would require higher time derivatives of the data which would become problematic since the data were approximated by polynomials.

Beck [5] first introduced the function specification method where the heat flux at the surface was assumed a functional form over each time interval – i.e., constant, line segment, parabola, etc. For a detailed discussion on this method, see [1, 5-8]. A number of future temperature data (user specified) were generally included in the formulation to overcome measurement error. A least squares approach was used to minimize the difference between the

temperature at the current time step and the future temperatures. This approach successfully limited the method's vulnerability to measurement error when more future temperatures were used; additionally, smaller time steps were possible, though the time step size was still limited. A difficulty with this method is that the exact number of future temperatures that should be incorporated is arbitrary; indeed this number depends on the (unknown) surface boundary condition. Also commonly used with the function specification method is Tikhonov regularization [1, 9] which is a modification of the least squares minimization.

D'Souza [10] first proposed the concept of "space-marching" where the inverse space-time domain was discretized, and the spatial and temporal derivatives of the heat equation were replaced by finite differences. A fully-implicit in time finite difference scheme was applied with temperature data at two locations as input. This method is very attractive because of its simplicity and its allowance for small time steps. However, no regularization was used which caused the surface projection to be unstable in the presence of measurement error.

Subsequent space-marching techniques have been shown to provide stability in the presence of measurement error through a variety of methods. Al-Khalidy [11] used a Savitzky-Gollay digital filter to remove the noise. This type of filter is essentially a least squares fit of the data to a polynomial. A similar filtering approach was used by Taler [12]; however, Gram orthogonal polynomials were used as a basis set. However, Frankel et al. [13] have shown that least squares does not assure good representation of derivatives. Mollification, a type of filtering which uses an integral kernel as the regularization parameter, has been shown to stabilize the space-marching approach [14-16]. Carasso [17] reviewed and proposed a class of different space-marching schemes where the heat equation was approximated with varying combinations

of space and time differences without external regularization. The most successful of these algorithms were those that included future information. Carasso [18] later incorporated Tikhonov regularization [1, 9] into space-marching schemes.

An alternative to traditional inverse techniques is a calibration approach. One such method is the non-integer system identification (NISI) technique [19-21]. This method generally uses a null-point calorimeter as the sensor, although the technique can be applied to other geometries as well. A known heat source (laser) is first used as a calibration source to determine the relationship between the surface heat flux and the observed sensor temperature response. In this way, the installed sensor characteristics, depth of the sensor, and material properties are accounted for in calibration coefficients which are determined via least squares. An unknown heat flux can then be determined from the observed sensor temperature response and the calibration coefficients. While useful, the NISI method [19, 21] is limited as it was derived assuming an isotropic material with constant properties and a one-dimensional, semi-infinite geometry.

Recently, a new integral calibration approach has been suggested by Frankel et al. [22]. For the case of a semi-infinite medium, a calibration run is conducted with a known heat source, and the transient sensor temperature response is stored. A second "real" run is then conducted and the unknown heat source is resolved by solving the Volterra integral of the first kind given by

$$\int_{u=0}^{t} q_{run}(0,u)K(d,t-u)du = f(t) \tag{1.1}$$

where the kernel involves the calibration temperature history, and $f(t)$ involves the calibration heat flux and the real run temperature history. In contrast to the NISI method which calculates

calibration coefficients from the calibration data, this approach incorporates the calibration data directly into the solution integral. Additionally, this approach was derived with a unified mathematical theory which will lead to higher dimensions, orthotropic materials, and finite-width samples. While the calibration approach is attractive as it eliminates the need to have accurate knowledge of the sensor depth, material properties, and sensor characteristics, conduction lead losses, caution must be used as the physics of the problem are hidden within the calibration data.

The above is merely a sample of the inverse methods available in the literature. Others include the control volume method [23, 24], maximum entropy method [25], conjugate gradient method [26], finite element method [6], boundary element methods [6, 27], Green's functions [7], neural networks [28, 29], wavelet-Galerkin method [30], and integral transforms [31].

Given the wide variety of projection schemes available, this work will first focus on finite difference based (space-marching) methods. There are three reasons for this. First, finite difference based methods are inherently simple in concept and straightforward. Second, the user is free to apply any form of external regularization to the scheme as needed. Third, finite difference methods are computationally inexpensive; therefore, parametric investigations can be easily conducted by varying the spatial mesh size, time step size, and any regularization parameters. However, given the promise of the newly developed calibration integral approach, this technique will also be investigated.

Errorless Data

The majority of previous investigations of inverse stability focus on the effect of measurement error on the stability and accuracy of the IHCP method. While this is important

(see Measurement Error section below), a small amount of round-off error will amplify in the ill-conditioned inverse projection. For example, Elden [32] provides an analysis of the effects of finite differencing the time derivative of the heat equation. His results show, however, that as the measurement error decreases to zero, the time step size should also decrease to zero. This cannot be true since round-off errors will propagate through the time differences even for errorless data as noted by Taler [12].

The author was only able to find one study where the effect of round-off error on the inverse projection was studied and even then only indirectly. Carasso [17] investigated the "amplification factor," a function of the spatial and temporal mesh, of 18 different space-marching algorithms. Carasso's expression for the error in the inverse projection involved, among other terms, the product of the amplification factor and the round-off error. His findings indicated that implicit in time formulations amplified round-off error more than finite difference formulations involving future information. However, a parametric analysis was not conducted by varying both the spatial and temporal mesh to obtain a stable and unstable region. The spatial mesh was fixed at 1000 nodes in the inverse domain. Clearly, there is a gap in the literature concerning the susceptibility of space-marching schemes to round-off error and the identification of a stability criterion.

Measurement Error

In practice, continuous errorless data does not exist. Random fluctuations (noise) are present in all temperature and heat flux measurements. The noise is amplified in the inverse projection process, which results in an unstable surface prediction, even if a stable mesh (as determined from errorless data) is used. Therefore some type of regularization must be used to

"smooth" the data. Considerable effort has been expended by previous researchers on the development of appropriate regularization techniques. A sampling of the literature is provided below.

One of the first regularization methods was proposed by Beck [1, 5, 33]. He suggested the use of future temperatures to stabilize the surface prediction at the current time step. The reason for this is that future sensor temperatures contain information about the current surface condition. A least squares procedure is utilized to incorporate the future temperatures. However, a clear guide is not provided as to 1) when future temperatures are required for stability and 2) how many future temperatures should be used when required. Indeed, if more future times are incorporated into the algorithm than necessary, the resulting surface heat flux prediction is shown to be attenuated and delayed.

A similar regularization method was proposed by Tikhonov and Arsenin [9]. In Beck's procedure [1], the difference between future temperatures and the current temperature were minimized in the least squares sense. In Tikhonov regularization, the product of a "regularization parameter" with heat flux terms was added to this minimization. Unfortunately, this parameter does not have a physical interpretation, and the value of the regularization parameter can vary by four or more orders of magnitude. Additionally a trial-and-error method is suggested for determining the necessary value of this parameter [1].

Digital filtering is another method used for regularizing the data. Recently, Beck [8] used the "filter coefficient method" in combination with Tikhonov regularization. In this scheme, an external regularization method is employed to determine the required filter coefficients. Digital filtering via mollification has been demonstrated to stabilize the inverse problem [14-16]. Al-

Khalidy employed both Kalman filtering [24] and a Savitzky-Gollay digital filter [11] in conjunction with the control volume method to resolve the inverse problem. Frankel [2] has also shown the effectiveness of filtering in removing noise from the data. While not employed for an IHCP, Frankel showed that only a single, physically based cutoff frequency was necessary to regularize the data and obtain a smooth curve.

Another important area for the understanding of real data is the penetration time. The parabolic heat equation assumes an infinite speed of heat propagation [34-36]. However, it is known that in reality this does not occur. A finite time is required for an in-situ sensor to "feel" the heat applied at the surface of a slab. This is called the penetration time. Recently, de Monte et al. [23] defined the penetration time as the amount of time for a thermal disturbance to propagate a distance, d, into the solid at a level of one part in 10^z. They recommended a value of z=2 for engineering purposes, and proposed the approximation of penetration time as $0.05d^2/\alpha$ where d is the depth of the sensor below the surface and α is the thermal diffusivity. This result was based on their numerical observations.

To further elaborate on the concept of penetration time, the classical integral method [37] can be used to solve the heat equation (in terms of temperature or heat flux) for a semi-infinite medium at uniform initial temperature subject to a constant heat flux boundary at $x = 0$. Rather than a threshold argument, the in-depth heat flux is assumed to have a fourth-degree polynomial profile. The integral method solution for the dimensionless time required for the thermal front to reach a depth of d in the solid is $Fo = 0.075$ where Fo is defined as $\alpha t/d^2$. The integral method solution of the heat equation for a constant surface temperature boundary condition yields an identical solution for the penetration time [37].

Effect of Sensor Characteristics

For the IHCP, experimental data is supplied from embedded sensors (i.e., thermocouples). Since the sensor and lead wires will have different material properties than the sample, the observed temperature of the sensor will be different from the undisturbed sample. Further, thermocouples have non-negligible sensor characteristicss due to bead size and contact resistance with its surroundings. Woodbury [38] demonstrated the effects of a finite thermocouple time constant on the inverse projection using the function specification method; the classical triangular surface heat flux was used as the surface boundary condition. As expected, increasing values of time constant caused greater surface prediction attenuation and lag; a dimensionless time constant of $\alpha\tau/d^2 = 0.05$ yielded approximately a 4% reduction in the maximum surface heat flux with a lag of 0.1 (dimensionless time) – i.e., twice the time constant. Clearly, it is essential to quantify the time constant of the sensors used for inverse prediction.

Orientation of the thermocouple lead wires perpendicular to the isotherm will result in further discrepancy between the positional, undisturbed temperature of the sample and the observed temperature. As noted above, the NISI [19-21] and calibration integral [22] methods account for the effect of the thermocouple via the calibration data. Woolley [39] exhaustively investigated variations on a technique suggested by Beck [40] for correcting thermocouple measurements of this type. This correction technique uses observed thermocouple temperature and undisturbed positional temperature to obtain a calibration kernel. This calibration kernel can then be used on a different dataset to obtain the undisturbed, positional temperature given thermocouple data. This is a similar approach to the calibration integral and NISI method to accounting for the effect of the sensor characteristics. However, one disadvantage of Beck's

correction method is that it still requires accurate knowledge of the sensor depth and material properties. Further, an accurate model must be constructed to provide the necessary undisturbed temperature history for the calibration, and a value of contact resistance between the sensor and the host must be assumed.

The Loop Current Step Response (LCSR) technique [41, 42] provides another method by which the in-situ sensor characteristics of the thermocouple can be measured. The thermocouple is installed in the sample, and the sample is allowed to be at uniform initial temperature. An electric current is passed through the installed thermocouple, and the emf decay of the thermocouple is observed. The time constant is then found as the time corresponding to 63.2% of the overall decay. This technique is heavily used in nuclear power plants for both time constant determination and health monitoring of thermocouples and other temperature sensors.

Treatment of the Time Domain

The treatment of the time domain in IHCP algorithms is of highest importance, as this usually determines the method's stability (or instability) in the presence of measurement error. For example, the space-marching method of D'Souza [10] utilizes all previous time steps in the calculation of the present time step, but no future information. With no external regularization, this method is unstable in the presence of measurement error. Carasso [17, 18] offers several space-marching schemes where information from future time steps are incorporated into the determination of surface heat flux at the current time step. Consequently, these methods can be stable for some choices of time step size. However, in the above examples, the time domain has been discretized. Therefore, only a small portion of the entire time domain is utilized, and (significant) round-off is introduced into the inverse prediction.

An alternative approach has been taken by Frankel and Keyhani [43]. They incorporate a weighted-residual method of collocation with Chebyshev polynomials of the first kind as a basis set, and resolve the entire space-time domain at once. By treating time in a global sense, the problem is stabilized without the introduction of round-off error. Regularization is employed by choosing the number of terms to include in the series. Other whole domain methods have also been proposed [1]. Whereas discrete time methods become unstable as the time step size is decreased, this is not a concern for whole domain methods since time is made continuous. In general, this benefit is at the cost of computational time.

Frankel [2] has proposed the use of a Gaussian low-pass filter for regularization. This can be used irrespective of the projection scheme used, and provides a global time regularization – i.e., all future and all past information is used in the regularization of the current time. This form of regularization is computationally inexpensive, and provides an analytical function as the output rather than discrete time values. However, it should be noted that incorporation of this filter into a traditional space-marching method will negate some of the "global time" benefits. This is because traditional space-marching schemes utilize a finite difference representation of the time derivative which will magnify measurement error.

To this end, Taler [23] has used a control volume technique without differencing the time derivative of the heat equation. Instead, the method of Burgraff [4] was used to obtain the heat flux at the sensor site, and a cubic spline (in time) was fit through the temperature and heat flux data. Temporal derivatives were then taken from the spline equations and incorporated directly into the inverse projection. Stability was achieved, but Taler's results were limited to three control volumes which utilized two time derivatives of the sensor temperature and heat flux.

As seen in Taler's algorithm [23], higher-time derivatives of the temperature and heat flux are needed at the sensor site. This is problematic since this involves differentiation of noisy data, which amplifies the error. Frankel et al. [44] have demonstrated a sensor capable of measuring the first time derivative of temperature. Additionally, their design can be cascaded in series so as to provide the higher time derivatives of temperature necessary for the global treatment of the time domain.

Experimental Verification

As noted above, experimental verification of inverse techniques is essential since the IHCP is ill-posed and, therefore, sensitive to measurement error present in all real data. Most inverse investigations simulate noise by adding Gaussian random error (fixed standard deviation and zero mean). This is generally acceptable, but a rigorous test of the inverse scheme should be performed utilizing real experimental data wherever possible.

One experimental investigation was performed by Beck et al. [7]. A 0.86mm thick mica heater was sandwiched between two identical layers of 9.14mm thick carbon-carbon, and identical outer layers of ceramic insulation. A thin heating element was located along the centerline of the mica heater. In this way, a line of symmetry was created through the center of the mica heater. Seven thermocouples were placed along the mica/carbon interface, which produced consistent temperature readings. The temperatures reported by each of these thermocouples were averaged at each time step to obtain one value of the mica/carbon interface temperature. A variety of inverse techniques were employed on the resultant data including function specification, Tikhonov regularization, and iterative regularization with Green's functions. The time scale for this experiment was very fast; using the definition of penetration

time as discussed later in Chapter 2, a meaningful signal should reach the mica/carbon interface in 0.2μs. However, the inverse results required approximately 1s to resolve the heat flux, despite a sufficiently fast sampling rate of 100 Hz.

Taler and Zima [45] conducted a one-dimensional experiment using a steel tube as the inverse domain. The tube had an inner diameter of 0.1085m and an outside diameter of 0.1385m. The external surface of the tube was stated to be "perfectly insulated." The temperature of the tube was at an initial uniform state; the inner wall is suddenly heated by hot water. The water temperature changed over time since the water did not flow through the tube. The tube/insulation interface temperature was sampled every 5s and supplied as input to a control volume inverse scheme. Though the number of control volumes used was not specified, previous research by Taler [23] used only three control volumes in the inverse projection. The inner wall temperature was monitored for comparison with the inverse scheme. The accuracy of the inverse scheme was only measured by comparison of the inverse temperature prediction with the inner wall temperature measurements. Agreement between these two values was high for large time ($t > 45$s), but low for the initial transient of the experiment. The reason for this is likely due to the distance of the sensor from the surface; the penetration time as defined later in Chapter 2 was 5.6s. Additionally, the uncertainties present in the temperature measurements were not quantified.

Ji and Jang [46] constructed a one-dimensional experiment utilizing a kapton film heater sandwiched between two identical copper plates with thickness of either 1mm or 2mm. A thermal flux meter (dimensions 1 x 1 x 0.055 in.) was placed on the back surface of one of the copper plates, and a type K thermocouple was soldered to the center of the same back plate. A

"heat sink paste" was used to coat all interfaces to ensure good contact and uniform heat transfer. For the case of a 1mm copper plate, the penetration as defined later in Chapter 2 was approximately 0.75ms. The entire assembly was wrapped in asbestos and placed in a chamber for insulation. Data were collected at 50 Hz, and although the researchers state that a resolution of 12 bits was used, the accuracy of the data is unknown since the range of the data acquisition device was not provided. An additional area of concern is the measurement of the back surface flux. The thickness of the flux meter is nontrivial given the thickness of the copper plates used. Since the flux meter was only mounted on one side, the problem is not truly symmetric. The source heat flux measurement is, therefore, suspect. A Kalman filtering technique was used as the inverse scheme. While the general trend of the inverse predictions matched that of the direct input measurements, a lag can be seen. Additionally, the predicted flux magnitude was seen to vary by as much as 33% at the peak value.

1.2 Scope of Dissertation

The overall goal of this work is to provide a systematic methodology by which the difficulties associated with the inverse heat conduction problem outlined above can be resolved. First, a space-marching IHCP method (discrete space, discrete time) utilizing a Gaussian low-pass filter for regularization is studied. Second, a new discrete time, global time IHCP method is presented which requires higher time derivatives of temperature. The stability and accuracy of both methods are investigated for errorless data and in the presence of simulated noise. A sensor capable of delivering higher time derivatives of temperature is demonstrated. Next, a physical experiment is presented, and methods for quantifying the sensor characteristics of embedded thermocouples are presented. Finally, the space-marching method, global time method and

calibration integral approach are used with the experimental temperature input data and the predicted surface heat flux is compared with the actual input surface heat flux.

Chapter 2: Space-Marching Method for Inverse Heat Conduction Problem

This chapter is a revised version of a paper to be submitted for publication authored by Bryan S. Elkins, Majid Keyhani, and Jay I. Frankel:

Elkins, B. S., Keyhani, M., and Frankel, J. I., in preparation, "Methodology for stable and accurate resolution of the inverse heat conduction problem." .

My primary contributions to this paper include (i) collaboration in conceptualization of work, (ii) development of the numerical method, (iii) writing of the computerized code, (iv) parametric investigation of the numerical method, and (v) most of the writing.

2.1 Space-Marching Method Introduction

The inverse heat conduction problem (IHCP) is highly sensitive to both measurement error and round-off error. The method presented in this chapter provides a simple means to circumvent both sources of error. The method consists of a systematic approach that may be summarized as:

- The role of penetration time on inverse analysis is clearly demonstrated, and the numerical value of the dimensionless penetration time (Fourier number) is established and experimentally verified.
- The dimensionless optimal temporal mesh (time-step normalized with the penetration time) for circumventing round-off error (limited to precision of the computation/computer) for the space-marching technique is established.

- To minimize the effect of measurement error on the inverse projection, a low-pass Gaussian filter with a physically-based cutoff frequency as the regularization parameter is utilized. The proposed procedure for determining the cutoff frequency exploits the physics of diffusion.
- The accuracy of an alternative method for obtaining heat flux data at the sensor site via an integral relationship between heating rate (using temperature data at sensor site) and heat flux (applicable to the case of a semi-infinite medium) is established.
- Using the proposed procedures to circumvent both round-off and measurement error, it is demonstrated that 10% error on temperature and heat flux data at sensor site results in less than 10% error on the resolved surface heat flux and temperature.

It is significant to note that the proposed methodology (a) does not amplify the input error as the data is projected to the surface (a common inverse prediction predicament), and (b) indeed reduces the projected error to the surface for both temperature and heat flux.

It is assumed that temperature and heat flux data are available with no delays, attenuation, etc. This is a significant assumption, and will be discussed further in Chapter 6. The focus of this chapter lies in the development of the numerical method to resolve the inverse heat conduction problem.

2.2 Problem Description

For demonstration, consider one-dimensional, constant property, isotropic heat conduction in a solid. The dimensional governing equation for this problem is given by

$$\frac{\partial T}{\partial t} = \alpha \frac{\partial^2 T}{\partial x^2}, \quad 0 \le x \le L, t \ge 0, \tag{2.1}$$

where $T = T(x,t)$, subject to the initial condition

$$T(x,0) = T_i,\ 0 \le x \le L, \tag{2.2}$$

where α is the thermal diffusivity and T_i is the initial condition. The solid is subjected to a surface (x=0) heat flux described by

$$q(0,t) = -k\frac{\partial T}{\partial x}(0,t), \quad t > 0, \tag{2.3}$$

where k is the thermal conductivity, and the back wall (x=L) is insulated

$$q(L,t) = -k\frac{\partial T}{\partial x}(L,t) = 0, \qquad t \ge 0. \tag{2.4}$$

Temperature and heat flux histories are known at the sensor site, $x = d$, where $d \le L$. The goal is to use the given sensor temperature $T(x=d,t)$ and heat flux $q(x=d,t)$ data to project and obtain the unknown surface conditions, $T(0,t)$ and $q(0,t)$. It is noted that for a finite domain of thickness $L > d$, the half-space condition exists in the solid up to the time that the thermal front reaches the $x = L$ boundary.

It is useful for analysis to non-dimensionalize the governing system. This is accomplished without loss of generality by employing the dimensionless variables θ for temperature, Fourier number Fo for time, η for space, and $\overline{q}$ for heat flux given as

$$\theta = \frac{T(\eta d, Fo\, d^2/\alpha) - T_i}{q_s d/k} = \theta(\eta, Fo), \tag{2.5}$$

$$Fo = \frac{\alpha t}{d^2}, \quad Fo \ge 0, \tag{2.6}$$

$$\eta = \frac{x}{d}, \tag{2.7}$$

and

$$\overline{q} = \frac{q_x}{q_s}, \tag{2.8}$$

where q_s is the maximum surface heat flux. The resulting equations are

$$\frac{\partial \theta}{\partial Fo} = \frac{\partial^2 \theta}{\partial \eta^2}, \quad Fo \geq 0,\ 0 \leq \eta \leq \frac{L}{d}, \tag{2.9}$$

$$\theta(\eta, 0) = 0, \qquad 0 \leq \eta \leq \frac{L}{d}, \tag{2.10}$$

$$\overline{q}(0, Fo) = -\frac{\partial \theta}{\partial \eta}(0, Fo), \quad Fo \geq 0, \tag{2.11}$$

$$\overline{q}(\frac{L}{d}, Fo) = 0, \ \ Fo \geq 0. \tag{2.12}$$

2.3 Penetration Time

The parabolic heat Eq. (2.1) assumes an infinite speed of heat propagation [34-36]. However, it is known that in reality this does not occur. A finite time is required for an in-situ thermocouple to "feel" the heat applied at the surface of a slab. This is called the penetration time and is denoted by t_p. Therefore, if a source at the surface is turned on at time $t = 0$, a sensor at a given depth, d, will measure a temperature $T = T_i$ for $t < t_p$ and a temperature $T > T_i$ for $t \geq t_p$. Inverse predictions will not be possible when using embedded measurements until $t > t_p$ since the thermal front has yet to reach the thermocouple.

The numerical experiments herein rely on the aforementioned parabolic heat equation, since $(T_{num} - T_i)$ at $x=d$ will be non-zero for $t > 0$. To circumvent this issue, we make an approximation of t_p and say that for $t < t_p$ all numerical results at $x=d$ are meaningless. The question is then how do we define penetration time? When using analytical data, we propose defining t_p as the time it takes the sensor to overcome a threshold value. For example, consider a

constant temperature boundary condition of T_0; for a threshold value of 1% of the surface temperature change ($T_0 - T_i$), the penetration time can be found to be $Fo = 0.075$ using the well-known exact solution for this problem [47]. For a constant surface heat flux case, the time for a sensor to feel 1% of the surface heat flux also occurs at $Fo = 0.075$. This 1% threshold concept suggests the definition of penetration time as

$$t_p = Fo_p \frac{d^2}{\alpha} = 0.075 \frac{d^2}{\alpha}, \tag{2.13}$$

A threshold concept was also proposed by de Monte et al. [48], where they defined the penetration time as the amount of time for a thermal disturbance to propagate a distance, d, into the solid at a level of one part in 10^z. A value of z=2 was recommended by [48] for engineering purposes (i.e., 1% of surface change), and proposed the approximation of penetration time given by

$$t_p = \frac{0.1 d^2}{\alpha z} = 0.05 \frac{d^2}{\alpha}, \tag{2.14}$$

which was based on their numerical observations.

Alternatively, the classical integral method [37] can be used to solve the heat equation (in terms of temperature or heat flux) for a semi-infinite medium at uniform initial temperature subject to a constant heat flux boundary at $x = 0$. If the heat flux is assumed to have a fourth-degree polynomial profile, the integral method solution for the dimensionless time required for the thermal front to reach a depth, d, is $Fo = 0.075$ where Fo is again defined in Eq. (2.6). The integral method solution of the heat equation for a constant surface temperature boundary condition yields an identical solution for the penetration time.

Experimentally, penetration time is defined as the instant at which the temperature data overcomes the uncertainty in the initial condition. In order to demonstrate this, a physical experiment was conducted (see Chapter 5 for full details). Two identical bronze plates were used (k = 58.7 W/(mK), ρ = 7450 kg/m^3, C_p = 419.0 J/(kgK)), [25] with dimension 0.1270m x 0.1397m and a thickness of 0.0403m. A 0.125 mm thick nichrome resistance heater with a resistance of 4.326 Ω was used as the source. The heater was sandwiched between two sheets of 0.002 in. thick mica for electrical insulation. This assembly was placed between the bronze plates to create a symmetric boundary condition. An in-house manufactured type T thermocouple with a bead diameter of 1.47mm was surface mounted on the back face of one of the plates. Temperature data were sampled at a rate of 10 Hz via TEMPpoint – a fully-isolated, low-noise data acquisition board manufactured by Data Translation. The source was activated with a voltage of 80.5 V_{RMS} after 15 seconds of lead data were taken. The resulting temperature history can be seen in Figure 2.1. The standard deviation of the lead temperature data was observed to be 6.96(10^{-3}) °C. The uncertainty in the initial condition was defined as

$$T_i(95\%) = T_{mean} \pm \sigma\tau_{95\%}, \tag{2.15}$$

where T_{mean} is the mean of the lead data, σ is the standard deviation of the lead data, and $\tau_{95\%}$ is student's t-distribution value for 95% confidence. Using a value of $\tau_{95\%}$ as 1.96 [49], the uncertainty in the initial condition was found to be ± 0.040 °C. The temperature was found to exceed the uncertainty in the initial condition after 6.8s of heating, which corresponds to a dimensionless penetration time of Fo_p = 0.079. Note that the difference between the experimental penetration time and the analytical value of Fo_p = 0.075 (1% change threshold) is

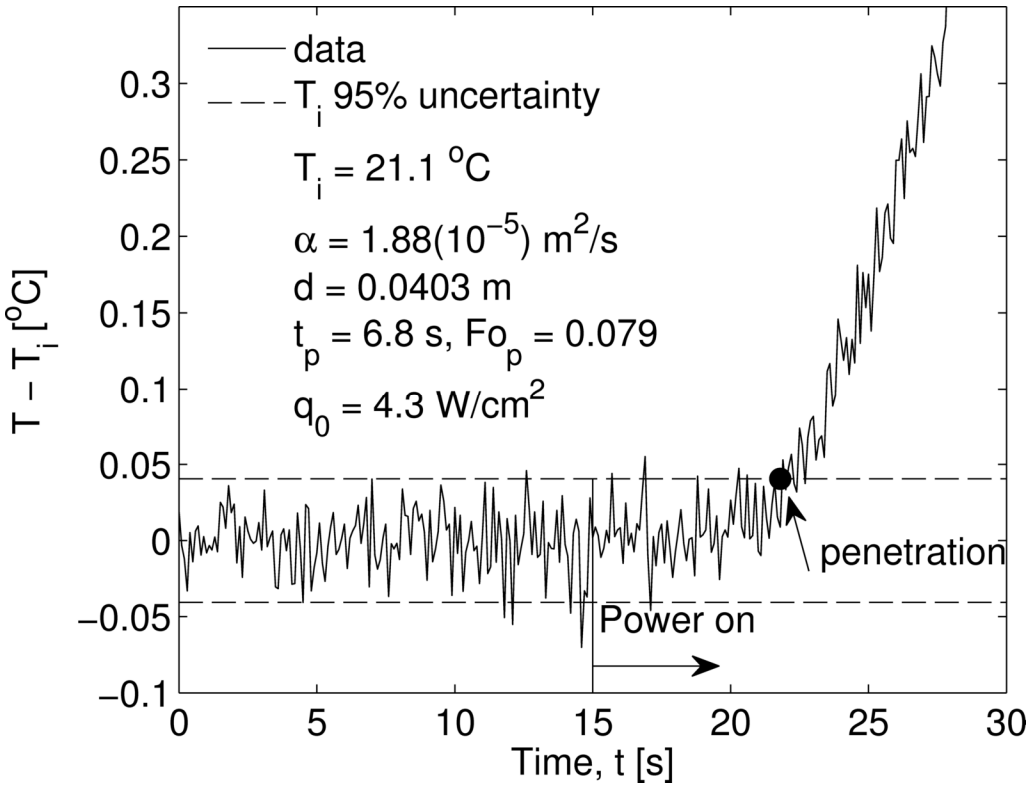

Figure 2.1: Illustration of lead data to capture background noise ($0 \leq t \leq 15$s) and experimental penetration time. Temperatures measured from a back face thermocouple resulting from a surface heat flux of 4.3 W/cm^2 switched on at 15s.

only 5%. The agreement between theses values suggests that $Fo_p = 0.075$ is a reasonable approximation for the dimensionless penetration time.

2.4 Inverse Method

For the inverse method presented here, it is assumed that the required temperature and heat flux data at $x = d$ ($\eta = 1$) are known via experimental data (with no delay or attenuation) or the exact solution. A straightforward implicit-in-time finite difference with space-marching approach is used to project the in-situ data to the surface. The domain $0 \le x \le d$ is discretized using equal spacing between all nodes such that

$$x_m = (m-1)\Delta x, \quad m = 1,2,..., M+1, \tag{2.16}$$

where $x_{m=1} = 0$ and $x_{m=M+1} = d$ are located at the surface and the sensor site, respectively. Control volume lines are drawn halfway between each node. This creates half control volumes at both $x = 0$ and $x = d$. The equations below are presented in dimensional form for clarity. The dimensionless forms can be easily derived using the dimensionless variables in Eqs. (2.5)-(2.8).

A general, implicit-in-time, finite difference formulation [50] is used to write the equations at each interior node "m" location such that

$$(a_P T)_m = (a_E T)_{m+1} + (a_W T)_{m-1} + (a_P^0 T^0)_m, \tag{2.17}$$

where the temperature subscript refers to the spatial node, superscript "0" refers to the previous time step, and temperatures without a superscript refer to the current time step. All "a" coefficients are given by Patankar's method [50] as

$$a_W = a_E = \frac{k}{\Delta x}, \tag{2.18}$$

$$a_P^0 = \frac{\rho C \Delta x}{\Delta t}, \tag{2.19}$$

$$a_P = a_W + a_E + a_P^0, \tag{2.20}$$

At the sensor node ($m=M+1$), we can manipulate Eq. (2.17) and solve for the temperature at the $m=M$ node such that

$$T_M = \frac{1}{a_W}\left(a_P^* T_d + q_d - a_p^{0*} T_d^0\right), \tag{2.21}$$

where T_d and q_d are the sensor data at the current time step, and T_d^0 is the sensor temperature at the previous time step. The coefficients are defined as

$$a_P^{0*} = \frac{\rho C \Delta x}{2\Delta t}, \tag{2.22}$$

$$a_P^* = a_W + a_P^{0*}. \tag{2.23}$$

Note that Eq. (2.21) solves directly for T_M in terms of sensor data. Similarly, the equations for nodes $2 < m < M$ are written as

$$T_{m-1} = \frac{1}{a_W}\left[(a_W T)_m - (a_E T)_{m+1} - (a_P^0 T^0)_m\right], \quad 2 < m < M. \tag{2.24}$$

Beginning with Eq. (2.21), we solve for the temperature just above the sensor; then using Eq. (2.24), we can project to the surface and find $T_{m=1} = T_{x=0}$. This provides a straightforward procedure where there is always only one equation and one unknown. No future times are used in the formulation. The surface heat flux is then given by

$$q_{x=0} = (a_P^* T)_{m=1} - (a_E T)_{m=2} - (a_P^{0*} T^0)_{m=1}. \tag{2.25}$$

For demonstration, three test cases of finite width slabs with an adiabatic boundary condition of $x=L$ are investigated. For test cases one and two, the temperature sensor is located at $x=d \ll L$

such that for the duration of the transient the thermal front does not reach the surface at $x=L$. Therefore, one can use the exact solution for the semi-infinite medium subjected to (case 1) a constant surface heat flux at $x=0$ [47] or (case 2) a pulse heat source at $x=0$ [51] to generate the temperature and non-zero heat flux data at $x=d$ and proceed with the inverse projection. For test case three, the temperature sensor is located at $x=d=L$ (an adiabatic boundary) and the surface at $x=0$ is subjected to the classical triangular heat source. The exact solution [1] is used to generate temperature data at $x=L$ with zero heat flux to proceed with the inverse projection. It should be added that in investigations with "data with error," error is added to the temperature and nonzero heat flux data at sensor site for test cases one and two. For test case three, error is added to the temperature data at $x=L$ and heat flux is taken to be zero which is the same approach used by other investigators who have studied this specific problem.

Test Case 1

Consider an isothermal semi-infinite solid subjected to a constant surface heat flux at time $t = 0$. The dimensionless exact solution [47] for this problem is

$$\theta(\eta, Fo) = \frac{2}{\sqrt{\pi}}\sqrt{Fo}\exp\left(\frac{-\eta^2}{4Fo}\right) - \eta\,\mathrm{erfc}\left(\frac{\eta}{2\sqrt{Fo}}\right), \quad \eta, Fo \geq 0, \tag{2.26}$$

and

$$\bar{q}(\eta, Fo) = \mathrm{erfc}\left(\frac{\eta}{2\sqrt{Fo}}\right), \quad \eta, Fo \geq 0, \tag{2.27}$$

where erfc(u) is the complementary error function with argument u [52]. A plot of the resultant inverse-predicted temperature and heat flux can be seen in Figure 2.2 using the exact data generated from Eqs. (2.26) and (2.27) as sensor data – i.e. no measurement error. The time axis

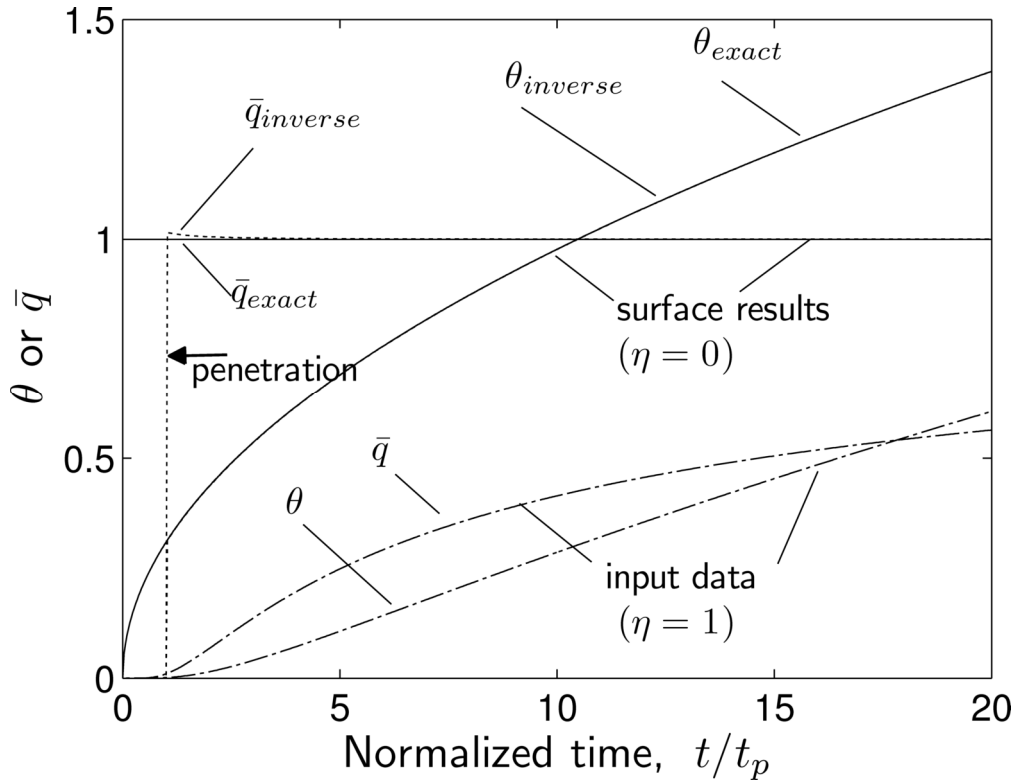

Figure 2.2: Inverse surface temperature and heat flux solution using "perfect," discrete data (ε = 0%) from the exact solution for test case 1. Mesh parameters used are $t_p/\Delta t = 30$ and $d/\Delta x = 9$.

is normalized by the penetration time, t_p. For this and all subsequent numerical simulations, dimensionless variables were used in double precision in MATLAB 7.8.0.347 (2009a) on a Dell Latitude E6400 with an Intel Core 2 Duo P8600 2.4 GHz processor. The simulation took 0.11 seconds to generate the "sensor" data and run the inverse code using the mesh parameters shown in Figure 2.2: $t_p/\Delta t = 30$ (number of temporal nodes per one penetration time) and $d/\Delta x = 9$ (number of spatial nodes). For $t > 2t_p$, the accuracy of the inverse predictions for the surface temperature and heat flux are 0.0029% and 0.0013%, respectively.

Clearly an inverse prediction for $t < t_p$ is very challenging since the thermal front has not reached the sensor yet; therefore the sensor temperature would remain at the initial condition value. However, it must be noted that the exact solutions, Eqs. (2.26) and (2.27), yield non-zero temperature and heat flux at $x=d$ for $t < t_p$ (infinite speed of propagation). Intuition suggests that we should, therefore, force the initial time step of the inverse method to be equal to the penetration time. The code would then be restricted to predicting the surface temperature and heat flux for $t > t_p$. However, this would remove the stabilizing effect that the lead data ($t < t_p$) has on the inverse method, and the surface prediction would blow up in the interval $t_p < t < 2t_p$. The sensor data for $t < t_p$ is, therefore, considered to be lead data and is allowed to be passed to the inverse code. The use of lead data is again utilized later when noise is added to the data and subsequently regularized with the aid of a digital filter. For the case of step change in surface heat flux imposed at time $t=0$ (no lead data taken), the presented inverse predictions do not show results for $t < t_p$ as the predictions are unreliable in this time interval.

2.5 Stability and Accuracy Investigation of the Inverse Method

When discussing the stability of a numerical method, it is important to note the subtle difference between stability and accuracy. We define accuracy as the percent difference between the inverse prediction and the exact solution at the surface. We define stability as a measure of the inverse prediction's smoothness. The difference between these two principles is demonstrated in Figure 2.3 which is generated using the exact solution for test case 1 with no measurement error as input to the inverse code. It is observed that a course mesh ($\Delta t = t_p$ and $\Delta x = d/2$), while stable, produces an inaccurate inverse prediction for time ($t < 5\ t_p$). Conversely, if the mesh is refined past the "optimized mesh," the inverse prediction becomes unstable due to significant round off error. The fine mesh results ($\Delta t = t_p/40$ and $\Delta x = d/30$), shown in Figure 2.3 clearly demonstrate the unstable nature of the results due to round off error. This instability is magnified if the mesh is further refined. It is also noted that the round off error amplifies as time progresses.

The distinction between accuracy and stability is further illustrated in Figure 2.4, which shows two plots of root-mean-square (RMS) error for the inverse prediction over the time interval $5t_p \leq t \leq 15t_p$ in percent of the surface exact solution as a function of nodal Fourier Number. The RMS error, Φ_{RMS}, is given by

$$\Phi_{\mathrm{RMS}} = \left[\left(i_{t2} - i_{t1} + 1 \right)^{-1} \sum_{i=i_{t1}}^{i_{t2}} \left(\frac{\Phi(t_i) - \Phi_i}{\Phi(t_i)} \right)^2 \right]^{1/2}, \tag{2.28}$$

where $\Phi(t_i)$ is the exact solution, Φ_i is the inverse prediction (temperature or heat flux) at time step i, and the time steps i_{t2} and i_{t1} correspond to the times $t = t_2$ and $t = t_1$, respectively, over which analysis is desired. Note that the chosen denominator does not vanish in the time interval

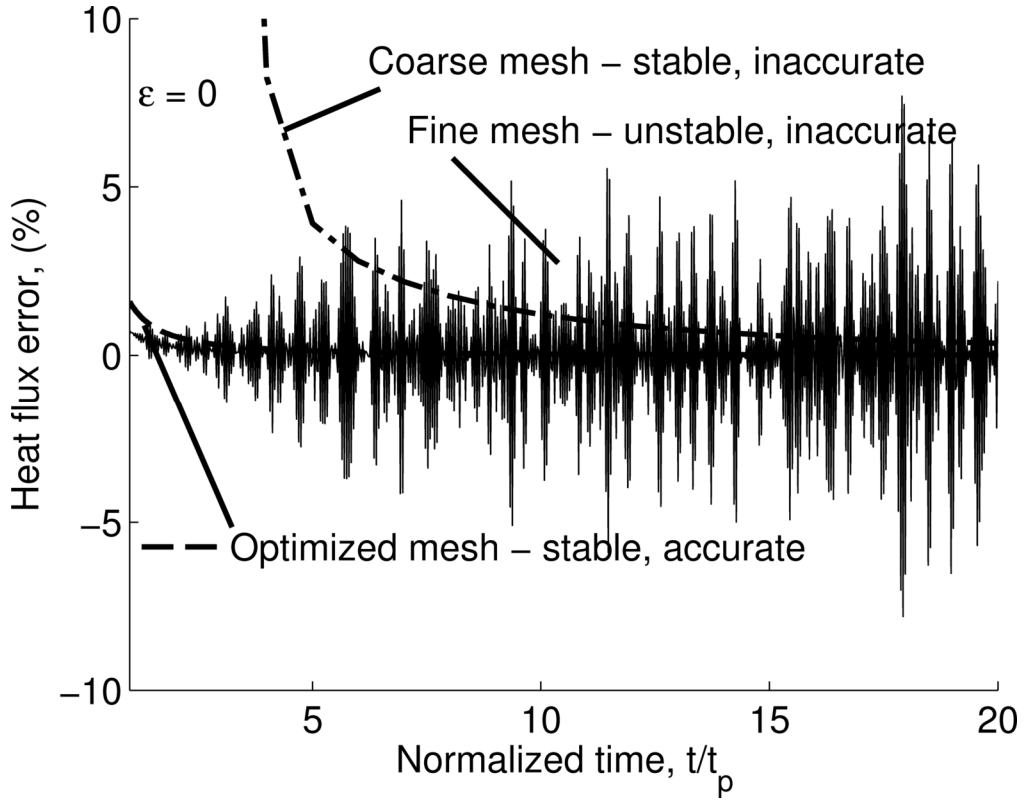

Figure 2.3: Comparison of inverse results for test case 1 using the exact solution as input data with varying mesh parameters: coarse mesh: $t_p/\Delta t = 1$, $d/\Delta x = 2$; fine mesh: $t_p/\Delta t = 40$, $d/\Delta x = 30$; and optimized mesh: $t_p/\Delta t = 30$, $d/\Delta x = 9$.

of interest. An alternative and potentially better suited denominator could involve the norm of the function $\Phi(t)$. The nodal (control volume) Fourier number is defined as

$$Fo_{CV} = \frac{\alpha \Delta t}{\Delta x^2}. \tag{2.29}$$

The exact solutions for temperature and heat flux at $\eta = 1$ with no measurement error for test case 1 are used as input to the inverse problem, and double precision is maintained for all variables. Figure 2.4(a) is created by fixing the spatial mesh and varying the temporal mesh while Figure 2.4(b) is created by fixing the temporal mesh and varying the spatial mesh.

In both plots, a coarse mesh results in a stable, but inaccurate prediction. As the mesh is refined, the accuracy improves until the prediction becomes unstable, i.e., the fine mesh causes the round-off error to become significant. Figure 2.4(a) (fixed spatial mesh) and Figure 2.4(b) (fixed temporal mesh) clearly show that by changing the "other" mesh parameter (temporal or spatial) and thus increasing or decreasing the nodal Fourier number, unstable-inaccurate or stable-inaccurate results will be obtained. These figures also show that the inverse prediction is more sensitive to the choice of temporal mesh than spatial mesh; Figure 2.4(a) shows a single optimized value for the temporal nodes, while Figure 2.4(b) suggests a range of optimum spatial nodes. Clearly, a definite stability criterion exists for this inverse method, which is a compromise between refining the spatial and temporal meshes.

Seeking this stability criterion, let us first explore the physics of the problem. For a constant heat flux surface boundary condition (test case 1), the heating rate, $\dot{\theta}(\eta = 0, Fo)$ should remain positive for $Fo > 0$. Similarly, $\ddot{\theta}(\eta = 0, Fo)$ should remain negative for $Fo > 0$. Taking advantage of these physical attributes, a stability condition is constructed such that if the inverse

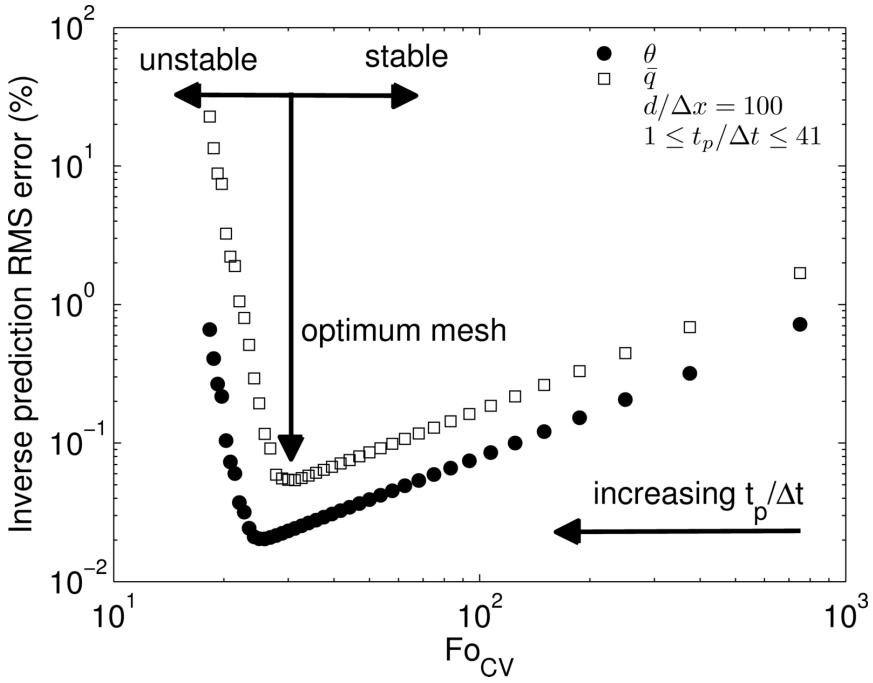

(a)

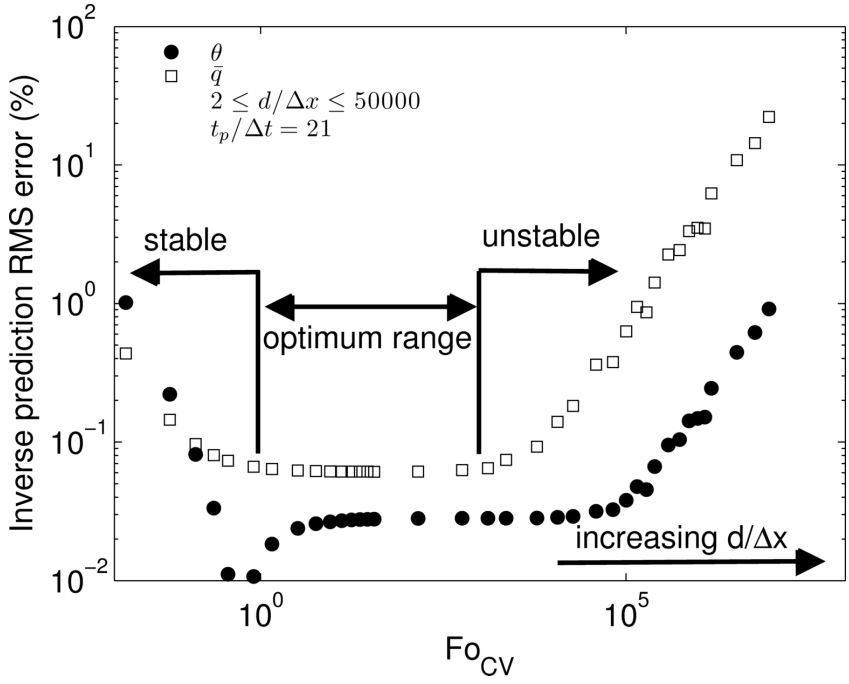

(b)

Figure 2.4: Inverse prediction RMS error for test case 1 over the interval $5 < t/t_p < 15$ for the dimensionless surface temperature and heat flux values using exact data for (a) fixed nodal spacing and (b) fixed temporal mesh.

prediction at the surface resulted in $\ddot{\theta}(\eta = 0, Fo) > 0$, the prediction is deemed unstable. An extensive stability analysis has been conducted using the exact solution as input and varying the spatial mesh as $3 \leq d/\Delta x \leq 10^6$ and the temporal mesh varying as $1 \leq t_p/\Delta t \leq 400$. Figure 2.5(a) shows the resulting stability criterion. This curve can be interpreted as follows: for a given spatial mesh (fixed location on vertical-axis), the temporal mesh may be refined (moving right on the horizontal-axis) until the stability limit is reached. Conversely, for a given temporal mesh (fixed location on the horizontal-axis) the spatial meshed may be refined (moving up on the vertical-axis) until the stability limit is reached.

This analysis provides a clear picture of how round-off error propagates, independent of measurement error (ε=0 for these results), through the inverse prediction. Using the derived stability criterion, mesh parameters can be chosen such that the effect of round-off error is minimized. As was shown in Figure 2.4, the accuracy is improved as the mesh is refined to the stability limit. Therefore, for optimum stability and accuracy, mesh parameters should be chosen such that they exactly lie on the stability line. Figure 2.5(b) shows a plot of the RMS error over the interval $5 \leq t/t_p \leq 15$ obtained using the stability lines to define mesh parameters. The minimum error is seen to be at $d/\Delta x = 9$ and $t_p/\Delta t = 30$, which is the optimum mesh. However, it should be noted that straying slightly from the optimum mesh (while remaining on the stability line) results in only a small change in accuracy. It should also be noted that the reported optimum mesh is obtained from a dimensionless analysis; therefore, it is applicable to any one-dimensional inverse heat conduction problem with a constant heat flux boundary condition. An optimum mesh for an alternative surface boundary condition could be easily developed using the methodology presented.

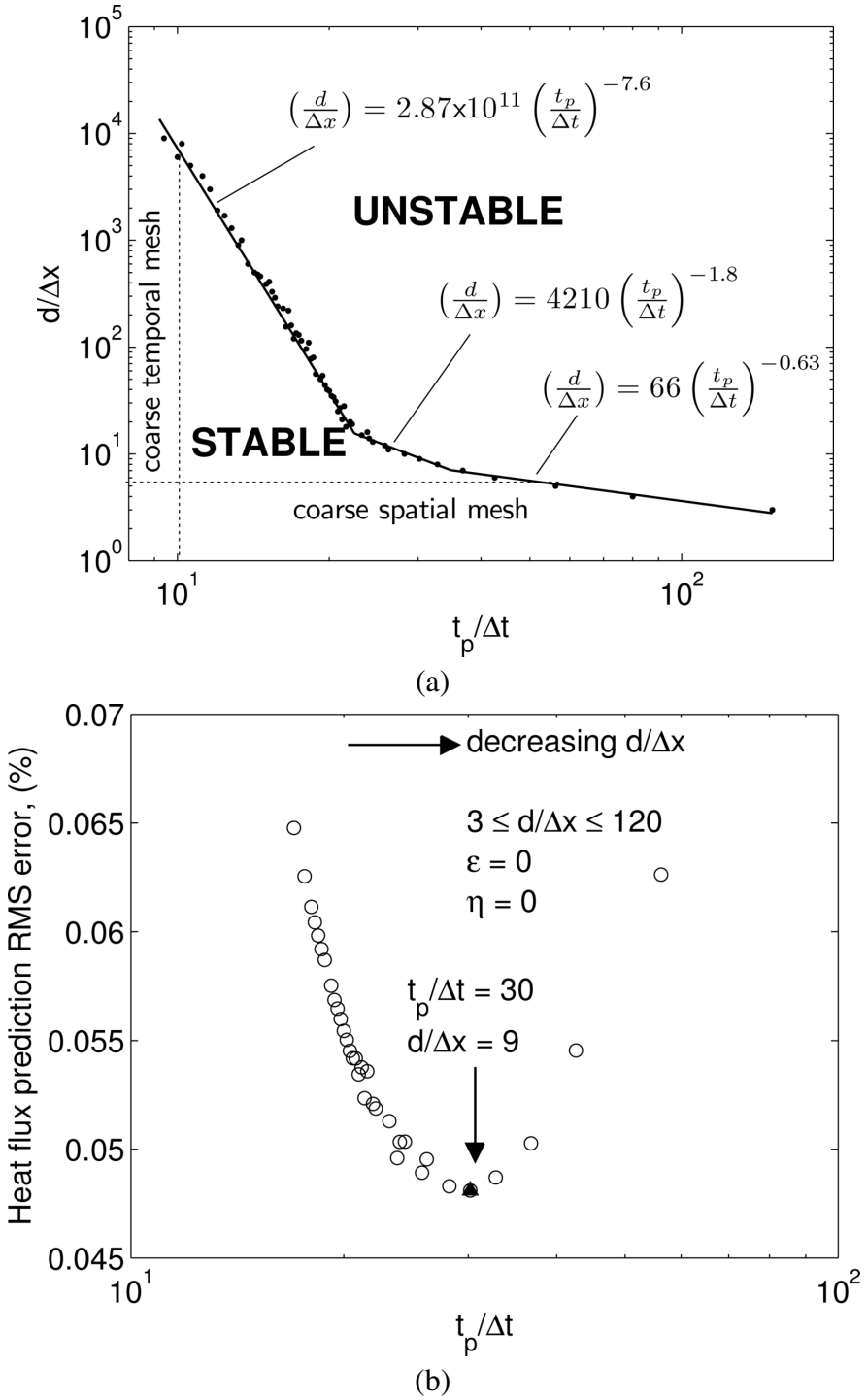

Figure 2.5: Optimization of mesh for test case 1. (a) Stability correlation relating the spatial mesh size ($d/\Delta x$) to the temporal mesh size ($t_p/\Delta t$) and (b) optimum mesh for both stability and accuracy.

2.6 Digital Filtering – Regularization with Physical Meaning

As with all space-marching methods, this inverse method will blow up in the presence of noisy data unless some type of regularization is employed. However, it is well-known that high frequency oscillations in the measurement data of an embedded sensor cannot be physically valid since conduction damps out any high frequency content in the signal. Alternatively phrased, a sensor should only receive low frequency information from conduction; all high frequency energies are associated with noise. The natural tool for removal of high frequency noise is a low-pass filter, where signal content above a user-specified cutoff frequency is significantly attenuated. The resulting regularized data contains only the low frequency portion of the data, which is the true signal. Therefore, a physically-based regularization method employs a low-pass filter for removing high frequency energy visible from the power spectrum of the Discrete Fourier Transform (DFT) [2].

The goal of the regularization method presented is to separate the projection scheme (discretization) from the regularization (filtering). Instability due to round-off error is addressed by choosing the optimum discretization parameters. In this way, either ideal (errorless) data, or noisy data that has been properly regularized can be supplied to the projection scheme and stability is guaranteed. The low-pass Gaussian filter described below, coupled with the physically-based cutoff frequency provides the regularization required for stable inverse predictions. Indeed, any choice of discretization parameters in the stable region of Figure 2.5(a) produces a stable inverse prediction whether errorless data or regularized noisy data are used. Additionally, any choice of discretization parameters in the unstable region of Figure 2.5(a) produces an unstable inverse prediction whether errorless data or regularized noisy data are used.

Recently, Beck [8] used the "filter coefficient method" in combination with an external regularization method such as Tikhonov Regularization. In this scheme, an external regularization method is employed to determine the required filter coefficients. Guo and Murio [14] have demonstrated digital filtering via mollification in combination with finite differences. Park and Jung [53] employed Kalman filtering in an inverse technique. Frankel [2] has also shown the effectiveness of filtering in removing noise from the data. While not employed for an IHCP, Frankel showed that only a single, carefully chosen cutoff frequency, f_c, was necessary to filter the signal and obtain a smooth curve. Building on previous contributors, it is proposed that a digital filtering scheme can provide the necessary regularization for an inverse analysis. Additionally, it is proposed that a single cut-off frequency is the only "regularization parameter" required to reduce the effect of measurement error on the inverse prediction and achieve a stable and accurate result.

Press et al. [54] suggest using Wiener filtering ideas to obtain the optimum choice of cutoff frequency. The goal of such a method is to remove content from the corrupted signal where the noise level overpowers the true signal level, i.e., a low signal-to-noise ratio. The DFT of a function, Φ, is given by [54]

$$\hat{\Phi}(\varpi_n) = \sum_{k=0}^{P-1} \Phi(t_k) e^{\frac{-2\pi i n k}{P}}, \quad n = 0,1,...,P-1, \tag{2.30}$$

where time is discretized as

$$t_k = k\Delta t, \quad k = 0,1,...,P. \tag{2.31}$$

Note that Φ can represent either temperature or heat flux. White noise is simulated and added to the data such that

$$\tilde{\Phi}_k = [1 + u_k \varepsilon]\Phi_k, \quad k = 0,1,...,P, \tag{2.32}$$

where u_k is a random number in the interval [-1,1] based on a uniform probability density function, ε is the noise level and P is the number of data points used in time. Figure 2.6 shows a plot of the magnitude (i.e., power spectrum) of the DFT for corrupted ($\varepsilon = 0.1$, i.e., 10% error) dimensionless temperature data from test case 1 as a function of dimensionless frequency given by

$$\bar{f}_n = \frac{f_n}{f_{ref}} = f_n t_{ref} = f_n \frac{d^2}{\alpha}. \tag{2.33}$$

As can be seen in Figure 2.6, the true signal is comprised of low-frequency content, while the noise dominates the data at high-frequencies. For this reason, the use of a low-pass filter is recommended. In order to obtain the cutoff frequency in Figure 2.6, a line is drawn tangent to the high frequency portion which extrapolates the noise level in the signal. A second line is drawn tangent to the low frequency portion which extrapolates the true signal. The cutoff frequency is defined at the intersection of the two tangent lines ($\bar{f}_c \cong 2$). Frankel [2] has shown that this method can be used with good success. This concept follows the basic premise of Wiener filtering involving signal-to-noise principles.

Unfortunately, this method requires a judgment to be made as to where each tangent line should be drawn. Additionally, this method can have a limited resolution due to the "eyeball" approximation used. As such, this technique of determining cutoff frequency is somewhat difficult to analytically implement. An alternate method of choosing the cutoff frequency analytically is the subject of future investigation. However, the inverse results are relatively insensitive to a small change in the value of the cutoff frequency as discussed below.

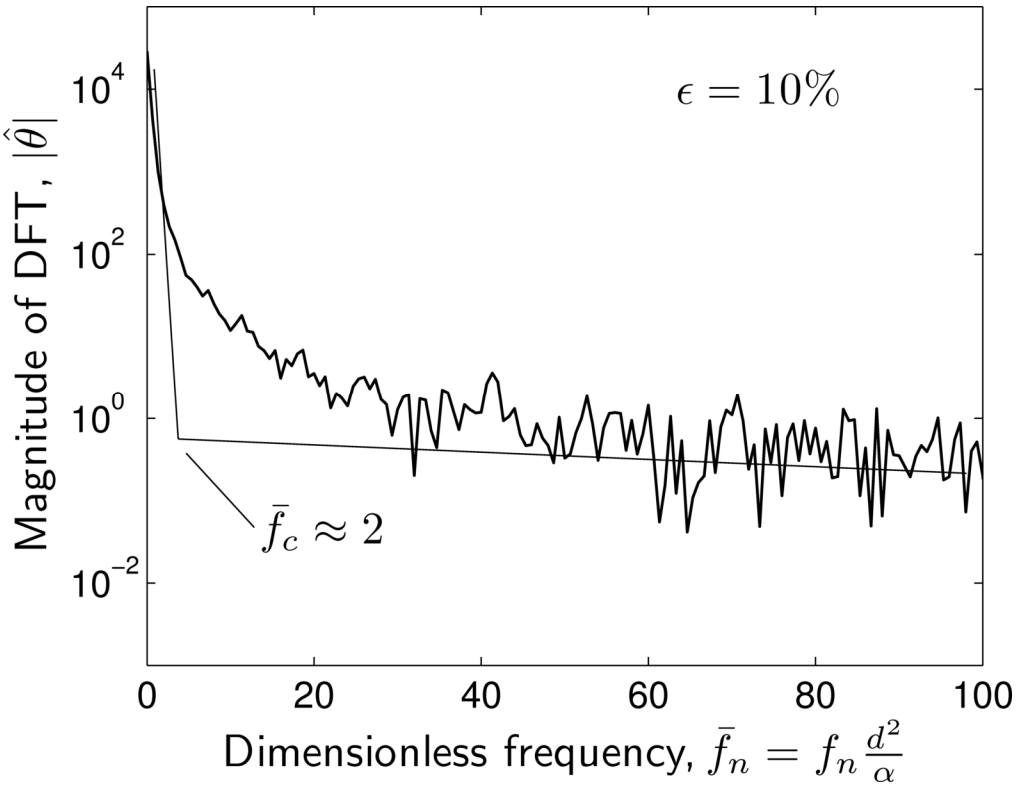

Figure 2.6: Choice of cutoff frequency by tangent line method.

Once the optimum cutoff frequency is determined, the noise can be removed using a Gaussian low-pass filter [2] given by

$$\hat{\Psi}(t)=\left(\sum_{k=0}^{P}\exp\left(-\pi^2 f_c^2\left(t-t_k\right)^2\right)\right)^{-1}\sum_{k=0}^{P}\tilde{\Psi}(t_k)\exp\left(-\pi^2 f_c^2\left(t-t_k\right)^2\right), \tag{2.34}$$

where Ψ can be heat flux or temperature, P is the number of time steps and f_c is the cutoff frequency chosen as described above. This filter encompasses all future and past information in acquiring the local filtered value. Figure 2.7(a) demonstrates the effectiveness of the filter at removing noise from the signal using $\varepsilon = 10\%$ and $\bar{f}_c = 2.0$. The filter output and the exact solution are graphically identical for $t > 3t_p$. Figure 2.7(b) shows the inverse results using the filtered data displayed in Figure 2.7(a). Good agreement is seen between the exact solution and the inverse results for $t > 2t_p$.

Figure 2.7(a) also shows the effect of the filter at the beginning and end of the time history. Around $t = 0$, the filtered temperature history over-predicts the temperature. This is known as the filter effect, and it can be combated in part by padding the data with "lead data." For the inverse problem presented in this chapter, padding the noisy input data reduces the filter-affected small time inverse results to be only for $t \lesssim 2t_p$. The procedure of padding the data is as follows: $2t_p$ of lead data are added to the noisy data before the filter. The lead data are forced to be exactly equal to the initial condition, i.e., there is no noise in the lead data, $(-2t_p \le t \le 0)$. This data set is then filtered, and the first $2t_p$ of data (padding) is subsequently removed. The remaining data are supplied to the inverse code as input.

Near $t = t_{max}$, the filtered temperature and heat flux histories begin to depart from the exact solution; this is the ending filter effect. The ending filter effect can also be overcome by

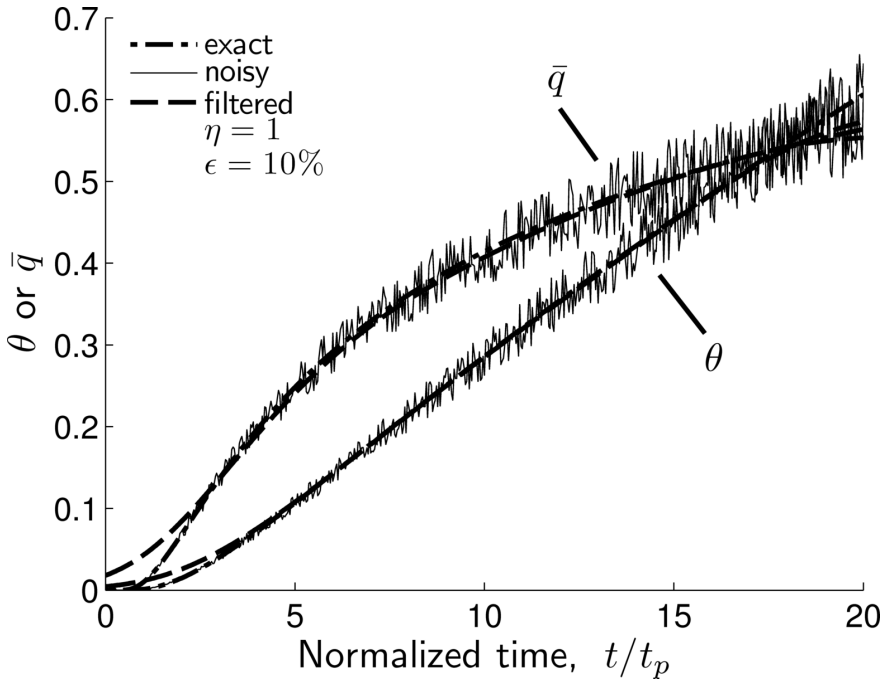

(a)

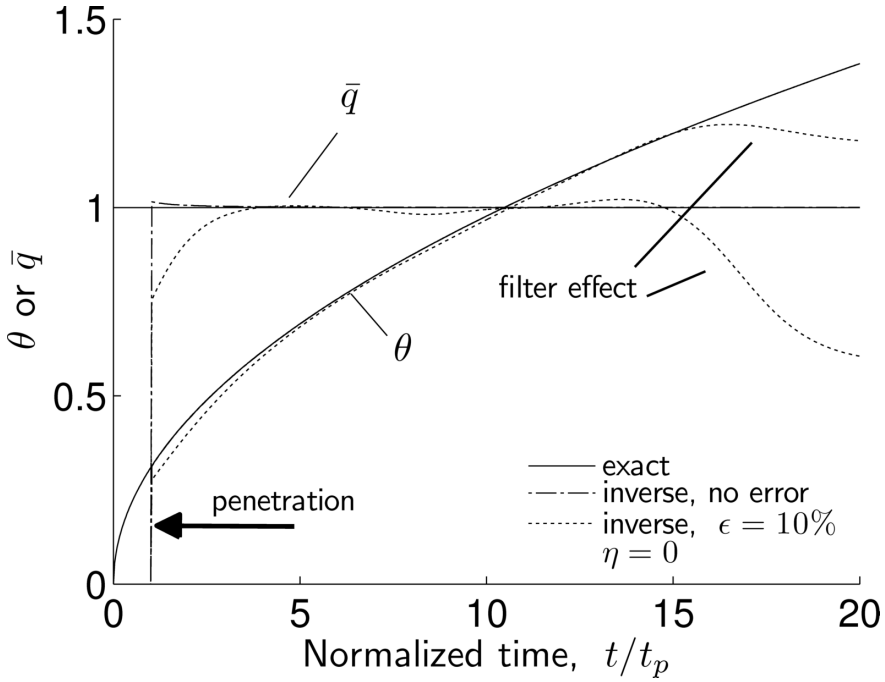

(b)

Figure 2.7: Effectiveness of filter at eliminating unwanted noise. (a) Noisy, filtered temperature and heat flux input data (η = 1) used to predict (b) surface (η = 0) conditions. Parameters used were $\bar{f}_c$ = 2.0, $d/\Delta x$ = 9 and $t_p/\Delta t$ = 30 for test case 1.

simply sampling data for a longer period of time. For example, if 15 seconds of inverse results are desired, one should take data for at least 20 seconds since approximately the last 25% of the data will be compromised due to the end filter effects.

It is also important to note that a slight change in the value of cutoff frequency has minimal effect on the resulting filtered data. Varying the cutoff frequency by 25% (say $\bar{f}_c = 2.0$ vs. $\bar{f}_c = 2.5$) shows little change in the resulting inverse temperature and heat flux histories. This was also shown by Frankel and Arimilli [55]. It should also be noted that if more of the oscillatory behavior of the signal is desired to be passed through the filter, a higher cutoff frequency can be used. This causes the inverse prediction to become more sensitive to changes in the surface condition at the expense of increasing noise sensitivity.

2.7 Results with Measurement Error

Figure 2.8 demonstrates the effects of measurement error in temperature and heat flux data for $\varepsilon = 0$, 5% and 10% on the inverse predictions for test case 1. Ideal input data are created by using the exact solutions for temperature and heat flux given in Eqs. (2.26) and (2.27). As described in the previous section, noise is added to the data via Eq. (2.32), and is subsequently filtered via Eq. (2.34). The filtered temperature and heat flux data at ($\eta = 1$) are then provided to the inverse code. The CPU time for one such simulation using mesh parameters $d/\Delta x = 9$ and $t_p/\Delta t = 30$ on the machine described in Section 2.4 was 0.26 seconds. As expected, Figure 2.8 shows that the inverse prediction error is directly related to the measurement error, i.e., an increase in measurement error produces a corresponding increase in the inverse prediction errors for both temperature and heat flux. Figure 2.8 shows that the inverse prediction is seen to be highly accurate, even in the presence of 10% random error distribution (shown in Figure 2.7(a));

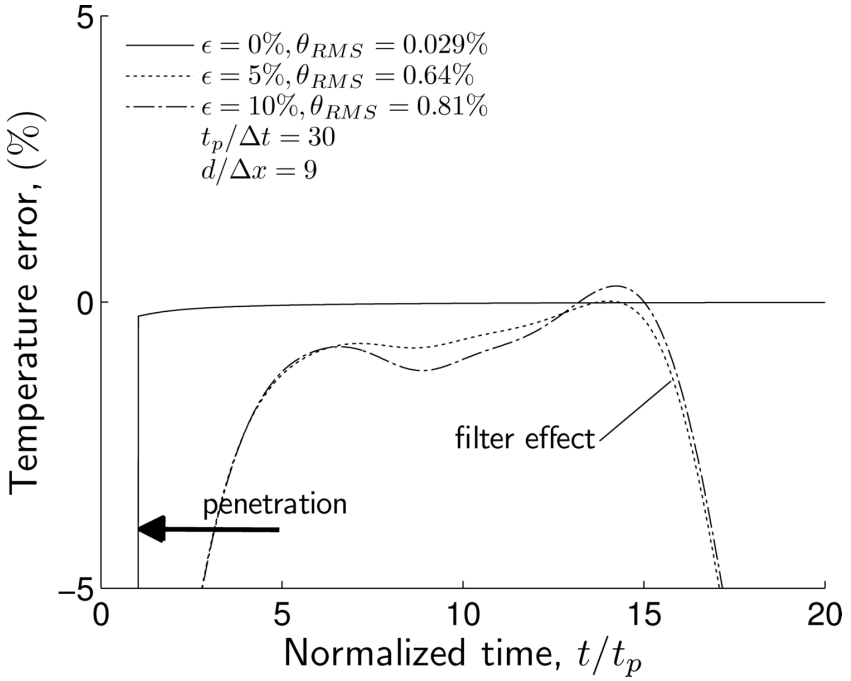

(a)

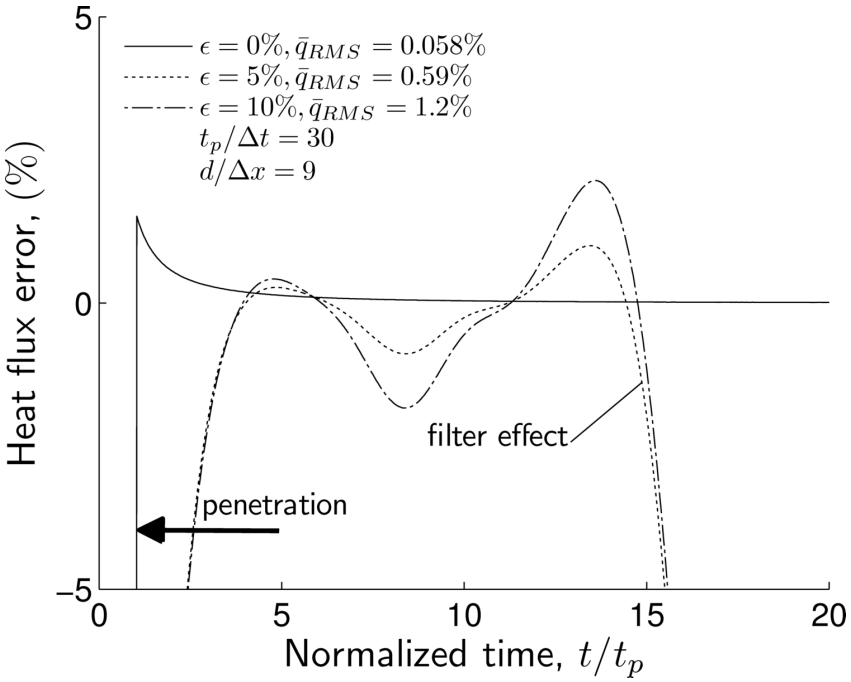

(b)

Figure 2.8: Effect of input error, ε on the surface temperature and heat flux error histories. The RMS error was calculated over the interval $5 < t/t_p < 15$ for test case 1.

the maximum temperature and heat flux prediction errors are found to be 0.28% and 2.14%, respectively, in the interval $3 < t/t_p < 15$. Since these results depend on the random error distribution used, 15 different cases were tested, each with a unique random error distribution and a noise level $\varepsilon = 10\%$. The maximum error found in any of these runs over the time interval of $3 < t/t_p < 15$ was found to be 1.96% for temperature and 6.45% for heat flux, with an average of maximum errors of 0.68% for temperature and 3.22% for heat flux (average of the 15 cases). It is significant to note that the proposed methodology (a) does not amplify the input error as the data are projected to the surface (a common inverse prediction predicament), and (b) indeed reduces the projected error to the surface.

Figure 2.9 is created by fixing the spatial mesh and refining the temporal mesh to the stability limit with a noise level of 10%. Further refinement of the temporal mesh produces unstable results. Figure 2.10 is similarly created by fixing the temporal mesh and refining the spatial mesh to the stability limit with a noise level of 10%. Further refinement of the spatial mesh produced unstable results. In both Figures 2.9 and 2.10, it is seen that marginal improvement can be gained by refining to the "optimum mesh." This is similar to the case of errorless data seen in Figure 2.5(b); the optimum mesh ($d/\Delta x = 9$ and $t_p/\Delta t = 30$) gave a heat flux RMS error of 0.05% while an alternate mesh of $d/\Delta x = 5$ and $t_p/\Delta t = 56$ produced a heat flux RMS error of 0.063%. The key point here is that while there is an "optimum mesh" which yields the minimum error, there is a significant amount of leeway in the choice of the mesh parameters, provided the choice is in the stable regions of Figure 2.5(a) and the data are regularized via an appropriate cutoff frequency.

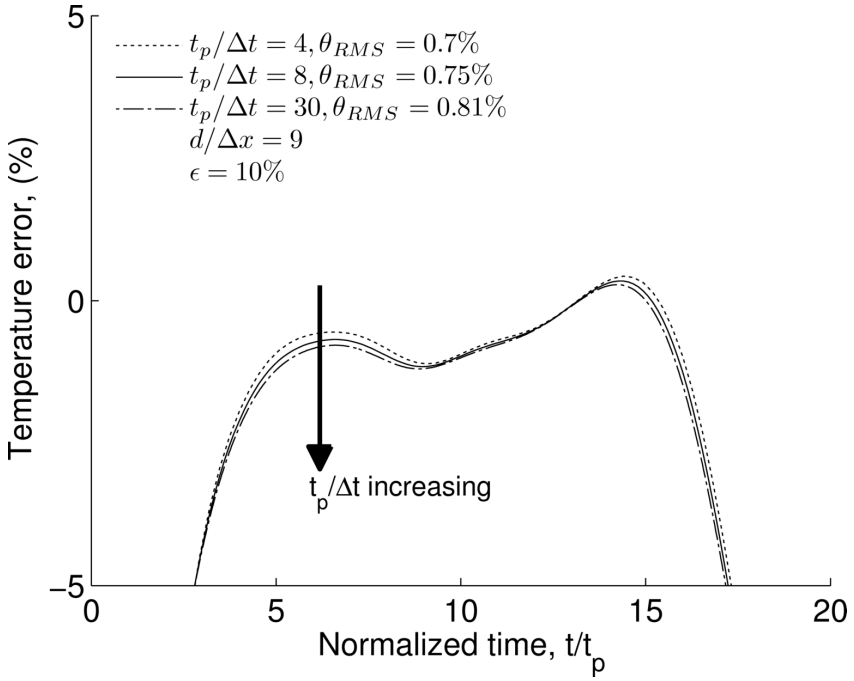

(a)

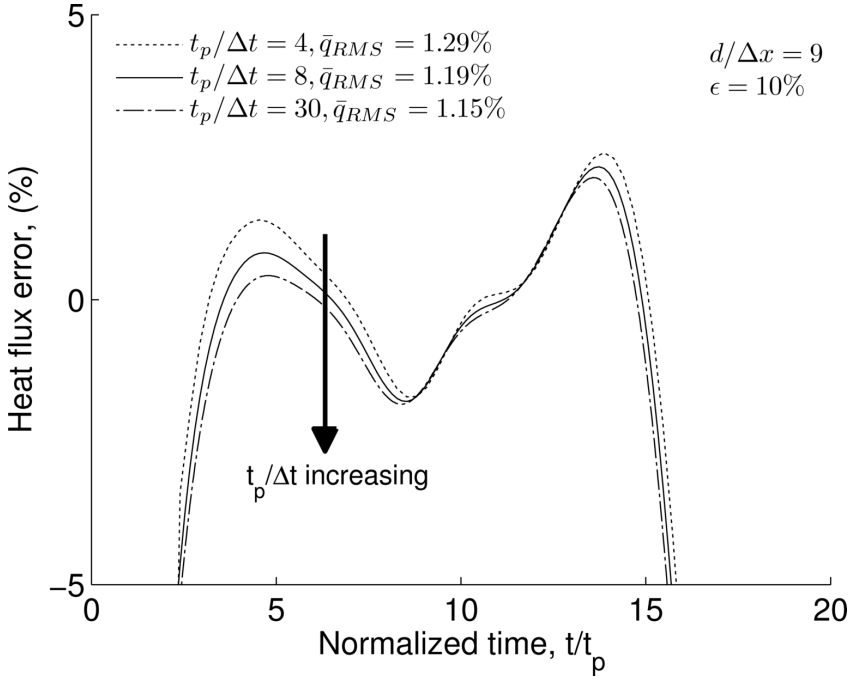

(b)

Figure 2.9: Effect of Δt using noisy ($\varepsilon = 10\%$), filtered data on the inverse-predicted surface (a) temperature error and (b) heat flux error histories. The RMS error was calculated over the interval $5 < t/t_p < 15$ for test case 1.

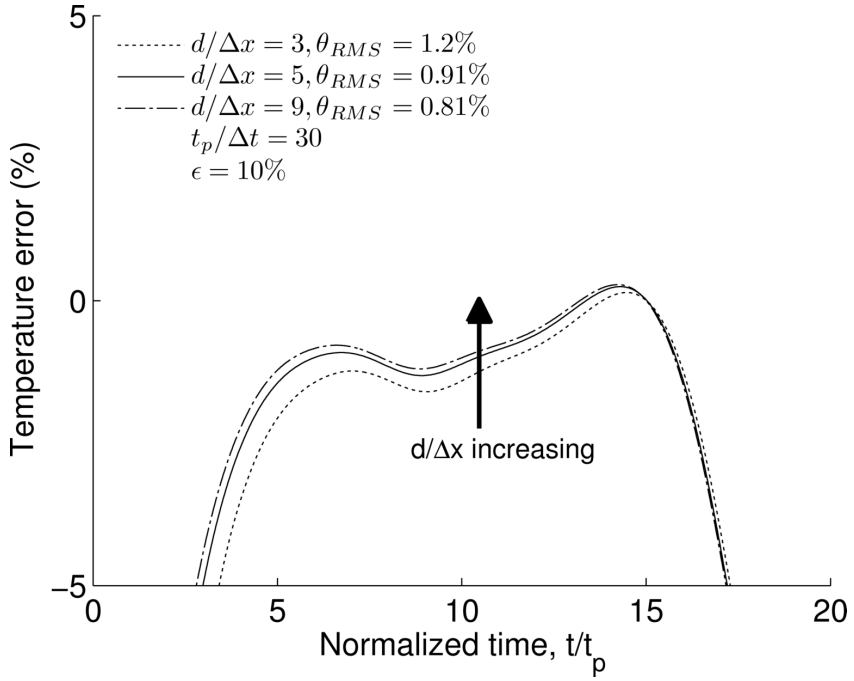

(a)

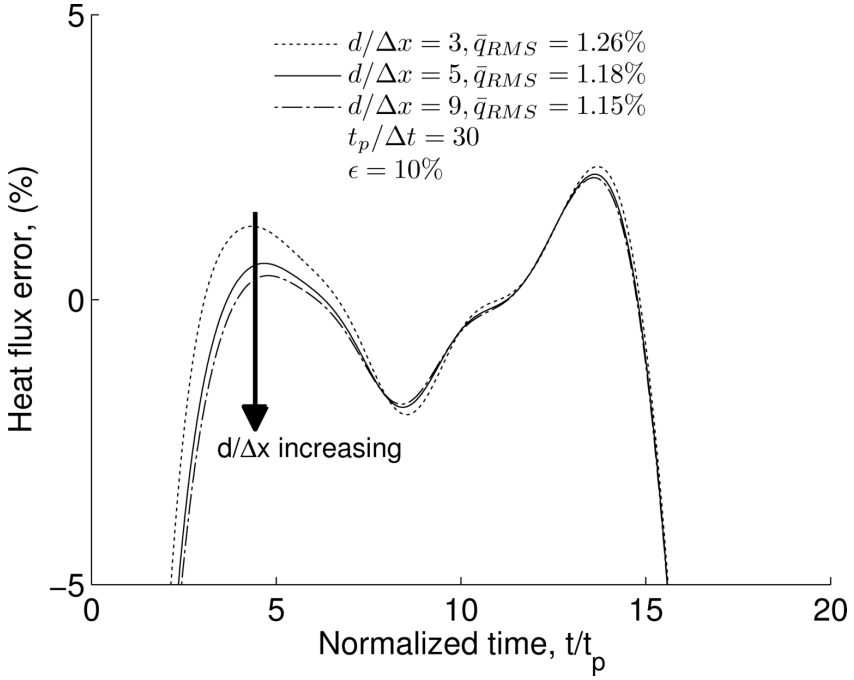

(b)

Figure 2.10: Effect of Δx using noisy ($\varepsilon = 10\%$), filtered data on the inverse-predicted surface (a) temperature error and (b) heat flux error histories. The RMS error was calculated over the interval $5 < t/t_p < 15$ for test case 1.

2.8 Heat flux Evaluation via Heating Rate

Frankel [2] has reported an integral relationship between the heating rate and the heat flux in a semi-infinite medium given by

$$q_x(x,t) = \sqrt{\frac{\rho C k}{\pi}} \int_{u=0}^{t} \frac{\partial T}{\partial u}(x,u) \frac{du}{\sqrt{t-u}}, \quad x,t \geq 0, \tag{2.35}$$

where ρ is the density and C is the specific heat capacity. Again, note that Eq. (2.34) is only valid on the half-space, i.e., the thermal front has not penetrated through the back wall of the sample for the duration of the experiment. Frankel et al. [44] (see also Chapter 4) have recently shown that the heating rate can be directly measured using a thermocouple and a simple analog filtering-differentiating circuit. Therefore, Eq. (2.35) is a novel way of obtaining the heat flux data at the sensor site with minimal instrumentation.

Figure 2.11(a) shows a comparison between two different sensor site heat flux inputs to the inverse problem along with the exact solution for the heat flux labeled as "exact" for test case 1. The input heat flux for the curve labeled ($\dot{\theta}, \theta$ data) refers to the case where temperature and heating rate data are obtained at the sensor site. In this case, the heating rate ($\dot{\theta}$) is obtained by differentiating the exact solution for the temperature, Eq. (2.26), extracting discrete exact $\dot{\theta}$ data, adding noise, and then filtering in a similar manner as previously described for temperature. Eq. (2.35) is then used to obtain the heat flux at the sensor site. The curve labeled "θ data only" refers to the case where only temperature data is collected at the sensor site; the input heat flux is obtained using the exact solution for the temperature, Eq. (2.26), with noise added and then filtered. A simple forward difference is used to obtain the heating rate which is then used in Eq.

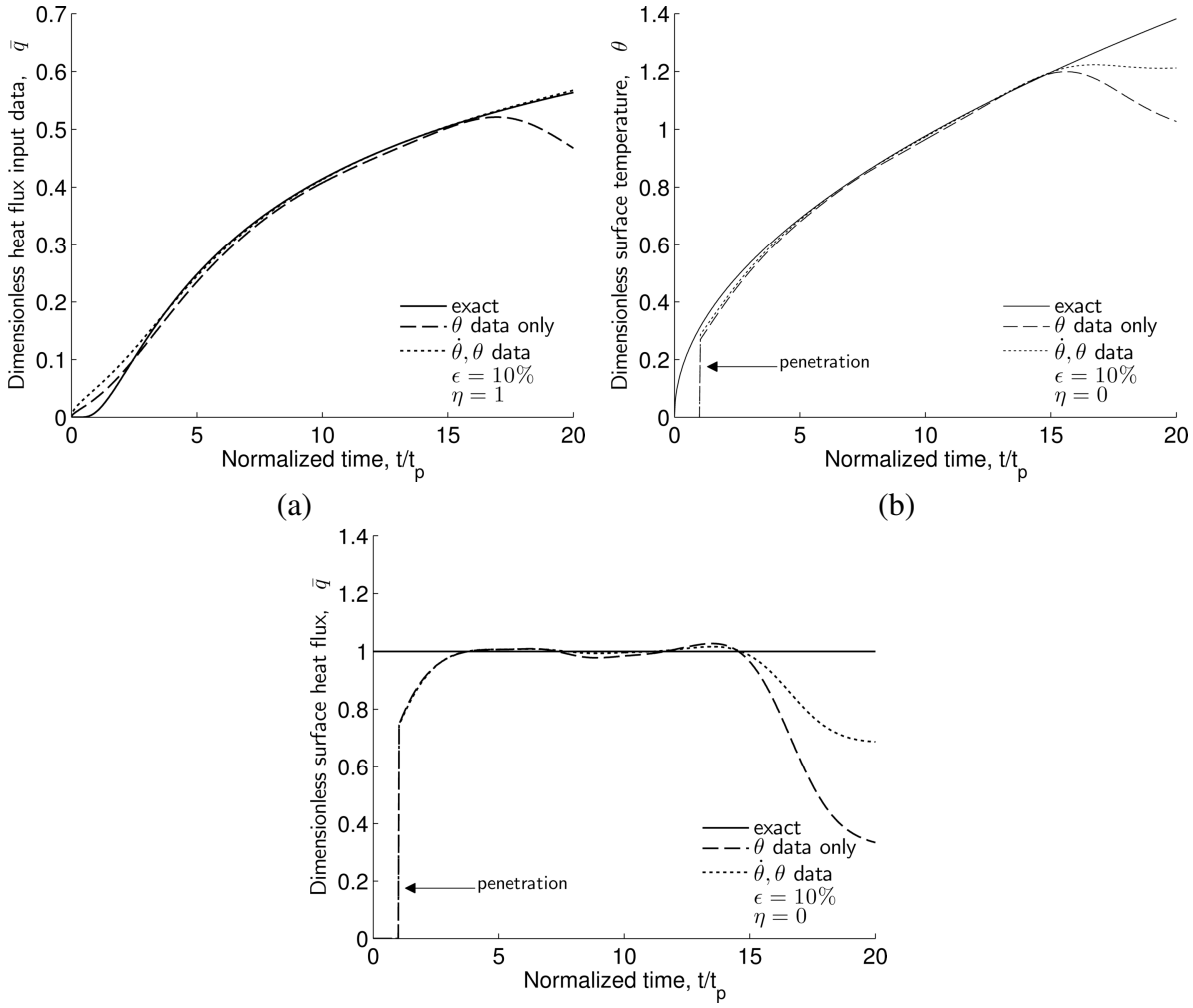

Figure 2.11: Half-space application: (a) input heat flux data obtained via the heat flux-heating rate integral relationship at sensor site ($\eta = 1$), (b) the resultant surface temperature ($\eta = 0$) and (c) the resultant surface heat flux ($\eta = 0$). Parameters used were $\varepsilon = 10\%$, $\bar{f}_c = 2.0$, $d/\Delta x = 9$ and $t_p/\Delta t = 30$, respectively for test case 1.

(2.35) to obtain the heat flux at sensor site. In both cases, Eq. (2.35) is evaluated using product integration given by

$$q_x(x,t_j) \approx \sqrt{\frac{\rho Ck}{\pi}} \sum_{i=0}^{j-1} \frac{\partial T}{\partial t}(x,t_i) \int_{t_i}^{t_{i+1}} \frac{du}{\sqrt{t_j - u}}, \quad x \geq 0,\ j = 1,2,..., \tag{2.36}$$

or

$$q_x(x,t_j) \approx \sqrt{\frac{\rho Ck}{\pi}} \sum_{i=0}^{P-1} \frac{\partial T}{\partial t}(x,t_i) \left[\left(t_j - t_i\right)^{1/2} - \left(t_j - t_{i+1}\right)^{1/2} \right], \quad x \geq 0,\ j = 1,2,..., \tag{2.37}$$

where $t_i = i\Delta t$ for $0 < t/t_p < 20$ using a time step size of $t_p/\Delta t = 150$ for a total of 3001 temporal nodes. If more computational nodes are used for the integral equation, better agreement is achieved for small time; however, since we are primarily interested in the accuracy of the solution for $t > t_p$, there is no tangible benefit to increasing the number of computational nodes. Only $t_p/\Delta t = 30$ temporal nodes are passed to the inverse method to achieve stability Figure 2.11(a) shows that the sensor site heat flux obtained via the forward difference heating rate is more sensitive to the filter effects at large time.

Figure 2.11(b) compares the predicted surface temperature using the two different input heat fluxes shown in Figure 2.11(a) with the exact solution. Figure 2.11(c) compares the predicted surface heat flux using the two different input heat fluxes shown in Figure 2.11(a) with the exact solution. These figures show that the sensor heat flux provided by Eq. (2.37) produces an accurate inverse result. Clearly, the results based on $\dot{\theta}, \theta$ data suggest that direct heating rate measurements are preferred (even if they contain substantial error [56]) in order to avoid strong filter end effects.

2.9 Transient Surface Heat flux With Measurement Error

Test Case 2

In order to fully demonstrate the effectiveness of the proposed method, two cases involving transient heat flux boundary conditions at $x = 0$ have been investigated. First, a pulsed heat source is applied at the surface for $10t_p \le t \le 30t_p$, before and after which the surface is insulated. The sensor is located at $x = d$ and the half space boundary condition exists at $x = L$ where $d < L$. Temperature and heat flux data are obtained at the sensor site [51]. Noise is simulated via Eq. (2.32) with a uniform distribution and a noise level of $\varepsilon = 10\%$ for both temperature and heat flux. The results can be seen in Figure 2.12(a). Mesh parameters of $d/\Delta x = 9$ and $t_p/\Delta t = 30$ and a dimensionless cutoff frequency of 2.0 are again found to yield favorable results. Results are seen to be highly accurate: an input error of 10% results in an inverse prediction error of less than 4% in the range of $13t_p \le t \le 27t_p$.

Test Case 3

A second transient surface boundary condition was investigated where the source was defined as

$$\overline{q}_{x=0}(t) = \begin{cases} 0, & 0 \le Fo \le 0.3 \\ \dfrac{Fo}{0.6} - 0.5, & 0.3 \le Fo \le 0.9 \\ -\dfrac{Fo}{0.6} + 2.5, & 0.9 \le Fo \le 1.5 \\ 0, & Fo \ge 1.5 \end{cases} \tag{2.38}$$

which results in the classical triangular heat source [1] with maximum of 1.0. The body is insulated at $x = L$, and the sensor is located at $x = d = L$. Temperature data with 10% simulated

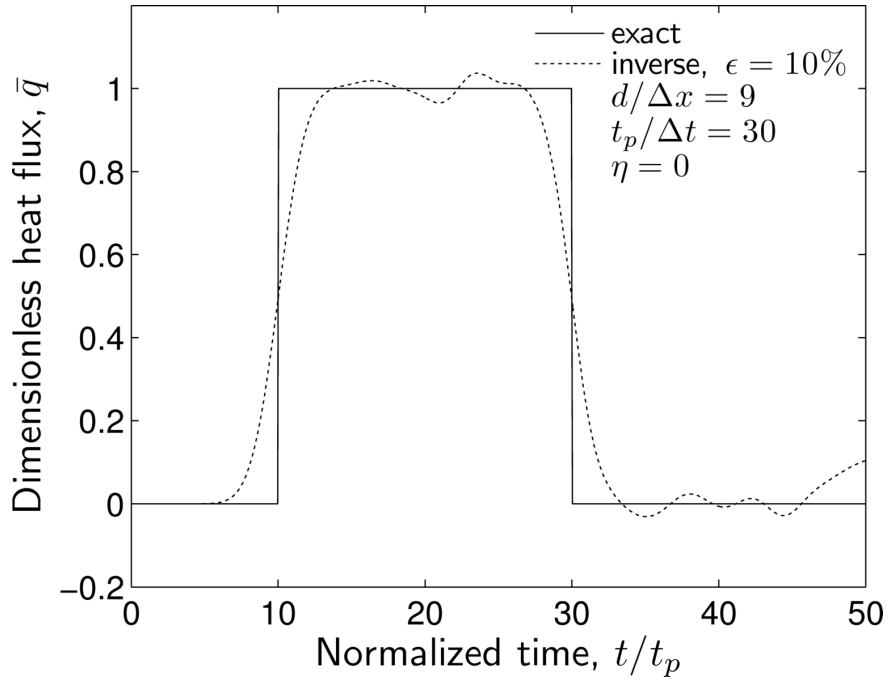

(a)

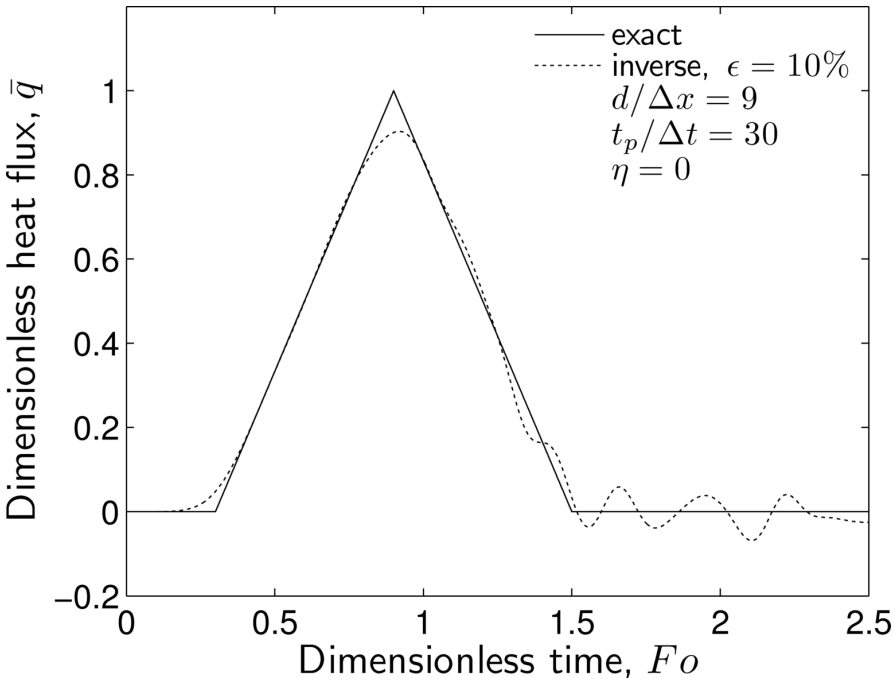

(b)

Figure 2.12: Inverse results with a transient surface boundary condition and 10% measurement error: (a) pulse flux (test case 2) and (b) triangular flux (test case 3). Both results used the parameters $\varepsilon = 10\%$, $\bar{f}_c = 2.0$, $d/\Delta x = 9$ and $t_p/\Delta t = 30$.

error were supplied to the inverse code, and the adiabatic condition was used as sensor heat flux data. The inverse projection is shown in Figure 2.12(b). Mesh parameters of $d/\Delta x = 9$ and $t_p/\Delta t = 30$ and a dimensionless cutoff frequency of 2.0 are again found to yield favorable results. The inverse code predicts a peak heat flux of 0.903 which is less than 10% prediction error for 10% input temperature error. Also good agreement between the exact surface condition and the inverse prediction is seen during the ramp up and ramp down times.

2.10 Chapter Summary

The inverse heat conduction problem is highly sensitive to both measurement error and round-off error. The method presented in this chapter provides a simple means to circumvent both sources of error. The method consists of a systematic approach that may be summarized as:

- The role of penetration time on inverse analysis is clearly demonstrated, and the numerical value of the dimensionless penetration time (Fourier number) is established and experimentally verified.
- The dimensionless optimal temporal mesh (time-step normalized with the penetration time) for circumventing round-off error is established (limited to precision of the computation/computer).
- To minimize the effect of measurement error on the inverse projection, a low-pass Gaussian filter with a physically-based cutoff frequency as the regularization parameter is utilized. The proposed procedure for determining the cutoff frequency exploits the physics of diffusion.

- The accuracy of an alternative method for obtaining heat flux data at the sensor site via an integral relationship between heating rate (using temperature data at sensor site) and local heat flux (applicable to the case of a semi-infinite medium) is established.

Using the proposed procedures to circumvent both round-off and measurement error, it is demonstrated that 10% error on input temperature and heat flux data at sensor site results in less than 10% error on the resolved surface heat flux and temperature. For example a 10% measurement error results in an average (over 15 cases of random number generator) maximum inverse prediction error of 0.68% for temperature and 3.22% for heat flux. It is significant to note that the proposed methodology (a) does not amplify the input error as the data is projected to the surface (a common inverse prediction predicament), and (b) indeed reduces the projected error to the surface for both temperature and heat flux.

Chapter 3: Global Time Method for Inverse Heat Conduction Problem

This chapter is a revised version of a conference paper published by Bryan S. Elkins, Majid Keyhani, and Jay I. Frankel:

Elkins, B. S., Keyhani, M., and Frankel, J. I., 2011, "Global Time Method for Inverse Heat Conduction Problem," 2011 International Conference on Inverse Problems in Engineering, Orlando, FL, May 4-6, 2011.

My primary contributions to this paper include (i) collaboration in conceptualization of work, (ii) development of the numerical method, (iii) writing of the computerized code, (iv) parametric investigation of the numerical method, and (v) most of the writing.

3.1 Global Time Method Introduction

Traditional space-marching techniques for solving the inverse heat conduction problem (IHCP) are highly susceptible to both measurement and round-off error. This difficulty is exacerbated if the problem requires small time steps to resolve rapid changes in the surface condition, since this can cause instability. The work presented in this chapter is motivated by the global time and global space paper of Frankel and Keyhani [43]. In this chapter, a global time and discrete space formulation of the inverse problem is presented. A novel treatment of the temporal derivative in the heat equation is utilized; namely, the time derivative in the heat equation is not finite differenced, and the in-depth data are projected directly to the surface without any need to compute the temperature at intermediate spatial nodes. A Gaussian low-pass filter is employed for regularization. There are three main benefits to using this type of filter.

First, this filter provides a global time regularization – i.e., all future and all past information is used in the regularization of the current time. Second, the output of this filter is an analytical function which can be analytically differentiated. Third, the filter ensures all time derivatives of the data to be smooth and bounded. The inverse technique presented in this chapter is demonstrated to be robust in the presence of noise.

3.2 Problem Description and Inverse Technique

Consider an isotropic, one-dimensional geometry with no internal generation and constant properties. The governing equation for this problem is given by the heat equation

$$\frac{\partial T}{\partial t} = \alpha \frac{\partial^2 T}{\partial x^2}, \quad 0 \le x \le L,\ t \ge 0, \tag{3.1}$$

where $T = T(x,t)$ is temperature, t is the time variable, x is the spatial variable, α is thermal diffusivity, and L is the length of the (direct) spatial domain. Equation (3.1) is subject to an initial condition

$$T(x, t=0) = T_i, \qquad 0 \le x \le L, \tag{3.2}$$

for the entire spatial domain. The surface (x=0) thermal condition is unknown

$$q(x=0,t) = -k \frac{\partial T}{\partial x}(x=0,t) = \text{unknown}, \tag{3.3}$$

where k is the thermal conductivity. Heat flux and temperature data are provided at the embedded sensor site (x=d) such that

$$q(x=d,t) = q_d(t) = -k \frac{\partial T}{\partial x}(x=d,t), \quad d \le L, \tag{3.4}$$

$$T(x=d,t) = T_d(t), \quad d \le L, \tag{3.5}$$

where $q_d(t)$ is the heat flux data and $T_d(t)$ is the temperature data.

The goal of the inverse problem is to resolve the unknown surface (x=0) thermal condition using the provided sensor (x=d) temperature and heat flux data. This can be accomplished by first discretizing space such that $x_j = (N\text{-}j)\Delta x$ – i.e., $x_{j=0}$ corresponds to the sensor site (x=d) and $x_{j=N}$ corresponds to the surface (x=0). The spatial derivative of the heat equation (3.1) is approximated using a central difference as

$$\frac{\Delta x^2}{\alpha}\frac{dT_j}{dt}(t) \approx T_{j+1}(t) - 2T_j(t) + T_{j-1}(t), \qquad j = 1,2,...,N-1. \tag{3.6}$$

Traditionally, the time derivative is also approximated using a difference formula. However, if the heating rate and higher-time derivatives of temperature are directly measured (see Chapter 4) or can be obtained via post-processing, then time need not be differenced. We, therefore, define the operator, F, as

$$F = \frac{\Delta x^2}{\alpha}\frac{d}{dt} + 2, \tag{3.7}$$

and solve Eq. (3.6) for T_{j+1} to obtain

$$T_{j+1}(t) = FT_j(t) - T_{j-1}(t), \qquad j = 2,3,..., N-1. \tag{3.8}$$

An energy balance at the sensor site (j=0) yields the result

$$T_1(t) = \frac{F}{2}T_d(t) + \frac{\Delta x}{k}q_d(t), \tag{3.9}$$

where T_d(t) and q_d(t) are the sensor data. Using a process of repeated analytical substitution with Eqs. (3.8-3.9), the temperature at the Nth spatial node (i.e., at the surface) can be solved for in terms of the sensor temperature and heat flux explicitly. As an example, for N = 4 and N=*7* the equations are

$$T_{N=4}(t)=\left(\frac{1}{2}F^4-2F^2+1\right)T_d(t)+\frac{\Delta x}{k}\left(F^3-2F\right)q_d(t), \tag{3.10}$$

$$T_{N=7}(t)=\left(\frac{1}{2}F^7-\frac{7}{2}F^5+7F^3-\frac{7}{2}F\right)T_d(t)+\frac{\Delta x}{k}\left(F^6-5F^4+6F^2-1\right)q_d(t), \tag{3.11}$$

respectively. For resolution of the surface temperature, N temporal derivatives of temperature data and N-1 temporal derivatives of the heat flux data are required. An energy balance at the surface yields

$$q_N(t)=\frac{k}{\Delta x}\left(\frac{F}{2}T_N(t)-T_{N-1}(t)\right), \tag{3.12}$$

which again can be found explicitly in terms of sensor temperature and heat flux only. As an example, Eq. (3.12) for $N = 4$ and $N = 7$ becomes

$$q_{N=4}(t)=\frac{k}{\Delta x}\left(\frac{1}{4}F^5-\frac{3}{2}F^3+2F\right)T_d(t)+\left(\frac{1}{2}F^4-2F^2+1\right)q_d(t) \tag{3.13}$$

$$\begin{aligned} q_{N=7}(t)=\frac{k}{\Delta x}&\left(\frac{1}{4}F^8-\frac{9}{4}F^6+\frac{13}{2}F^4-\frac{25}{4}F^2+1\right)T_d(t)+\\ &\left(\frac{1}{2}F^7-\frac{7}{2}F^5+7F^3-\frac{7}{2}F\right)q_d(t). \end{aligned} \tag{3.14}$$

For resolution of the surface heat flux, N+1 temporal derivatives of the temperature data, and N temporal derivatives of the heat flux data are required. Therefore, if noise exists in the sensor data, the projection process is clearly ill-posed. Additionally, if the derivatives are obtained numerically, significant round-off error will accumulate as N increases, and again the process is ill-posed. However, if the data and the required number of temporal derivatives are bounded and smooth, the projection process is well-posed. This can be accomplished via a low-pass Gaussian filter.

3.3 Regularization via Digital Filtering

As discussed above, high frequency oscillations present in the data (noise) cause the inverse projection to become unstable. The reason for this is made clear through inspection of Eq. (3.13). For $N = 4$, five time-derivatives of the temperature data and four time-derivatives of the heat flux data are required to resolve the surface heat flux. Time differentiating noisy data produces an unbounded and unstable result. A physically meaningful way of stabilizing the inverse problem is to remove the non-physical high frequency energies from the signal by way of a low-pass digital filter. Consider the Gaussian low-pass filter given by

$$\hat{T}(t) = \left(\sum_{k=0}^{P} \exp\left(-\pi^2 f_c^2 (t - t_k)^2 \right) \right)^{-1} \sum_{k=0}^{P} \tilde{T}(t_k) \exp\left(-\pi^2 f_c^2 (t - t_k)^2 \right), \tag{3.15}$$

where f_c is the cutoff frequency in Hz, P is the number of time steps, $\hat{T}$ is the filtered temperature and $\tilde{T}$ denotes the raw, discrete sensor data. Derivatives of Eq. (3.15) can be obtained analytically; the first time derivative is given by

$$\begin{aligned} \frac{d\hat{T}}{dt}(t) = 2\pi^2 f_c^2 \left(\sum_{k=0}^{M} \exp\left(-\pi^2 f_c^2 (t - t_k)^2 \right) \right)^{-2} \left[\sum_{k=0}^{M} (t - t_k) \tilde{T}(t_k) \exp\left(-\pi^2 f_c^2 (t - t_k)^2 \right) \bullet \right. \\ \left. \sum_{j=0}^{M} \left(\frac{t - t_j}{t - t_k} - 1 \right) \exp\left(-\pi^2 f_c^2 (t - t_j)^2 \right) \right], \quad t \geq 0. \end{aligned} \tag{3.16}$$

The outputs of Eqs. (3.15-3.16) are analytical functions which remove high frequency energies (noise) from the signal and ensure continuous, smooth temporal derivatives [2] as required by the inverse technique. Therefore, a carefully chosen cutoff frequency is the only parameter necessary to regularize the data, and make the problem well-posed.

The cutoff frequency of the filter can be determined using residual minimization in the least-squares sense. Traditional least squares would seek to minimize the difference between the

filtered and noisy data – i.e. the residual. However, some authors [13, 57] have noted that the difference between the filtered data and the exact data should be minimized. First, let us define the noisy data to be

$$\tilde{T}(t) = T_{exact}(t) + \varepsilon(t), \quad t \geq 0, \tag{3.17}$$

where ε is the noise which is considered to be of a Gaussian distribution with a constant standard deviation, σ, and has a zero mean. Next, we define the residual as the difference between noisy and filtered data such that

$$R(t_k) = \tilde{T}(t_k) - \hat{T}(t_k) = T_{exact}(t_k) - \hat{T}(t_k) + \varepsilon(t_k), \qquad k = 0,1,2,..., \tag{3.18}$$

Clearly, minimizing the difference between the filtered and exact data is the same principle as setting the residual equal to the noise. Therefore, we utilize the Euclidean norm and seek to minimize the function

$$\phi_1 = \left\| \tilde{T}(t_k) - \hat{T}(t_k) \right\|_2 - \left\| \varepsilon(t_k) \right\|_2, \qquad t_{on} \leq t_k \leq t_{\max}, \tag{3.19}$$

where t_{on} is the time at which the source at the surface is switched on, and t_{max} is the time at the final data sample. The discrete 2-norm is defined here as

$$\left\| \varphi \right\|_2 = \sqrt{\sum_{j=0}^{P} \varphi^2(t_j)}. \tag{3.20}$$

The function, ϕ_1, now contains the noisy data, filtered data, and the noise history. Additionally, lead data is commonly taken before the source is turned on. We use the mean of the lead data, T_i (initial condition), to define ϕ_2 as

$$\phi_2 = \left\| T_i - \hat{T}(t_k) \right\|_2, \qquad 0 \leq t_k \leq t_{on}, \tag{3.21}$$

where T_i is again the initial condition. The cutoff frequencies which produce minimums of ϕ_1 and ϕ_2 provide a range of optimal cutoff frequencies from which the user can choose. It should be noted that the Gaussian low-pass filter of Eq. (3.15) is not overly sensitive to the choice of cutoff frequency; a change of 15-20% will not dramatically influence the filtered data.

At first, this procedure does not seem useful since in the real world both the exact data and the noise history are unavailable (apart from the initial condition). However, we utilize a procedure of estimating the noise outlined in [13]. A first-order polynomial is fit to the noisy data, and the residual, $R_1(t_k)$, between the noisy data and the first-order least squares fit is calculated. Next, a higher order function, $\hat{R}_1(t_k)$, is used to approximate $R_1(t_k)$ via least squares. The error is then estimated as

$$\varepsilon_{est}(t_k) = \hat{R}_1(t_k) - R_1(t_k), \qquad k = 0,1,... \tag{3.22}$$

3.4 Errorless Data

For demonstration, consider a pulsed surface heat flux given by

$$q(x=0,t) = q_S \sum_{m=0}^{M} H(t-t_m)(-1)^m, \qquad t \geq 0, \tag{3.23}$$

where q_S is the peak source heat flux, H is the Heaviside step function [52], and t_m are the time values for switching the surface flux on and off. For this chapter, we wish to observe lead data (before surface heat flux is turned on), one pulse, and cooling data. Therefore, $t_{m=0} = t_{on}$ and $t_{m=1} = t_{off}$. Without loss of generality, we use the half-space as the domain, noting that this is valid until the thermal front reaches the back wall ($x = L$). The exact solution for the forward problem is given by [51]

$$T(x,t)=\frac{q_S\sqrt{\alpha}}{k}\sum_{m=0}^{M}(-1)^m H(t-t_m)\left[\sqrt{\frac{4(t-t_m)}{\pi}}\exp\left(-\frac{x^2}{4\alpha(t-t_m)}\right)\right.$$
$$\left.-\frac{x}{\sqrt{\alpha}}\operatorname{erfc}\left(\frac{x}{\sqrt{4\alpha(t-t_m)}}\right)\right],\qquad x,t\geq 0, \tag{3.24}$$

and

$$q(x,t)=q_S\sum_{m=0}^{M}(-1)^m H(t-t_m)\operatorname{erfc}\left(\frac{x}{\sqrt{4\alpha(t-t_m)}}\right),\qquad x,t\geq 0. \tag{3.25}$$

Without loss of generality, the results we present are made dimensionless via

$$Fo=\frac{\alpha t}{d^2}, \tag{3.26}$$

$$\eta=\frac{x}{d}, \tag{3.27}$$

$$\theta(\eta,Fo)=\frac{T-T_i}{q_S d/k}, \tag{3.28}$$

$$\bar{q}(\eta,Fo)=\frac{q}{q_S}, \tag{3.29}$$

$$\bar{f}=\frac{d^2}{\alpha}f, \tag{3.30}$$

where Fo is dimensionless time, η is dimensionless space, θ is dimensionless temperature, $\bar{q}$ is dimensionless heat flux, and $\bar{f}$ is dimensionless frequency. Note that although the peak source heat flux, q_S, is unknown apriori, it is merely a scaling factor in Eqs. (3.28-3.29). Therefore, the actual value of q_S is unimportant for this analysis.

Although the exact solution for this problem is available, the digital filter was used to show its performance. The exact solution for temperature and heat flux Eqs. (3.24-3.25) were

"sampled" at a given rate, $\bar{f}_s$, and the data were provided to the Gaussian low-pass filter. Since errorless data were used (i.e., no regularization needed), a suitably high dimensionless cutoff frequency of $\bar{f}_c$=50 was used in the filter for both temperature and heat flux data. The output of the filter was then provided as input the to the projection scheme.

Inverse temperature and heat flux results for $N = 4$ can be seen in Figure 3.1 using a sampling rate of $\bar{f}_s = 265$. The inverse method does an excellent job of capturing the jump in heat flux at $Fo = 0.5$, with only a short lag. The accuracy of the inverse method should improve as the order of the projection (N) increases. Figure 3.2(a) shows the inverse heat flux results for $N = 7$ with all other parameters unchanged. Although increasing the projection order should have had a positive effect on the results, a bias in the heat flux prediction is observed. This is because the dimensionless sampling rate of $\bar{f}_s = 265$ for $N = 7$ is slow; as the projection order increases, the data density required to resolve the higher order temporal derivatives via the filter also increases. Figure 3.2(b) shows the inverse heat flux results for $N = 7$, but with an increased sampling rate of $\bar{f}_s = 400$. As the sampling rate is increased, the results are still stable, and the bias in the heat flux prediction vanishes.

If the sampling rate is appropriately fast, use of more spatial nodes will also enable the inverse method to capture a change in the surface condition more quickly. Figures 3.1(b) and 3.2(b) illustrate this quite well. For $N = 7$, the response time for when the source is turned on and off is much faster than for $N = 4$. Additionally, the Gibbs' spike is also seen to decrease with increasing N. These observations make physical sense for two reasons. First, as N increases, space is becoming less lumped and more continuous – i.e., more accurate. Second, increasing N increases the highest order of time derivative used in the inverse prediction. Each higher time

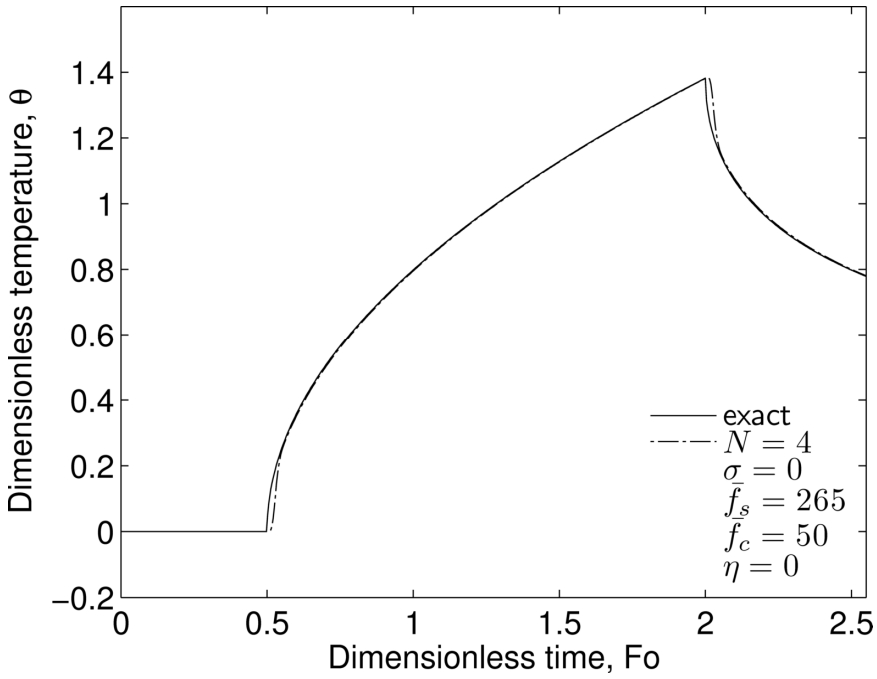

(a)

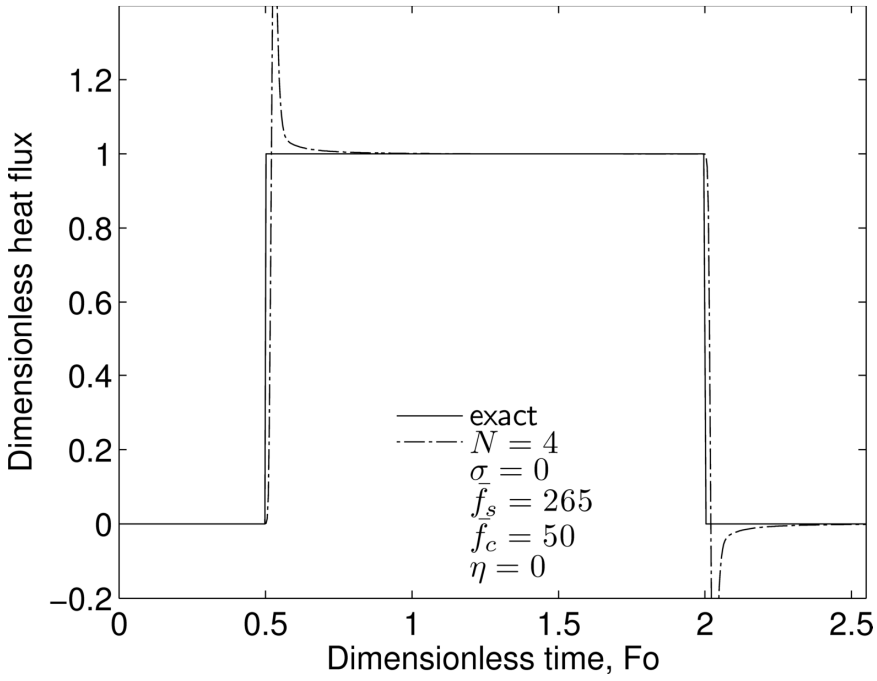

(b)

Figure 3.1: Inverse results using *N*=4 using errorless, discrete data. (a) temperature and (b) heat flux inverse predictions.

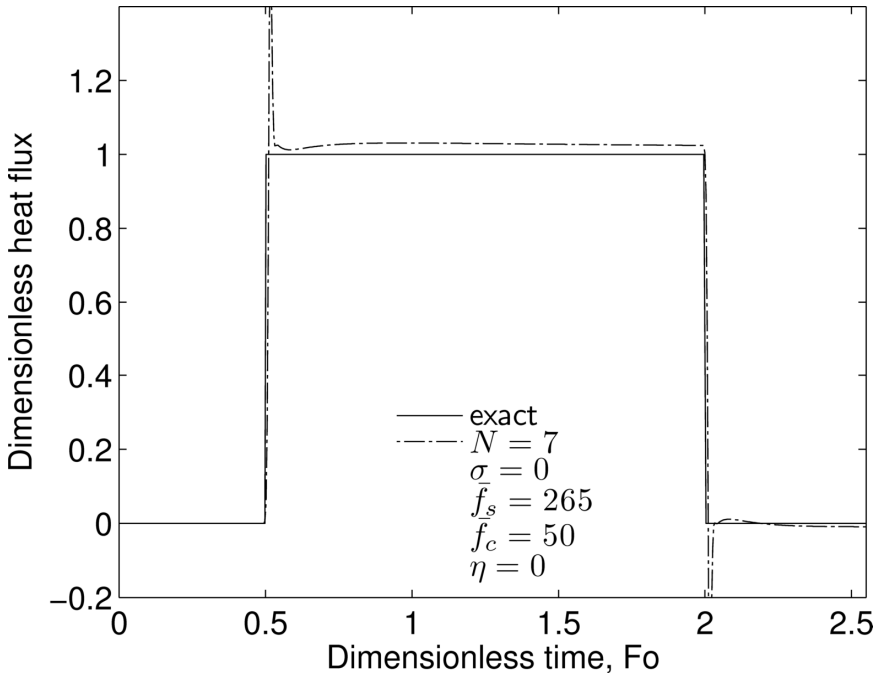

(a)

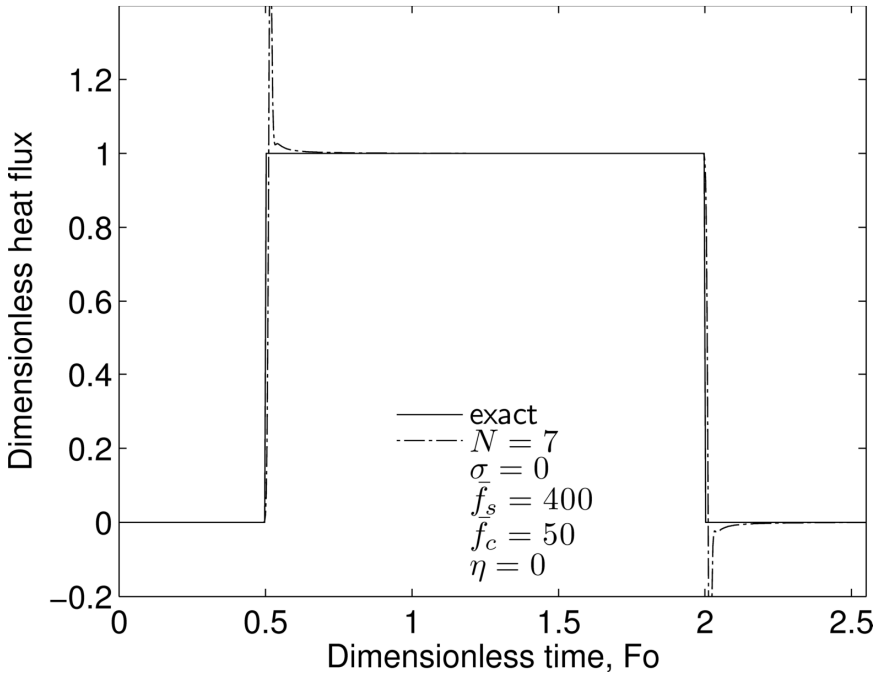

(b)

Figure 3.2: Effect of the sampling rate on the inverse heat flux prediction with *N*=7 using errorless data. (a) $\bar{f}_s = 265$ and (b) $\bar{f}_s = 400$.

derivative picks up on changes in boundary conditions faster than the previous derivative, which will result in a faster response time. In sharp contrast to other inverse methods, this implies one should use the largest N consistent with the highest available sampling rate.

3.5 Noisy Data

For demonstration, again we consider a pulsed surface heat flux given by Eq. (3.23) with the exact solution given by Eqs. (3.24-3.25). Noise is simulated using dimensionless variables and a random Gaussian distribution with a constant dimensionless standard deviation of 0.01 and a zero mean. This noise is added to the temperature and heat flux data as in Eq. (3.17). The cutoff frequency for the low-pass Gaussian filter must then be found. This is accomplished by first obtaining an estimate for the noise history as outlined in [13]. A first order polynomial is fit to the noisy data, and the residual, R_1, between the noisy data and the first order least squares fit is calculated. Next, a higher order function is used to approximate R_1, and the residual between this fit and R_1 is used as the estimated noise history. Figure 3.3(a) shows the noisy data and a one-term least squares fit of the data. Figure 3.3(b) shows the residual, R_1, and an eighth order least squares fit of R_1. Here, the function used to fit the residual is of the form

$$\Psi(t) \approx \Psi_0 + \sum_{m=1}^{M} a_m \Omega_m(t), \tag{3.31}$$

where $\Omega_m(t)$ are the basis functions and a_m are the unknown coefficients. We have used Hardy multiquadric radial basis functions [58] given by

$$\Omega_m(t) = \sqrt{\beta_m + (t - t_m)^2} - \sqrt{\beta_m + t^2} - \sqrt{\beta_m + t_m^2} + \sqrt{\beta_m}, \qquad m = 1,2,...,M, \tag{3.32}$$

where t_m and β_m are the mth center and shape factor, respectively. As in [13], we have used equidistant centers $t_m = mt_{max}/M$ and set $\beta_m = \beta = (t_{max}/M)^2$. The recreated noise and the actual

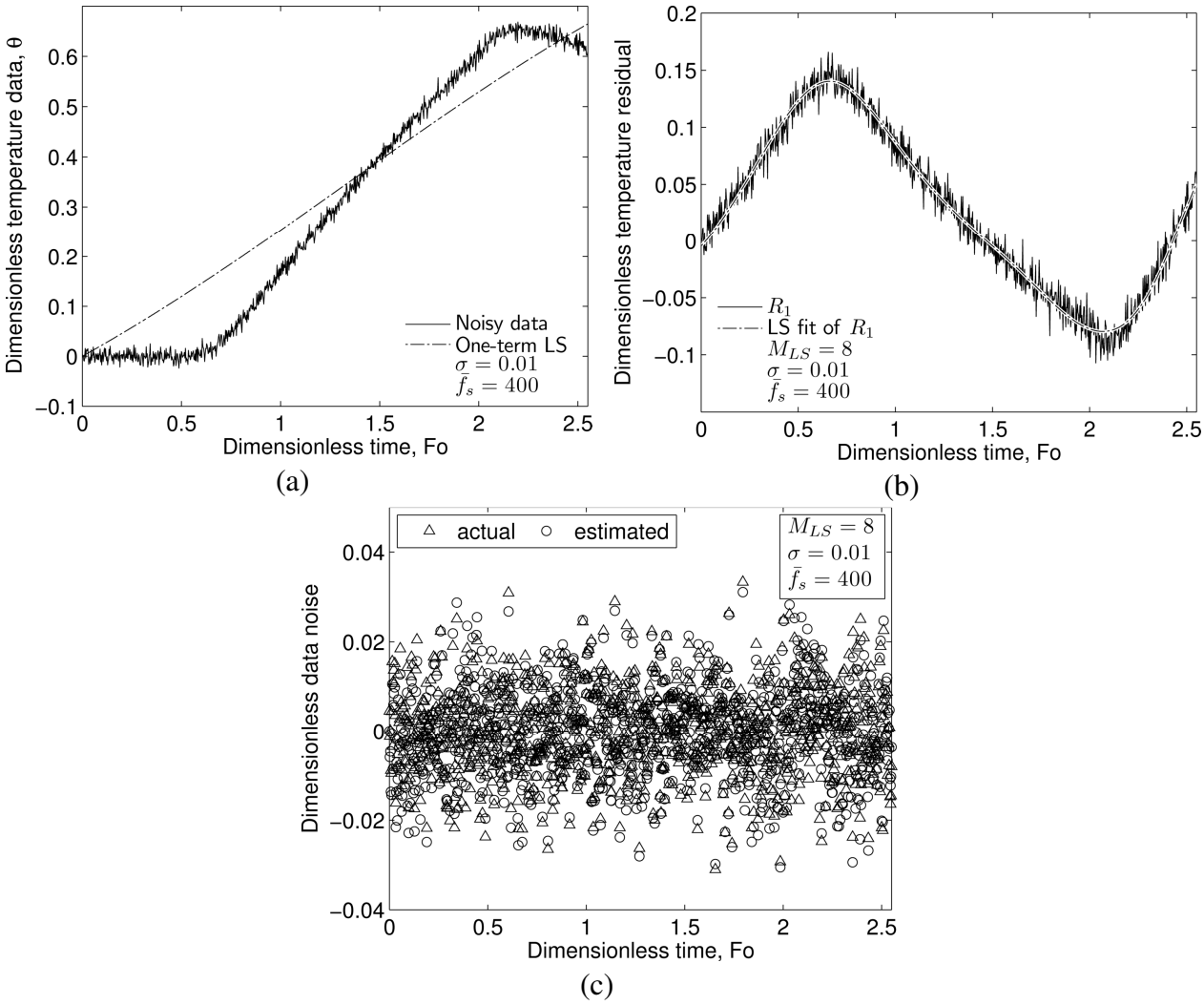

Figure 3.3: Technique for estimating the noise present in the data: (a) first order fit to data (b) least squares fit to residual and (c) actual and estimated noise.

noise can be seen in Figure 3.3(c). Clearly, this is an effective tool for estimating the noise present in the data.

Once the noise history has been estimated, ϕ_1 and ϕ_2 from Eqs. (3.19) and (3.21) can be used to provide a range of appropriate cutoff frequencies. This can be seen in Figure 3.4(a) where the reported optimum dimensionless cutoff frequency range is 2.4 - 2.8. As noted above, the Gaussian low-pass filter used here is relatively insensitive to the actual choice of cutoff frequency. Figure 3.4(b) shows the noisy and filtered temperature histories using cutoff frequencies of 2.4 and 2.8. Although there is a 17% difference between these two values of cutoff frequency, the filter outputs are nearly graphically identical.

Figure 3.5 shows the effectiveness of the inverse method in the presence of noise. Noise was simulated using a normal distribution with a standard deviation of 0.01 for both dimensionless temperature and heat flux data and can be seen in Figure 3.5(a) using a sampling rate of $\bar{f}_s = 400$. Optimum cutoff frequency ranges were determined to be 2.4 – 2.8 for the temperature data and 1.7 – 3.9 for the heat flux data. For simplicity, a common cutoff frequency of 2.6 was used for both temperature and heat flux data. The data were filtered and passed to the inverse scheme. The resulting inverse predictions of the surface temperature and heat flux histories can be seen in Figure 3.5(b-c), respectively. A smoothing effect is observed near t_{on} and t_{off}; Once the inverse prediction settles, the standard deviation of the error is calculated to be 0.01 in the domain $0.75 \leq Fo \leq 1.75$ – which is exactly the same as input error. Additionally, further refinement of the sampling rate does not adversely affect the inverse results. The regularization and inverse method combination effectively makes the problem well-posed.

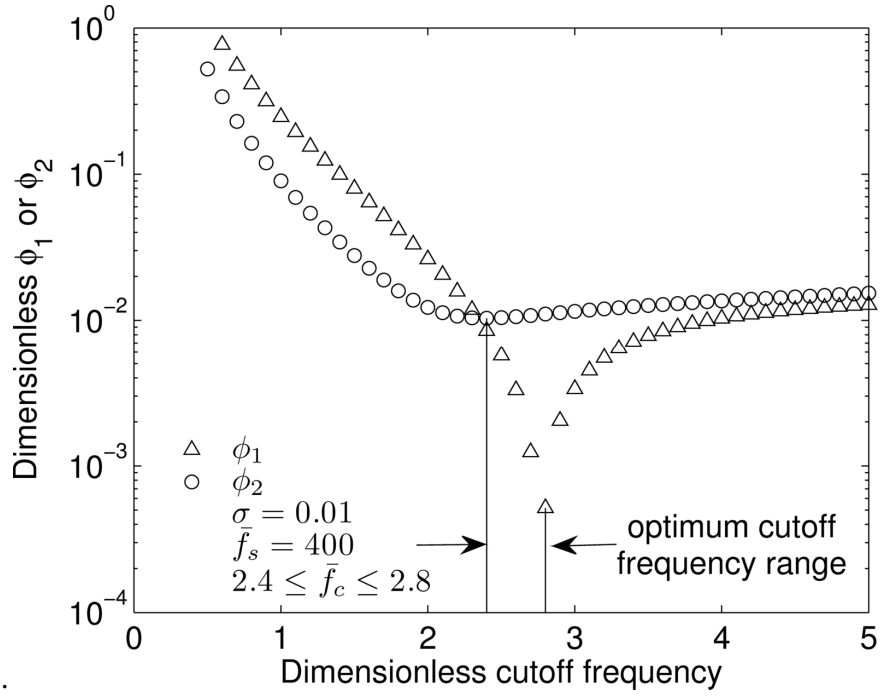

(a)

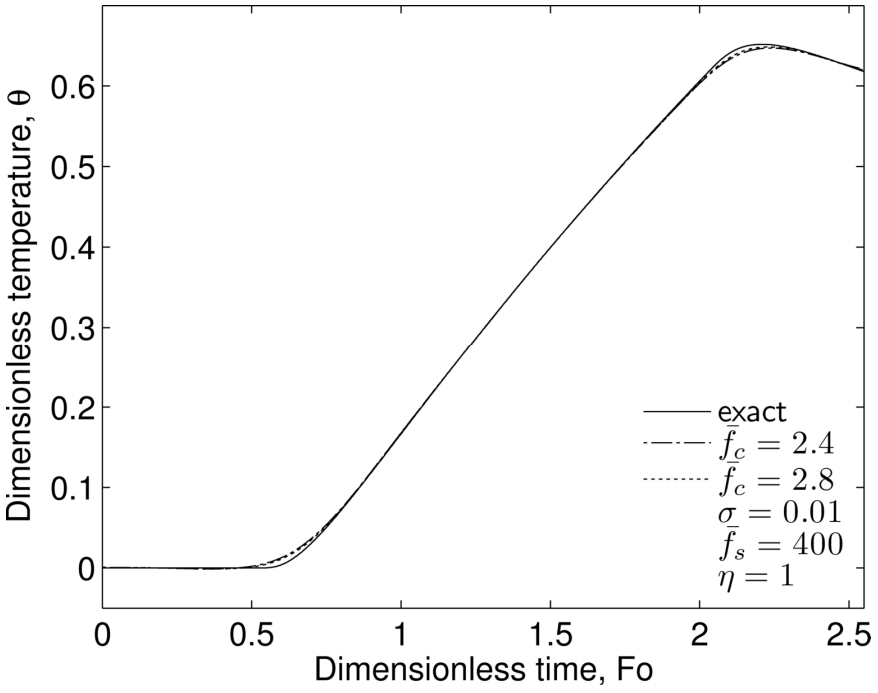

(b)

Figure 3.4: Gaussian low-pass filter exploration. (a) optimum cutoff frequency range and (b) insensitivity of Gaussian filter to a small change in cutoff frequency.

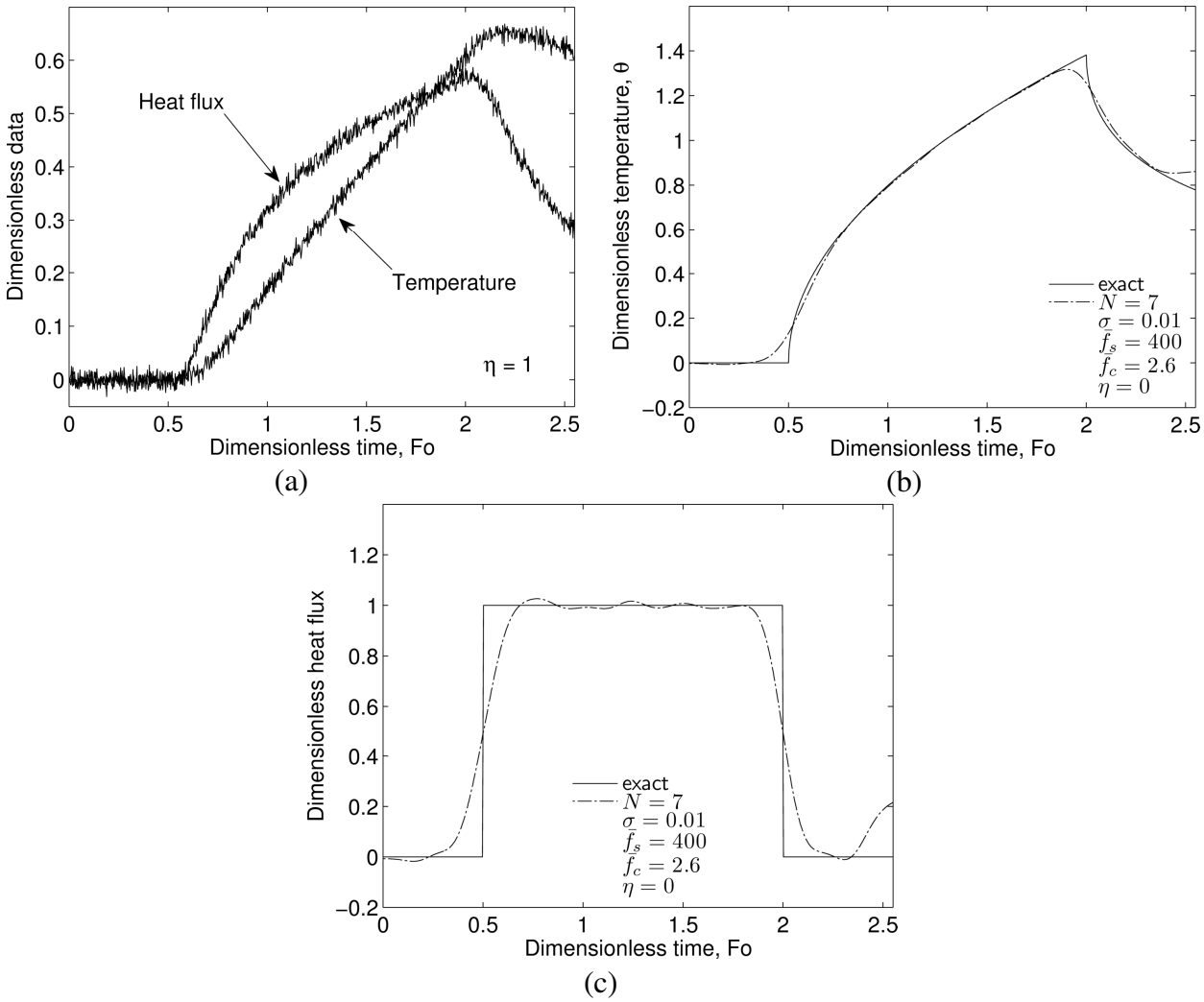

Figure 3.5: Inverse results using a normal distribution, with a standard deviation of 0.01 and a dimensionless cutoff frequency of 2.6. (a) Noisy data used as input to the inverse code, (b) inverse temperature results and (c) inverse heat flux results.

In order to demonstrate the generality of this inverse technique, we also present the classical Beck triangle problem [1]. The surface boundary condition is defined as

$$\bar{q}_{x=0}(t) = \begin{cases} 0, & 0 \le Fo \le 0.3 \\ \dfrac{Fo}{0.6} - 0.5, & 0.3 \le Fo \le 0.9 \\ -\dfrac{Fo}{0.6} + 2.5, & 0.9 \le Fo \le 1.5 \\ 0, & Fo \ge 1.5. \end{cases} \tag{3.33}$$

The body is insulated at $x = L$, and the sensor is located at $x = d = L$. For a dimensionless sampling rate of $\bar{f}_s = 1200$, noise is simulated as in Eq. (3.17) using a normal distribution with a zero mean and a standard deviation of 0.01 for dimensionless temperature which can be seen in Figure 3.6(a). The optimum cutoff frequency range for the data presented was determined to be 2.1 – 4.9. As noted above, the Gaussian low-pass filter used here is relatively insensitive to the actual choice of cutoff frequency. Figure 3.6(b) shows the exact and filtered temperature histories using cutoff frequencies of 2.1 and 4.9. Although there is a large difference between these two values of cutoff frequency, both filter outputs approximate the temperature data well. As a compromise between these two values, a dimensionless cutoff frequency of 3.5 was used to filter the data. The filter output was then passed to the inverse code; the results for the predicted surface temperature and heat flux histories can be seen in Figure 3.7. The peak value of heat flux is underestimated by only 7.0%.

An investigation of the accuracy of the proposed inverse method as a function of the sampling rate was conducted using the surface heat flux of Eq. (3.33) as the test case. The sampling rate was varied from $100 \le \bar{f}_s \le 1200$. Five unique random error distributions were

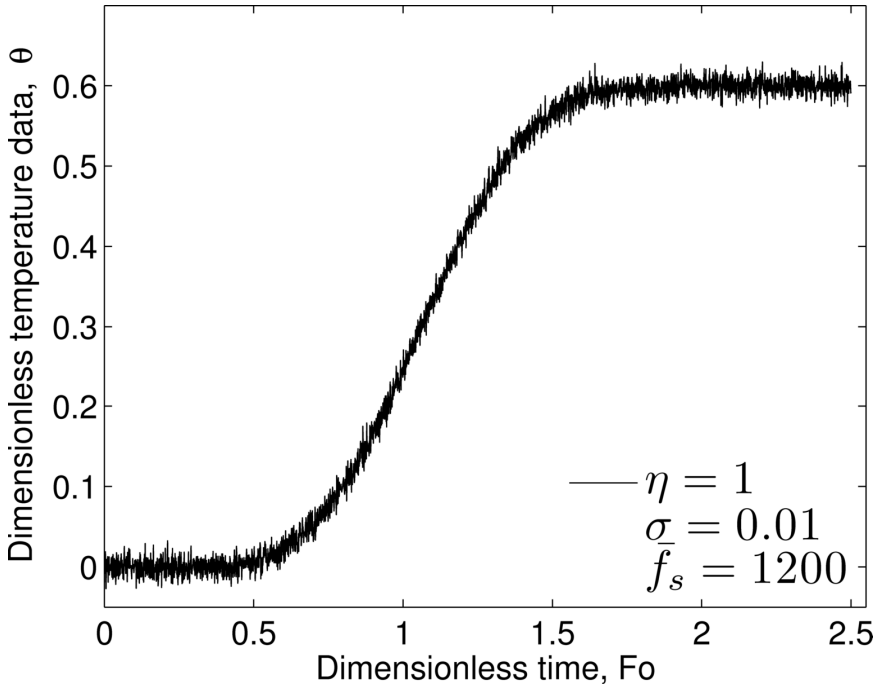

(a)

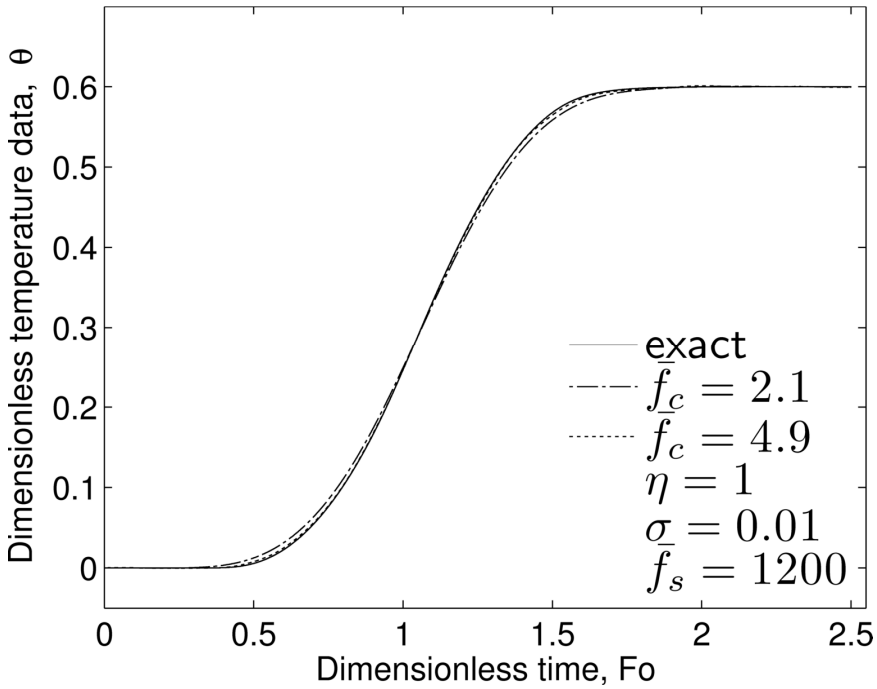

(b)

Figure 3.6: Temperature data for Beck triangle problem (a) raw data with $\sigma = 0.01$ and $\bar{f}_s = 1200$ (b) insensitivity of Gaussian filter to change in cutoff frequency.

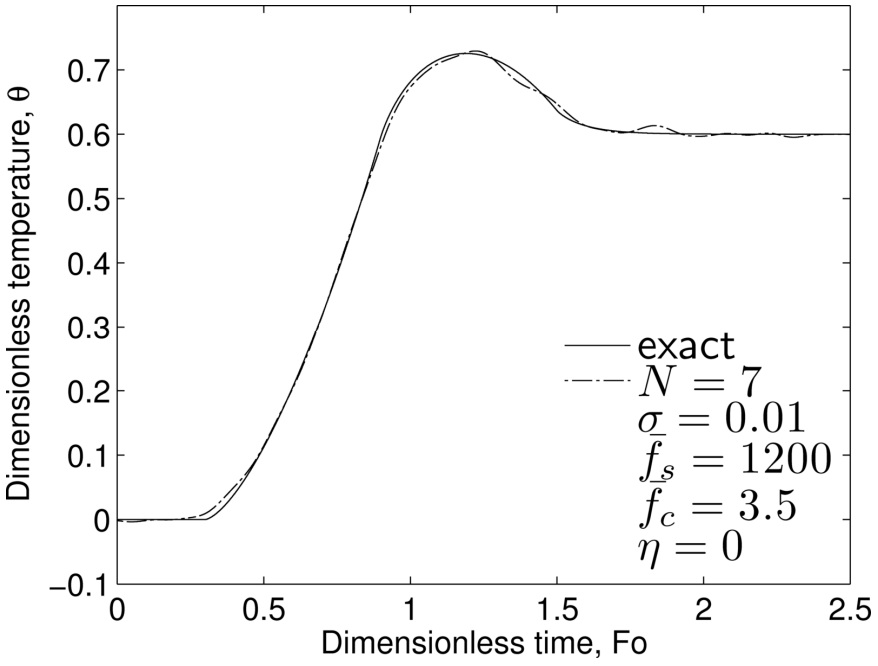

(a)

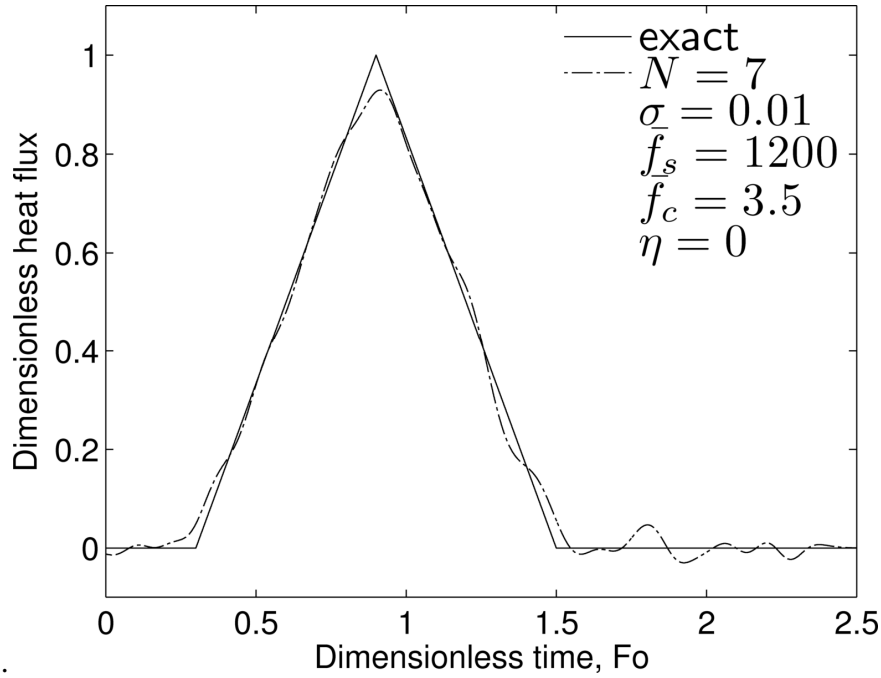

(b)

Figure 3.7: Inverse results for the classical Beck triangle problem for (a) surface temperature prediction and (b) surface heat flux prediction. Noise was simulated using a normal distribution, $\sigma = 0.01$ and $\bar{f}_c = 3.5$ used for regularization.

generated for each sampling rate and added to the data as in Eq. (3.17). The RMS of the surface inverse heat flux prediction was calculated for each dataset such that

$$q_{RMS} = \left[\frac{1}{M} \sum_{k=1}^{M} \left(q_{inv}(t_k) - q_{exact}(x=0,t_k) \right)^2 \right]^{1/2} \tag{3.34}$$

where M is the number of time samples. The RMS error was averaged for the five runs at each sampling rate. Two different values for the order of the inverse scheme, N=4 and N=7, were used. The cutoff frequency was chosen as the midpoint of the optimum range from ϕ_1 and ϕ_2 for both values of N. Also, for N=7, $\bar{f}_c$ was held constant at $\bar{f}_c$ = 3.0 to investigate the effect of sampling rate independent of the cutoff frequency.

Table 3.1 shows the results of the accuracy investigation. In sharp contrast to other inverse methods [1], for N=4 or N=7, increasing the sampling rate resulted in a decrease of the error norm. This is because the time derivatives of the temperature data are more accurately resolved at higher sampling rates. These results hold whether the cutoff frequency is kept constant at 3.0, or chosen as the midpoint of the optimum range. Additionally, greater accuracy was achieved by using the proposed analytical method of determining cutoff frequency over holding the cutoff frequency constant at $\bar{f}_c$=3. Next, it was observed that the error norm improved as N was increased (i.e., more spatial nodes) from N=4 to N=7 using the proposed cutoff frequency determination method. Minimal improvement occurred for low sampling rates, while greater improvement occurred as the sampling rate was increased. Again, this is because the higher-time derivatives of the temperature data are more accurately resolved at higher sampling rates; hence greater improvement is seen at higher sampling rates. These results suggest that optimum inverse predictions are obtained by sampling the data at the highest

Table 3.1: Predicted heat flux RMS error as a function of the sampling rate, $\bar{f}_s$, projection order, N, and choice of cutoff frequency, $\bar{f}_c$; $\bar{f}_{c,mean}$ and $q_{RMS,mean}$ are average values resulting from five independent noise distributions.

	$N=4$ $\bar{f}_c=\left(\bar{f}_{c,\phi 1}+\bar{f}_{c,\phi 2}\right)/2$		$N=7$ $\bar{f}_c=\left(\bar{f}_{c,\phi 1}+\bar{f}_{c,\phi 2}\right)/2$		$N=7$ $\bar{f}_c=3$	
$\bar{f}_s$	$\bar{f}_{c,mean}$	$q_{RMS,mean}$	$\bar{f}_{c,mean}$	$q_{RMS,mean}$	$\bar{f}_{c,mean}$	$q_{RMS,mean}$
100	2.56	0.0370	2.56	0.0368	3.00	0.0439
200	2.86	0.0352	2.83	0.0301	3.00	0.0357
400	3.11	0.0335	3.09	0.0273	3.00	0.0245
1200	3.41	0.0301	3.49	0.0212	3.00	0.0246

possible rate, using higher number of spatial nodes (N), with the proposed cutoff frequency determination method.

3.6 Chapter Summary

A robust global time inverse heat conduction method has been demonstrated. In stark contrast to traditional inverse methods, increasing the data density does not compromise stability of the inverse prediction. Indeed, the inverse results improve with faster data sampling. The time-derivative of the heat equation is not finite differenced. Instead, a functional representation of the higher-time derivatives of temperature are employed to project directly to the surface without the need to calculate the temperatures at intermediate spatial nodes. This is accomplished via a low-pass Gaussian filter with a physically based cutoff frequency which provides an analytical function as output. The proposed regularization scheme presented provides bounded, continuous, analytical time derivatives of the sensor data. Additionally, an analytical method for determining the optimum filter cutoff frequency range is demonstrated. The novel treatment of the temporal derivative in the heat equation, combined with the global time Gaussian low-pass filter provides the regularization required for stable, accurate results. Future studies with this concept should involve extension to two- and three-dimensional geometries.

Chapter 4: In-Situ Higher-Time Derivative of Temperature Sensors for Aerospace Heat Transfer

This chapter is revised based on a paper under review by Bryan S. Elkins, Manguo Huang, and Jay I. Frankel:

Elkins, B. S., Huang, M., and Frankel, J. I., in review, "In-situ higher-time derivative of temperature sensors for heat transfer," International Journal of Thermal Sciences.

My primary contributions to this paper include (i) collaboration in conceptualization of work, (ii) design and construction of the sensor, (iii) collection and analysis of experimental data, and (iv) most of the writing.

4.1 Motivation for Higher-Time Derivatives of Temperature Sensor

This chapter presents a novel sensor that delivers higher-time derivatives of temperature in combination with a thermocouple calibration curve. This highly attractive quantity has been demonstrated to be of critical importance in the global time inverse heat conduction method presented in Chapter 3. Further, higher-time derivatives are useful for acquiring both stable and accurate in-depth heat fluxes, predicting sudden changes in surface heat fluxes from an in-depth array of sensors, and predicting the future temperature in a thermal control environment. This chapter outlines the motivation for developing such a sensor, presents the salient and poignant features of the initial design and processes required for arriving at the sensor while incurring minimal component delay times. Finally, preliminary predictions are presented using an experimental thermocouple drop facility that allows for comparison with an analytic model. The presented results are highly encouraging for stability, accuracy and repeatability.

Heat Flux

This chapter builds on recent previous analytic results [2, 51, 55, 59-63] that produce insightful heat flux-temperature integral relationships that explicitly display the heating rate, $\partial T/\partial t$ as a desirable quantity of physical importance. For example, in one-dimensional half-space studies involving an isotropic material subject to a trivial initial condition, the heat flux at the location $x = d < L$ in the interior can be mathematically expressed as

$$q(x=d,t)=\sqrt{\frac{k^2}{\alpha\pi}}\int_{t_0=0}^{t}\frac{\partial T}{\partial t_0}(d,t_0)\frac{dt_0}{\sqrt{t-t_0}}, \qquad (x,t)\geq 0. \tag{4.1}$$

This equation is valid until the thermal front penetrates the back wall at $x = L$ (see Section 2.3 for a discussion of penetration time). Physically, Eq. (4.1) states that one can acquire the local (in-depth) heat flux at a point within the half space from the local heating rate, $\partial T/\partial t$.

The ill-posed nature of Eq. (4.1), when using experimental temperature measurements, is clearly described in [2, 55]. If the error is bounded in temperature, T, the resulting error in $\partial T/\partial t$ is unbounded as the sample density is increased for fixed run time (i.e., the numerical approximation goes unbounded as sampling density is increased). However, it should be noted that heat flux reconstruction is well-posed if the heating rate, $\partial T/\partial t$ is directly measured since a finite error bound would exist. That is, the heat flux error decreases as the sample density increases [51, 55]. In other words, the time derivative of the temperature is the key ingredient for stability and accuracy [2, 55]. Additionally, this viewpoint is not limited to one-dimensional analysis. Similar relationships exist for two- [60] and three-dimensional [61] space, as well as for orthotropic materials [63].

Global Time Inverse Heat Conduction Method

Chapter 3 presented a global time inverse heat conduction method which requires higher time derivatives of the embedded temperature measurements. A Gaussian low-pass filter was used in functional form which allowed analytical derivatives to be obtained. However, this was required to be done in the post-processing of the data, and the procedure is not computationally cheap. For a semi-infinite medium, a real-time sensor capable of delivering the required higher-time derivatives of temperature could enable a real-time local heat flux via Eq. (4.1) and associated time derivatives; therefore, a real-time inverse surface heat flux prediction could be made. Further, the Gaussian filter can over-smooth changes in temperature data. This in turn can cause attenuation in the resulting derivatives of the Gaussian filter function. A sensor capable of delivering higher-time derivatives of temperature directly from the embedded thermocouple could reduce this attenuation and result in a more accurate inverse surface prediction.

Locating Sudden Jumps in a Surface Heat Flux by In-Depth Determination

Figure 4.1 displays a two-dimensional, isotropic half space subject to a square, steady surface heat flux. For the given surface heat flux, an exact solution is available [59, 60]. Assuming errorless data for demonstration purposes, the objective involves locating or identifying the position (above sensor "0") where the sudden change in surface heat flux takes place from in-depth rate-based measurements. Per the property and geometric data displayed in Table 4.1 and Figure 4.1, Figures 4.2-4.3 display a progressive series of higher-time derivatives of temperature plotted against time at the indicated sensor sites. It is evident that as the time derivatives increase, a coalescence of curves about the jump condition appears. This permits a

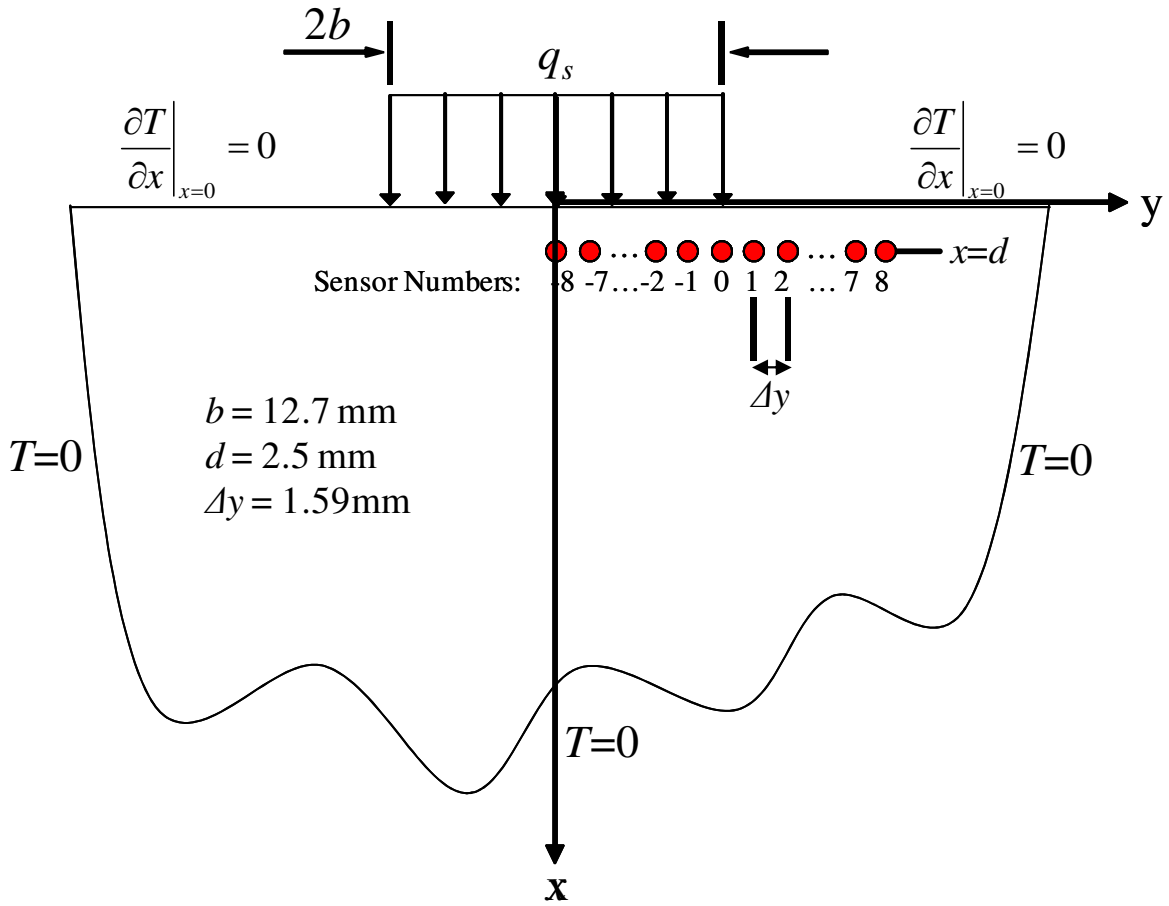

Figure 4.1: Schematic of probe placement (below surface) for surface flux jump location simulation.

Table 4.1: Properties of Copper Bronze.

Property	Value
Thermal conductivity, k	58.7 W/m·K
Thermal diffusivity, α	1.88 x 10^{-5} m^2/s
Density, ρ	7450 kg/m^3
Specific heat capacity, C_p	419 J/kg·K

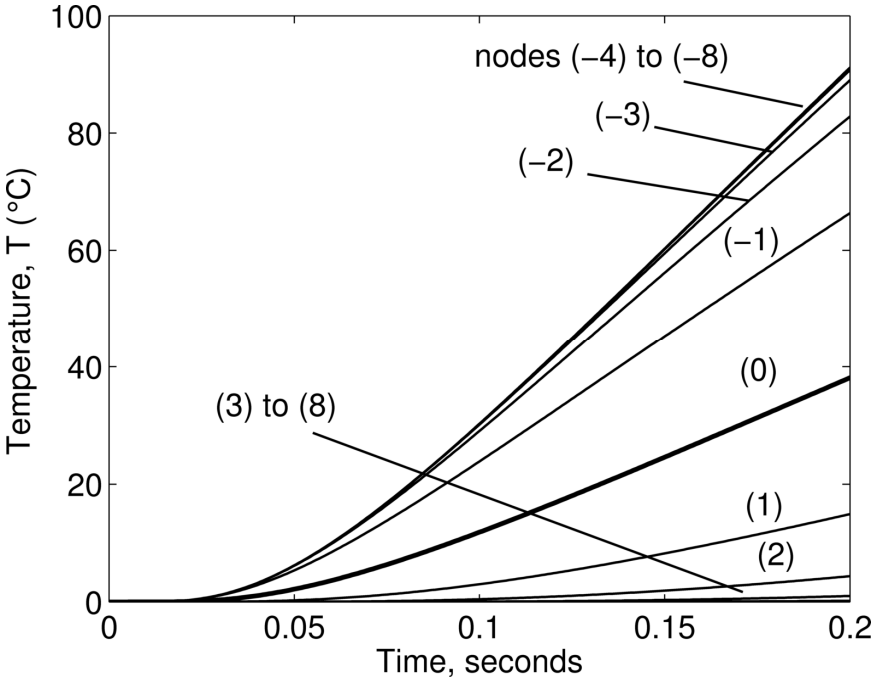

(a)

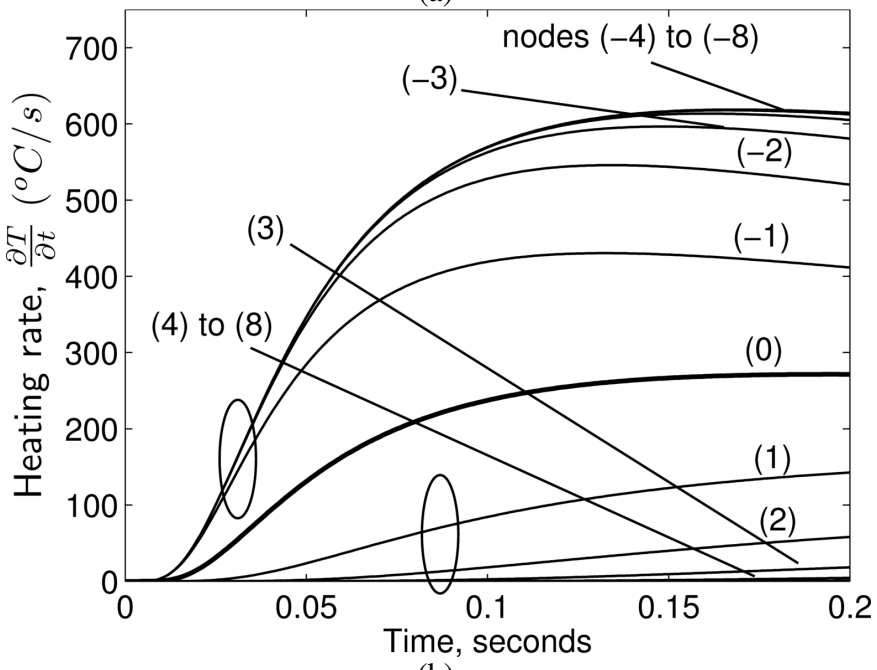

(b)

Figure 4.2: (a) Temperature and (b) heating rate histories at indicated embedded sites. Boundary condition is shown in Figure 4.1 with $q_s = 10^6$ W/m^2.

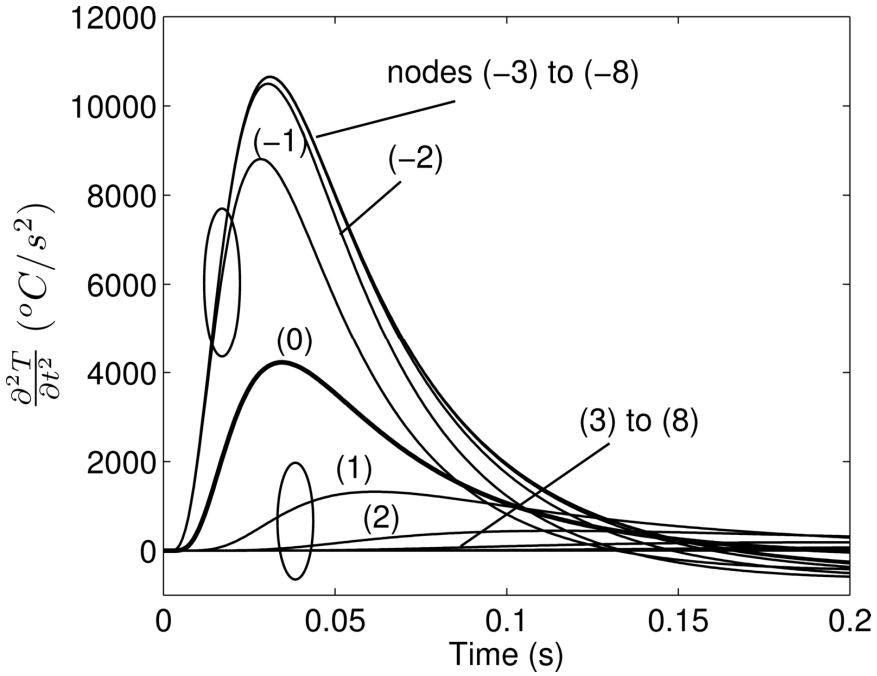

(a)

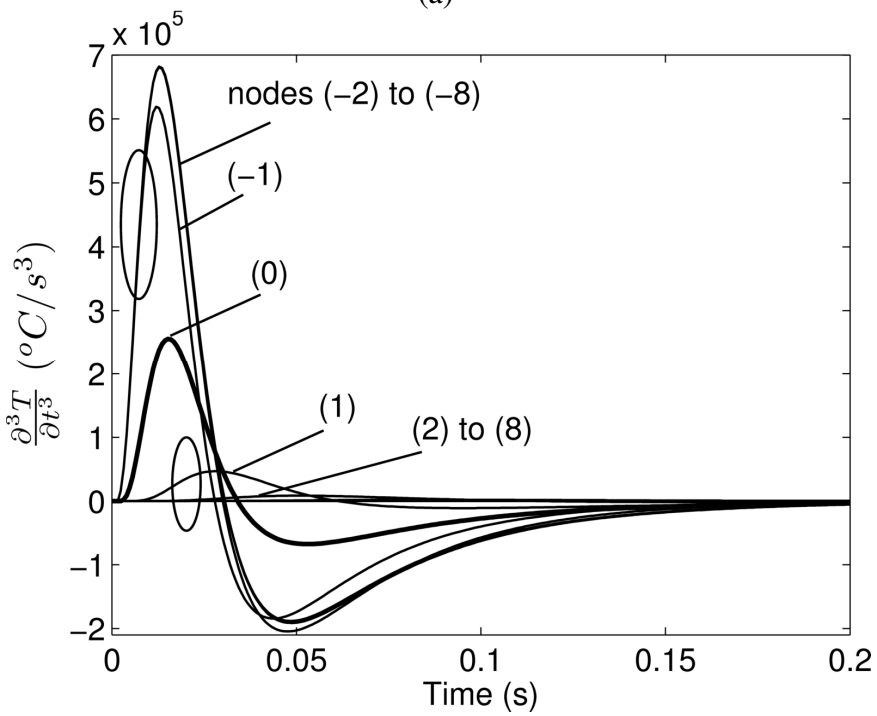

(b)

Figure 4.3: (a) Second and (b) third time derivatives of temperature histories at indicated embedded sites. Boundary condition is shown in Figure 4.1 with $q_s = 10^6$ W/m^2.

direct interpretation (i.e., no inverse analysis required) for the location of the jump using an array of in-depth sites.

A second and important observation can be made from Figures 4.2 and 4.3. By diffusion theory, the effect among the sensors is picked up earlier as the time derivative increases. That is, it is well known that differentiation has a "roughening" effect while integration has a "smoothing" effect. Numerical "roughening" translates to amplifying physics useful for early detection. If noise is controlled in the differentiation, then this concept can be used for detecting sudden changes in surface heat fluxes. This concept may have application for locating transition in hypersonic flows.

Thermal Management and Feedback/Controls.

If higher time derivatives of temperature are available then it appears possible to predict the future in the sense of analytic continuation. That is, the Taylor series of temperature at time t+ can be estimated through an expansion about the point t as

$$T(t+\gamma) = T(t) + \gamma \left.\frac{dT}{dt}\right|_t + \frac{\gamma^2}{2}\left.\frac{d^2T}{dt^2}\right|_t + \frac{\gamma^3}{6}\left.\frac{d^3T}{dt^3}\right|_t + \ldots \qquad (4.2)$$

where γ represents a small increment in time. This will be demonstrated in Section 4.5.

4.3 Time Derivatives of Temperature Sensor

Section 4.2 presented some preliminary but revealing findings that clearly describe the need for a new array of rate-based sensors. Three immediate choices are conceptually available for obtaining higher-time derivatives of temperature.

1. Find a material that has a property that is dT/dt dependent (an electrical property is an ideal choice if available, e.g., Pyroelectric materials).
2. Obtain the derivatives via post-processing.
3. Develop a highly accurate electrical interface (sensor) that can be used with a known property (such as a calibration curve) through differential calculus.

The first option does not seem viable since higher-time derivatives will be difficult to obtain. The second option involves numerical differentiation of data with measurement error which will amplify the noise; however, post-processing can be an acceptable technique provided the data is carefully filtered (see section 3.3). Additionally, obtaining the derivatives through post-processing eliminates the possibility of using real-time analysis. Case 3 does not represent a true temperature rate sensor; however, the desired temperature rates are estimated through a voltage-rate interface that accounts for the nature of diffusion. The third option both allows for real time analysis and presents the possibility of higher-time derivatives without noise amplification. Therefore, the sensor presented herein relies is based on the voltage rate interface.

Thermocouples and Well-Designed Voltage-Rate Interface:

In order to arrive at the necessary number of time derivatives of temperature, we must first propose a strategy. The strategy starts by noting that a thermocouple is a well-behaved and a mainstay sensor. The calibration curve normally follows the form given by the simple polynomic expansion[64]

$$T(V_i) = \sum_{n=0}^{N} a_n V_i^n \tag{4.3}$$

where $\{a_n\}_{n=0}^{N}$ are experimentally determined coefficients. Here, the reference point is taken as the freezing temperature of pure water. The desired time derivatives of temperature follow from the chain rule of calculus as

$$\frac{dT}{dt} = \frac{dT}{dV}\frac{dV}{dt}, \tag{4.4}$$

$$\frac{d^2T}{dt^2} = \frac{d^2V}{dt^2}\frac{dT}{dV} + \left(\frac{dV}{dt}\right)^2 \frac{d^2T}{dV^2}, \tag{4.5}$$

$$\frac{d^3T}{dt^3} = \frac{d^3V}{dt^3}\frac{dT}{dV} + 3\frac{dV}{dt}\frac{d^2V}{dt^2}\frac{d^2T}{dV^2} + \left(\frac{dV}{dt}\right)^3 \frac{d^3T}{dV^3}, \tag{4.6}$$

where $T \to T(V)$. Thus, for a third time derivative of temperature, three voltage-rate circuits must be cascaded in series with minimal error amplification in the analog differentiation process. Eqs. (4.4-4.6) require calibration data for determining the properties, d^nT/dV^n (n=0,1,…) which is available per Eq. (4.3). Additionally, if the calibration curve is linear over the temperature range of interest, Eqs. (4.5-4.6) simplify to become

$$\frac{d^2T}{dt^2} = \frac{d^2V}{dt^2}\frac{dT}{dV} \tag{4.7}$$

$$\frac{d^3T}{dt^3} = \frac{d^3V}{dt^3}\frac{dT}{dV} \tag{4.8}$$

It then remains to obtain the higher-time derivatives of voltage, which can then be mapped back to higher-time derivatives of temperature. For this task, we rely on the circuit shown in Figure 4.4. The time derivatives are obtained using the basic architecture of the "practical differentiator" [65] seen in Figure 4.5 with a modified design procedure. This choice of differentiator stabilizes the differentiation process by reducing the level of high frequency

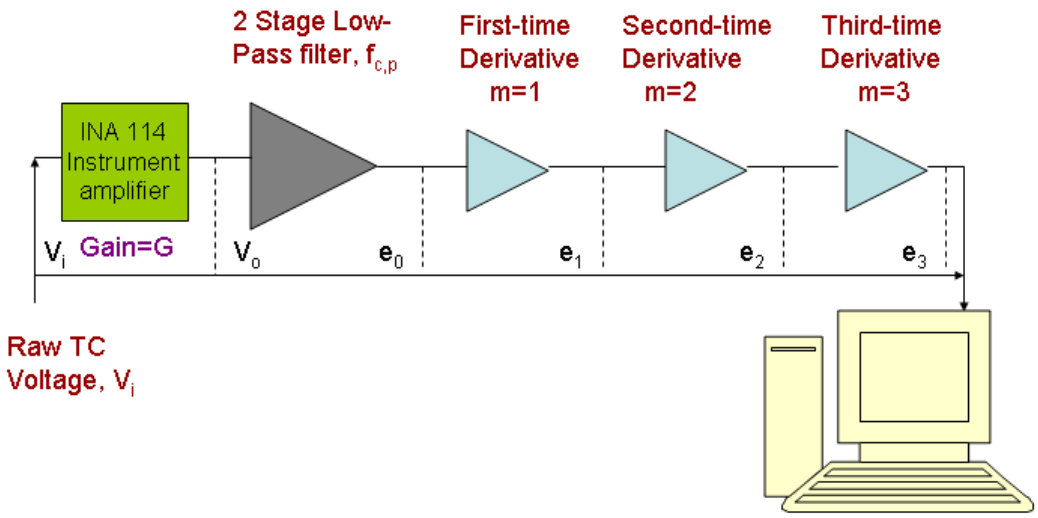

Figure 4.4: Schematic of concept for acquiring necessary voltage rates with minimal high frequency content and minimal time lag. Here, e_m, m=1,2.. are voltage outputs from differentiator that are mathematically related to the thermocouple voltage, V_i.

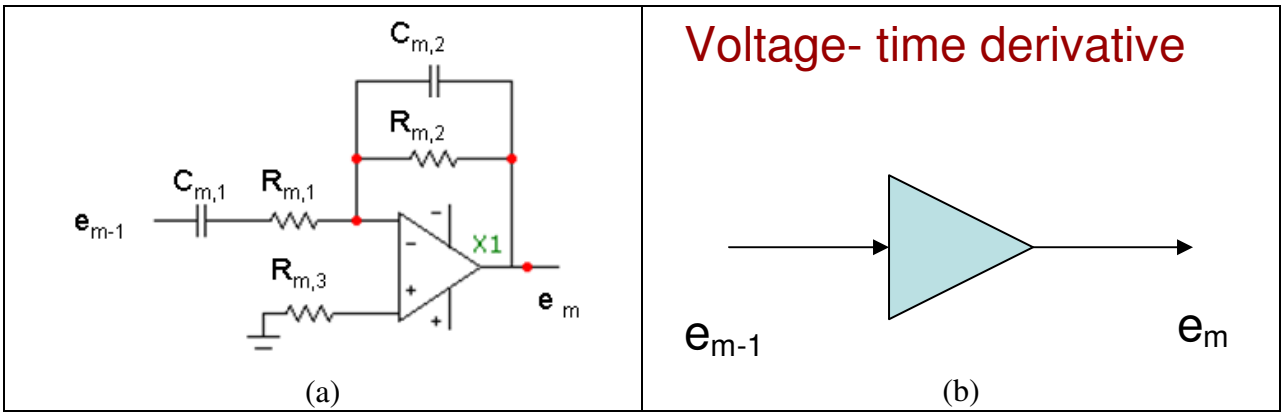

Figure 4.5: (a) Basic differentiating circuit used in practice (m=1,2,…) and (b) symbolic element as expressed in Figure 4.4.

noise allowed to be passed; a 20dB/decade rolloff is present for input frequencies greater than the corner frequency, f_2.

The practical differentiator [65] has two characteristic frequencies given by

$$f_1 = \frac{1}{2\pi R_{m,2} C_{m,1}} \tag{4.9}$$

$$f_2 = \frac{1}{2\pi R_{m,1} C_{m,1}} = \frac{1}{2\pi R_{m,2} C_{m,2}} \tag{4.10}$$

where f_1 is chosen as the highest frequency of the signal (cutoff frequency), and traditional design procedure suggests setting the corner frequency $f_2 = 10f_1$. However, this allows nonphysical frequency content one order of magnitude greater than the cutoff frequency to be passed. Therefore, the proposed modified design procedure of the practical differentiator instead sets the corner frequency, f_2, equal to the cutoff frequency, f_c. This allows proper attenuation of noise. Rather that arbitrarily setting $f_1 = 10f_2$, we next examine the differential equation of the practical differentiator given by

$$\tau_{dif}^2 \frac{d^2 e_m(t)}{dt^2} + 2\tau_{dif} \frac{de_m(t)}{dt} + e_m(t) = -R_{m,2} C_{m,1} \frac{de_{m-1}(t)}{dt}, \qquad m = 1,2,..., \tag{4.11}$$

$$\tau_{dif} = R_{m,1} C_{m,1} = R_{m,2} C_{m,2}, \qquad m = 1,2,..., \tag{4.12}$$

where $e_{m\text{-}1}(t)$ is the input to the differentiator and $e_m(t)$ is the output. For low input frequencies, the differential equation simplifies to

$$e_m(t) = -R_{m,2} C_{m,1} \frac{de_{m-1}}{dt}(t), \quad m = 1,2,... \qquad f << f_2, \tag{4.13}$$

where $(-R_{m,2}C_{m,1})$ is the differentiation gain, G_D. We therefore propose using f_1 to set the differentiator gain to user-defined value, suitable to the application at hand. This is chosen to a)

avoid saturation of the analog-to-digital interface and b) maximize the resolution of the differentiated signal. The ground resistor, $R_{m,3}$, is determined by $R_{m,1}||R_{m,2}$ in the differentiator. Using basic calculus following from Eqs. (4.3-4.5) in combination with Eq. (4.13), we can then obtain the higher-temporal derivatives as

$$\frac{dT}{dt}(t) = \frac{e_1(t)}{GR_{1,2}C_{1,1}}\frac{dT}{dV_i} = \frac{e_1(t)}{GR_{1,2}C_{1,1}}\sum_{n=0}^{N} na_n V_i^{n-1}, \tag{4.14}$$

$$\frac{d^2T}{dt^2}(t) = -\frac{e_2(t)}{GR_{2,2}C_{2,1}R_{1,2}C_{1,1}}\sum_{n=0}^{N} na_n V_i^{n-1} + \left(\frac{e_1(t)}{GR_{1,2}C_{1,1}}\right)^2 \sum_{n=0}^{N} n(n-1)a_n V_i^{n-2}. \tag{4.15}$$

The cutoff frequency can be chosen using Wiener filtering concepts outlined in Section 2.6. Figure 4.6 presents the power spectra, as obtained from the DFT via Eqs. (2.30) and (2.32), from a thermocouple dropped into a constant temperature, well-stirred hot bath described in Section 4.4. The noise level in the signal is extrapolated via a line is drawn tangent to the high frequency portion. The true signal is extrapolated by a line drawn tangent to the low frequency portion. The intersection of these two tangent lines is the cutoff frequency.

Consider the two differentiator designs seen in Table 4.2. Both designs have a differentiation gain of 0.091; one has a cutoff frequency of 35 Hz, and the other has a cutoff frequency of 350 Hz. Using the input given by $e_{m-1}=A_{m-1}\sin(2\pi ft)$ we can obtain the theoretical output $e_m(t)$. Trivial initial conditions are assumed. A plot of the differentiators' experimental input-output magnification ratio can be seen in Figure 4.7 compared with the theoretical ratio. Figure 4.8 displays the differentiators' experimental delay times as a function of frequency. The component delay, or lag time, for this application is defined by the maximum value in the range of $f \in [0, f_{c,dif})$. Theoretical results were obtained from the circuit differential equation given by

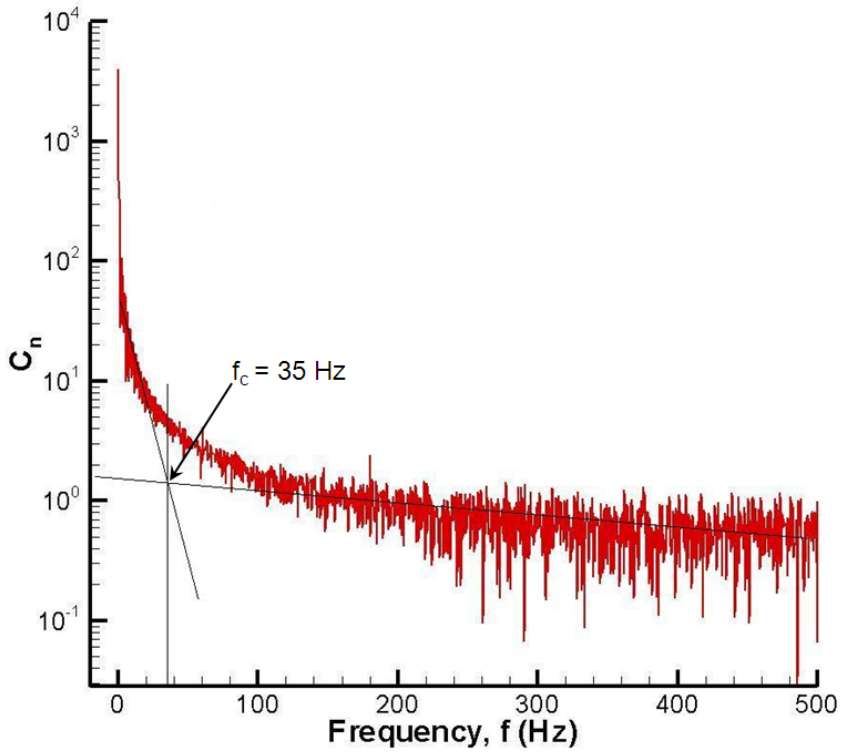

Figure 4.6: Typical power spectra from DFT for a thermocouple drop test. The physical cut-off frequency is estimated as $f_{c,p}$=35 Hz.

Table 4.2: Differentiator components used in generating results displayed in Figure 4.10 where $\left\|\tau_{lag}\right\|_{\infty} = \max_{f\in[0,f_{c,dif})}\left|\tau_{lag}\right|$.

Item	$f_{c,dif}$ = 35 Hz	$f_{c,dif}$ =350 Hz
Operational Amplifier	OP07DP	OP07DP
$R_{m,1}$	10.02kΩ	1.002kΩ
$C_{m,1}$	0.454μf	0.455μf
$R_{m,2}$	19.96kΩ	19.96kΩ
$C_{m,2}$	0.228μf	22.8nf
$R_{m,3}$	6.617kΩ	0.954kΩ
$\left\|\tau_{lag}\right\|_{\infty}$ (theoretical)	9ms	0.9ms

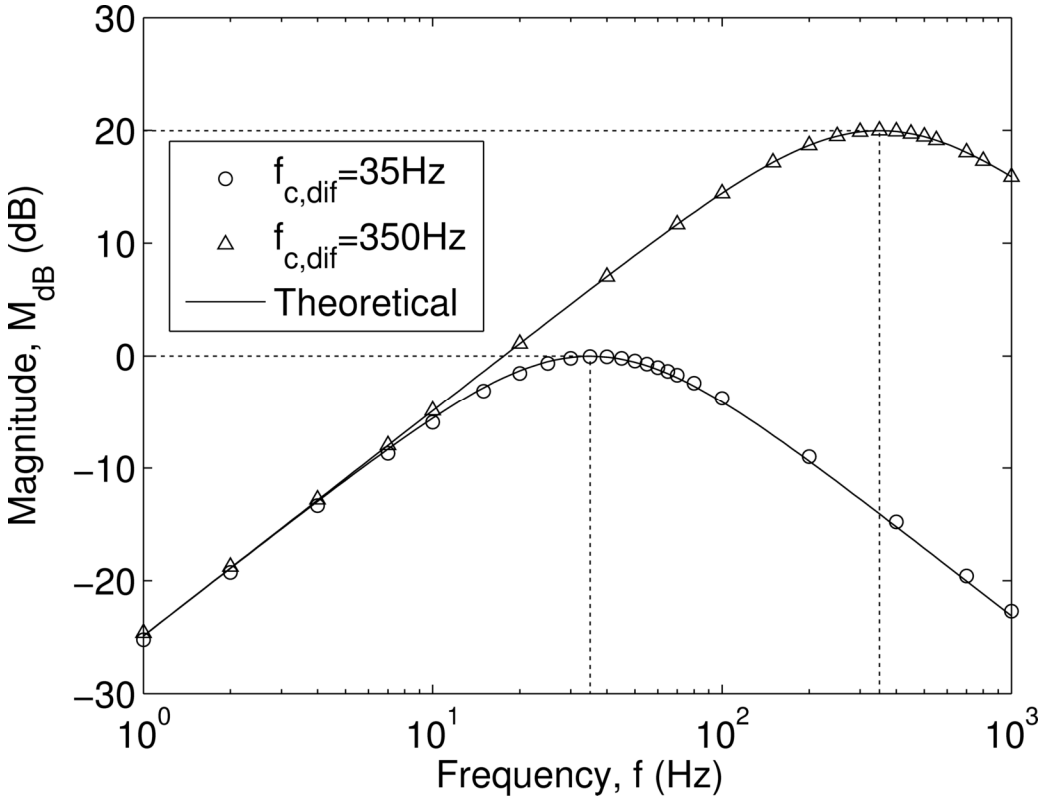

Figure 4.7: Filtering effect in the designed differentiator as a function of frequency for two sample cut-off frequencies.

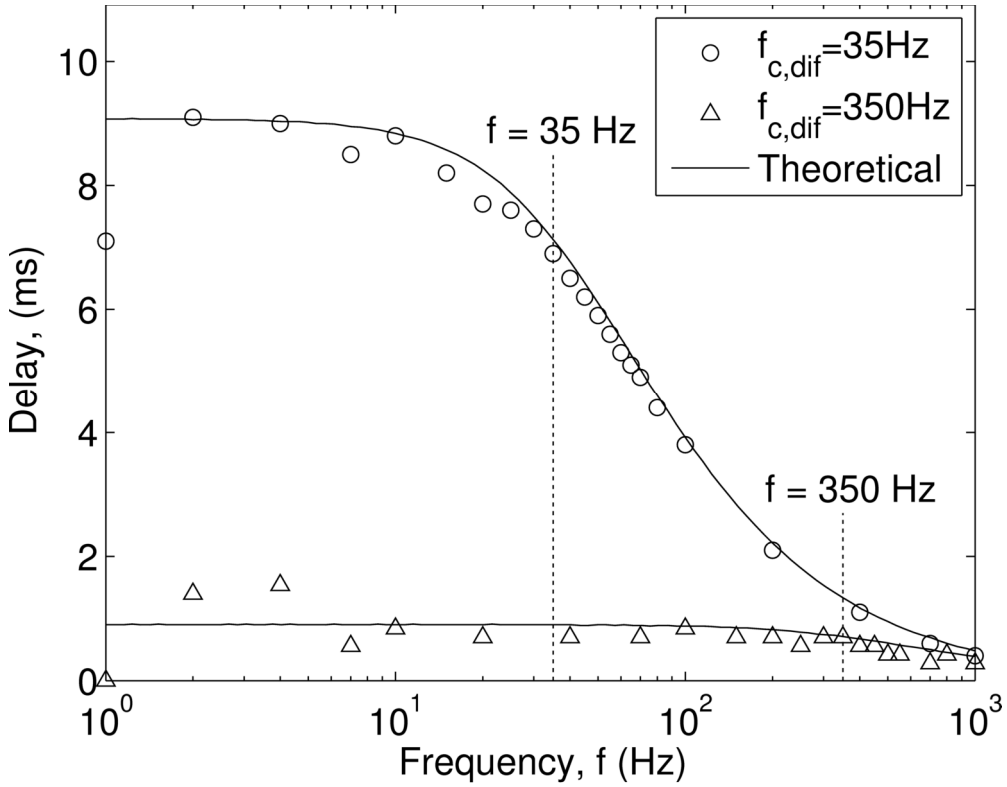

Figure 4.8: Lag times as a function of frequency to demonstrate that increasing the differentiator cut-off frequency produces a corresponding decrease in circuit component delay times.

Eq. (4.11). It is apparent from Figure 4.8 that an increase in the differentiator cutoff frequency by one order of magnitude correspondingly decreases the lag time by one order of magnitude.

Reduction in time lags (component delays) is necessary in many applications, particularly in aerospace experiments involving short-time durations (ex. arc-jets). Thus, a delay time of 1 millisecond (or less) may be necessary in the entire circuit design. This can be accomplished by exploiting the physics of the problem; both heat transfer by diffusion in a solid body and the present thermocouple drop tower experiment are dominated by energy at the low frequencies as previously depicted by the power spectra displayed in Figure 4.6. Therefore, it is possible to reduce the component delay times of the differentiators by (1) increasing the differentiator cut-off frequency and (2) introducing a multistage low-pass filter after the low-noise instrument amplifier but prior to the cascaded differentiators. This negates the adverse effect of permitting high frequency information to freely pass to the differentiator by filtering it before it reaches the differentiators. Therefore, a multistage low-pass filter is used as the pre-filter, with offset control and filter cut-off frequency, $f_{c,fil}$, based on the physical cut-off frequency, $f_{c,p}$, obtained from a sample run of the experiment (for example, see Figure 4.6).

The Butterworth 2-stage, fourth-order, low-pass filter was initially chosen as the pre-filter for simplicity. This filter will be later replaced by a higher-order filter for additional control and accuracy. This filter is displayed in Figure 4.9. The Butterworth filter behaves as designed having an 80 db/decade rolloff to the stopband as shown in Figure 4.10. Theoretical calculations are acquired from the filter's transfer function while the experimental values are determined by

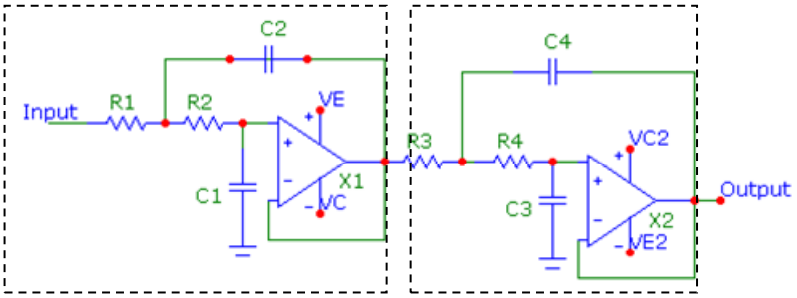

(a)

2 Stage Low-Pass Filter

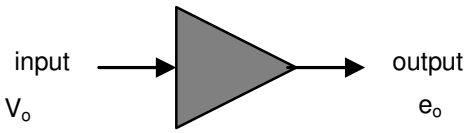

(b)

Figure 4.9: 2-Stage Low-Pass filter (Butterworth) designed to remove signal frequency content $f>f_{c,p}$. (a) Circuit schematic and (b) symbolic element for use in Figure 4.4.

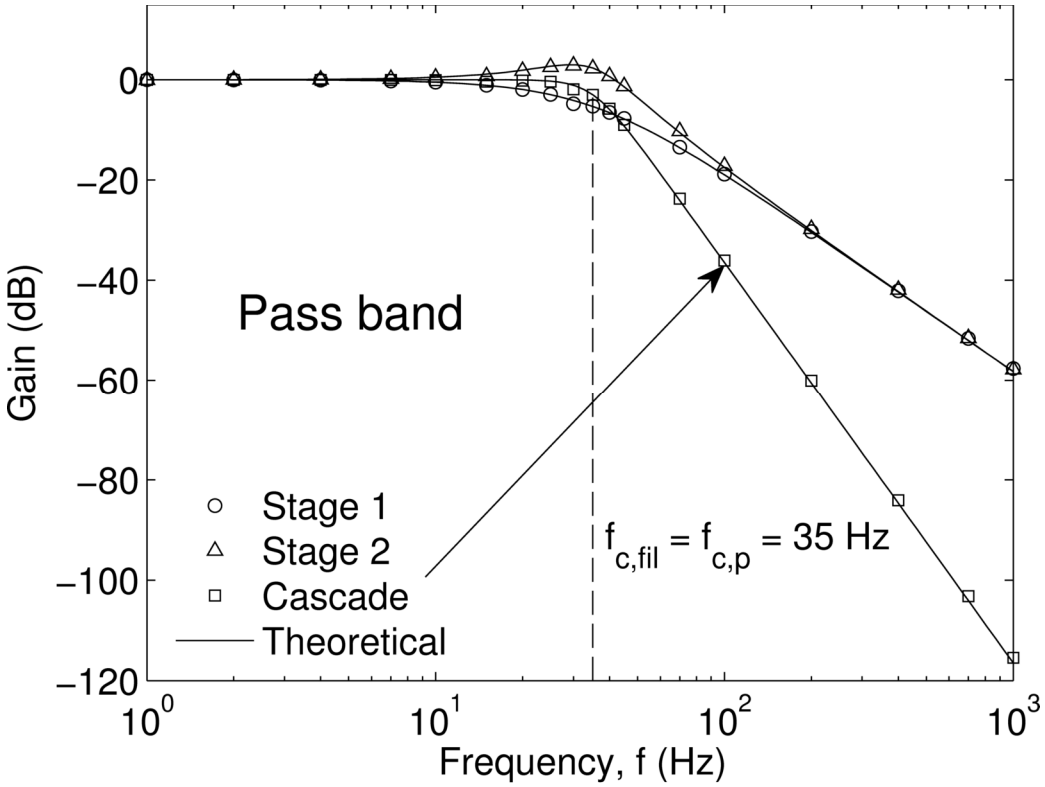

Figure 4.10: Butterworth filter characteristics as a function of frequency for each stage and as a cascaded filter indicating $f_{fil} = f_{c,p}$=35 Hz as designed.

comparing the output amplitude to the input amplitude. Tables 4.3 and 4.4 contain the specific component details and test equipment, respectively used in the present investigation.

4.4 Heat Transfer Experiment

In order to verify the designed sensor, a simple experiment was developed using the drop facility shown in Figure 4.11. A type T thermocouple in equilibrium with ambient air at 20.3 °C was plunged into an isothermal, stirred water bath at 46.6 °C. The insulation was pulled away from the thermocouple junction (bead) to reduce conductive lead losses as the bead plunges into the hot bath. In this way, the leads and bead experience similar environmental conditions. The drop facility has been demonstrated to produce a highly repeatable drop [44]. Table 4.5 presents the calibration curve data used for this experiment. The calibration data was obtained using the specific thermocouple for this experiment. The collected voltage converted to temperature as per Eq. (4.3) and verified by comparison to a NIST calibrated thermometer, which is accurate to 0.1°C.

The thermocouple was connected to the circuit as seen in Figure 4.4. An instrument amplifier (INA) with a gain of -1507.1 was used as input to the pre-filter. A 4^{th} order Butterworth filter with a cutoff frequency of 35 Hz was used as the pre-filter in order to minimize the component lag time in the differentiators as described above. A cutoff frequency of 350 Hz was used in the differentiators (see Tables 4.2 and 4.3 for specific components). Voltages from the INA, pre-filter, and derivative sensors were collected at 10 kHz.

An idealized thermocouple model is normally developed based on a lumped capacitance formulation producing [44]

Table 4.3: Components used in constructing the low-pass filter displayed in Figure 4.12.

Item	Stage1	Item	Stage2
Operational Amplifier	OP07EP	Operational Amplifier	AD 818AN
R1	147.9kΩ	*R3*	56.28kΩ
C1	47.5nF	*C3*	48.4nF
R2	29.07kΩ	*R4*	15.67kΩ
C2	101.3nF	*C4*	485nF

Table 4.4: List of test equipment used in generating all displayed electronic data.

Equipment	Purpose
Data Acquisition Function Module (DT9806)	Collection of voltages e_0,e_1,e_2 as in Figure 4.7
Fluke 87V Multimeter	Measurement of resistors and capacitors displayed in Tables 4.1 and 4.2
Agilent Waveform Generator (Model 33220A)	Testing of the basic circuits after construction for characterizing the frequency response of the circuit
NIST Calibrated Thermometer	Calibration of TC
RTE-110 isothermal bath	Well-stirred isothermal bath for plunge test

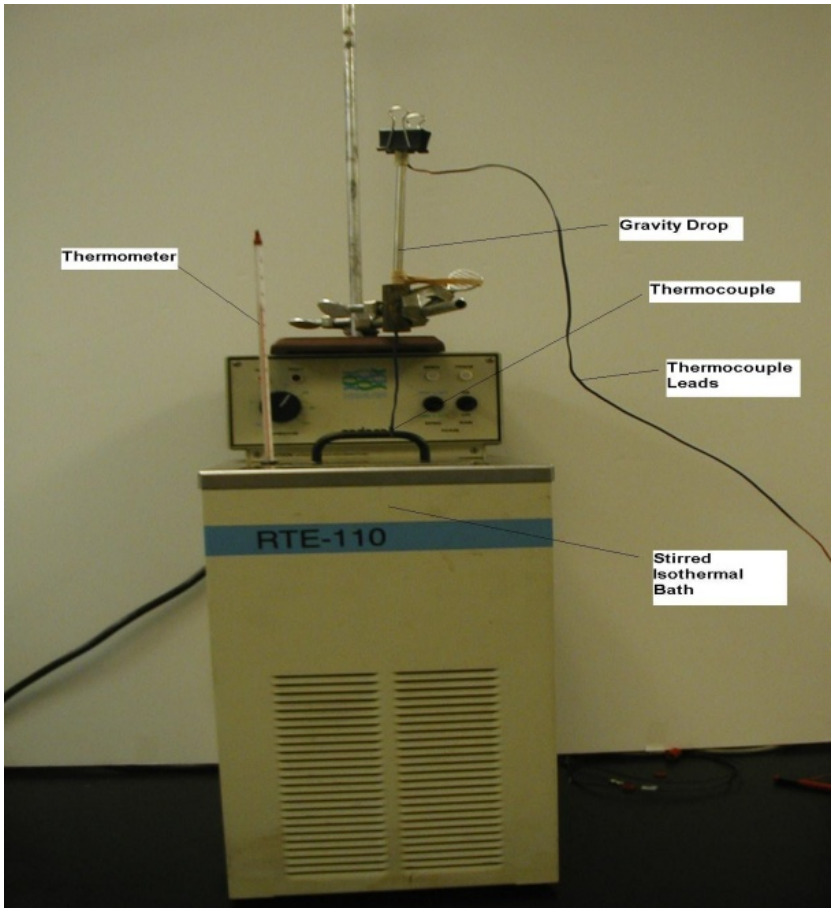

(a)

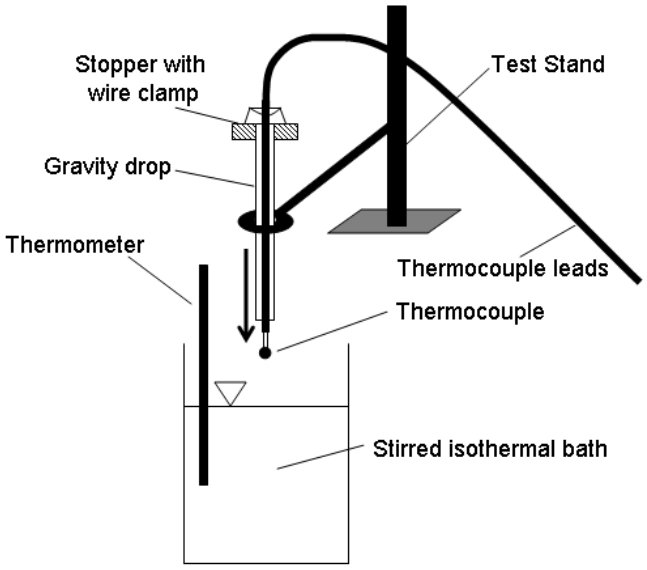

(b)

Figure 4.11: Isothermal hot bath used for experimentally verifying sensor along with a schematic diagram. (a) Picture of setup and (b) labeled sketch of setup.

Table 4.5: Type T thermocouple calibration data T [20.3°C, 46.6°C]. Calibration performed after amplification.

Coefficient	Value
a_0	3.7252 ^{o}C
a_1	25.536 ^{o}C/V
a_2	0 ^{o}C/V^2

$$\tau_{TC}\frac{dT}{dt}(t)+T(t)=T_{\infty}, \qquad t\geq 0, \tag{4.16}$$

$$\tau_{TC}=\frac{hA}{\rho C_p Vol_{TC}}, \tag{4.17}$$

subject to the initial condition

$$T(0)=T_i, \tag{4.18}$$

where τ_{TC} is the thermocouple time constant; T_{∞} is the ambient temperature; h is the convection heat transfer coefficient; and ρ, C_p, and Vol_{TC} are the thermocouple bead density, heat capacity and volume, respectively. The analytic solution to Eq. (4.16) subject to the initial condition given in Eq. (4.18) is

$$T(t)=T_{\infty}+(T_i-T_{\infty})\exp\left(-\frac{t}{\tau_{TC}}\right), \qquad t\geq 0, \tag{4.19}$$

with the first time derivative

$$\frac{dT}{dt}=\frac{T_{\infty}-T_i}{\tau_{TC}}\exp\left(-\frac{t}{\tau_{TC}}\right), \qquad t\geq 0. \tag{4.20}$$

The time constant is experimentally determined as the time when the system has responded to 63.21% of the step change [44]. Higher-time derivatives with respect to time, t can be analytically determined from Eqs. (4.19-4.20) for later comparison with the collected experimental data. However, it should be noted that the ideal responses for the heating rate, Eq. (4.20) and all higher time derivatives of temperature are nonphysical; the theoretical model assumes an instantaneous jump in the heating rate at time t=0 which cannot be replicated.

Therefore, an alternative method of verifying the accuracy of the derivative sensors is necessary. It is well-known that numerical differentiation of data with measurement error

amplifies the error [1, 66]. Therefore, a Gaussian low-pass filter (previously used in Chapters 2 and 3) has been used to filter the temperature data before numerical differentiation such that

$$\hat{T}(t) = \left(\sum_{k=0}^{P} \exp\left(-\pi^2 f_c^2 (t - t_k)^2 \right) \right)^{-1} \sum_{k=0}^{P} \tilde{T}(t_k) \exp\left(-\pi^2 f_c^2 (t - t_k)^2 \right), \tag{4.21}$$

where f_c is the cutoff frequency in Hz, P is the number of time steps, $\hat{T}$ is the filtered temperature and $\tilde{T}$ denotes the raw, discrete sensor temperature data. Once again, we highlight that this filter uses discrete data as input, while the output to the filter is an analytical function. As previously noted in Chapter 3, the filtered temperature can therefore be differentiated analytically; the first time derivative is given by

$$\begin{aligned} \frac{d\hat{T}}{dt}(t) = 2\pi^2 f_c^2 \left(\sum_{k=0}^{M} \exp\left(-\pi^2 f_c^2 (t - t_k)^2 \right) \right)^{-2} \left[\sum_{k=0}^{M} (t - t_k) \tilde{T}(t_k) \exp\left(-\pi^2 f_c^2 (t - t_k)^2 \right) \bullet \right. \\ \left. \sum_{j=0}^{M} \left(\frac{t - t_j}{t - t_k} - 1 \right) \exp\left(-\pi^2 f_c^2 (t - t_j)^2 \right) \right], \quad t \geq 0, \end{aligned} \tag{4.22}$$

and the higher time derivatives can be similarly obtained analytically. Therefore, the Gaussian low-pass filter and its derivatives are used as a comparison to the sensor output.

4.5 Results

In this section, we present time derivative (rate) of temperature results up to the second-time derivative using the proposed sensor. The time constant of the thermocouple was determined to be 0.0222 seconds from the temperature history plot shown in Figure 4.12 following the previously outlined procedure [44]. Due to the high sampling rate used, a solid line is used to represent the experimental discrete data for clarity. The dashed line denotes the ideal solution given in Eq. (4.19), and the dash-dot line represents the Gaussian low-pass filtered

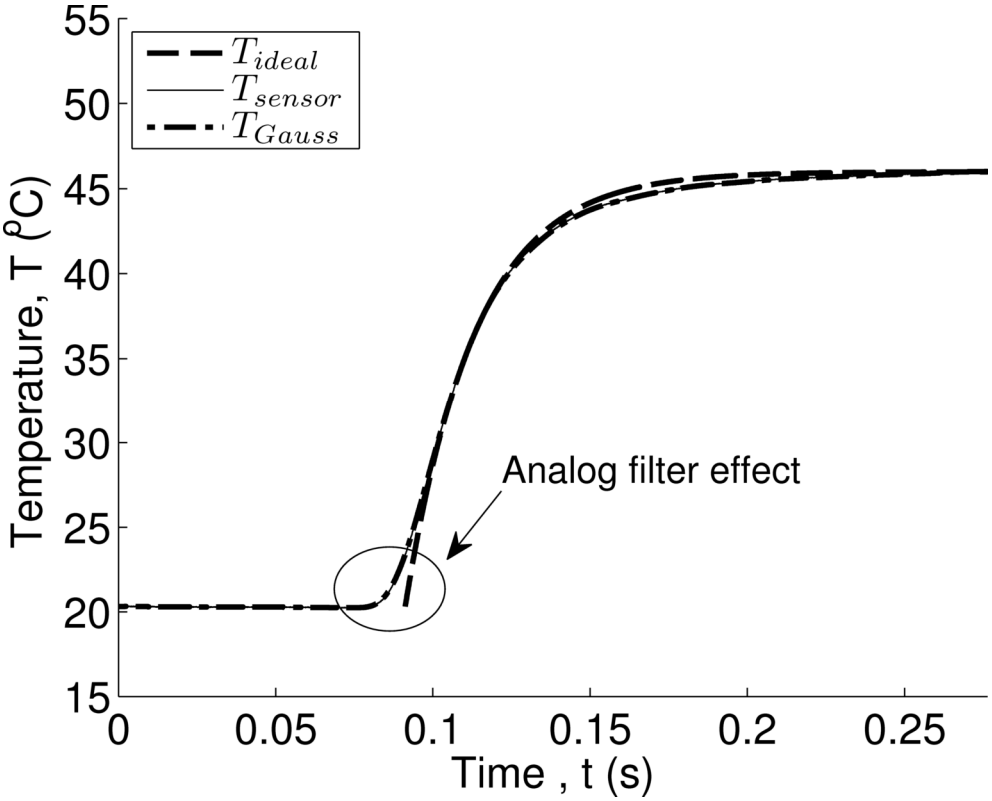

Figure 4.12: Experimentally acquired thermocouple data, Gaussian filter, and analytic model results.

temperatures using a cutoff frequency of 100 Hz. This high cutoff frequency was used since the data was already pre-filtered, and hence relatively clean.

Figure 4.12 displays a favorable comparison between the ideal model, the acquired experimental data, and the Gaussian filter output. Again, we point out that the ideal model is nonphysical. Additionally, the use of the analog pre-filter caused smoothing of the sensor data when the thermocouple was plunged into the hot water bath. This smoothing was not observed in the INA output, and is therefore due to the analog filter. The experimental data is seen to conform reasonably well to the ideal model during the transient portion and again moves toward the ideal model as time increases. The Gaussian filter output is seen to be graphically identical to the raw temperature data.

Figures 4.13 and 4.14 present higher-time derivative of temperature results. The initial physics of the plunge (reality) cannot conform to the ideal model which is well known. However, the experimental results do conform to physical expectations, appear highly favorable, and move toward the analytic model shortly after the instant of the thermocouple plunge. Additionally, the Gaussian derivatives obtained via post-processing are seen to be graphically identical with the sensor outputs. This demonstrates that the sensor does indeed function as an accurate time derivative of temperature sensor.

An alternative way to assess the accuracy of the sensor results involves using the concept of analytic continuation as expressed by the Taylor series given in Eq. (4.2) – i.e., overlay the analytically continued approximation over the acquired temperature data. Figure 4.15 presents the results using Eq. (4.3) in conjunction with the data presented in Figures 4.12-4.14 for estimating the future temperature. The expansion presented in Eq. (4.2) contains the arbitrary

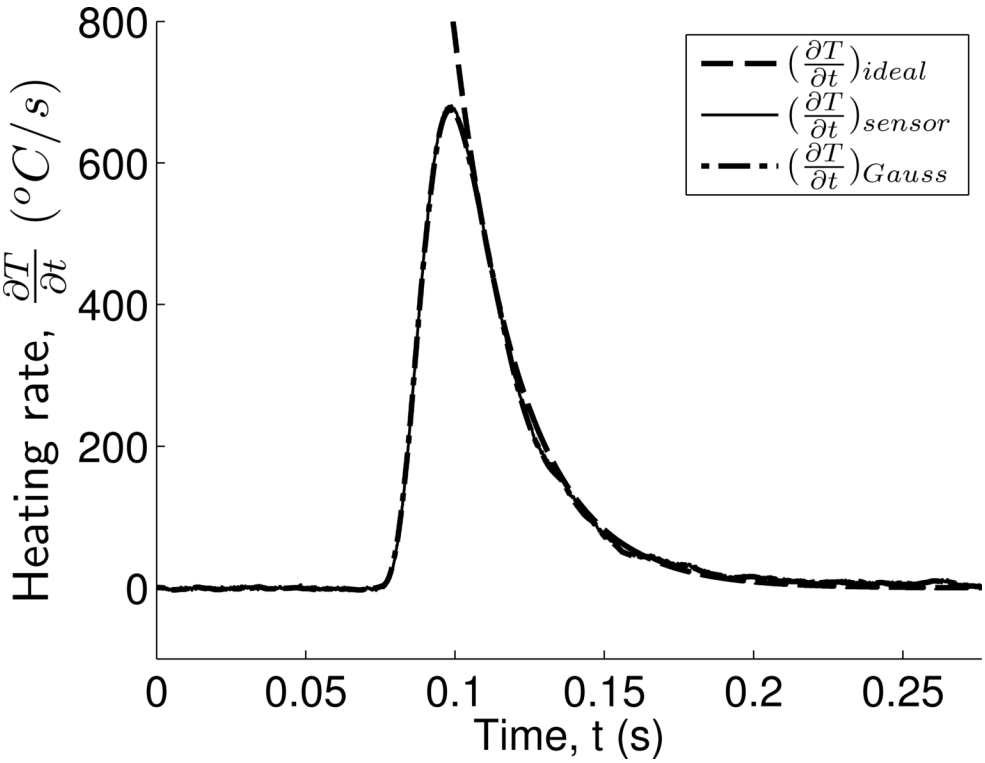

Figure 4.13: Analytic model results, Gaussian filter and sensor output results for first-time derivative of temperature.

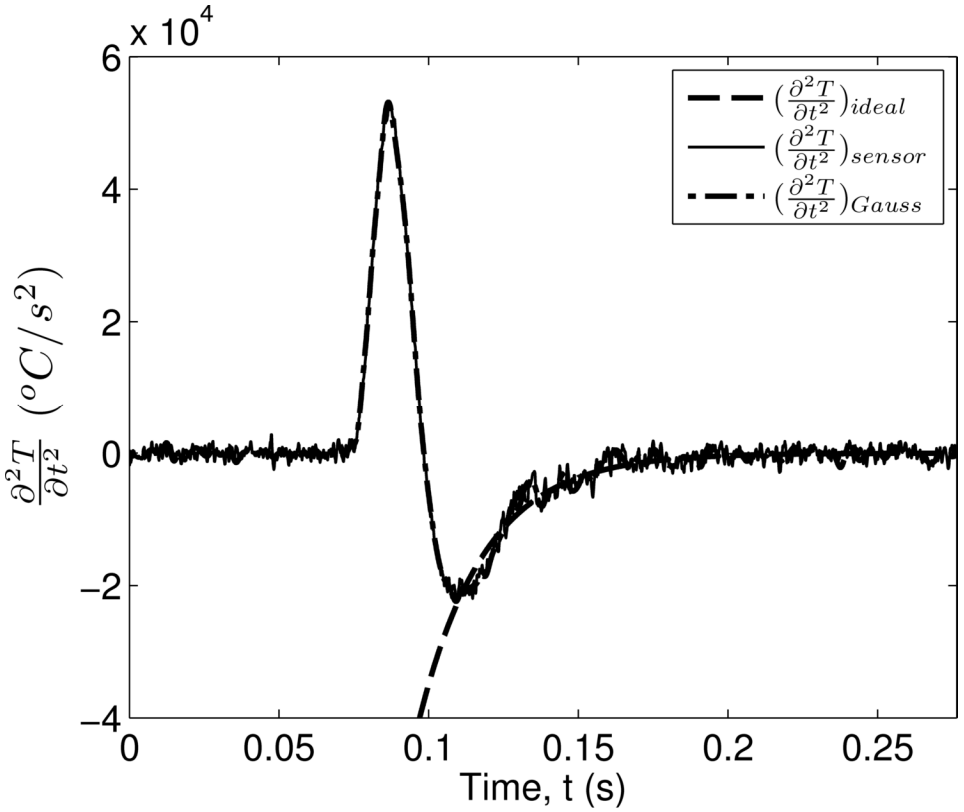

Figure 4.14: Analytic model results, Gaussian filter and sensor output for second-time derivative of temperature.

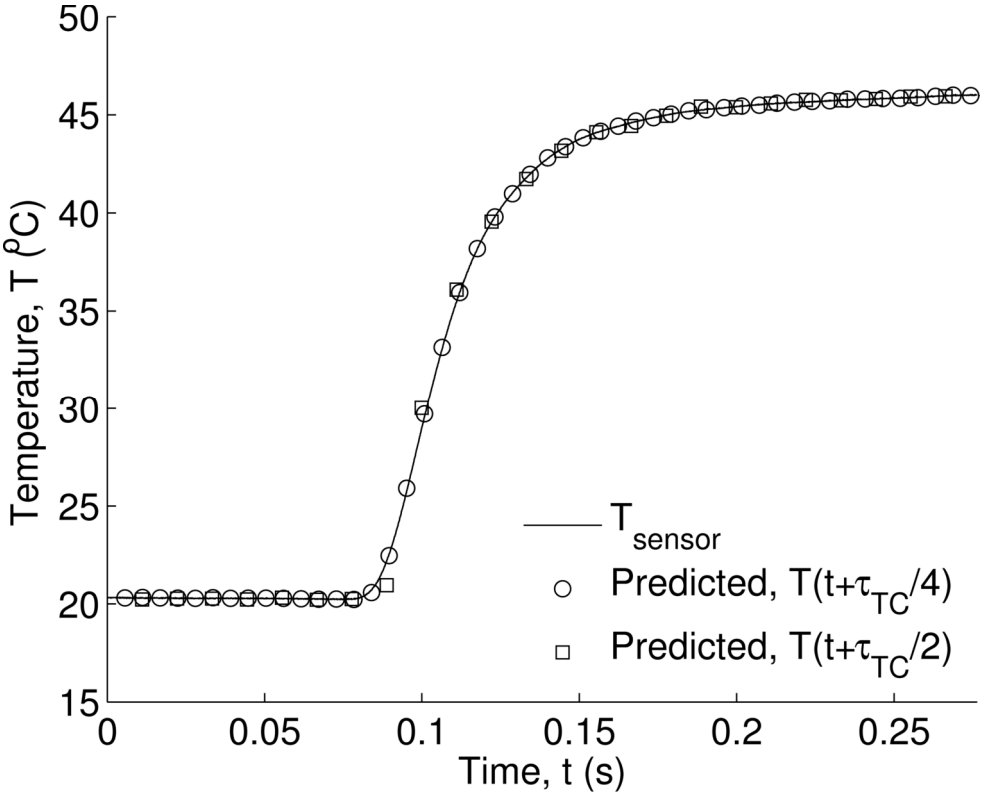

Figure 4.15: Analytic continuation, as defined with the aid of Eq. (4.2), indicates that future temperatures can be estimated based on using rate-based sensors.

constant given by . Let us now assign this parameter as a fraction of the thermocouple time constant. It is apparent that the future temperatures are accurately predicted based on $\gamma = \tau_{TC}/4$. At first glance, predicting $\gamma = \tau_{tc}/4$ into the future seems like a short time. However, consider that the rise time, τ_{rise}, of a first order system - time to reach 90% of step change – is only 2.3 τ_{tc}. In other words, the sensor is able to predict 11% of the total rise time into the future (see Table 4.6).

4.6 Chapter Summary

The time derivatives of temperature are developed from a voltage-rate interface used in conjunction with the thermocouple calibration curve. For the heating rate, d*T*/d*t*, this sensor construction represents a balance between theory and practice. This sensor concept is not a true heating rate sensor; however, it does take into account the physics of diffusion in its design and permits generalization to higher time derivatives of temperature. The time-domain viewpoint mathematically described in this chapter has led to the development of rate-based sensors for use in the global time inverse heat conduction method; estimating local heat flux; detection of sudden jumps in surface heat flux from embedded sites; and, accurately predicting the future temperature based on analytic continuation.

Table 4.6: Descriptive times for the thermocouple drop tower run.

Time	Value
τ_{tc}	0.0222 s
τ_{rise}	0.0512 s
$\tau_{tc}/2$	0.0111 s
$\tau_{tc}/4$	0.0056 s

Chapter 5: Sandwich Experiment

The inverse heat conduction techniques described in the Chapters 2 and 3 use temperature and heat flux data at an embedded sensor site to predict the surface thermal condition. Both the space-marching and global time techniques were proven accurate and stable using simulated data from exact solutions with random noise added. However, these techniques need to be validated with experimental data. The aim of this chapter is to present a physical experiment capable of generating the in-situ temperature and heat flux data required by these inverse techniques.

5.1 Experimental Setup

Figure 5.1 shows a diagram of an electrical heating experiment with embedded and surface mounted sensors. Two identical bronze plates were coated with a thin layer of Omegatherm 201 thermal paste on the heated face. Since the purpose of the thermal paste was to reduce contact resistance, the thinnest layer possible (nearly transparent) was used. A two mil thick layer of muscovite mica was adhered to the thermal paste. The bronze/paste/mica layers were then used to sandwich a 0.125 mm thick custom nichrome heater element. This created a line of symmetry across the centerline of the heater. Figure 5.2 shows a sketch of the custom heater designed by Dr. Majid Keyhani. The sides of the sandwich were then thermally insulated. Thermophysical and electrical properties of these materials can be seen in Table 5.1, while material thicknesses are summarized in Table 5.2.

Fine gage (30 AWG wire) surface mount thermocouples (Omega SA1XL-T) were affixed to the back (unheated) surface of each bronze plate. Probes were also embedded at roughly two

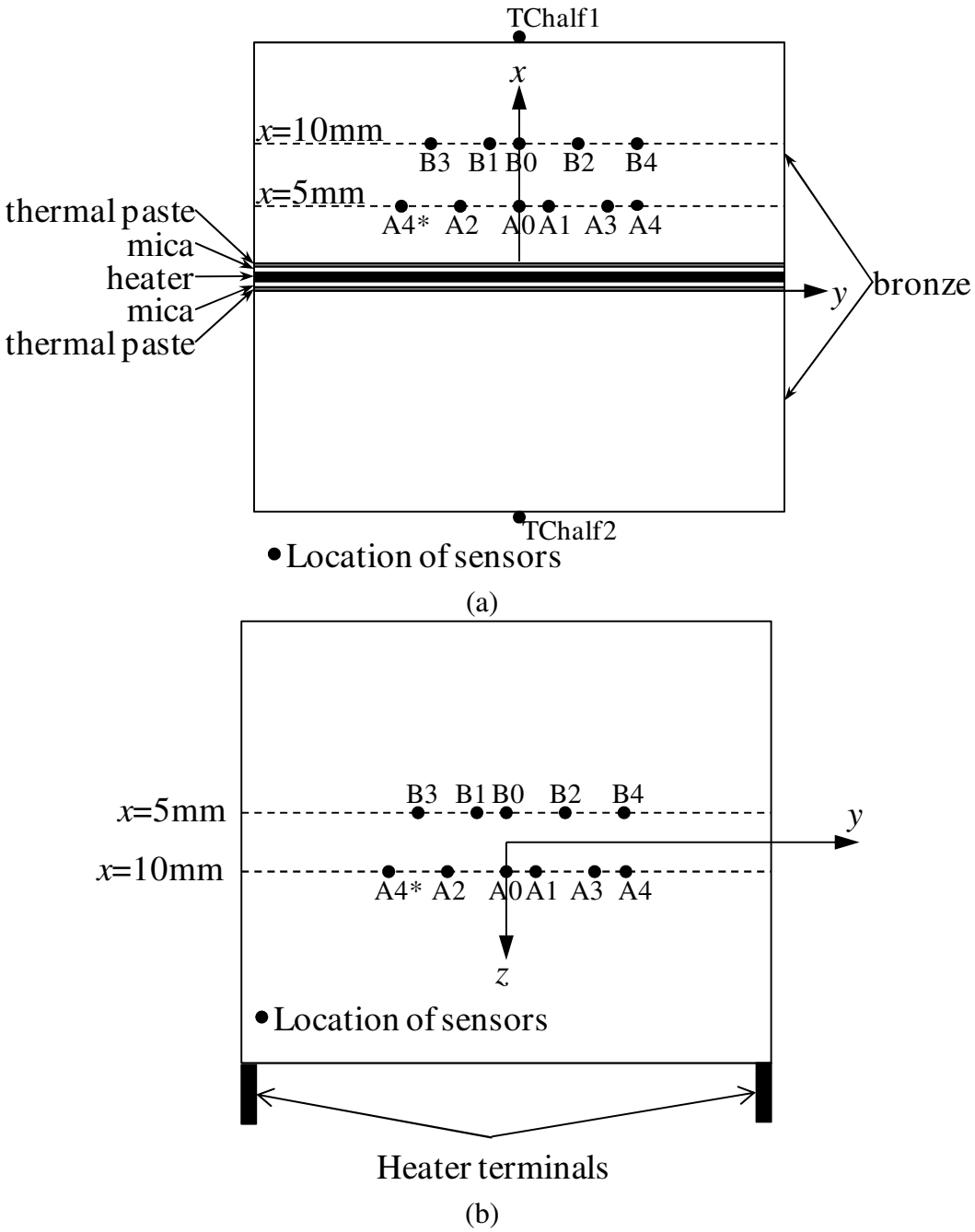

Figure 5.1: Sandwich electrical heating experimental setup shown with (a) side view and (b) planview. Line of symmetry exists along the centerline of the heater.

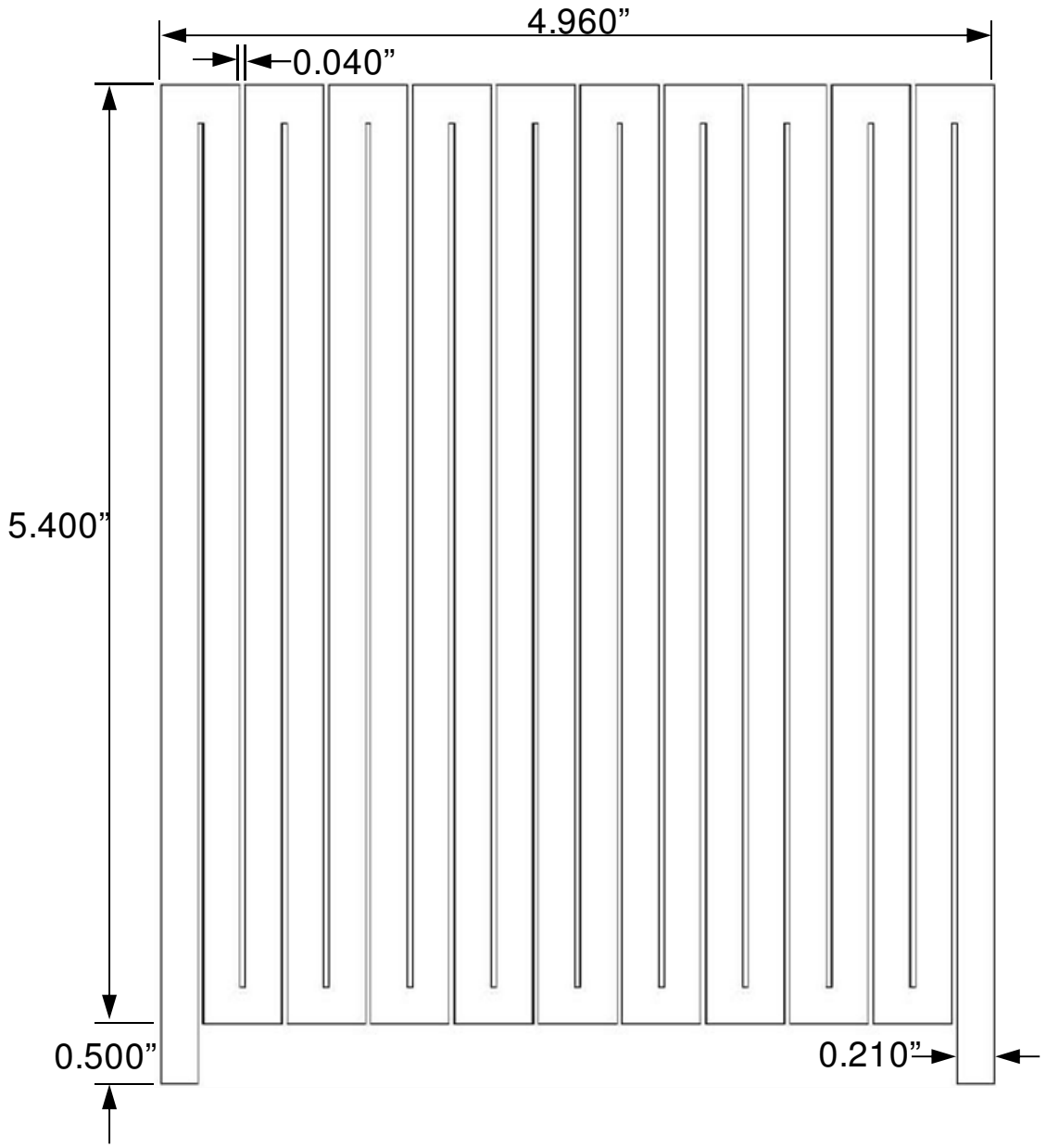

Figure 5.2: Dimensioned sketch (not to scale) of custom heater. The heater was machined from a 0.125mm thick nichrome foil.

Table 5.1: Thermophysical and electrical properties of materials used.

Property	Value
Bronze	
Thermal diffusivity, α	1.88×10^{-5} m^2/s
Density, ρ	7450 kg/m^3
Specific heat, C	419 J/(kg K)
Mica	
Thermal diffusivity	4.73×10^{-3} m^2/s
Density	300 kg/m^3
Specific heat	0.5 J/(kg K)
Thermal paste (Omegatherm 201)	
Thermal conductivity	2.3 W/(m K)
Heater (nichrome)	
Thermal diffusivity	7.75×10^{-5} m^2/2
Density	1420 kg/m^3
Specific heat	1.09 J/(kg K)
Heater resistance	4.326 Ω
Potting compound (Cotronics 989F)	
Thermal conductivity	1.7 W/(m K)

Table 5.2: Measured distances for the sandwich experiment.

Parameter	Value
L_{Bronze}	40.3 mm
L_{Mica}	0.051 mm
L_{Paste}	$\lesssim$ 0.03 mm
L_{Heater}	0.125 mm

different depths. All "A" thermocouples were installed at a distance of 5mm from the heated surface, while "B" thermocouples were installed at a distance of 10mm from the heated surface. Hole A4* was originally designed to be drilled to a 5mm depth; however, this was over-drilled to approximately 4.5mm depth. Therefore, this hole was filled in, and the corresponding A4 hole was drilled and used instead. The holes were first drilled with a 0.070 in. diameter to within 10mm of the final probe depth. The final 10mm of each hole was drilled out at a 0.040 in. diameter. These holes were drilled from the back surface (perpendicular to the heated surface). The distances from the bottom of each hole to the heated surface are tabulated in Table 5.3. The deepest point within each hole was measured using a pointed probe in combination with the MicroVal coordinate measuring machine; these values are reported as d_{tip} in Table 5.3. As seen in Figure 5.1, the locations of the holes were staggered to reduce disturbance of the sample near each hole. A summary of the instruments used can be seen in Table 5.4.

A type T thermocouple probe (Omega TMTSS transition junction style, 38 AWG thermocouple wire, with exposed bead with a diameter of 0.142 mm) with a sheath diameter of 0.020 in. was potted into each hole seen in Figure 5.1 using Cotronics 989F (alumina paste), diluted with 10% (volume) distilled water. One hole at a time was filled with the paste, and the thermocouples were inserted into the hole until the sheath began to slightly bend. This indicated that the bead was in contact with the bottom of the hole. It was attempted to x-ray the bronze sample to determine the exact location of the thermocouple beads. However, this was not possible since the bronze was nearly opaque to this wavelength. Since the holes were drilled with a pitched drill bit, the bottom of the hole is sloped. The height of this slope was estimated to be 0.30mm. Therefore, the uncertainty in the actual position of the thermocouple beads was

Table 5.3: Probe distance and resistance measurements.

Probe	d_{tip} [mm]	d [mm]	y [mm]	z [mm]	$R_{Cu\text{-}Brz}$
A0	5.04	5.19	0.0	6.4	1.9 Ω
A1	4.94	5.09	6.4	6.4	2.1 Ω
A2	5.04	5.19	-12.7	6.4	0.8 Ω
A3	4.89	---[1]	+19.1	6.4	45 MΩ
A4	5.01	5.16	+25.4	6.4	> 50 MΩ
B0	9.99	10.14	0.0	-6.4	12.8 MΩ
B1	9.97	10.12	-6.4	-6.4	4.0 MΩ
B2	10.00	10.15	12.7	-6.4	430 kΩ
B3	10.02	10.17	-19.1	-6.4	4.3 Ω
B4	9.73	---[2]	25.4	-6.4	---[2]

[1]Probe A3 was improperly installed, and was not seated in the bottom of hole A3.
[2]No probe was installed in hole B4.

Table 5.4: List of equipment and material used in sandwich experiment.

Instrument/Material	Description	Purpose
Data Translations DT9824	Fully-isolated, simultaneous, 24 bit, 4 differential channel DAQ	TC probe and surface-mount histories
Data Translations DT9806	Multiplexed, 16 bit, 8 differential channel DAQ	Power and ice TC histories; control of solid state relay
Kaye Instruments K140-4 Ice Point	Constant 0°C reference	Compensation for installed and surface-mounted TCs
Dell Latitude E5400 laptop	PC with MATLAB	Data collection and control
Potter and Brumfield SSR-240D80	80A, AC solid state relay	Heater activation
Brown and Sharpe MicroVal	Coordinate measuring machine ± 0.004 mm	Measurement of hole depths
Data Precision 3500	Multimeter, ± 0.005 Ω	Measurement of all resistances
Omegatherm 201	Thermally conductive paste	Reduction of contact resistance between mica and bronze
Cotronics Resbond 989F	Alumina paste with particle size of 600 nm	Thermocouple potting compound
Bronze	Atlas Bronze alloy C95400	Sandwich sample
Mica	Axim Mica muscovite V3 grade	Sandwich experiment electrical insulator
Nichrome	Goodfellow (Ni80/Cr20) 0.125mm thick foil	Heater material
Omega TMTSS-020E-6	Type T thermocouple probe, 0.020 in. stainless steel sheath, exposed bead, 38AWG wire	Installed probes
Omega SA1XL-T	Type T surface mount thermocouple, 30AWG	Surface mount thermocouple for back face temperature/symmetry

estimated to be ± 0.15mm, and the nominal depth, d, used for analysis was d_{tip} + 0.15mm. These values for each hole are tabulated in Table 5.3.

Retrospectively, a method of confirming contact between the thermocouple bead and the bronze was discovered. The electrical resistance between the thermocouple's copper lead wire and the bronze slab was measured. Since the potting compound was an electrical insulator, a small value (<10Ω) indicated good contact. These resistance values can be seen in Table 5.3 as $R_{Cu\text{-}Brz}$. Probes A0, A1, A2, and B3 were seen to have excellent contact with bronze. However, it is not possible from this data to describe the quality of contact between the thermocouple bead and the surrounding potting material. This contact is also important as it contributes to the response time of the probe. Therefore, techniques used to quantify the response time of each probe will be discussed in Chapter 6. Nevertheless, this technique offers promise for instrumentation of future samples.

5.2 Electrical Wiring

Figure 5.3 shows a sketch of the electrical wiring used in the sandwich experiment. The Data Acquisition Toolbox in MATLAB was used to control the experiment. All devices were software triggered to begin sampling/outputting at the same instant. Unregulated alternating current (60 Hz) was supplied from a $120V_{RMS}$, 50A line. This supply was wired to a Variac which was capable of boosting the voltage to $137V_{RMS}$. The output of the Variac was wired to an 80A solid state relay, which was controlled by a 0/+5V DC signal on an analog output channel on a DT9806 DAQ. The output of the relay was wired to copper bus bars which were in turn connected to the nichrome heater. The voltage across the heater was also connected to a

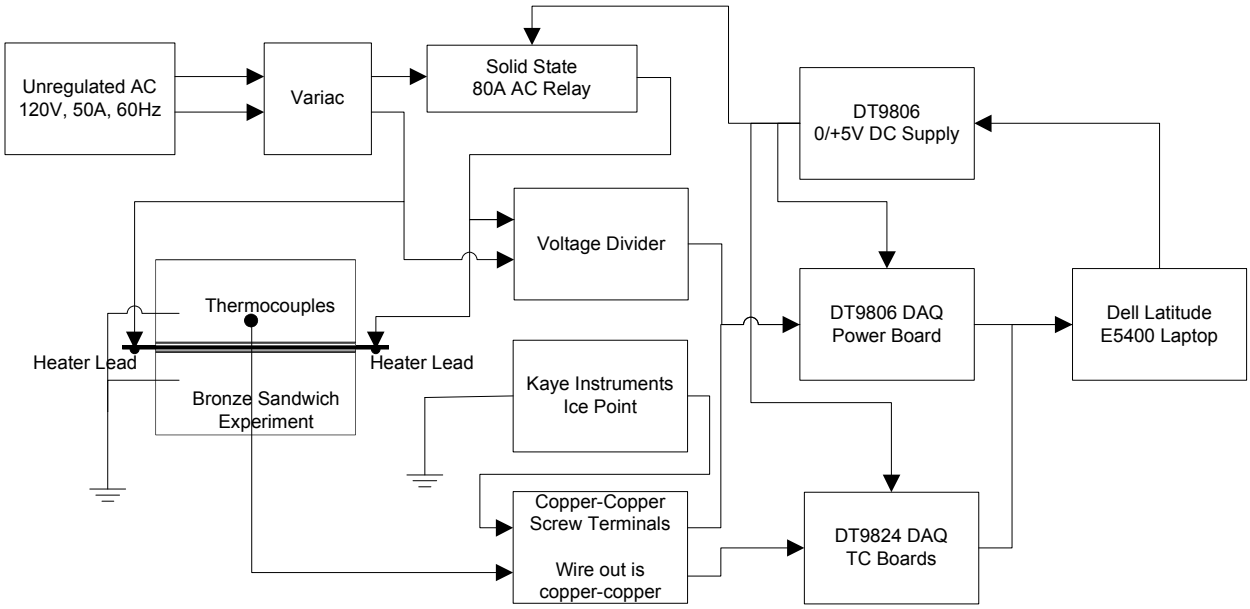

Figure 5.3: Electrical wiring diagram of sandwich experiment.

voltage divider which was sampled at 7500 Hz via a separate DT9806 data acquisition board, labeled as the power board.

The thermocouples' emf outputs were sampled at 200 Hz with a gain of 32 via two DT9824 data acquisition boards (DAQs). The DT9824 is a 24 bit, low noise, fully isolated DAQ with simultaneous measurements. Two DT9824 DAQs were used, each with four differential channels. This provided a total of eight thermocouple channels available.

A Kaye Instruments Ice Point machine was used to maintain a reference thermocouple at 0 °C. Since the ice voltage was constant, it was not sampled by one of the expensive DT9824 DAQs so as to leave these channels available for the embedded and surface mounted thermocouples. Instead, the ice thermocouple was sampled on the DT9806 power board. To eliminate noise in the ice signal, the average emf of the ice TC over the entire sampling time was used for compensation.

Since three different DAQs were used to collect data, it was necessary to synchronize the boards. As seen in Figure 5.3, the 0/+5V DC supply output used to control the AC relay was also wired to each of the DAQs. This was sampled on the DT9806 power board on an extra analog input channel. On the DT9824 DAQs, this was wired to the digital input channel which was sampled on the same clock as the analog input channels. After each experimental run, data were shifted in time to synchronize with the activation of the heater.

The connectors on the DT9824 DAQs used to sample the thermocouples' emf outputs are not isothermal which can cause large drift and oscillation in the reported thermocouple temperatures if thermocouple wire is taken directly to the DAQs. Therefore, all thermocouples (embedded, surface mounted, and ice) were compensated individually at separate copper-copper

screw terminals. The terminals were mounted onto an aluminum plate and placed in an insulated enclosure. This ensured all thermocouples were compensated at the same temperature and allowed copper-copper wire to be taken to the DAQs rather than thermocouple (copper-constantan) wire. The ice emf measurement was subtracted from the emf outputs of the embedded and surface mounted thermocouples in the post-processing. Since all TCs were also compensated at room temperature, this algebraically subtracted the room temperature emf from the final compensated TC voltage. The resulting compensated voltages were converted to temperature via the NIST polynomial calibration curve for type T thermocouples [64].

Since AC power was used to activate the heater, great care was taken to isolate the thermocouples from "power-on" noise. If this was not done, 60Hz noise would have leaked into the thermocouples when the heater was activated; the low voltage (~ 0.8 mV at room temperature) thermocouple signal-to-noise ratio would quickly deteriorate in this environment. For this experiment, thermocouple isolation was accomplished by first using an electrical insulator (mica) between the heater and the sample. A high quality, fully-isolated DAQ (DT9824) was used to sample the embedded and surface-mounted thermocouples – i.e., one analog-to-digital card per channel, one independent ground for each channel, and full isolation between channels and chassis ground. Wiring the bronze slabs to wall ground was also necessary to prevent power-on noise in the installed TCs. The laptop used to collect the data was also operated on battery power to prevent ground loops from forming. Using this arrangement, power-on noise was completely eliminated in most TC channels, and effectively minimized in the remaining channels.

5.3 Sandwich Experimental Procedure

The procedure for running a sandwich experiment was as follows. With the exception of the Kaye Instruments Ice Point which was never turned off, all instruments were turned on and allowed to warm-up for at least one hour prior to collecting data. The heater resistance was measured before each experimental run to verify none of the heater legs were in contact with each other which could cause electrical arcing. Before connecting the heater terminals to the relay, the electrical resistance was measured between the heater and the bronze sample using the Fluke multimeter. A reading of "overload" verified the integrity of the mica electrical insulation; the heater was then connected as in Figure 5.3, and all electrical connections were verified. The thermal insulation was checked to ensure a snug fit around the sample.

A final check was made by running the MATLAB driver program with the Variac unplugged from the 120V source. This ensured all software settings were correct, all instruments performed properly, data was saved, and allowed a final check of the thermocouple noise levels and temperatures. If uniformity of the sample temperature was verified by this preliminary run (± 0.1°C), the Variac was connected to the 120V source, and the run was initialized in MATLAB by running the driver program.

Table 5.5 shows the experimental runs conducted. For all experimental runs, 15 seconds of lead data were collected. At t = 15s, the heater was activated for a set amount of time (10 seconds or less). Heating and subsequent cooling data was then collected up to t = 60s. Most runs were conducted by applying a constant voltage across the heater during the heating time. For these runs, either a low (approximately 85V) or a high (approximately 135V) voltage was used. However, for one run, the voltage was (nearly) linearly increased to the maximum

Table 5.5: Experimental details of the 9 sandwich experiment runs performed.

Run #	Run Name	Date of Run	V_{max} [V_{RMS}]	Δt_{heat} [s]	V Profile	f_s [Hz]	V_{div}
1	qCLOt3f200	04/15/2011	85	3	Constant	200	19.76
2	qCLOt3f1200	04/15/2011	85	3	Constant	1200	19.76
3	qCHIt3f200	04/16/2011	135	3	Constant	200	28.67
4	qCHIt10f200	04/18/2011	135	10	Constant	200	28.67
5	qCHIt10f1200	04/19/2011	135	10	Constant	1200	28.67
6	qCHIt10f60	04/19/2011	135	10	Constant	60	28.67
7	qRHIt5f200	04/24/2011	135	5	Ramp	200	28.67

voltage, held constant for approximately two seconds, and then linearly decreased to the off position.

For ease of discussion, a naming convention for each experimental run was adopted where the name of a run is given by "qWXtYfZ." In this nomenclature, "W" can be C for a constant voltage applied or R for a ramped voltage; "X" is HI for maximum voltage applied to the heater or LO for the lower voltage level; "Y" is the duration of the heating cycle; "Z" is the sampling rate used in Hz. Using this naming convention, run qCHIt3f200 would indicate a constant voltage of 135V was applied for 3s, and temperature data was sampled at a rate of 200Hz. A run named qRHIt5f200 indicates that a ramped voltage was used with a peak voltage of 135V. The total heating duration was 5 seconds, and thermocouple data was sampled at 200Hz.

5.4 Direct Model

A three layer (half-heater, mica and bronze), one-dimensional implicit-in-time finite difference (FD) code was used to model the forward problem. A diagram of the discretization used in the FD model can be seen in Figure 5.4. The heater power was modeled as volumetric heat generation, where the amount of power dissipated by the heater was given by the Joule heating equation such that

$$u_{gen}(t) = \frac{V_{RMS}^2(t)}{VolR_{heater}}, \tag{5.1}$$

where Vol is the volume of the heater, R_{heater} is the resistance of the heater, and V_{RMS} is the voltage applied to the heater. It is emphasized here that the direct FD model is one-dimensional. Therefore, using the actual heater volume in Eq. (5.1) (i.e., accounting for the individual element

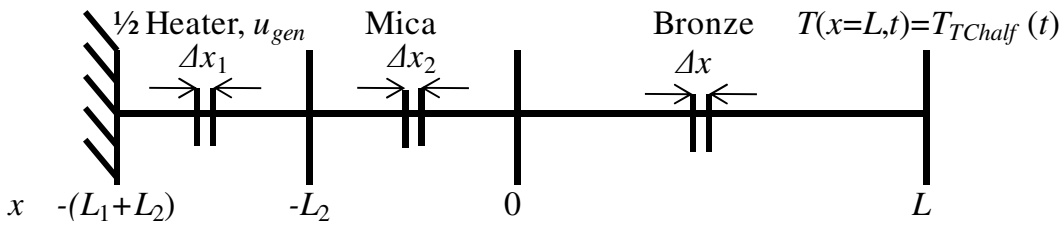

Figure 5.4: Discretization sketch for three layer finite difference model of sandwich experiment.

width, element gap, etc.) is inappropriate. Instead, the volume of the heater used in the FD model, *Vol*, was calculated as the surface area of the bronze multiplied with the thickness of the heater. The measured transient voltage was supplied to the FD model. The effect of the thermal paste was neglected, and perfect contact was assumed between each layer. The direct FD model calculated incident heat flux to the bronze layer; this was used as the surface heat flux input for comparison with the inverse prediction. A mesh convergence study was conducted for this model. For convergence, the half-heater layer required 1000 nodes, the mica layer required 100 nodes, and the bronze layer required 2000 nodes. A time step of 0.008s or smaller was found to accurately resolve the time domain.

Chapter 6: Characterization of In-Depth Probes

It is well-known that the temperature reported by an installed thermocouple is different from the positional temperature of an undisturbed sample [38, 39]. In steady-state measurements, this problem stems from material property differences between the sample and the thermocouple bead and axial conduction along the wires if the wires are not parallel to isotherm. In transient measurements, the problem is further exacerbated by the response time of the thermocouple. The space-marching and global time inverse algorithms presented in Chapters 2 and 3, respectively, assume that the undisturbed sample temperature history is provided as input data. If uncorrected thermocouple data are used as input to these algorithms, the surface thermal condition will be under predicted and delayed.

For illustration, consider sandwich experiment data from run qRHIt5f200. Figure 6.1(a) shows the raw and filtered thermocouple temperature history for probe A0. The data were used to calculate the in-situ heat flux using semi-infinite medium heat flux-heating rate integral relationship as in Section 2.8. The global time inverse method was then employed to predict the surface temperature and heat flux which can be seen in Figure 6.2. Although the method has been proven accurate when noisy, positional temperature data are provided, the inverse prediction severely under-predicts the actual surface condition. We, therefore, seek a method by which the thermocouple data can be transformed into the actual positional temperature of the sample.

The orientation of the thermocouple leads must be considered when seeking a probe characterization technique. Figure 6.3 shows a sketch of two installed thermocouples with the

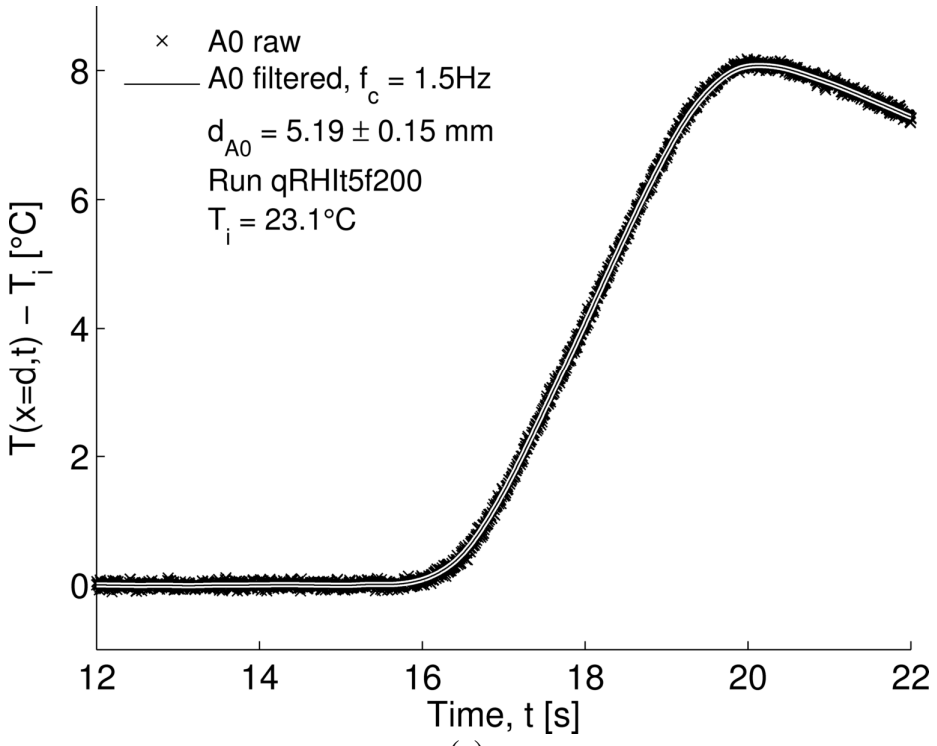

(a)

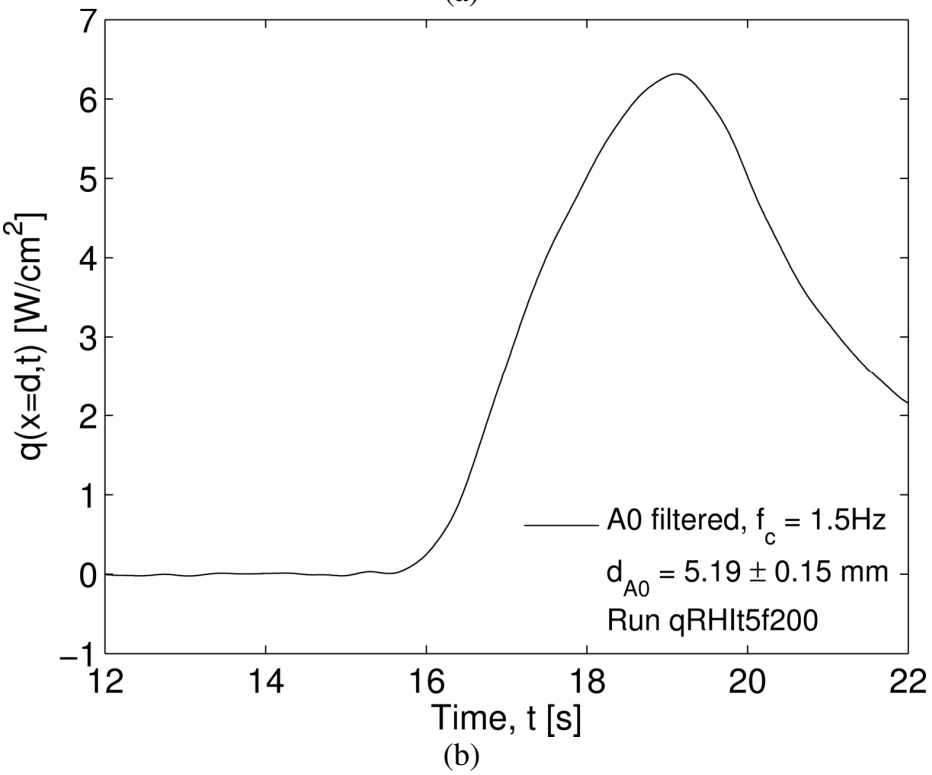

(b)

Figure 6.1: Temperature and heat flux data uncorrected for response time. (a) Raw and filtered temperature data and (b) resulting semi-infinite heat flux. Data for probe A0 from run qRHIt5f200.

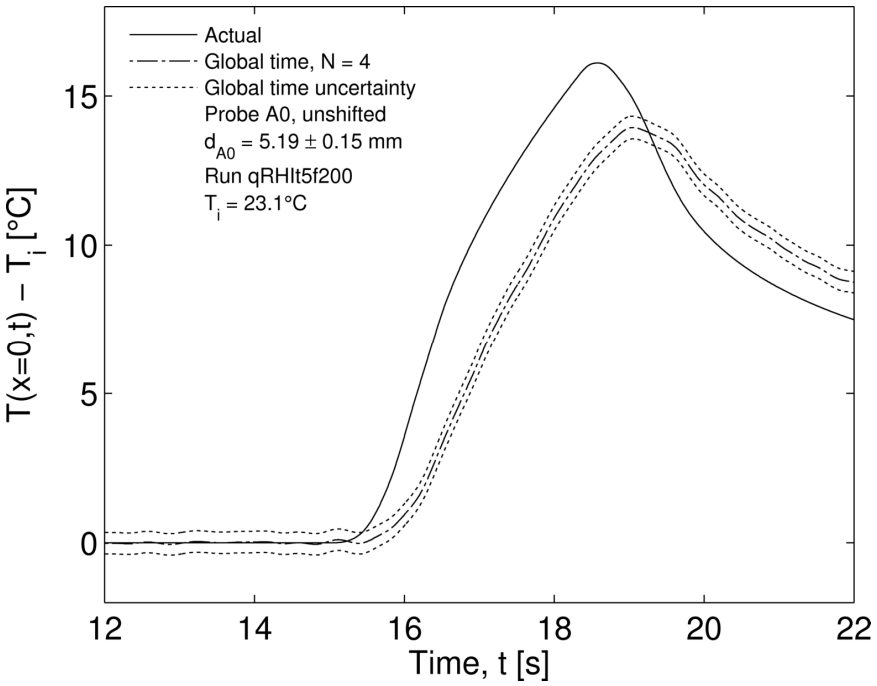

(a)

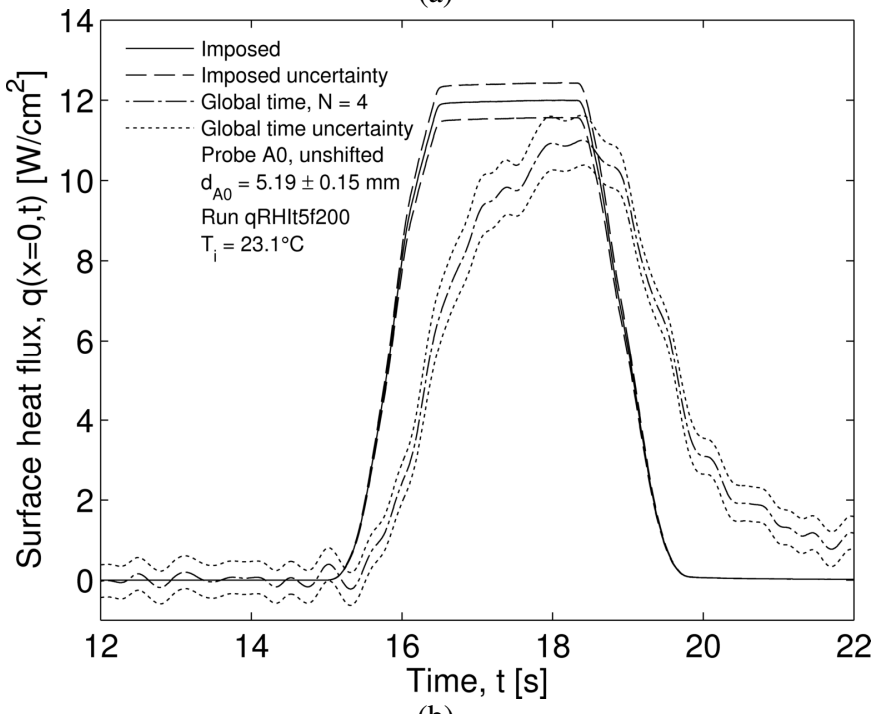

(b)

Figure 6.2: Inverse predicted surface temperature and heat flux using sandwich experiment data from run qRHIt5f200, uncorrected for response time. (a) Surface temperature with uncertainty band and (b) surface heat flux with uncertainty band. Data used can be seen in Figure 6.1.

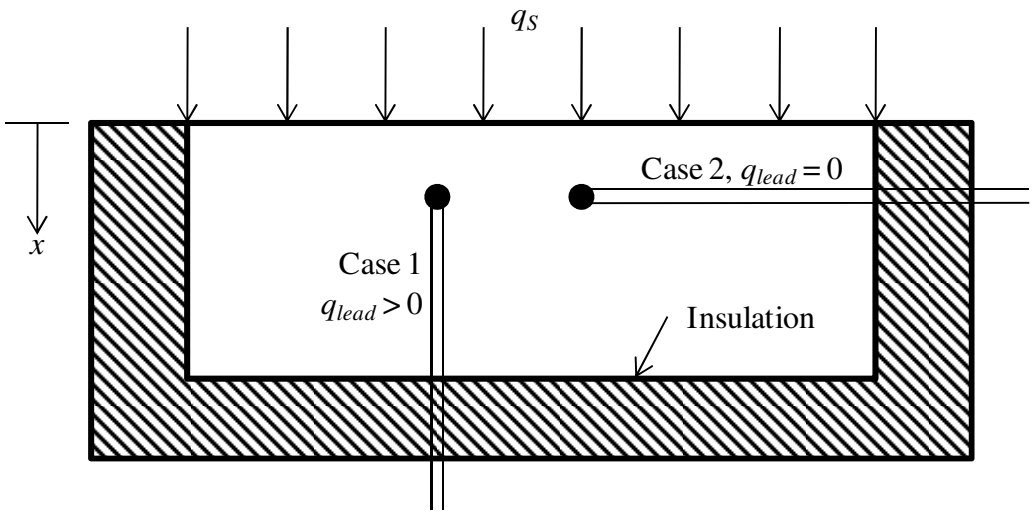

Figure 6.3: Effect of thermocouple wire orientation on lead losses.

lead wires oriented in two different arrangements. If the surface at x=0 is heated uniformly, the lead wires of Case 1 are oriented perpendicular to the isotherm. During this process, $q_{lead} > 0$ since the lead wires will pull heat away from the bead. In contrast, the lead wires of Case 2 are oriented parallel to the isotherm; therefore, $q_{lead} = 0$ during a uniform surface heating process. For the sandwich experiment presented in Chapter 5, all thermocouples were installed with a Case 1 arrangement. Therefore, a proper characterization technique should account for both the response time of the thermocouple and the lead losses.

6.1 Thermocouple model

Let us first look at the energy balance of the thermocouple bead given by

$$\dot{E}_{in} + \dot{E}_{gen} = \dot{E}_{out} + \dot{E}_{stor}. \tag{6.1}$$

It is assumed the environment is hot, and therefore heat transfer is incident from surroundings to the thermocouple bead. It is also assumed heat is lost from the bead to its leads. Eq. (6.1) then becomes

$$hA_{TC}\left(T_{\infty}(t) - T_{TC}(t)\right) = A_{lead,1}q_{lead,1}(t) + A_{lead,2}q_{lead,2}(t) + \left(\rho CV\right)_{TC}\dot{T}_{TC}(t), \tag{6.2}$$

where h is the effective heat transfer coefficient, A_{TC} is the surface area of the bead in contact with surroundings, T_{∞} is the temperature of the surroundings, $A_{lead,1}$ and $A_{lead,2}$ are the surface area of the bead which is in contact with each lead wire, $q_{lead,1}$ and $q_{lead,2}$ are the heat lost from the bead to the each lead wire, ρ_{TC} is the density of the bead, C_{TC} is the heat capacity of the bead, and V_{TC} is the volume of the bead. It is emphasized here that h is not the convective heat transfer coefficient, but is the *effective* heat transfer coefficient which encompasses contact resistance. After rearranging, Eq. (6.2) becomes

$$\frac{(\rho CV)_{TC}}{hA_{TC}}\dot{T}_{TC}(t)+T_{TC}(t)=T_{\infty}(t)-\frac{A_{lead,1}}{hA_{TC}}q_{lead,1}(t)-\frac{A_{lead,2}}{hA_{TC}}q_{lead,2}(t). \tag{6.3}$$

The constants τ_0 and λ are defined as

$$\tau_0=\frac{\rho CV_{TC}}{hA_{TC}}, \tag{6.4}$$

and substitute Eq. (6.4) into Eq. (6.3) yielding

$$\tau_0\dot{T}_{TC}(t)+T_{TC}(t)=T_{\infty}(t)-\frac{A_{lead,1}}{hA_{TC}}q_{lead,1}(t)-\frac{A_{lead,2}}{hA_{TC}}q_{lead,2}(t). \tag{6.5}$$

For small time, the lead heat loss from each lead can be described using the half-space integral relationship (see Section 2.8 for discussion) given by

$$q_{lead,i}(t)=\sqrt{\frac{(\rho Ck)_{lead,i}}{\pi}}\int_{u=0}^{t}\dot{T}_{TC}(u)\frac{du}{\sqrt{t-u}}, \qquad i=1,2 \tag{6.6}$$

where subscript *i* refers to lead wires one and two. The constant, λ, is now defined as

$$\lambda=\frac{1}{hA_{TC}}\left[A_{lead,1}\sqrt{\frac{(\rho Ck)_{lead,1}}{\pi}}+A_{lead,2}\sqrt{\frac{(\rho Ck)_{lead,2}}{\pi}}\right], \tag{6.7}$$

and substitute Eqs. (6.6-6.7) into Eq. (6.5) which yields

$$\tau_0\dot{T}_{TC}(t)+T_{TC}(t)=T_{\infty}(t)-\lambda\int_{u=0}^{t}\dot{T}_{TC}(u)\frac{du}{\sqrt{t-u}}. \tag{6.8}$$

It is noted that the sign of λ should always be positive since the directionality of heat transfer is determined by sign of $\dot{T}_{TC}$.

Insight into the behavior of the lead loss term can be gained by expanding $\dot{T}_{TC}(u)$ about *t* in Eq. (6.6) which leads to

$$\int_{u=0}^{t} \dot{T}_{TC}(u)\frac{du}{\sqrt{t-u}} = 2t^{1/2}\dot{T}_{TC}(t) + \frac{4}{3}t^{3/2}\ddot{T}_{TC}(t) + O(t^{5/2}). \tag{6.9}$$

Substituting only the low-order term from Eq. (6.9) into Eq. (6.8) yields

$$\left(\tau_0 + 2\lambda\sqrt{t}\right)\dot{T}_{TC}(t) + T_{TC}(t) \approx T_\infty(t). \tag{6.10}$$

Therefore, including the lead loss term in Eq. (6.8) effectively introduces a time-dependent time "constant" given by

$$\tau(t) = \tau_0 + 2\lambda\sqrt{t}. \tag{6.11}$$

Assuming T_∞ is constant, Eq. (6.10) has an exact solution via Laplace Transform [67] given by

$$\theta_{TC}(t) = \exp\left\{\frac{1}{2\lambda^2}\left[\tau_0 \ln\left(\tau_0 + 2\lambda\sqrt{t}\right) - \tau_0 \ln\left(\tau_0\right) - 2\lambda\sqrt{t}\right]\right\}, \qquad t \geq 0, \tag{6.12}$$

where

$$\theta_{TC}(t) = \frac{T_{TC}(t) - T_\infty}{T_{TC}(0) - T_\infty}. \tag{6.13}$$

Clearly, the definition of $\tau(t)$ reduces to the classical first order system if lead losses are neglected (i.e., set λ=0). This leads to the exact solution

$$\theta_{TC}(t) = \exp\left(-\frac{t}{\tau_0}\right), \quad t \geq 0. \tag{6.14}$$

The goal of this chapter is to accurately resolve the sensor characteristics of an installed thermocouple. The two methodologies by which this can be accomplished are now presented.

6.2 Loop-Current Step Response

Loop-current step response (LCSR) is a technique developed by [41, 42]. An electric current (AC or DC) is applied to the sensor leads for a specified heating time (Δt_{heat}), then the current is removed and the decay of the thermocouple emf is observed and recorded. Figure 6.4

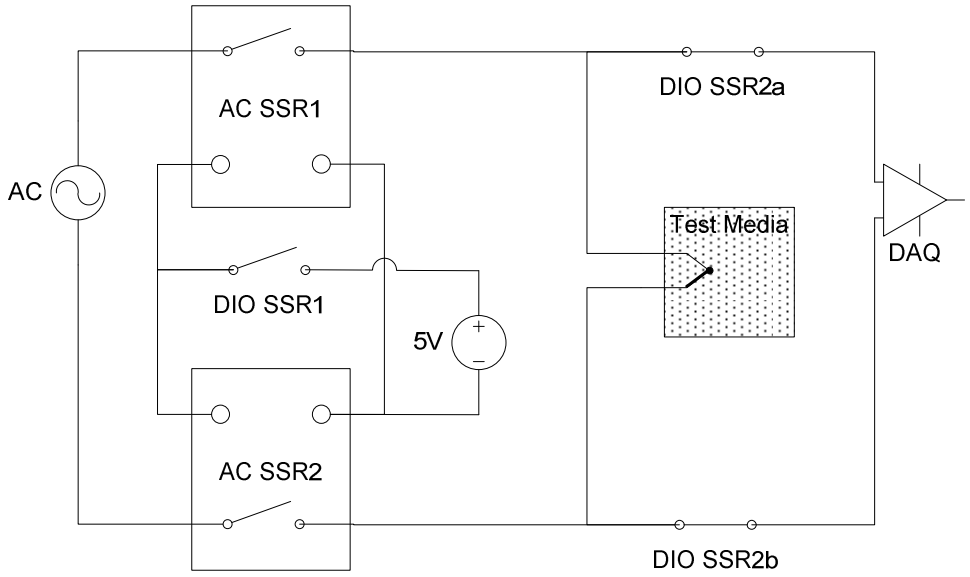

Figure 6.4: LCSR test circuit setup using AC current for heating. DIO SSR1 closes when DIO SSR2a and DIO SSR2b open to prevent damage to the data acquisition board.

shows an experimental setup for LCSR testing. During heating, the thermocouple leads are isolated from the data acquisition system via solid state relays to prevent damage. The experimental procedure used to collect data for the LCSR tests in the present work is as follows:

1) Lead data is collected to establish the initial condition.
    a. Relay configuration:
        i. DIO SSR1 is open; therefore AC SSR1 and 2 are open
        ii. DIO SSR2a and b are closed; therefore DAQ is collecting data
2) AC voltage is applied (V_{RMS}) to the thermocouple leads for a specified heating time (Δt_{heat}). V_{RMS} and Δt_{heat} are chosen to provide at least a ΔT of 10°C.
    a. Relay configuration:
        i. DIO SSR1 is closed; therefore AC SSR1 and 2 are closed
        ii. DIO SSR2a and b are open; therefore DAQ is not collecting data
3) Cooling data is collected.
    a. Relay configuration:
        i. DIO SSR1 is open; therefore AC SSR1 and 2 are open
        ii. DIO SSR2a and b are closed; therefore DAQ is collecting data
4) The total temperature change is recorded (ΔT).
5) Steps 1-4 are repeated with shorter Δt_{heat} until a decrease in ΔT is observed. The test data of the shortest heating period that results in the desired ΔT is analyzed.

For all data presented herein, thermocouple data were collected via DT9824 with f_s = 200 Hz. All DIO solid state relays employed were on the digital output channels of the DT9824.

When AC current is used as in Figure 6.4, both the lead wires and the thermocouple bead are heated. When the current is removed, the thermocouple bead cools by transferring heat to the surrounding medium initiating axial conduction heat transfer from the leads to the bead. LCSR cooling test data for probe A0 can be seen in Figure 6.5. For very small time, the rate of heat transfer is dominated by τ_0. After a significant gradient occurs between the bead and the leads, conduction from the leads into the bead significantly slows the bead cooling process. This is noted in Figure 6.5 as "middle time" which is dominated by λ. Eventually, a maximum effective time constant is reached. This is noted in Figure 6.5 as "large time" which is dominated by τ_{max}.

The thermal process created by LCSR testing is similar to the case of a thermocouple installed with leads perpendicular to the isotherm. In LCSR testing, the cooling of the bead is slowed by conduction along the leads. In the sandwich experiment, the heating of the bead is slowed by conduction along the leads. Therefore, LCSR testing is an appropriate way to characterize the response of the installed probes for use in the sandwich experiment.

Analysis of LCSR data

Consider the LCSR data presented in Figure 6.5. For all models used to fit this data, a nonlinear least squares procedure (NLS) can be used to determine the unknown parameters. This can been accomplished with Newton's method using

$$\beta_j^{k+1} = \beta_j^k + \alpha_r \Delta\beta_j^k, \tag{6.15}$$

$$\Delta y_i = \theta_{TC,i} - \theta(t_i, \beta^k), \tag{6.16}$$

$$J_{ij} = \frac{\partial \theta_{TC}}{\partial \beta_j}(t_i, \beta^k), \tag{6.17}$$

$$\left(J^T J\right)\Delta\beta = J^T \Delta y, \tag{6.18}$$

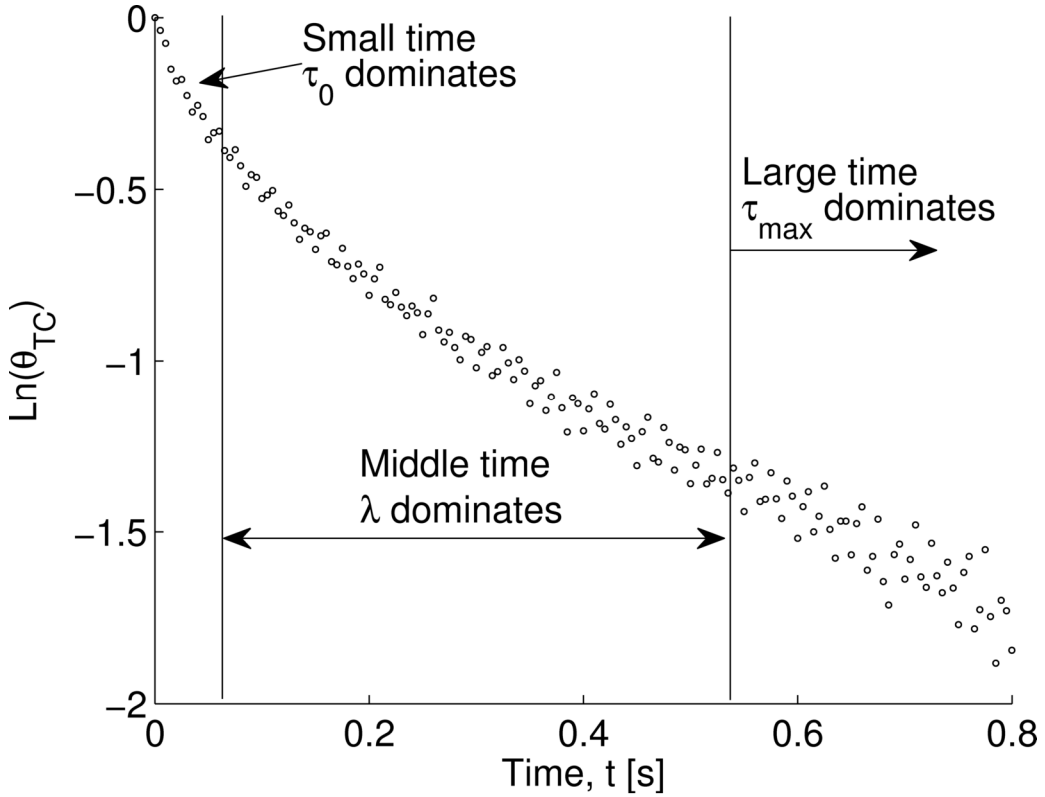

Figure 6.5: LCSR data for probe A0 for V_{RMS} = 16.3V, Δt_{heat} = 0.25s, ΔT = 12.7 °C, and f_s = 200 Hz.. Time regions where parameters have the strongest influence are shown.

where β^k contains the unknown parameters at the kth iteration, α_r is a relaxation factor, $\theta_{TC,i}$ is the ith data point, $\theta_{TC}(t_i,\beta^k)$ is the NLS fit to the data, and J is the Jacobian. The relaxation factor is necessary to prevent the estimation of τ_0 from diverging. A value of $\alpha_r = 0.001$ was found to stabilize the NLS procedure.

A NLS algorithm seeks to minimize the difference between each data point and the NLS fit at that time step. Equal weighting is given to each time point. Only the data that is most sensitive to the parameter being estimated should be passed to the NLS algorithm. Therefore, the sensitivity coefficients for each unknown parameter must be found. The procedure for using the NLS algorithm is as follows:

1. Make an initial guess for the unknown parameters.
2. Plot the resulting sensitivity coefficients.
3. Send only data near the peak value of the sensitivity coefficients to the NLS algorithm.
4. Repeat steps 2 and 3 until convergence is met.

This procedure is used for all models described below.

Model 1: First Order System

As a first step in the analysis procedure, it is assumed lead losses are negligible. This leads to a first order system with exact solution in Eq. (6.14). Therefore, the first order system sensitivity coefficient $Z_{\theta 1,\tau 0}$ is next defined as

$$Z_{\theta 1,\tau 0} = \tau_0 \frac{\partial \theta_{TC}}{\partial \tau_0} = \frac{t}{\tau_0} \exp\left(-\frac{t}{\tau_0} \right), \tag{6.19}$$

which peaks at $t = \tau_0$. Figure 6.6 shows the sensitivity coefficient and converged first order system model for LCSR data using probe A0. Only data near the peak sensitivity

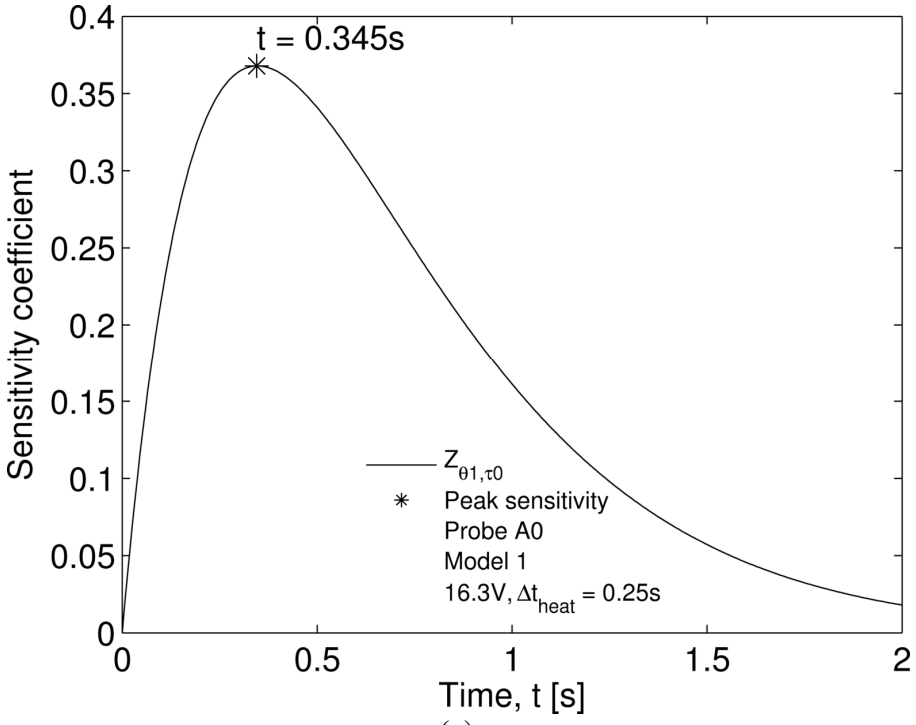

(a)

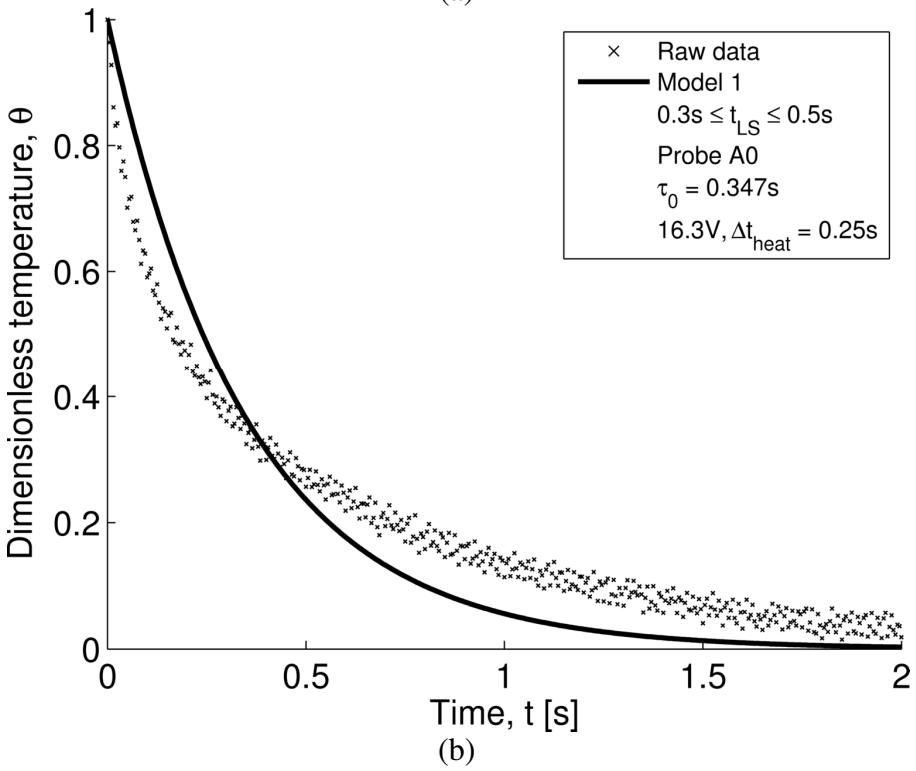

(b)

Figure 6.6: Model 1 results for LCSR testing of probe A0. (a) Sensitivity coefficient and (b) comparison of model with raw data. Testing parameters were V_{RMS} = 16.3V, Δt_{heat} = 0.25s, ΔT = 12.7 °C, and f_s = 200 Hz.

($0.3\text{s} \le t \le 0.5\text{s}$) were used to calculate τ_0. However, a large residual can be seen between the NLS fit and the data for both early and large time. Clearly, modeling the probe as a first order system is inappropriate, and the model should be refined.

Model 2: Semi-infinite lead loss

As the next step in the analysis, the leads loss term is approximated as in Eq. (6.9) which leads to the exact solution of Eq. (6.12). The modified sensitivity coefficients for τ_0 and λ are given by

$$Z_{\theta 2,\tau 0} = \tau_0 \frac{\partial \theta_{TC}}{\partial \tau_0} = \frac{\tau_0}{2\lambda^2}\theta_{TC}\left[\ln\left(\tau_0 + 2\lambda\sqrt{t}\right) + \frac{\tau_0}{\tau_0 + 2\lambda\sqrt{t}} - \ln\tau_0 - 1\right], \tag{6.20}$$

$$Z_{\theta 2,\lambda} = \lambda \frac{\partial \theta_{TC}}{\partial \tau_0} = \frac{1}{2\lambda^2}\theta_{TC}\left[2\lambda\sqrt{t} + \frac{2\lambda\tau_0\sqrt{t}}{\tau_0 + 2\lambda\sqrt{t}} + 2\tau_0\ln\tau_0 - 2\tau_0\ln\left(\tau_0 + 2\lambda\sqrt{t}\right)\right], \quad t \ge 0. \tag{6.21}$$

This approach can be seen in Figure 6.7 for probe A0. As compared to the first order system, significant improvement is seen in the agreement between the NLS fit and the data, especially for early time. This makes intuitive sense when viewing the sensitivity coefficients. The model is much more sensitive to the values of τ_0 and λ for early time than large time. A significant departure between the model and the data is seen for $t > 1\text{s}$. Therefore, a better model is needed for large time.

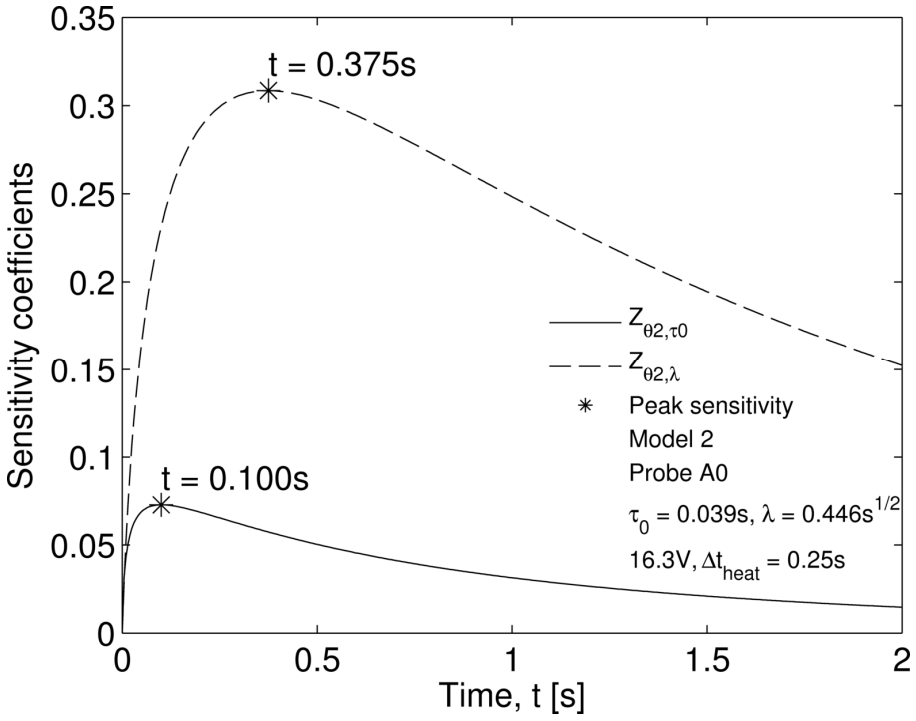

(a)

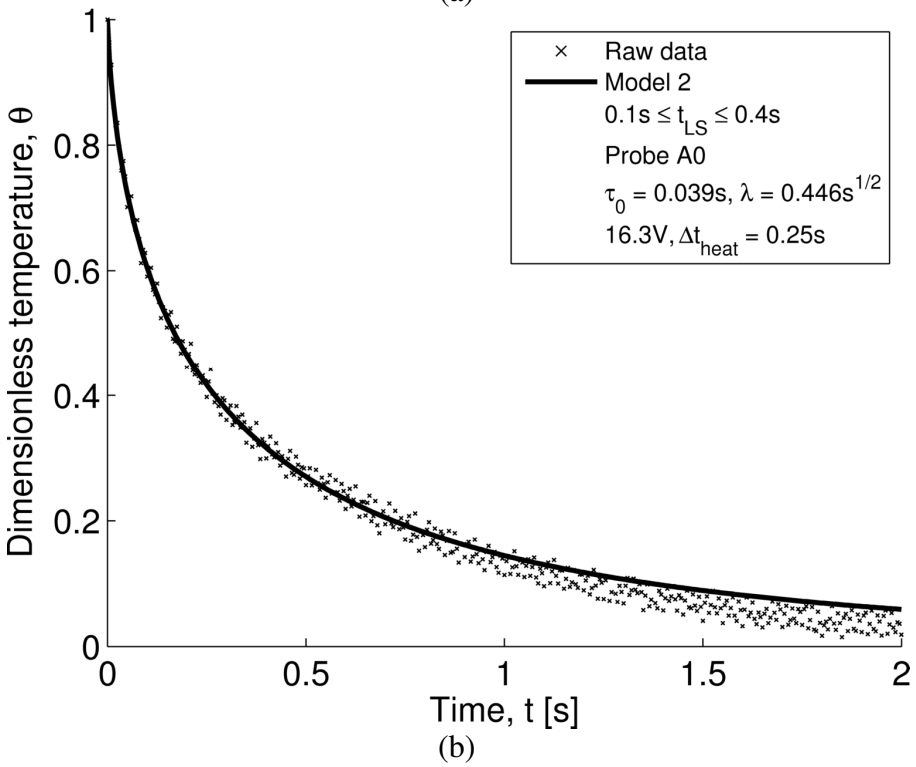

(b)

Figure 6.7: Model 2 results for LCSR testing of probe A0. (a) Sensitivity coefficients and (b) comparison of model with raw data. Testing parameters were V_{RMS} = 16.3V, Δt_{heat} = 0.25s, ΔT = 12.7 °C, and f_s = 200 Hz.

Model 3: Modified first order system

A different model is needed to improve the agreement between the model and the data for large time. To this end, the first order system model can be modified to allow for a non-unity constant such that

$$\theta_{TC}(t) = C\exp\left(-\frac{t}{\tau_{\max}}\right), \qquad t \geq 0. \tag{6.22}$$

The resulting modified sensitivity coefficients are given by

$$Z_{\theta 3,C} = C\frac{\partial \theta_{TC}}{\partial C} = C\exp\left(-\frac{t}{\tau_{\max}}\right), \tag{6.23}$$

$$Z_{\theta 3,\tau\max} = \tau_{\max}\frac{\partial \theta_{TC}}{\partial \tau_{\max}} = C\frac{t}{\tau_{\max}}\exp\left(-\frac{t}{\tau_{\max}}\right), \quad t \geq 0. \tag{6.24}$$

A nonlinear least squares approach is again used to estimate the parameters C and τ_{max}, and the results for probe A0 can be seen in Figure 6.8. Excellent agreement is seen between the data and the model for $t > 0.4$s. However, as expected, this model has extremely poor agreement with the data for early time.

Model 4: Matched Models 2 and 3

In order to improve the degree of fit to the data, a modification of τ defined in Eq. (6.11) is proposed such that

$$\tau(t) = \begin{cases} \tau_0 + 2\lambda\sqrt{t}, & t \leq t_{cr} \\ \tau_{\max}, & t > t_{cr}, \end{cases} \tag{6.25}$$

where t_{cr} is given by

$$t_{cr} = \left(\frac{\tau_{\max} - \tau_0}{2\lambda}\right)^2. \tag{6.26}$$

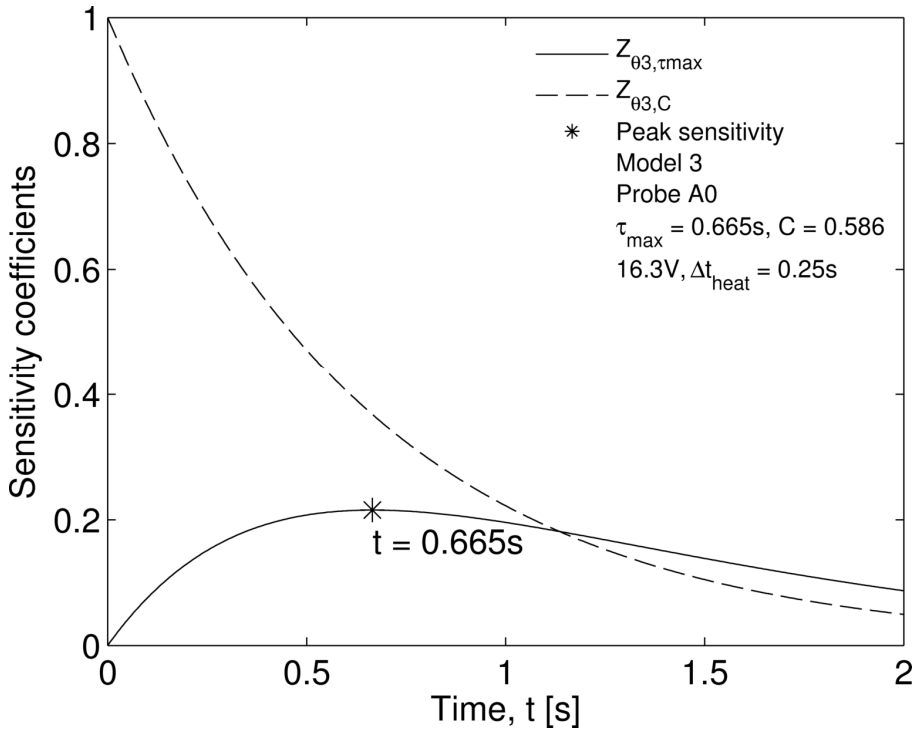

(a)

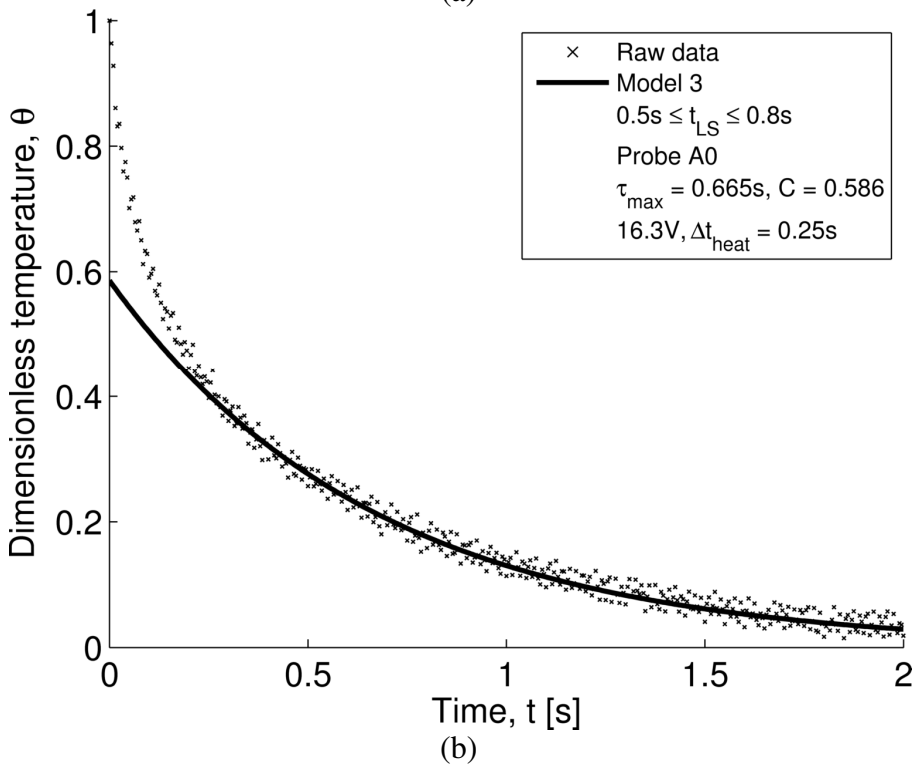

(b)

Figure 6.8: Model 3 results for LCSR testing of probe A0. (a) Sensitivity coefficient and (b) comparison of model with raw data. Testing parameters were V_{RMS} = 16.3V, Δt_{heat} = 0.25s, ΔT = 12.7 °C, and f_s = 200 Hz.

Essentially, this is matching the good early time model of Eq. (6.12) with the good large time model of Eq. (6.22). This leads to the exact solution given by

$$\theta_{TC}(t)=\begin{cases}\exp\left\{\dfrac{1}{2\lambda^2}\left[\tau_0\ln\left(\tau_0+2\lambda\sqrt{t}\right)-\tau_0\ln\left(\tau_0\right)-2\lambda\sqrt{t}\right]\right\}, & t\le t_{cr}\\ \exp\left\{\dfrac{1}{2\lambda^2}\left[\tau_0\ln\left(\tau_0+2\lambda\sqrt{t_{cr}}\right)-\tau_0\ln\left(\tau_0\right)-2\lambda\sqrt{t_{cr}}-2\lambda^2\dfrac{t-t_{cr}}{\tau_{\max}}\right]\right\}, & t>t_{cr}.\end{cases} \tag{6.27}$$

The sensitivity coefficients for τ_0, λ, τ_{max}, and t_{cr} are given by

$$Z_{\theta 4,\tau 0}=\begin{cases}\dfrac{\tau_0}{2\lambda^2}\theta_{TC}\left[\ln\left(\tau_0+2\lambda\sqrt{t}\right)+\dfrac{\tau_0}{\tau_0+2\lambda\sqrt{t}}-\ln\tau_0-1\right], & t\le t_{cr}\\ \dfrac{\tau_0}{2\lambda^2}\theta_{TC}\left[\ln\left(\tau_0+2\lambda\sqrt{t_{cr}}\right)+\dfrac{\tau_0}{\tau_0+2\lambda\sqrt{t_{cr}}}-\ln\tau_0-1\right], & t>t_{cr},\end{cases} \tag{6.28}$$

$$Z_{\theta 4,\lambda}=\begin{cases}\dfrac{1}{2\lambda^2}\theta_{TC}\left[2\lambda\sqrt{t}+\dfrac{2\lambda\tau_0\sqrt{t}}{\tau_0+2\lambda\sqrt{t}}+2\tau_0\ln\tau_0-2\tau_0\ln\left(\tau_0+2\lambda\sqrt{t}\right)\right], & t\le t_{cr}\\ \dfrac{1}{2\lambda^2}\theta_{TC}\left[2\lambda\sqrt{t_{cr}}+\dfrac{2\lambda\tau_0\sqrt{t_{cr}}}{\tau_0+2\lambda\sqrt{t_{cr}}}+2\tau_0\ln\tau_0-2\tau_0\ln\left(\tau_0+2\lambda\sqrt{t_{cr}}\right)\right], & t>t_{cr},\end{cases} \tag{6.29}$$

$$Z_{\theta 4,\tau\max}=\begin{cases}0, & t\le t_{cr}\\ \theta_{TC}\dfrac{t-t_{cr}}{\tau_{\max}}, & t>t_{cr},\end{cases} \tag{6.30}$$

$$Z_{\theta 4,tcr}=\begin{cases}0, & t\le t_{cr}\\ \dfrac{t_{cr}}{2\lambda^2}\theta_{TC}\left[-\lambda t_{cr}^{-1/2}+\dfrac{2\lambda^2}{\tau_{\max}}+2\tau_0^2t_{cr}^{1/2}+4\tau_0\lambda t_{cr}\right], & t>t_{cr}.\end{cases} \tag{6.31}$$

These sensitivity coefficients and the resulting converged NLS fit to the data for probe A0 can be seen in Figure 6.9. It can be seen that Model 4 has excellent agreement over the entire time domain. Therefore, the definition of τ given by Eq. (6.25) is proposed as the best representation of the LCSR data.

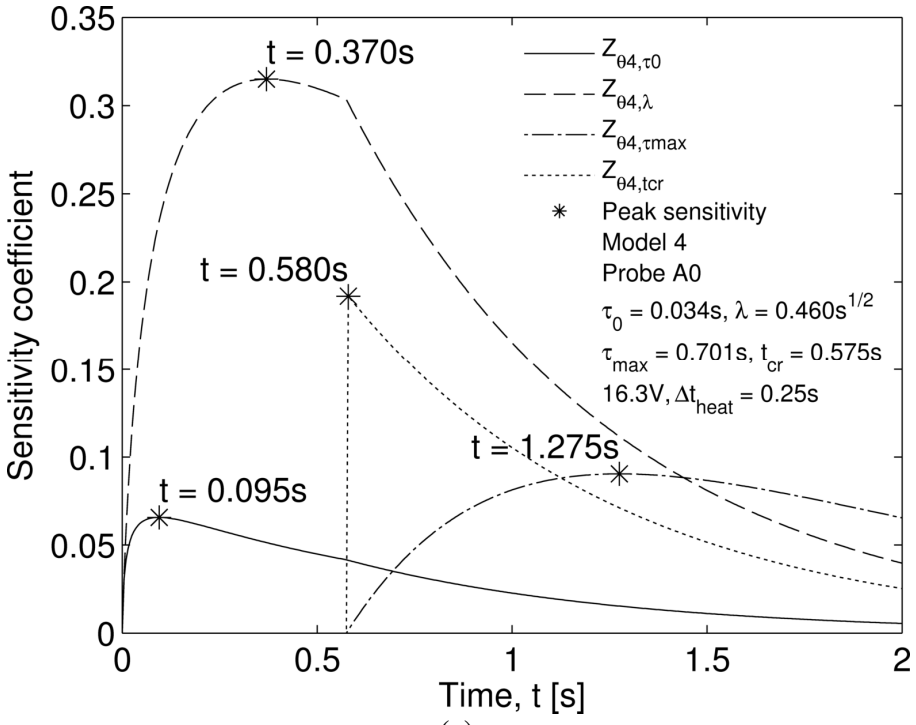

(a)

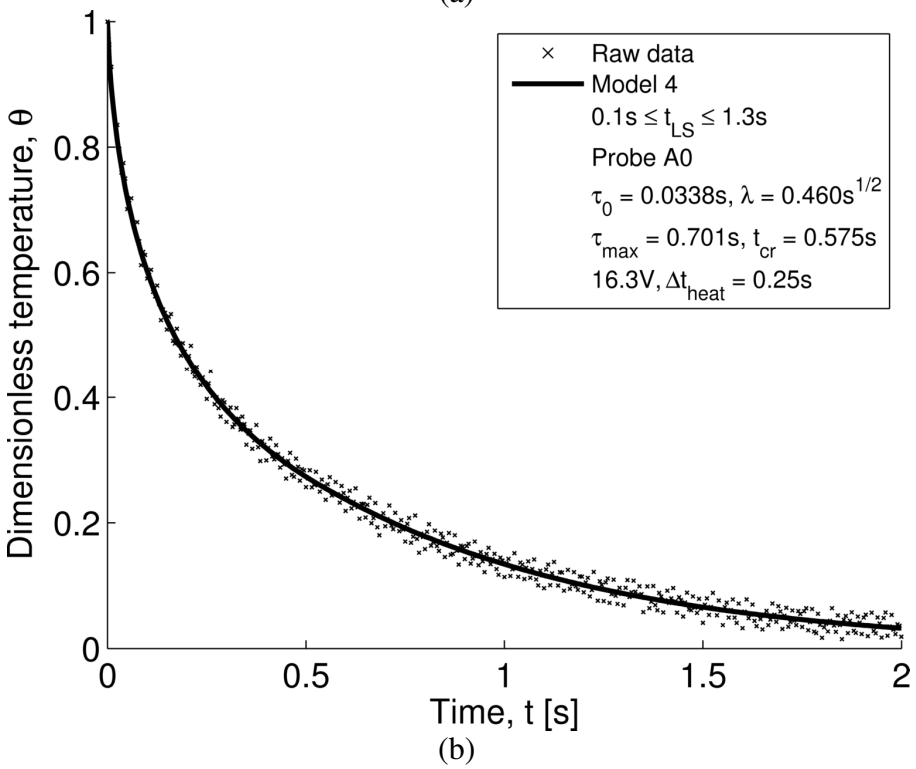

(b)

Figure 6.9: Model 4 results for LCSR testing of probe A0. (a) Sensitivity coefficient and (b) comparison of model with raw data. Testing parameters were V_{RMS} = 16.3V, Δt_{heat} = 0.25s, ΔT = 12.7 °C, and f_s = 200 Hz.

A summary of the results for each installed probe can be seen in Table 6.1. All probes except for B3 were successfully modeled by Model 4. Probe B3 was better described by Model 2 – i.e., no maximum value of $\tau(t)$ was reached. This implies that $\tau(t)$ for probe B3 continues to increase with time, which is nonphysical. Therefore, probe B3 was not used for any of the sandwich experiments.

Application of LCSR characterization values to sandwich experiment data

The characterization values for probe A0 are now applied to the example presented at the beginning of this chapter. The raw thermocouple data from run qRHIt5f200 are filtered using the Gaussian low-pass filter previously discussed. The filtered data were then adjusted for τ_0, λ, τ_{max}, and t_{cr} via Eq. (6.10). These results can be seen in Figure 6.10(a). The in-situ heat flux data are then obtained via the semi-infinite medium integral relationship as in Section 2.8 and can be seen in Figure 6.10(b). These adjusted temperature and heat flux data are then passed to the global time inverse method (details discussed in Chapter 2 and further in Chapter 7) and the resulting inverse surface temperature and heat flux predictions can be seen in Figure 6.11 where the uncertainty bounds on the actual and inverse surface temperature and flux are discussed in the Appendix. Whereas the inverse results for uncorrected data resulted in attenuated and delayed predictions (Figure 6.2), the inverse results after correcting for the response time are significantly more accurate. Indeed, the uncertainty bands of the actual and inverse surface flux are seen to overlap. However, since the physics of the LCSR testing do not exactly match the physics of the sandwich experiment, this is the best inverse result one can achieve with LCSR characterization.

Table 6.1: LCSR results for all installed sandwich experiment probes.

Probe	V_{RMS} [V]	Δt_{heat} [s]	ΔT [°C]	τ_0 [s]	λ [$s^{1/2}$]	τ_{max} [s]	t_{cr} [s]
A0	16.3	0.25	12.7	0.0338	0.460	0.701	0.575
A1	12.7	0.25	13.4	0.0046	0.809	1.256	0.605
A2	16.9	0.25	12.9	0.0001	0.458	0.746	0.556
A3	11.2	0.25	12.4	0.0874	0.443	0.553	0.224
A4	14.6	0.25	16.5	0.0404	0.038	0.103	0.033
B0	17.4	0.25	14.2	0.0534	0.038	0.116	0.044
B1	16.8	0.25	11.3	0.0140	0.396	0.349	0.113
B2	17.0	0.30	11.0	0.0334	0.174	0.103	0.043
B3	13.0	0.25	14.2	0.0280*	0.382*	---	---

* B3 was unable to be modeled via Model 4. Values presented are for Model 2.

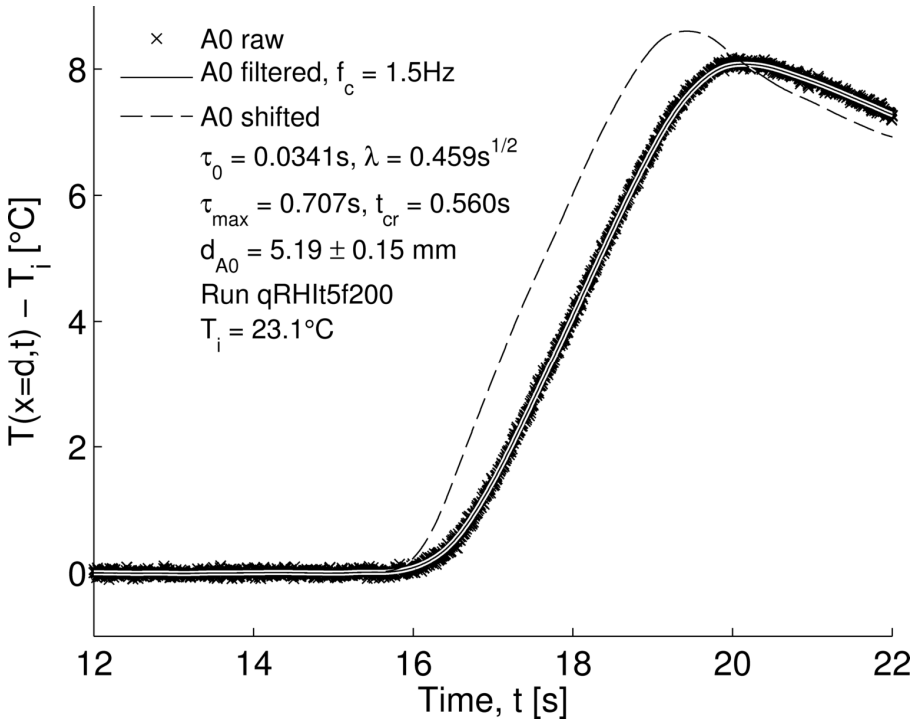

(a)

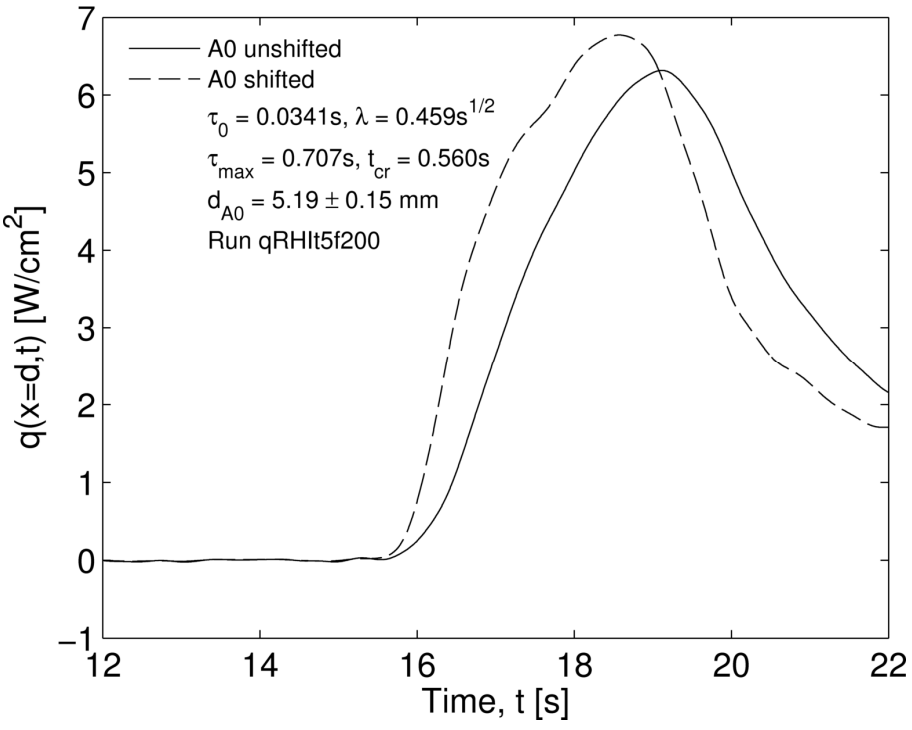

(b)

Figure 6.10: (a) Temperature and (b) heat flux for probe A0 showing the effect of shifting for LCSR characterization values. One-probe analysis used as detailed in Chapter 7.

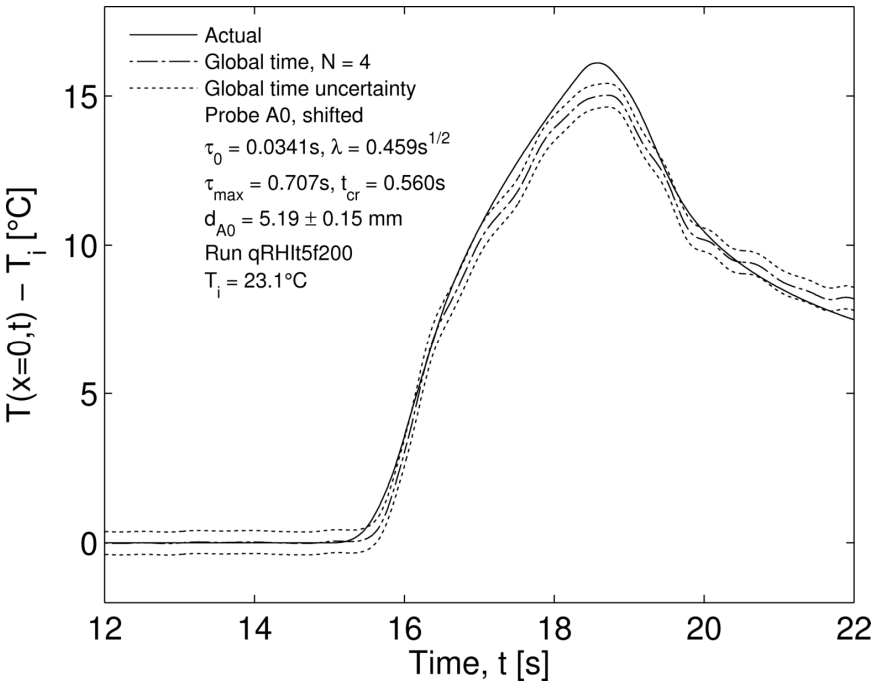

(a)

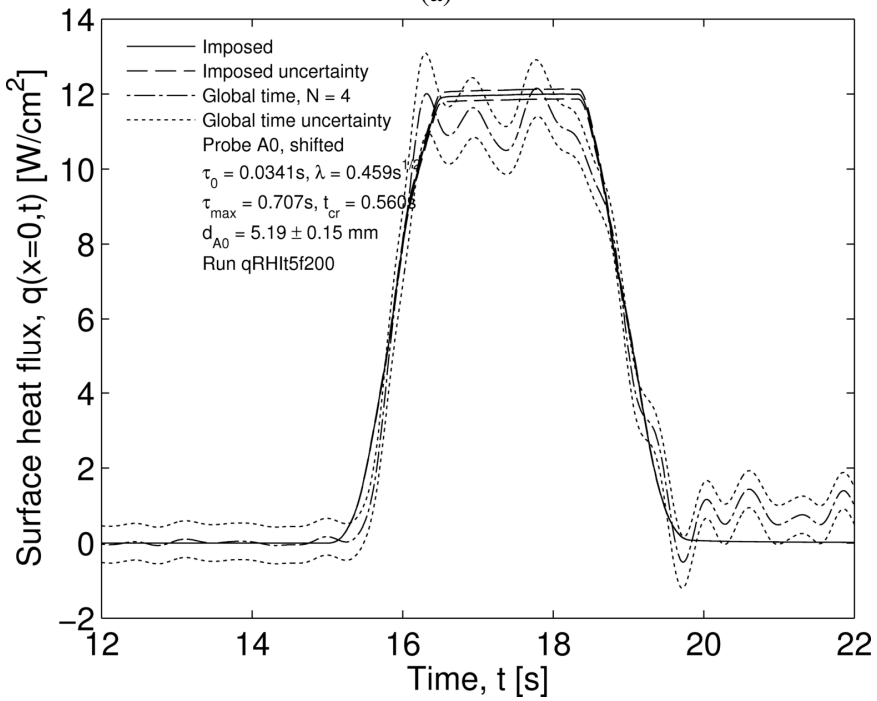

(b)

Figure 6.11: Inverse predicted surface temperature and heat flux using data corrected for response time. (a) Surface temperature prediction with uncertainty band and (b) Surface heat flux with uncertainty band. Data used for prediction can be seen in Figure 6.10 with one-probe analysis as detailed in Chapter 7.

6.3 Two-Probe Taylor Series Method

While the LCSR technique relies on a separate experiment to determine the response time of thermocouples, the Two-Probe Taylor Series (TPTS) method presented herein utilizes data from the run of interest – i.e., the sandwich run data. The TPTS method utilizes thermocouple temperature histories from two probes installed at different depths. This technique relies on the first-order system model of a thermocouple bead and is valid for the case of a semi-infinite medium and simultaneously determines the response time of both probes.

Derivation of Method

Let us take a second look at Eq. (6.8) for the case where thermocouple lead losses are negligible and $T_\infty(t) = T(x=d,t)$. Therefore, $\tau(t)$ is no longer a function of time, and the thermocouple model equation becomes

$$\tau \dot{T}_{TC}(t) + T_{TC}(t) = T(x=d,t), \;\; t \geq 0, \tag{6.32}$$

with exact solution

$$T_{TC}(t) = \frac{1}{\tau} e^{-t/\tau} \int_{u=0}^{t} e^{u/\tau} T(x=d,u)du, \qquad t \geq 0. \tag{6.33}$$

Consider the case of one-dimensional conduction in a semi-infinite medium with two embedded thermocouples subject to the trivial initial condition. The goal of this analysis is to obtain a system of equations relating measurable quantities (temporal derivatives of temperature) with the unknown thermocouple time constants. For all equations, unless otherwise noted, the domain is given by $x, t \geq 0$. The governing equation for this domain is the heat equation

$$\frac{\partial T}{\partial t}(x,t) = \alpha \frac{\partial^2 T}{\partial x^2}(x,t), \tag{6.34}$$

or in terms of heat flux

$$\frac{\partial q}{\partial t}(x,t) = \alpha \frac{\partial^2 q}{\partial x^2}(x,t). \tag{6.35}$$

At our disposal is Fourier's Law

$$q(x,t) = -k \frac{\partial T}{\partial x}(x,t), \tag{6.36}$$

and the half-space relationship between the heating rate and the heat flux given by

$$q(x,t) = \frac{k}{\sqrt{\pi\alpha}} \int_{u=0}^{t} \frac{\partial T}{\partial u}(x,u) \frac{du}{\sqrt{t-u}}, \qquad (x,t) \geq 0. \tag{6.37}$$

Using Taylor Series, the temperature at any point $x < x_2$ can be written as

$$T(x,t) = \sum_{n=0}^{N} \frac{(x-x_2)^n}{n!} \frac{\partial^n T}{\partial x^n}(x_2,t), \tag{6.38}$$

and the heat flux as

$$q(x,t) = \sum_{n=0}^{N} \frac{(x-x_2)^n}{n!} \frac{\partial^n q}{\partial x^n}(x_2,t). \tag{6.39}$$

Therefore, a temporal derivative representation for the spatial derivatives in Eqs. (6.38-6.39) is needed. The first temporal derivative of temperature is readily available from Eq. (6.36) as

$$\frac{\partial T}{\partial x}(x,t) = -\frac{1}{k} q(x,t), \tag{6.40}$$

and the second derivative is also available from Eq. (6.34) as

$$\frac{\partial^2 T}{\partial x^2}(x,t) = \frac{1}{\alpha} \frac{\partial T}{\partial t}(x,t). \tag{6.41}$$

Differentiating Eq. (6.41) with respect to x, and utilizing the commutative property of continuous variables, we obtain

$$\frac{\partial^3 T}{\partial x^3}(x,t) = \frac{1}{\alpha}\frac{\partial}{\partial t}\left(\frac{\partial T}{\partial x}(x,t)\right) = -\frac{1}{k\alpha}\frac{\partial q}{\partial t}(x,t), \tag{6.42}$$

$$\frac{\partial^4 T}{\partial x^4}(x,t) = \frac{1}{\alpha}\frac{\partial}{\partial t}\left(\frac{\partial^2 T}{\partial x^2}(x,t)\right) = \frac{1}{\alpha^2}\frac{\partial^2 T}{\partial t^2}(x,t), \tag{6.43}$$

or

$$\frac{\partial^n T}{\partial x^n}(x,t) = \frac{1}{\alpha}\frac{\partial}{\partial t}\left(\frac{\partial^{n-2} T}{\partial x^{n-2}}(x,t)\right), \qquad n = 2,3,4,...,N. \tag{6.44}$$

Using Eqs. (6.40-6.41), a closed form solution is obtained for the *n*th spatial derivative of temperature in terms of temporal derivatives from the recursive relation of Eq. (6.44) as

$$\frac{\partial^n T}{\partial x^n}(x,t) = \begin{cases} -\dfrac{1}{k\alpha^{(n-1)/2}}\dfrac{\partial^{(n-1)/2} q}{\partial t^{(n-1)/2}}(x,t), & n = 1,3,5,... \\ \dfrac{1}{\alpha^{n/2}}\dfrac{\partial^{n/2} T}{\partial t^{n/2}}(x,t), & n = 0,2,4,... \end{cases} \tag{6.45}$$

Similarly, the spatial derivatives of heat flux can be replaced by temporal derivatives using

$$\frac{\partial^n q}{\partial x^n}(x,t) = \begin{cases} -\dfrac{\rho C}{\alpha^{(n-1)/2}}\dfrac{\partial^{(n+1)/2} T}{\partial t^{(n+1)/2}}(x,t), & n = 1,3,5,... \\ \dfrac{1}{\alpha^{n/2}}\dfrac{\partial^{n/2} q_x}{\partial t^{n/2}}(x,t), & n = 0,2,4,... \end{cases} \tag{6.46}$$

Temperature and its temporal derivatives are measurable quantities (see Chapter 4) or can be obtained via post-processing (see Chapter 3), while heat flux and its derivatives are not always so readily available. Therefore, Eq. (6.37) can be differentiated using integration by parts followed by Leibniz Rule [67] to obtain the general relationship

$$\frac{\partial^n q}{\partial t^n}(x,t) = \frac{k}{\sqrt{\pi\alpha}}\int_{u=0}^{t}\frac{\partial^{n+1} T}{\partial u^{n+1}}(x,u)\frac{du}{\sqrt{t-u}}. \tag{6.47}$$

A system of two equations and two unknowns (time constants) can be obtained by substituting Eq. (6.32) along with Eqs. (6.45-6.47) into Eqs. (6.38-6.39) to obtain

$$\begin{aligned}
&\tau_1 \frac{dT_{TC1}}{dt} + \tau_2 \Bigg[\frac{1}{\sqrt{\pi}} \sum_{n=1,3,\ldots}^{N} \frac{(x_1 - x_2)^n}{\alpha^{n/2} n!} \int_{u=0}^{t} \frac{d^{(n+3)/2} T_{TC2}}{du^{(n+3)/2}}(u) \frac{du}{\sqrt{t-u}} - \\
&\qquad - \sum_{n=0,2,\ldots}^{N} \frac{(x_1 - x_2)^n}{\alpha^{n/2} n!} \frac{d^{(n+2)/2} T_{TC2}}{dt^{(n+2)/2}} \Bigg] = \\
&-T_{TC1} - \frac{1}{\sqrt{\pi}} \sum_{n=1,3,\ldots}^{N} \frac{(x_1 - x_2)^n}{\alpha^{n/2} n!} \int_{u=0}^{t} \frac{d^{(n+1)/2} T_{TC2}}{du^{(n+1)/2}}(u) \frac{du}{\sqrt{t-u}} + \\
&\qquad \sum_{n=0,2,\ldots}^{N} \frac{(x_1 - x_2)^n}{\alpha^{n/2} n!} \frac{d^{n/2} T_{TC2}}{dt^{n/2}}, \qquad t \geq 0,
\end{aligned} \tag{6.48}$$

$$\begin{aligned}
&\tau_1 \frac{1}{\sqrt{\alpha\pi}} \int_{u=0}^{t} \frac{d^2 T_{TC1}}{du^2}(u) \frac{du}{\sqrt{t-u}} + \tau_2 \Bigg[\sum_{n=1,3,\ldots}^{N} \frac{(x_1 - x_2)^n}{\alpha^{(n+1)/2} n!} \frac{d^{(n+3)/2} T_{TC2}}{dt^{(n+3)/2}} - \\
&\qquad \frac{1}{\sqrt{\pi}} \sum_{n=0,2,\ldots}^{N} \frac{(x_1 - x_2)^n}{\alpha^{(n+1)/2} n!} \int_{u=0}^{t} \frac{d^{(n+4)/2} T_{TC2}}{du^{(n+4)/2}}(u) \frac{du}{\sqrt{t-u}} \Bigg] = \\
&-\frac{1}{\sqrt{\alpha\pi}} \int_{u=0}^{t} \frac{dT_{TC1}}{du}(u) \frac{du}{\sqrt{t-u}} - \sum_{n=1,3,\ldots}^{N} \frac{(x_1 - x_2)^n}{\alpha^{(n+1)/2} n!} \frac{d^{(n+1)/2} T_{TC2}}{dt^{(n+1)/2}} + \\
&\qquad \frac{1}{\sqrt{\pi}} \sum_{n=0,2,\ldots}^{N} \frac{(x_1 - x_2)^n}{\alpha^{(n+1)/2} n!} \int_{u=0}^{t} \frac{d^{(n+2)/2} T_{TC2}}{du^{(n+2)/2}}(u) \frac{du}{\sqrt{t-u}}, \qquad t \geq 0.
\end{aligned} \tag{6.49}$$

One interesting observation is that for N = even, increasing N by one will still require the same number of temporal derivatives. Therefore, it is wise to always use an odd value for N. Further, this method of determining the time constants simultaneously always requires 2 temporal derivatives of probe 1 temperature data regardless of N. For odd N, (N+3)/2 temporal derivatives of probe 2 temperature data are required. It is also important to note that the TPTS method is limited by the response of probe 2 – i.e., the probe furthest away from the surface.

Results with Simulated Data

In order to validate this technique of simultaneously obtaining τ_1 and τ_2, a simulation was run using semi-infinite medium with a pulsed constant surface heat flux as the boundary condition at x=0 given by

$$q(x=0,t) = q_{\max} \sum_{j=0}^{M} H(t-t_j)(-1)^j, \qquad t \geq 0. \tag{6.50}$$

The exact solution for this problem subject to the trivial initial condition is given by [51]

$$T_{exact}(x,t) = \frac{q_{\max}\sqrt{\alpha}}{k} \sum_{j=0}^{M} (-1)^j H(t-t_j) \left[\sqrt{\frac{4(t-t_j)}{\pi}} \exp\left(-\frac{x^2}{4\alpha(t-t_j)} \right) - \frac{x}{\sqrt{\alpha}} \operatorname{erfc}\left(\frac{x}{\sqrt{4\alpha(t-t_j)}} \right) \right], \quad x,t \geq 0, \tag{6.51}$$

where $H(z)$ is the Heaviside function [52], erfc is the complementary error function [52] and $\{t_j\}_{j=0}^{N}$ are the times when the source is "switched" on or off. The source remains off until $t \geq t_{j=0}$. The exact solution of Eq. (6.33) is then used to obtain the simulated thermocouple response. The integration of Eq. (6.33) was attempted by hand using integration by parts, and using MATHEMATICA; however, an analytical form was not possible. Therefore, the integral was performed numerically.

The analysis procedure is as follows:

1) Exact data for two probes (dimensionless properties, x_1=d_1=1, x_2=d_2=2) was generated with Eq. (6.51).
2) Two unique time constants were chosen (τ_1=0.2, τ_2 = 0.1) for each probe, and Eq. (6.33) was used to generate the thermocouple data using trapezoidal integration.

3) In order to simulate how real data would be processed, the Gaussian filter of Eq. (3.15) was used to obtain the higher temporal derivatives of the data. Since no noise was added, a significantly high dimensionless cutoff frequency of 5 was used.
4) The two-probe time constant model in Eqs. (6.48-6.49) was used to simultaneously solve for τ_1 and τ_2 at each time step. Integrals were evaluated using product integration.

Figure 6.12(a) shows a plot of the temperature histories at two locations d_1=1, d_2=2. The source was turned on and off at Fo = 1 and Fo = 3.25, respectively. This roughly corresponds to a three second heating time for probes located at 5mm and 10mm in bronze (see Table 5.1 for properties). The resulting prediction for τ_1 and τ_2 can be seen in Figure 6.12(b) for N=9 (6 temporal derivatives of probe 2 data) and a dimensionless sampling rate of 1000. This corresponds to dimensional sampling rate of 750 Hz for the sandwich experiment of this dissertation.

Comparing Figure 6.12(b) with Figure 6.13(a), it can be seen that increasing the number of derivatives reduces the bias in the time constant prediction. This makes physical sense as increasing N is essentially making space more continuous. It is analogous to using more spatial nodes in a finite difference scheme. Comparing Figure 6.12(b) with Figure 6.13(b) shows the effect of increasing the sampling rate on the predicted time constant values. Clearly, a higher sampling rate will provide better resolution for the integrals of Eqs. (6.48-6.49).

Results with Experimental Data

Figure 6.14 shows the resulting time constant prediction using data from sandwich experiment run qCHIt10f1200 with probes A0 and B0 (d_{A0} = 5.19mm, d_{B0} = 10.14mm) using N = 9. It is noted that the sampling rate is faster than was used for the case of dimensionless

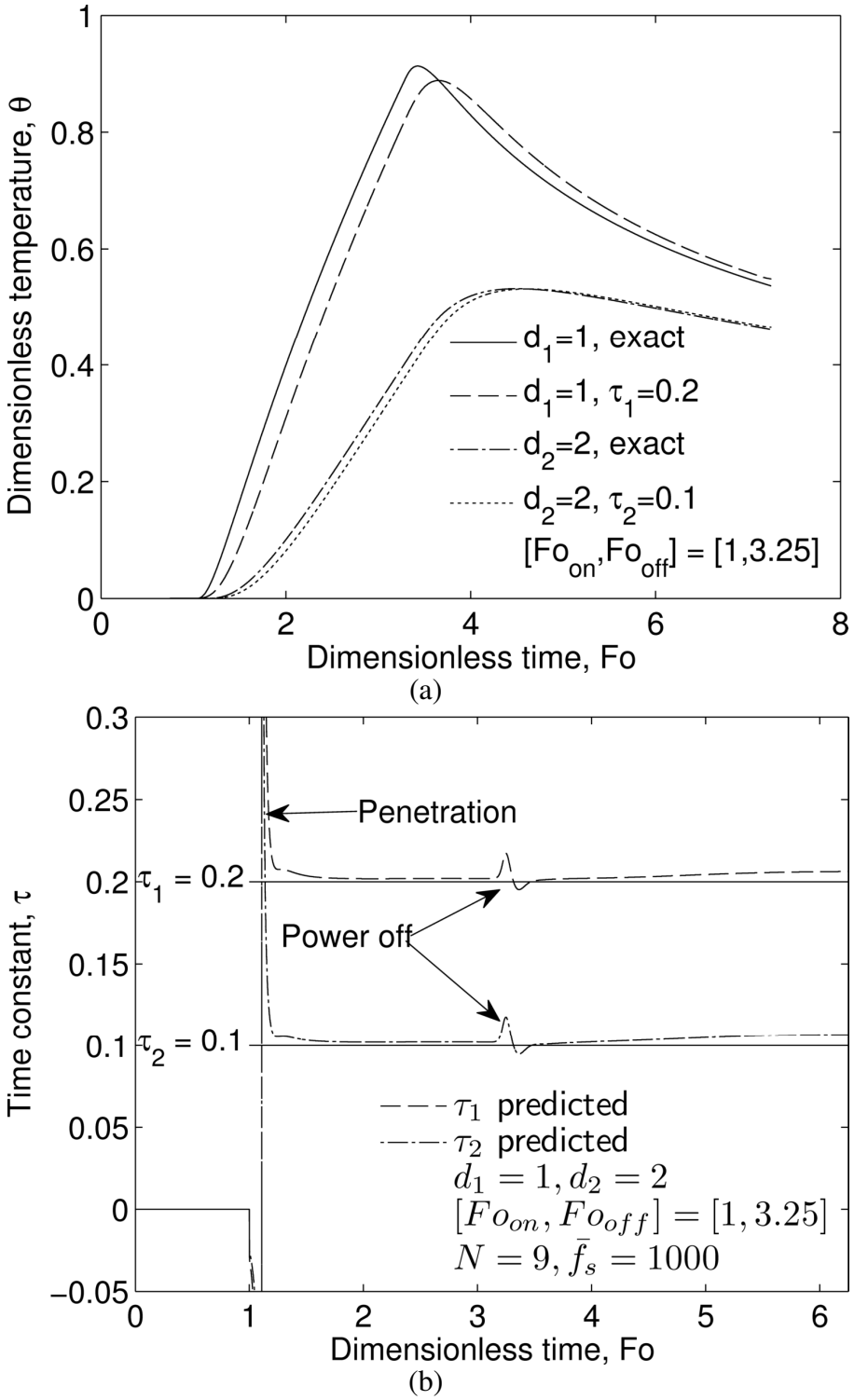

Figure 6.12: Two-Probe Taylor Series method results with simulated data. (a) Input dimensionless data and (b) resulting time constant prediction with $N = 9$, $\bar{f}_s = 1000$.

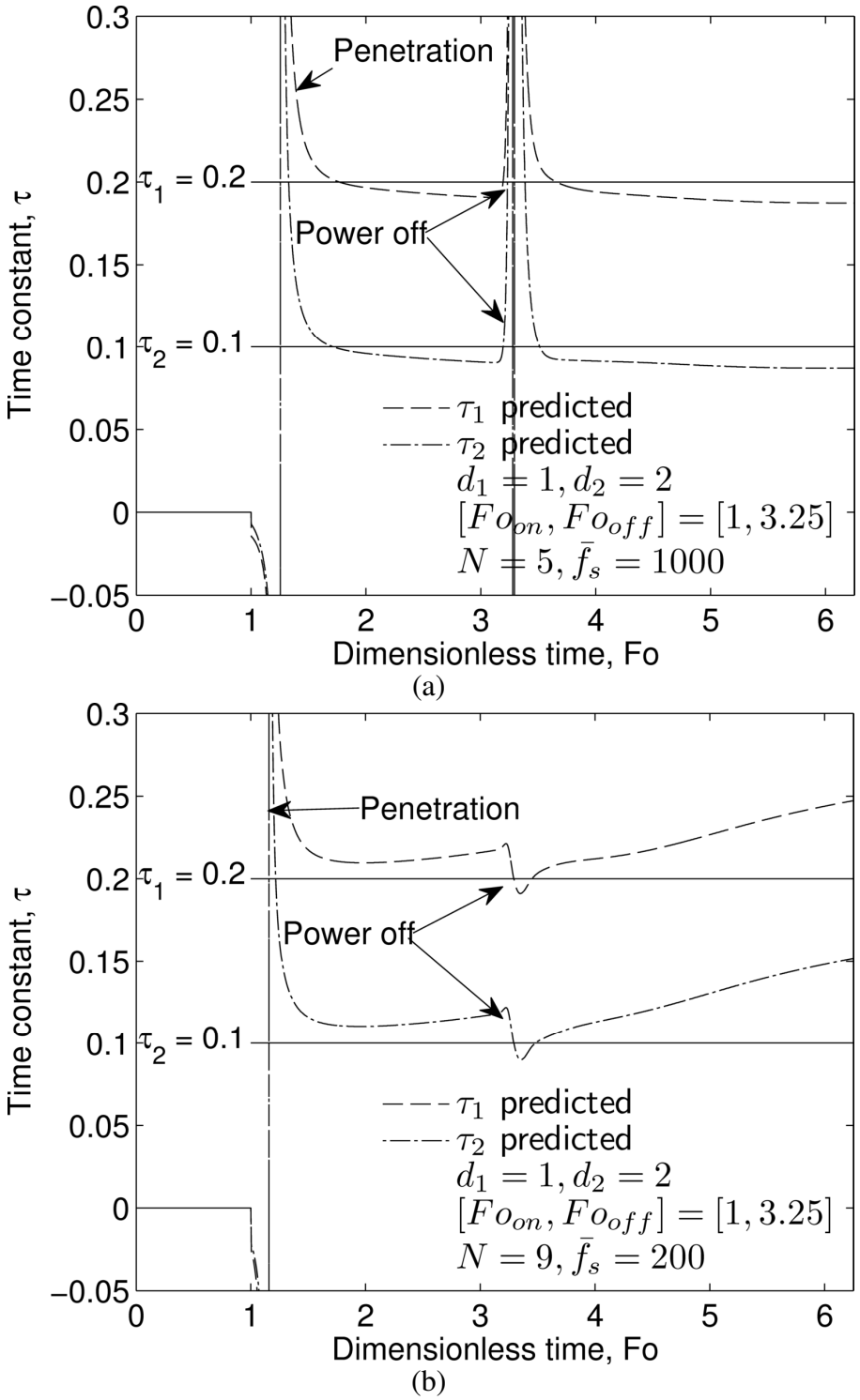

Figure 6.13: Effect of varying (a) number of derivatives used and (b) sampling rate on the resulting Two-Probe Taylor series results using simulated data.

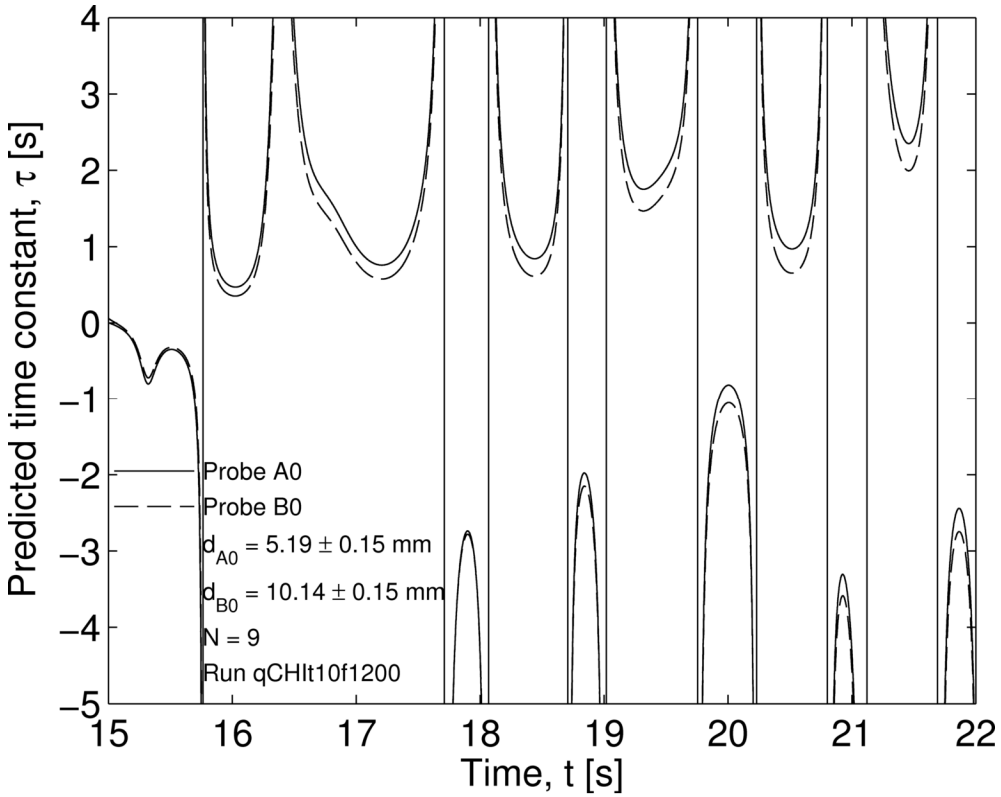

Figure 6.14: Two-Probe Taylor Series results using sandwich experiment data from run qCHIt10f1200 with $N = 9$.

probes change from positive to negative throughout the entire heating cycle, and a converged value is not found. A second simulation was run with $N = 15$; however, the results remained unchanged from the $N = 9$ case. These results show that the model used does not accurately describe the experimental data. Recall that the TPTS method is based on the assumption that τ in Eq. (6.32) is constant which leads to the subsequent derivation of the two-probe time constant model. However, the leads for the sandwich experiment are oriented perpendicular to the isotherms. Therefore, lead losses are not negligible, and the assumption of constant τ is not applicable. The results from the TPTS method verify the physics of the problem, and show that this technique should not be used to characterize probes that are subject to axial conduction along its wires.

6.4 Recommended Characterization for Sandwich Experiment

As noted by previous investigators [38-40, 44], it has been shown that determination of the response time of an embedded thermocouple plays a significant role in the determination of the inverse-predicted surface temperature and heat flux. In this chapter, two techniques for characterizing embedded thermocouples have been presented. The first technique, loop current step response, was shown to be effective. The uncertainty in the inverse projection of the surface heat flux using the LCSR characterization method was seen to overlap the uncertainty in the experimental surface heat flux.

In contrast, the two-probe Taylor Series method was unable to characterize the probes of the sandwich experiment. The reason for this is in the underlying assumptions of the TPTS method; namely, this technique assumes the thermocouples have a constant τ. Since the thermocouples in the sandwich experiment have non-negligible conduction lead losses, the TPTS

technique is an inappropriate characterization technique. However, the Two-Probe Taylor Series method is promising for the case where leads are oriented parallel to the isotherm.

Chapter 7: Experimental Results with One-Probe Analysis

The goal of this chapter is to experimentally validate the inverse heat conduction methods discussed in Chapters 2 and 3. Additionally, the new inverse technique of the calibration integral method developed by Frankel et al. [22] will be also be investigated. There are some key differences between the calibration integral method and the other two inverse techniques. First, no knowledge of thermal properties or probe depth is required. Second, the calibration integral method does not require the thermocouple data to be corrected to represent the actual positional temperature. Third, as the name implies, the surface heat flux from a "real run" is predicted using data from a preliminary calibration run. To date, this is the first study to implement this calibration integral with experimental data.

Section 7.1 first discusses the details of the experimental data reduction process. Section 7.2 presents preliminary results using each of the three inverse techniques. Finally, Section 7.3 compares the results from the three techniques, and conclusions are drawn as to the "best" one-probe data inverse method.

7.1 Data Analysis

One-Probe Embedded Heat Flux Calculation

The inverse techniques presented herein require temperature and heat flux data at an embedded location in order to project to the surface. The sandwich experiment presented in Chapter 5 provided a test bed where embedded thermocouple measurements could be obtained. Chapter 6 presented a technique whereby thermocouple measurements could be (nearly) transformed into positional temperature measurements. However, the inverse methods presented in Chapters 2 and 3 also require local heat flux data at the sensor site for use in the projection

scheme. For one-probe analysis, our only choice is to employ the semi-infinite medium relationship between heating rate and in-situ heat flux presented Section 2.8 such that

$$q(x,t) = \sqrt{\frac{\rho C k}{\pi}} \int_{u=0}^{t} \frac{\partial T}{\partial u}(x,u) \frac{du}{\sqrt{t-u}}, \quad x,t \geq 0. \tag{7.1}$$

Higher time derivatives of the heat flux can be found by integrating Eq. (7.1) by parts, then time differentiating both sides (via Leibniz' rule [67]) such that

$$\frac{\partial^n q}{\partial t^n}(x,t) = \sqrt{\frac{\rho C k}{\pi}} \int_{u=0}^{t} \frac{\partial^{n+1} T}{\partial u^{n+1}}(x,u) \frac{du}{\sqrt{t-u}}, \quad x,t \geq 0. \tag{7.1}$$

The time derivatives required by Eqs. (7.1-7.2) can be obtained using the post-processing technique described in Section 3.3 or using the rate sensor described in Chapter 4. For the results presented herein, the temporal derivatives of temperature are obtained as in Section 3.3 using the Gaussian filter which is an analytical function such that

$$\hat{T}(t) = \left(\sum_{k=0}^{P} \exp\left(-\pi^2 f_c^2 \left(t - t_k\right)^2 \right) \right)^{-1} \sum_{k=0}^{P} \tilde{T}(t_k) \exp\left(-\pi^2 f_c^2 \left(t - t_k\right)^2 \right). \tag{7.2}$$

The first derivative is obtained via

$$\begin{aligned} \frac{d\hat{T}}{dt}(t) = 2\pi^2 f_c^2 \left(\sum_{k=0}^{M} \exp\left(-\pi^2 f_c^2 \left(t - t_k\right)^2 \right) \right)^{-2} \left[\sum_{k=0}^{M} \left(t - t_k\right) \tilde{T}(t_k) \exp\left(-\pi^2 f_c^2 \left(t - t_k\right)^2 \right) \bullet \right. \\ \left. \sum_{j=0}^{M} \left(\frac{t - t_j}{t - t_k} - 1 \right) \exp\left(-\pi^2 f_c^2 \left(t - t_j\right)^2 \right) \right], \quad t \geq 0. \end{aligned} \tag{7.3}$$

This approach provides all of the data required by the inverse methods in Chapters 2 and 3.

LCSR Shifting and Higher-Time Derivatives of Temperature

Both the space-marching and global time inverse methods require time-derivatives of LCSR-shifted temperature. The theory and approach used to characterize installed

thermocouples via LCSR was presented in Chapter 6, and the final result is that the positional temperature is related to the thermocouple data such that

$$T(x=d,t)=\tau(t)\dot{T}_{TC}(t)+T_{TC}(t), \tag{7.4}$$

$$\tau(t)=\begin{cases}\tau_0, & t\le t_{p'}\\ \tau_0+2\lambda\sqrt{t-t_{p'}}, & t\le t_{cr}+t_{p'}\\ \tau_{\max}, & t>t_{cr}+t_{p'},\end{cases} \tag{7.5}$$

where $T(x=d,t)$ is the positional, shifted temperature, $T_{TC}(t)$ is the thermocouple data, $\tau(t)$ is the time-dependent response time of the thermocouple (Section 6.2), and $t_{p'} = t_p + t_{on}$.

One detail that must be elaborated on here is the specific numerical procedure by which the higher-time derivatives of positional temperature are obtained. Eq. (7.5) can be time-differentiated to yield

$$\frac{\partial T}{\partial t}(x=d,t)=\tau(t)\frac{d^2T_{TC}}{dt^2}(t)+\frac{d\tau}{dt}(t)\frac{dT_{TC}}{dt}+\frac{dT_{TC}}{dt}(t). \tag{7.6}$$

Therefore, the first method of obtaining higher-time derivatives of positional temperature from thermocouple data is:

- Filter the thermocouple data via Eq. (7.3).
- Obtain analytical derivatives of the filtered thermocouple data via Eq. (7.4) (and subsequent derivatives).
- Use Eq. (7.7) and subsequent analytical derivatives to obtain $\partial^n T/\partial t^n$.

This approach is denoted as the "single filter method". However, $\tau(t)$ is not smooth (i.e., the slope is discontinuous); therefore, $d\tau/dt$ and each subsequent derivative are not smooth, continuous functions. As will be shown in the global time inverse method discussion of Section 7.2, if this first method of obtaining the higher time-derivative of temperature is used for inverse

predictions, it will result in discontinuous inverse predictions. Therefore, a "band aid" is needed in the data reduction procedure to provide continuous, smooth inverse predictions. To this end, the second method of obtaining the higher-time derivatives is:

- Filter the thermocouple data via Eq. (7.3).
- Obtain ONE analytical derivative of the filtered thermocouple data via Eq. (7.4).
- Use Eq. (7.5) to obtain the positional temperature.
- Filter the positional temperature via Eq. (7.3) to smooth out the effect of $\tau(t)$.
- Use Eq. (7.4) to obtain the higher-time derivatives, $\partial^n T/\partial t^n$.

This approach is denoted as the "double filter method". The benefit of this approach is that it does solve the problem of having discontinuous derivatives. However, as the name implies, this is at the cost of filtering the data twice which can over-smooth. Even though this is less than ideal, this second approach to obtaining the higher time derivatives of temperature is employed herein, and alternative approaches should be the subject of future work.

Penetration Time of Back Face

The half-space relationship of Eq. (7.1) can be used as long as the semi-infinite medium condition is valid. Phrased alternatively, this equation is valid until the back face temperature departs from the initial condition. Therefore, the experimental penetration time of the sample must be obtained. This was accomplished by making an experimental run, qCHIt10f60. The highest power possible was used to produce the largest response at the back face thermocouple. The sampling rate of 60 Hz was chosen as the best compromise between measurement noise and temporal accuracy. Figure 7.1 shows the resulting temperature history for this run. The heater was activated at t_{on} = 15s; therefore, the initial condition was calculated to be 23.6 °C from the

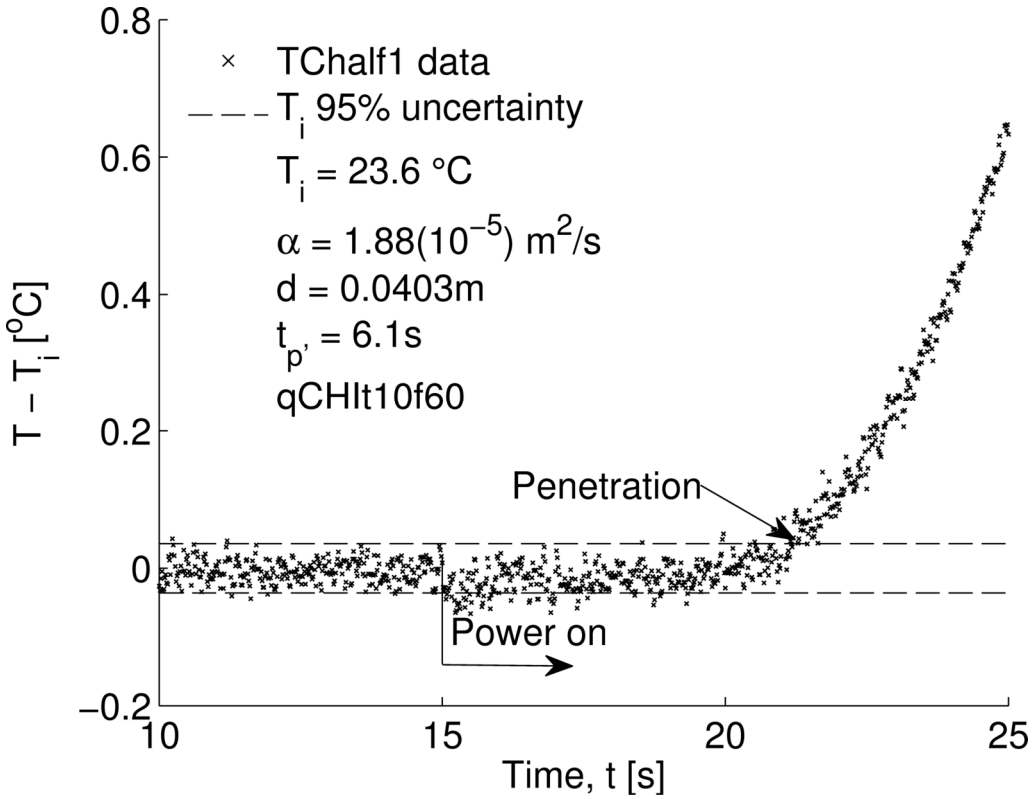

Figure 7.1: Penetration time of back surface with run qCHIt10f60 where $t_{p'} = t_{on} + t_p$.

average of all temperature readings up to 15s. The uncertainty in the initial condition was calculated as

$$U_{Ti} = \pm\sigma\gamma_{95\%}, \tag{7.7}$$

where σ is the standard deviation of the lead data and $\gamma_{95\%}$ is the corresponding Student's t-distribution value [49]. As shown in Figure 7.1, the back face temperature is seen to have a statistically significant departure from the initial condition at $t_p = t - t_{on} = 6.1$s. This corresponds to a dimensionless penetration time of $Fo_p = 0.071$; this compares well with the discussion of penetration time theory presented in Section 2.3 which proposed a dimensionless penetration time of 0.075 – a 5% difference. However, while thermal penetration is observed 6.1s after heater activation, the back face temperature only increased to 0.1 °C by $t - t_{on} = 7$s. Therefore, up to 7s of data past t_{on} is used henceforth for semi-infinite analysis.

Actual Surface Heat Flux

As discussed in Chapter 5, the heater resistance and transient heater voltage were measured for each run. Since AC voltage at 60 Hz was used, the transient RMS of the voltage was found such that

$$V_{RMS}(t_j) = \left[\frac{1}{n_2 - n_1 + 1}\sum_{n=n_1}^{n_2}\left(V_{heater}(t_n)\right)^2\right]^{1/2}, \qquad j = 0,1,2,..., \tag{7.8}$$

$$n_1 = t_j - \frac{\Delta t_{pb}}{120}, \qquad j = 0,1,2,..., \tag{7.9}$$

$$n_2 = t_j + \frac{\Delta t_{pb}}{120}, \qquad j = 0,1,2,... \tag{7.10}$$

Two interpretations of the actual bronze surface heat flux could be used. First, the thermal conductance effect of the nichrome volumetric generation, mica and thermal paste could be

neglected, and the bronze surface heat flux be assumed to be equal to the power supplied to the heater divided by twice (two plates) the heated area of one bronze plate such that

$$q_{S,1}(t) = \frac{V_{RMS}^2(t)}{2A_{heat}R_{heat}}. \tag{7.11}$$

This is called the "direct flux model." Second, the three layer FD model described in Section 5.4 could be used to account for the effects of the heater volumetric generation and the mica layer. The volumetric generation of the heater is then calculated as

$$u_{gen}(t) = \frac{V_{RMS}^2(t)}{2L_1A_{heat}R_{heat}}, \tag{7.12}$$

where L_1 (one-half of the heater thickness) is defined as in Figure 5.4. The bronze surface heat flux is then obtained from the FD model via an energy balance at the bronze/mica interface, and the resulting heat flux is denoted as $q_{S,2}$. Figure 7.2 shows a comparison of $q_{S,1}$ and $q_{S,2}$ for run qCHIt10f60. Note that the power board was sampled at 7500 Hz for this and all other sandwich runs. The effect of the thermal conductance can be seen mainly near the power on and power off "corners." Since the FD model better accounts for the actual physics of the heater, this method of determining the incident flux to the bronze layer is employed henceforth. The FD model bronze surface flux will be called the "actual" surface heat flux and denoted as q_S.

Choice of Probe to Use in Inverse Analysis

For data collection, two thermocouple DAQs (DT9824s) were available, each with four channels. Two channels were reserved for the back face thermocouples, TChalf1 and TChalf2. For all runs, the remaining six channels were used by three 5mm depth "A" probes (A0, A1, and A4) and three 10mm depth "B" probes (B0, B1, and B3). All other probes were eliminated from analysis for the following reasons. Preliminary analysis using probe A2 showed that the depth of

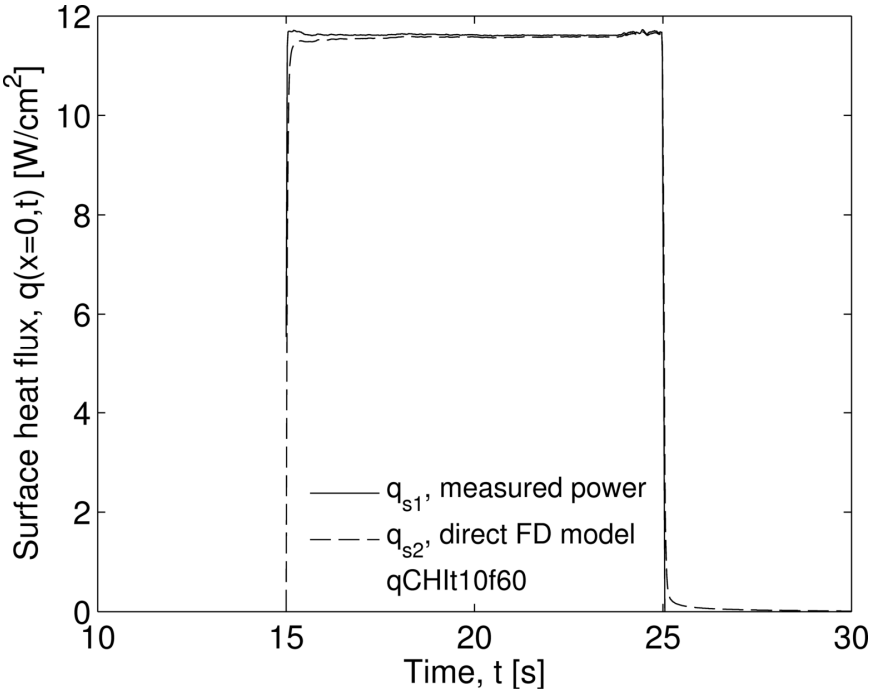

Figure 7.2: Comparison of surface flux obtained direct measured power history (q_{s1}) and direct FD model which accounts for heater capacitance and mica layer (q_{s2}). Heater voltage was sampled at 7500 Hz.

the hole was improperly measured. Probe A3 was not properly seated into the bottom of its drill hole during installation. LCSR test data and analysis of Probe B3 indicated poor health.
The physics of conduction damp out higher frequencies as one proceeds deeper into the sample. Therefore, a sensor closer to the surface will be able to capture changes in the surface condition more easily. Since the focus of this chapter is on one-probe data analysis, only the data from 5mm depth probes will be discussed. Some authors [1, 26] recommend the use of multiple sensors at an identical depth and incorporating them into the inverse algorithm via some form of averaging. Unfortunately, the depths of the A probes (see Table 5.3) are not identically equal; therefore, averaging the temperature readings from these three probes does not make physical sense. Therefore, one probe must be selected as the "best" probe and used for analysis. Probe A0 was selected for this task since it is healthy, and it is along the centerline of the sample. This means that it should suffer the least from multi-dimensional effects. For all of the analysis presented in this chapter, data from probe A0 is used.

7.2 Experimental Validation of Inverse Techniques

Each of the three inverse techniques will be investigated below individually. In order to illustrate the differences between the approaches employed for each method, Figure 7.3 shows a flow chart of the data analysis procedure for the three techniques. The space-marching and global time methods use an identical pre-processing procedure; the only difference between these two approaches is the numerical procedure itself. However, the calibration integral method is quite different. Sensor characteristics, sensor depth, and thermal properties are all stored in the calibration data. Therefore, regularization of the data is all that is required for preprocessing.

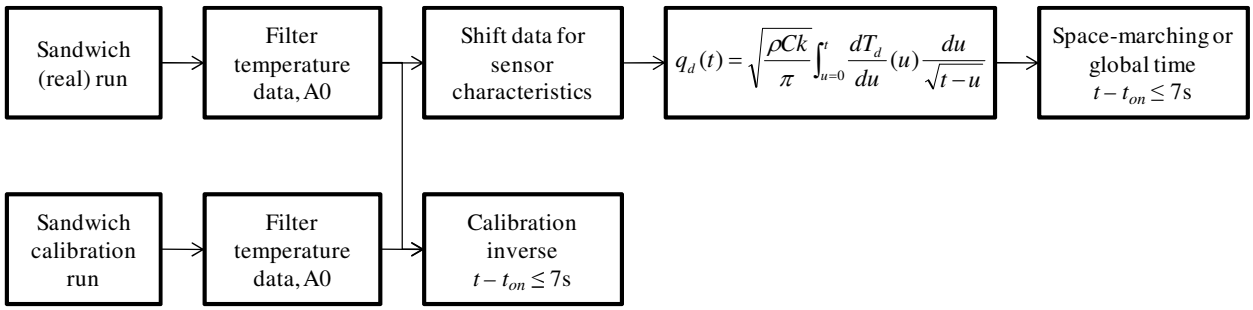

Figure 7.3: Flow chart for preprocessing of data for use in one-probe inverse analysis.

As an example of the preliminary details that must be handled for each run, let us examine the experimental data for run qCLOt3f200 (constant 85V applied to heater, 3 second heating cycle, thermocouples sampled at 200 Hz). The actual surface heat flux for run qCLOt3f200 of approximately 4.5 W/cm^2 can be seen in Figure 7.4(a). Figure 7.4(b) shows the resulting back face thermocouple histories for thermocouples TChalf1 and TChalf2. This figure indicates that the symmetry assumption is valid. Figure 7.5(a) shows the raw and LCSR-shifted (see Table 6.1) temperature data for probe A0, along with the direct FD model temperature history. As expected, the LCSR characterization values shift the raw data backwards in time, and amplify the measured values. The method of Section 3.3 was used to determine the cutoff frequency. Figure 7.5(b) shows the plot of the error norms, ϕ_1 and ϕ_2 as defined in Eqs. (3.19) and (3.21); the optimum range appears to be 0.9 Hz $\leq f_c \leq$ 2.1 Hz. While this range is very large, it is seen that the error norm ϕ_2 is relatively unchanged over this range. Conversely, ϕ_1 varies by almost two orders of magnitude over this range. Therefore, the cutoff frequency was set to 0.9 Hz, corresponding with ϕ_1.

One way to validate the experimental data is comparison of the shifted thermocouple data with the direct FD analytical model discussed in Section 5.4. The actual heater power and actual temperature observed on the back face are used as input to this code, and the resulting positional, FD model temperature data at probe location A0 can be seen in Figure 7.6(a) compared against the measured, shifted temperature data. It is important to note here that the FD model assumes one-dimensional diffusion, with no contact resistance between layers. In reality, the problem is three-dimensional due to non-uniform surface heating of the bronze and heat loss from the sides of the experiment. Additionally, there are thermocouple lead losses which are not completely

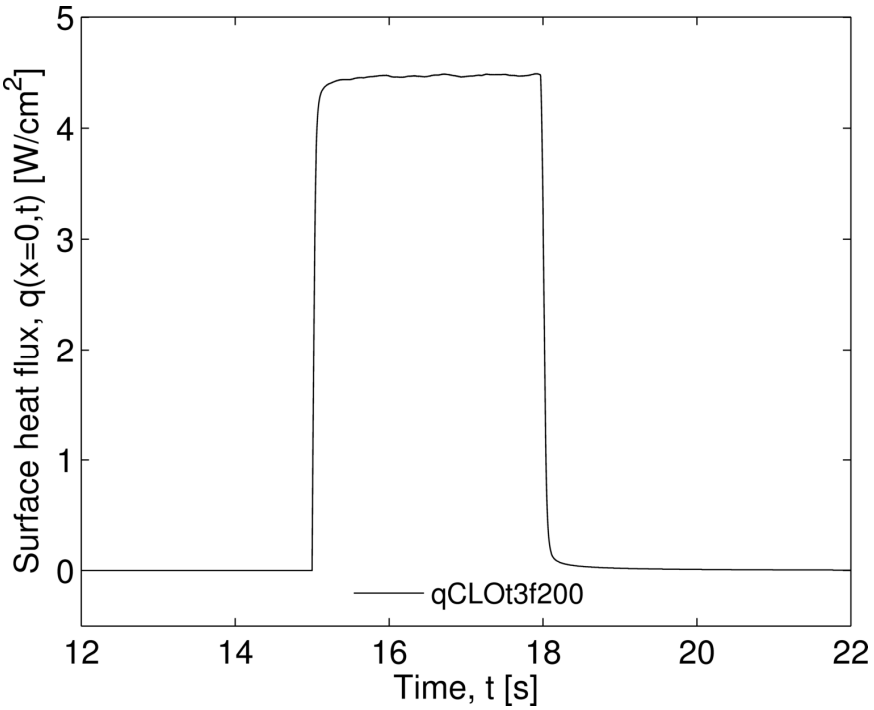

(a)

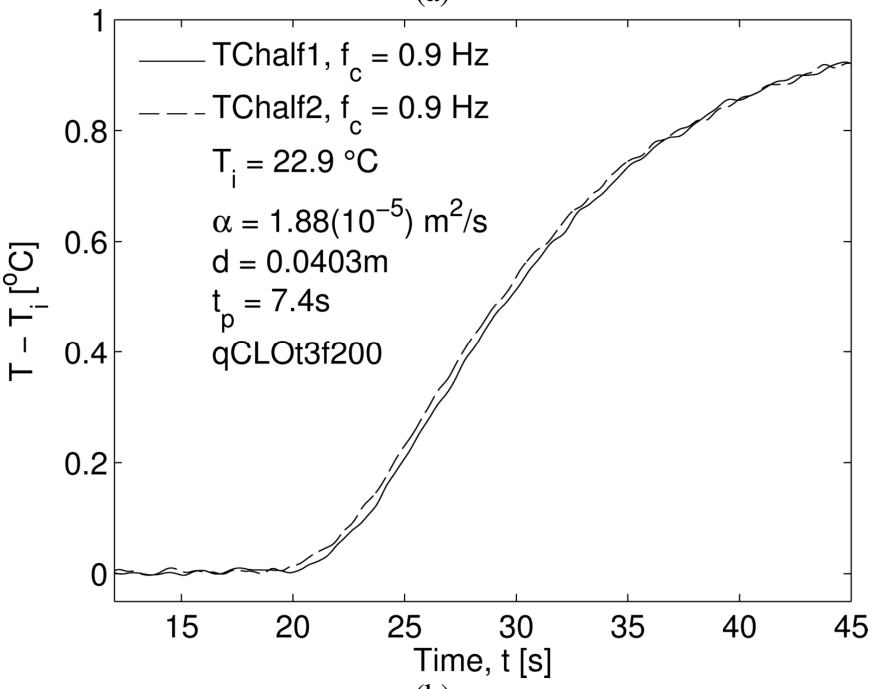

(b)

Figure 7.4: (a) Imposed surface flux and (b) back face thermocouple histories for run qCLOt3f200. Maximum difference between TChalf1 and TChalf2 was 0.02°C.

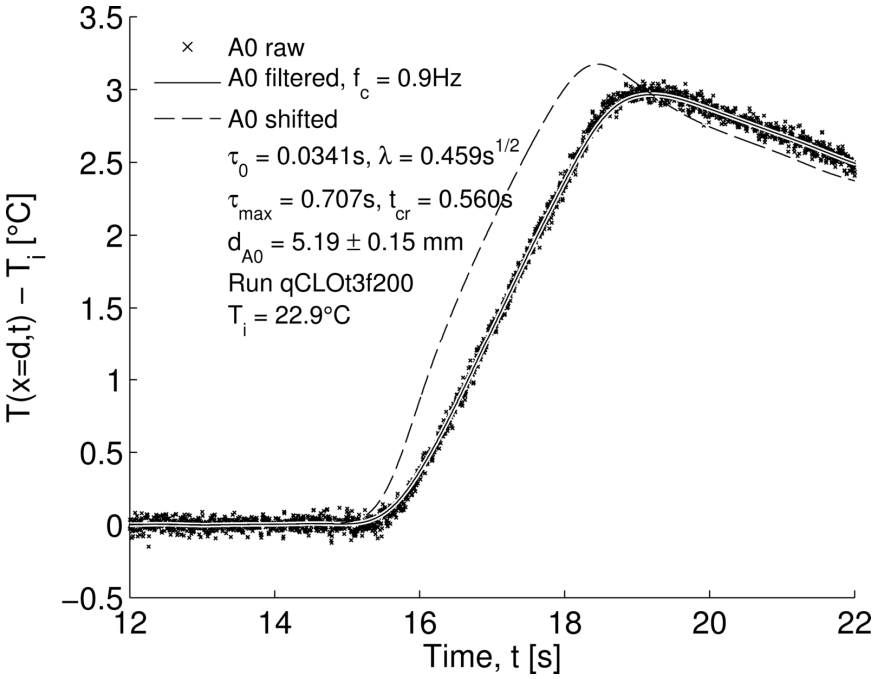

(a)

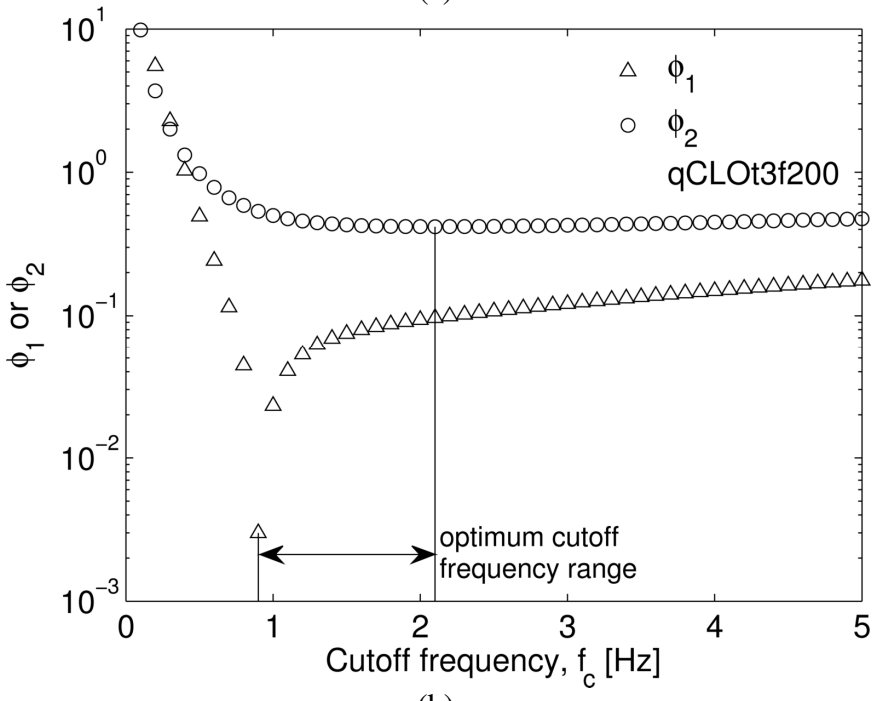

(b)

Figure 7.5: Details of post-processing the data for run qCLOt3f200. (a) Raw and LCSR-shifted experimental A0 data and (b) optimum cutoff frequency range.

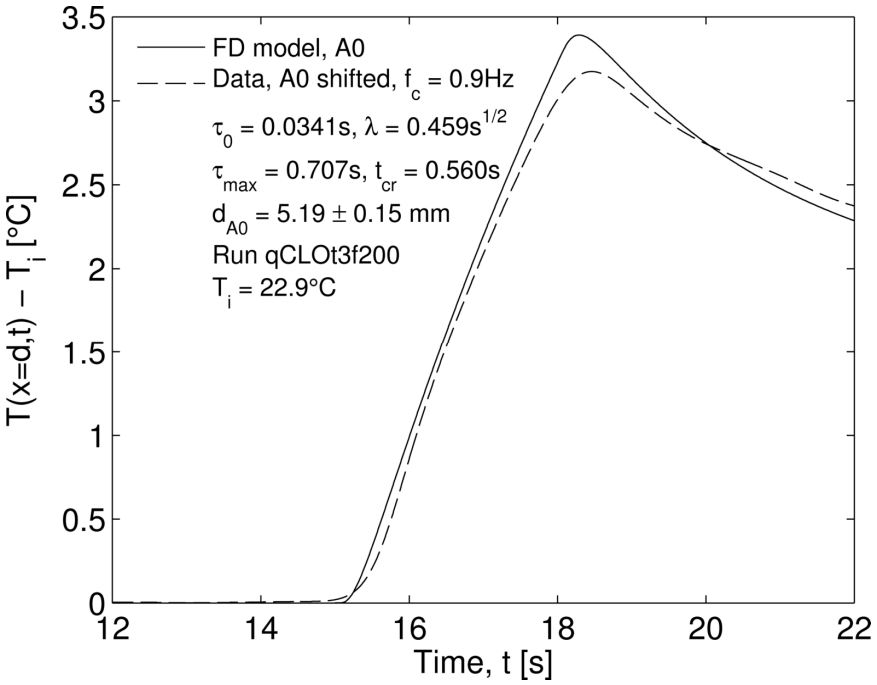

(a)

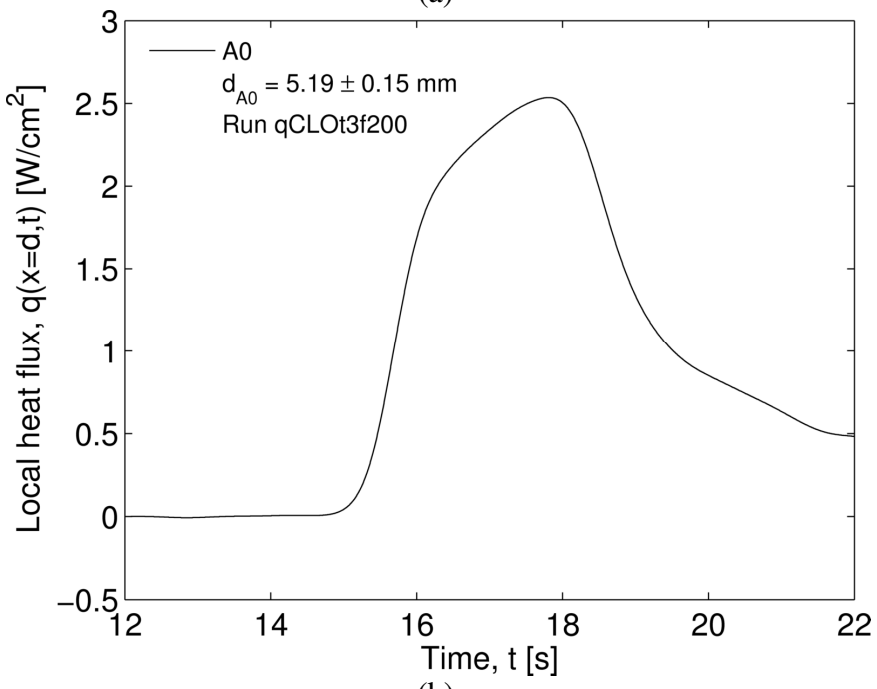

(b)

Figure 7.6: (a) Direct FD model temperature history at probe A0 depth compared with LCSR-shifted experimental A0 data and (b) resulting local heat flux using semi-infinite medium integral equation. Experimental data was regularized with f_c = 0.9 Hz.

accounted for via LCSR shifting. Furthermore, there are uncertainties associated with the inputs to the FD model such as the exact probe location and thermophysical properties. It is suspected that the contact resistance between the layers and the unaccounted portion of the thermocouple lead losses may have dominant roles. Therefore, it is expected that the FD model-predicted probe temperatures should be greater than the observed, LCSR-shifted temperatures. Indeed, this is seen to be the case in Figure 7.6(a). Therefore, it is not reasonable to attempt to draw further conclusions from a comparison of the FD model in-depth temperatures with the shifted thermocouple temperatures; henceforth, the FD model is not used for this purpose. The FD model is only used for generating the actual surface flux of the bronze.

Space-Marching Method

The space-marching method of Chapter 2 requires temperature and heat flux data at the sensor site as input. The local heat flux is obtained via Eq. (7.1), using the LCSR-shifted temperature procedure outlined above for run qCLOt3f200. The resulting local heat flux can be seen in Figure 7.6(b). For this run, the ratio of penetration time to time step size was $t_p/\Delta t = 21.5$; therefore, for the greatest stability and accuracy (see Figure 2.5(a)), 21 spatial nodes were used in the inverse prediction. The resulting inverse-predicted surface temperature and heat flux can be seen in Figure 7.7. Despite the three-dimensional nature of the experiment, losses, etc., the trend of the actual surface temperature and heat flux is captured by the space-marching inverse method. However, it is prudent to find conditions under which the accuracy of this method could be further improved. In order to compare the accuracy of the various inverse schemes across different runs, an error norm is defined as

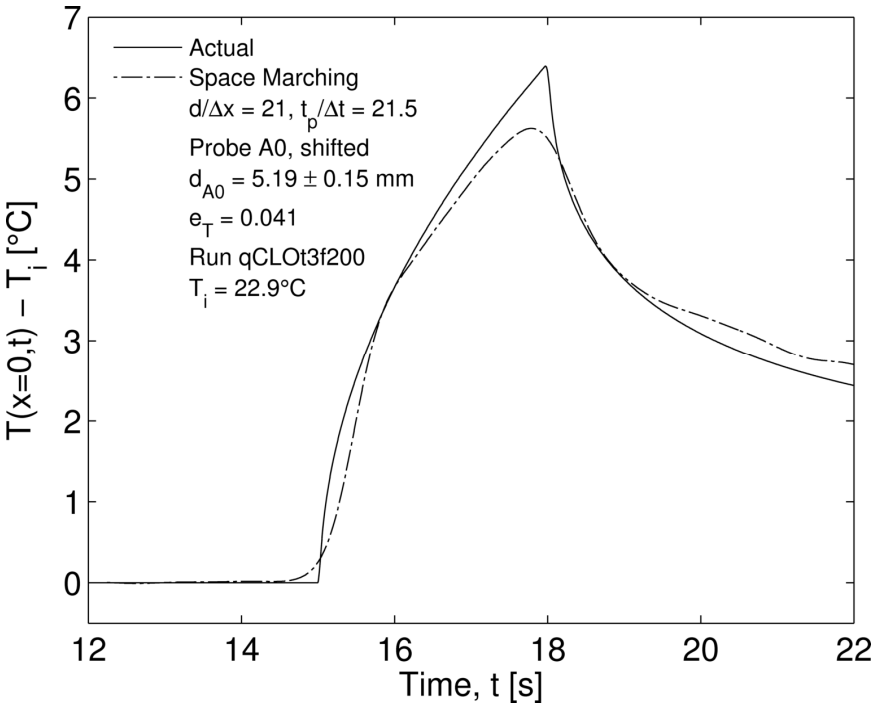

(a)

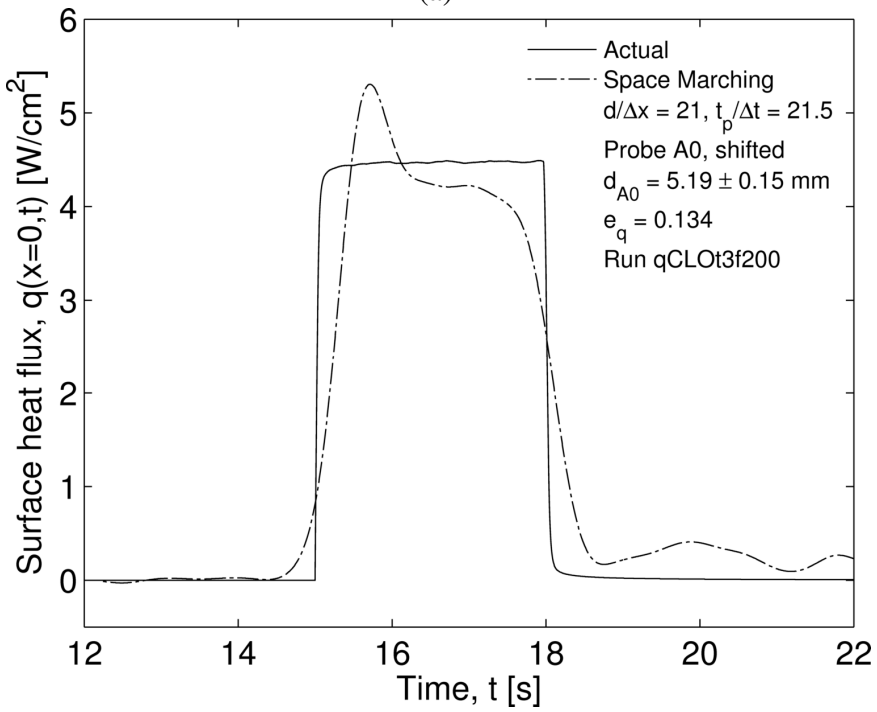

(b)

Figure 7.7: Space-marching inverse results for run qCLOt3f200 for (a) surface temperature and (b) surface heat flux. Parameters used were $d/\Delta x = 21$, $t_p/\Delta t = 21.5$, and $f_c = 0.9$ Hz. The error norms were calculated over $12\text{s} \leq t \leq 22\text{s}$.

$$e_{\varphi} = \sqrt{\frac{1}{j2 - j1 + 1} \sum_{j=j1}^{j2} \left(\varphi_{exact}(t_j) - \varphi_{inverse}(t_j) \right)^2}, \tag{7.13}$$

where φ can be either T or q, and $j1$ and $j2$ correspond to the time range over which the error norm is calculated. For this chapter, three seconds of lead data and seven seconds of heating/cooling data were included as the time range for the error norm – i.e., $j1$ corresponds to t = 12s, and $j2$ corresponds to t = 22. The error norms of predicted surface thermal conditions for this and all subsequent inverse analysis can be seen in Table 7.1.

Figure 2.5(b) suggests the optimal mesh for the space-marching method is for $t_p/\Delta t$ = 30 and 9 spatial nodes. However, the data density for run qCLOt3f200 is not high enough for this requirement. Therefore, a second run was performed at a higher sampling rate. Run qCLOt3f1200 (sampling rate of 1200 Hz) was conducted, and the resulting filtered (f_c = 0.9Hz) positional temperature and heat flux data (seen in Figure 7.8) were down-sampled to correspond with the optimal mesh parameters of $t_p/\Delta t$ = 30 and $d/\Delta x$ = 9. The space-marching inverse prediction with this data can be seen in Figure 7.9. Contrary to the hypothesis, the space-marching method prediction for this run is seen to have a higher error norm than run qCLOt3f200 for both temperature and heat flux. The reason for this is clear when comparing the data used for these two runs seen in Figure 7.5(a) with Figure 7.8(a). While qCLOt3f1200 does have a higher data density available, the signal-to-noise ratio is significantly degraded from that of run qCLOt3f200. This is due to the higher noise associated with sampling at higher rates with the DT9824 DAQ.

The accuracy of the space-marching inverse method after increasing the signal-to-noise ratio of the data is next investigated. This can be accomplished by either 1) decreasing the noise in the data (i.e., better DAQ or lower sampling rate) or 2) increasing the temperature change at

Table 7.1: Inverse error norms for temperature and heat flux calculated over $12s \leq t \leq 22s$. Global time method uses the double filter for derivatives. Calibration Integral uses the thermocouple temperature as the kernel (rather than the heating rate).

	Space-Marching		Global Time		Calibration Integral	
Run Name	e_T	e_q	e_T	e_q	e_T	e_q
qCLOt3f200	0.041	0.134	0.041	0.132	0.024	0.099
qCLOt3f1200	0.045	0.149	0.045	0.147	0.022	0.099
qCHIt3f200	0.039	0.122	0.039	0.120	0.019	0.097
qRHIt5f200	0.030	0.058	0.030	0.058	0.009	0.037

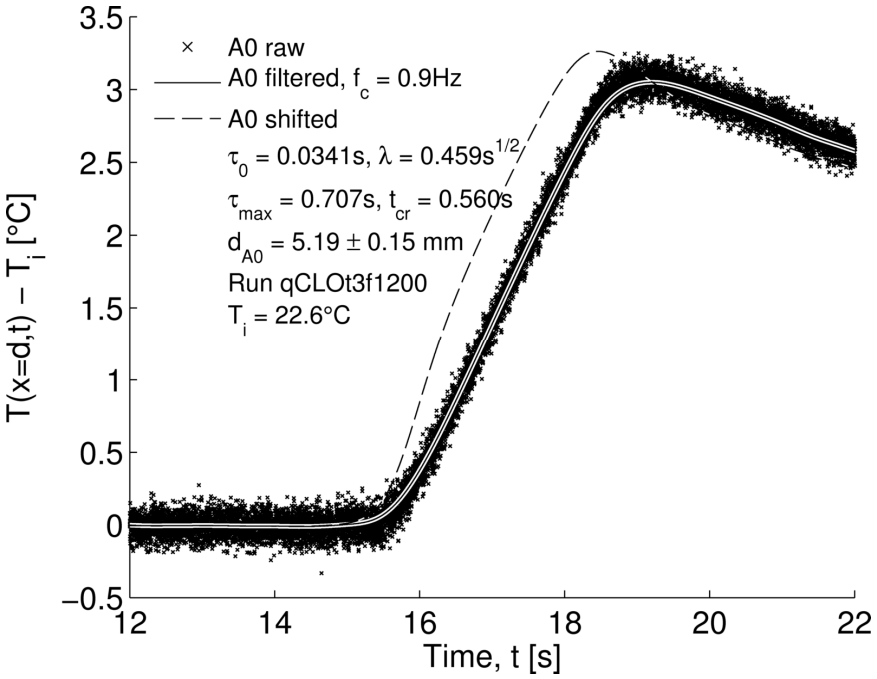

(a)

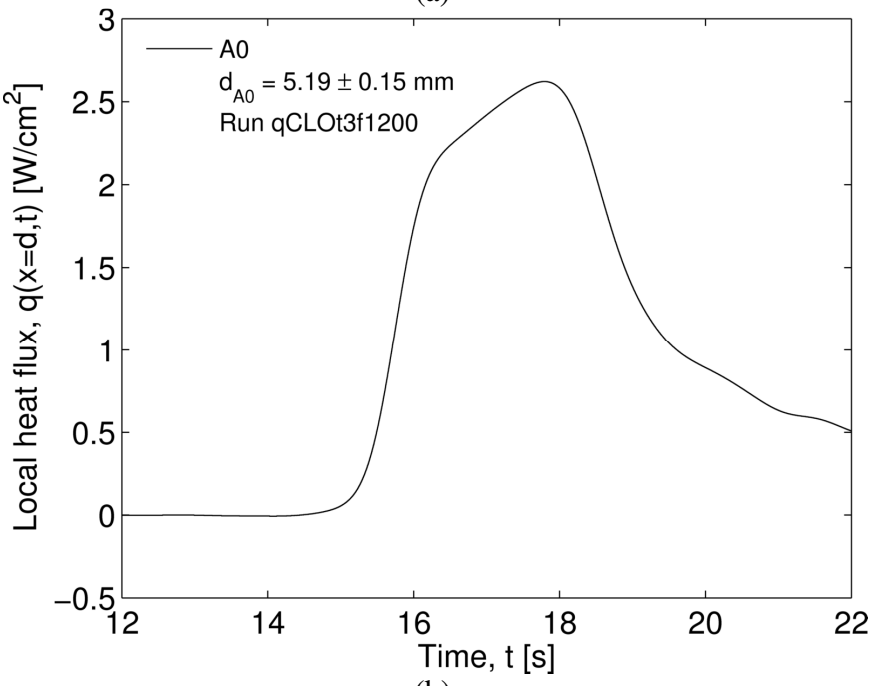

(b)

Figure 7.8: (a) Raw and LCSR-shifted experimental A0 data for run qCLOt3f1200 and (b) resulting local heat flux for probe A0.

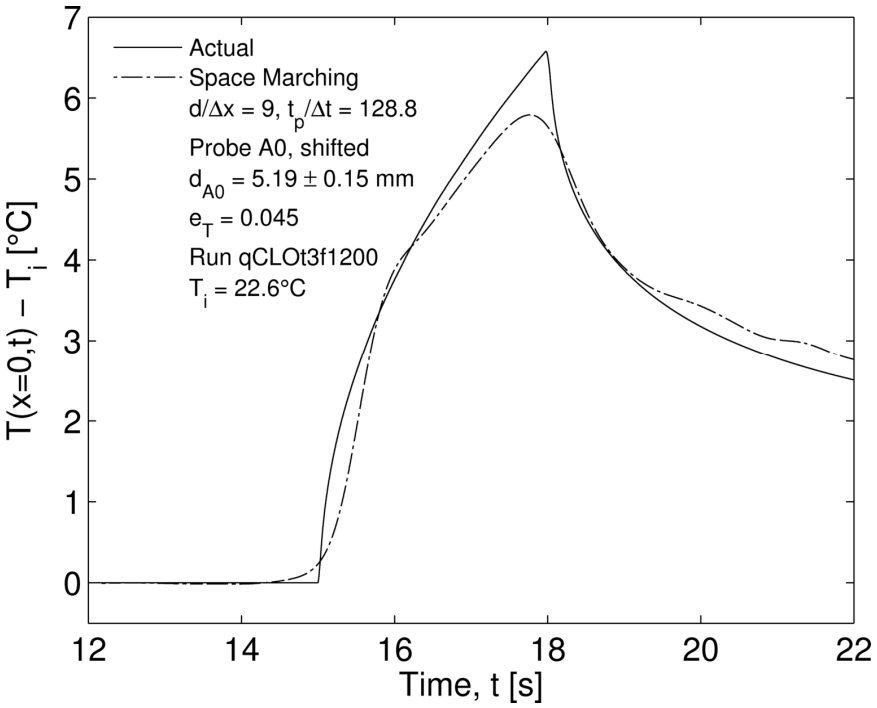

(a)

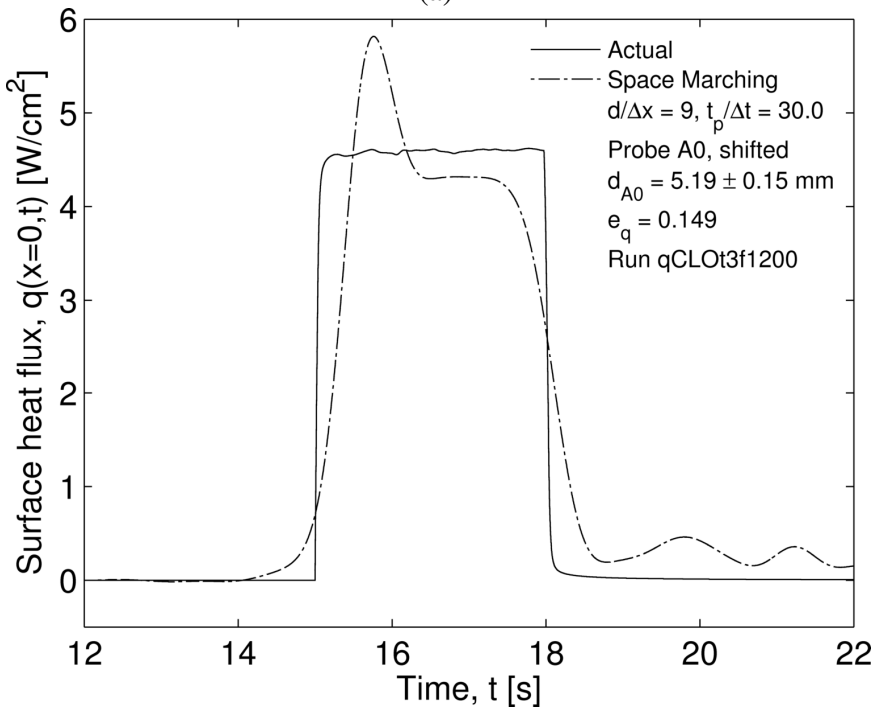

(b)

Figure 7.9: Space-marching inverse results for run qCLOt3f1200 for (a) surface temperature and (b) surface heat flux. Parameters used were $d/\Delta x = 9$, $t_p/\Delta t = 30$, and $f_c = 0.9$ Hz. The error norms were calculated over $12\text{s} \leq t \leq 22\text{s}$.

the probe site. Since the investigation is limited to the DAQ on hand (which is already of high quality), and lowering the sampling rate contradicts the findings of Chapter 2, increasing the temperature change at the probe site is the preferred way to improve the signal-to-noise ratio. Therefore, an additional run qCHIt3f200 was conducted where the surface flux was increased from 4.5 W/cm^2 to approximately 12 W/cm^2. The resulting filtered (f_c = 0.9 Hz), shifted temperature and heat flux data can be seen in Figure 7.10, and the space-marching inverse prediction can be seen in Figure 7.11. As expected the inverse predictions are more accurate (in a relative sense) for the higher temperature rise; compared to run qCLOt3f200, the temperature error norm decreased from 0.041 to 0.039, and the heat flux error norm decreased from 0.134 to 0.122.

Sharp changes in the surface boundary are very difficult to recreate with inverse techniques. Therefore, an additional run qCHIt5f200 was conducted to see how well the space-marching inverse method was able to recreate a linear change in the surface heat flux. The heater voltage was increased (nearly) linearly to a peak flux of approximately 12 W/cm^2, held constant for about two seconds, then linearly decreased to the off position. Figure 7.12 shows the shifted temperature and heat flux data for this run, and Figure 7.13 shows the resulting space-marching inverse run. As expected, the space-marching inverse method is seen to be the most accurate for this boundary condition with temperature and heat flux error norms of 0.030 and 0.058, respectively.

Global Time Inverse Method

In addition to the shifted temperature and heat flux data at the sensor site, the global time method requires higher time derivatives of each of these quantities. In Section 7.1, two methods

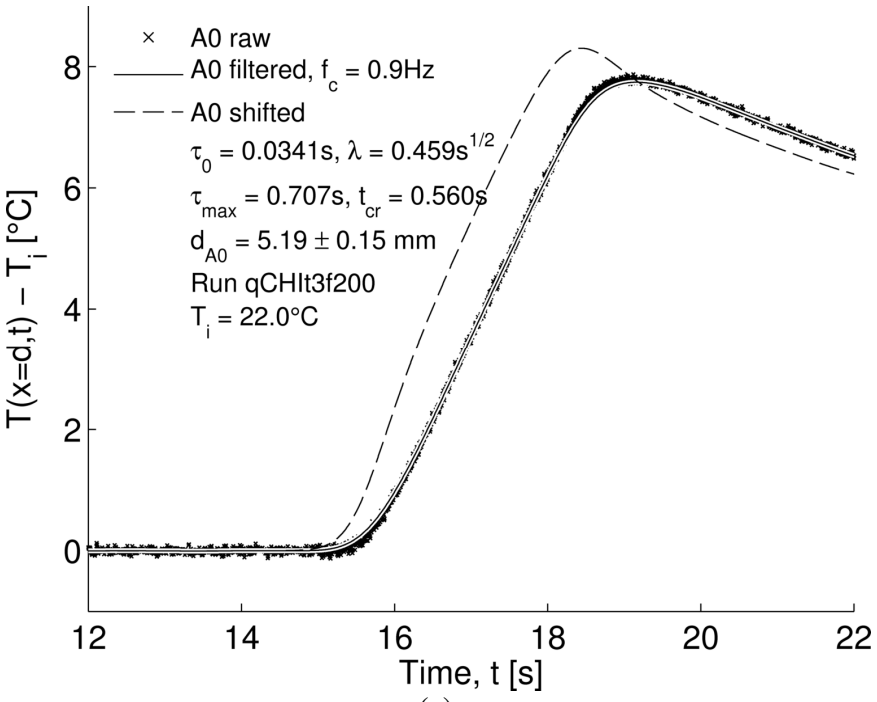

(a)

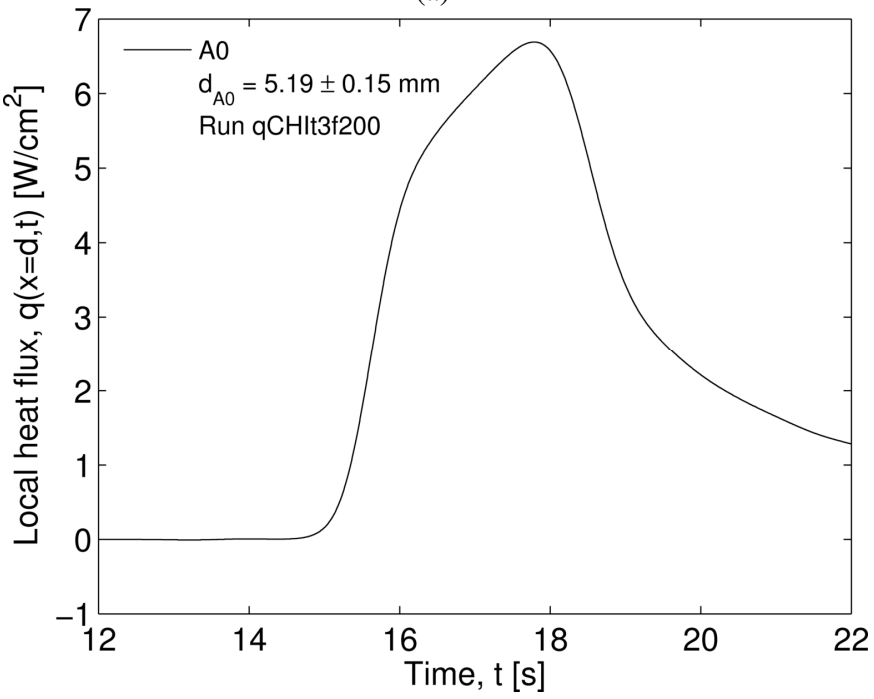

(b)

Figure 7.10: (a) Raw and LCSR-shifted experimental A0 data for run qCHIt3f200 and (b) resulting local heat flux for probe A0.

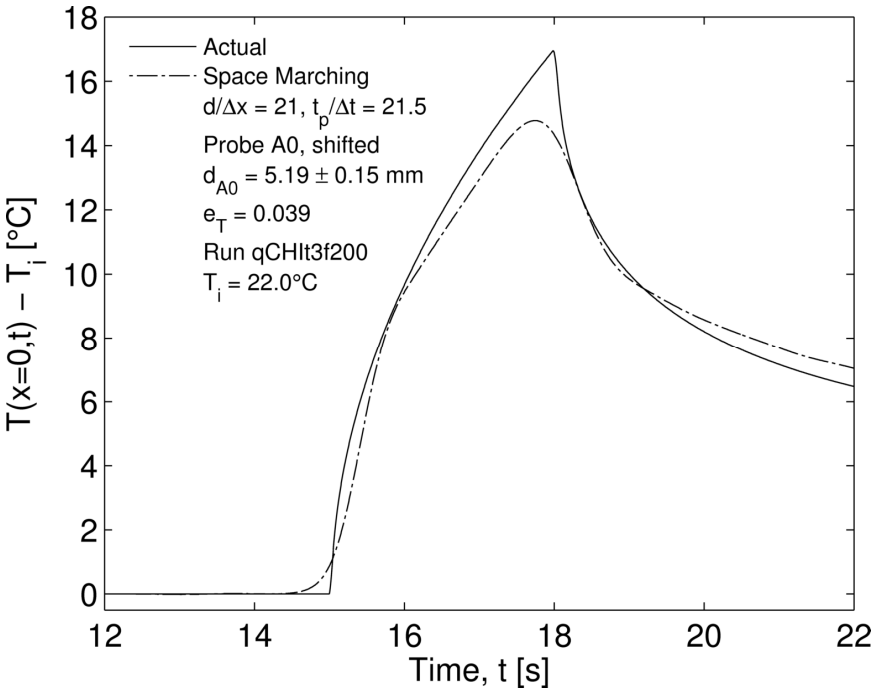

(a)

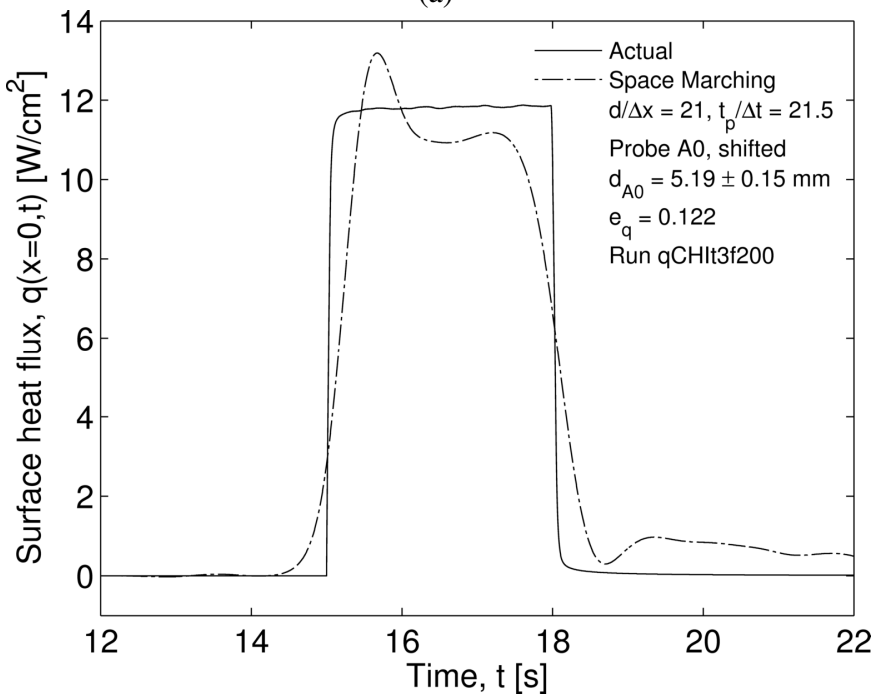

(b)

Figure 7.11: Space-marching inverse results for run qCHIt3f200 for (a) surface temperature and (b) surface heat flux. Parameters used were $d/\Delta x = 21$, $t_p/\Delta t = 21.5$, and $f_c = 0.9$ Hz. The error norms were calculated over $12\text{s} \leq t \leq 22\text{s}$.

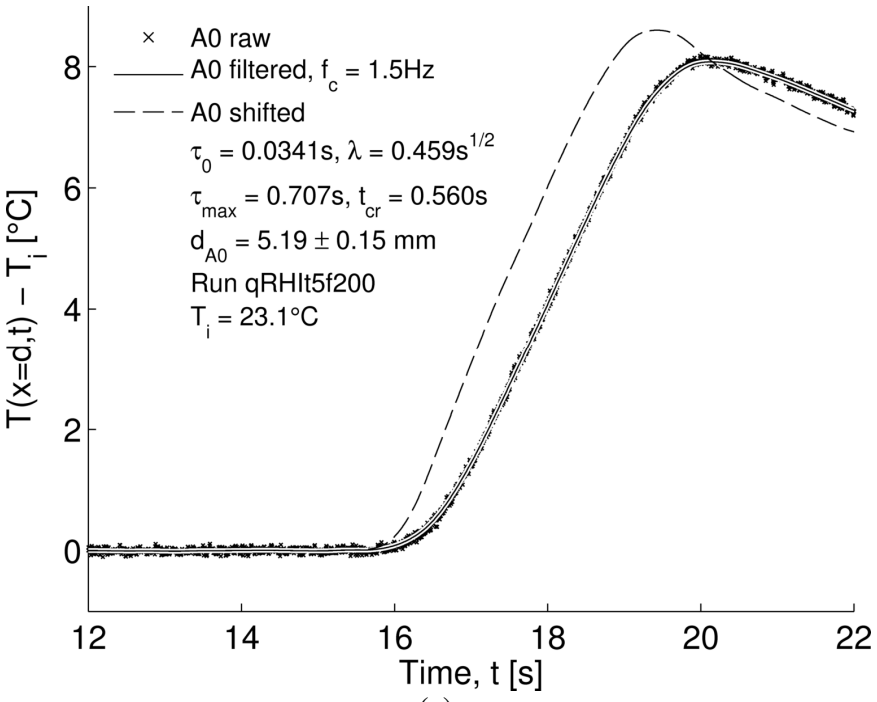

(a)

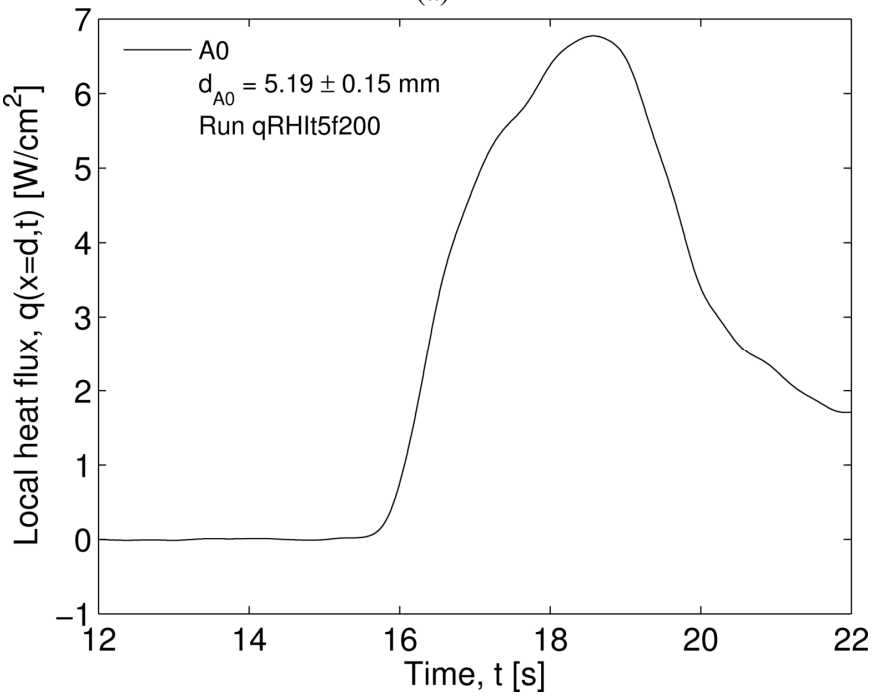

(b)

Figure 7.12: (a) Raw and LCSR-shifted experimental A0 data for run qRHIt5f200 and (b) resulting local heat flux for probe A0.

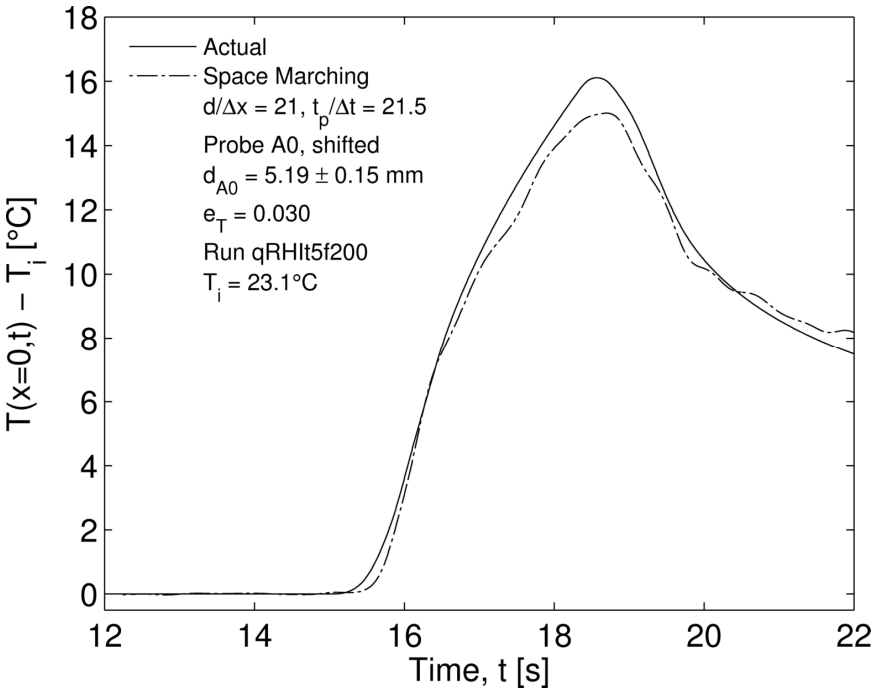

(a)

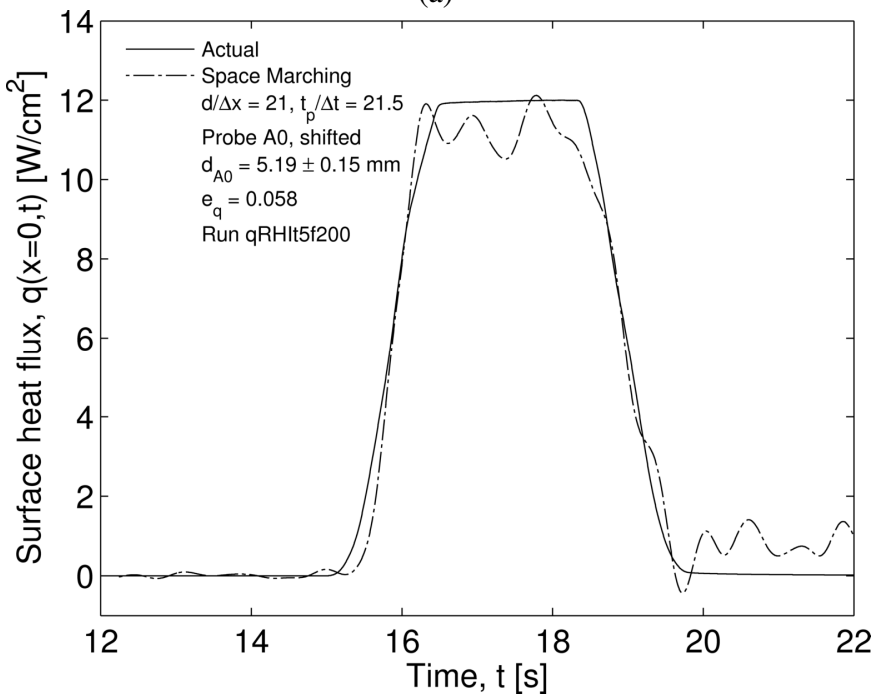

(b)

Figure 7.13: Space-marching inverse results for run qRHIt5f200 for (a) surface temperature and (b) surface heat flux. Parameters used were $d/\Delta x = 21$, $t_p/\Delta t = 21.5$, and $f_c = 1.5$ Hz. The error norms were calculated over $12\text{s} \leq t \leq 22\text{s}$.

of obtaining the higher time derivatives of the temperature data were discussed. It was stated that use of the first method (single filter) would produce a discontinuity in the inverse projection. The second method (double filter) provided a means by which the discontinuity was removed, enabling higher time derivatives of the temperature data. This is demonstrated by using data from run qCLOt3f200. Figure 7.14 shows the first and fifth time derivatives of the LCSR shifted temperature data. Figure 7.14(a) shows the discontinuity in the first time derivative when the single filter method is used. In addition to this discontinuity, the single filter method also allows too much noise to be passed into the derivatives. Figure 7.14(b) shows the signal-to-ratio (SNR) for the fifth derivative with the single filter method is approximately 1, whereas the SNR with the double filter method is approximately 4.

Figure 7.15 shows the resulting global time inverse method predictions using $N = 4$ for both the single and double filter methods. Both the inverse temperature and heat flux results for the single filter method produce a discontinuity in the inverse prediction. Further, the error norms for the single filter method are worse than the space-marching method. In contrast, the double filter method performs well; the temperature error norm is as good as the space-marching method ($e_T = 0.041$), and the heat flux error norm shows slight improvement over the space-marching method (0.134 vs. 0.0132). Therefore, for all subsequent results, only the double filter method is presented as the global time inverse results.

The global time inverse method was next applied to the same experimental runs tested with the space-marching method discussed earlier. Inverse results for runs qCLOt3f1200, qCHIt3f200, and qRHIt5f200 can be seen in Figures 7.16 – 7.18, and the corresponding error norms are tabulated in Table 7.1. Very little improvement (if any) is seen when comparing the

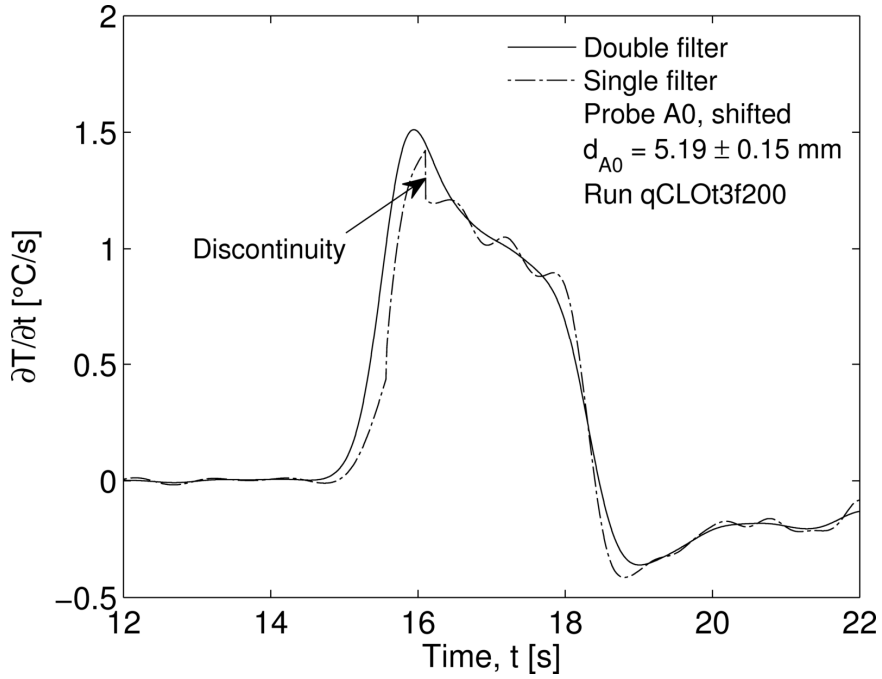

(a)

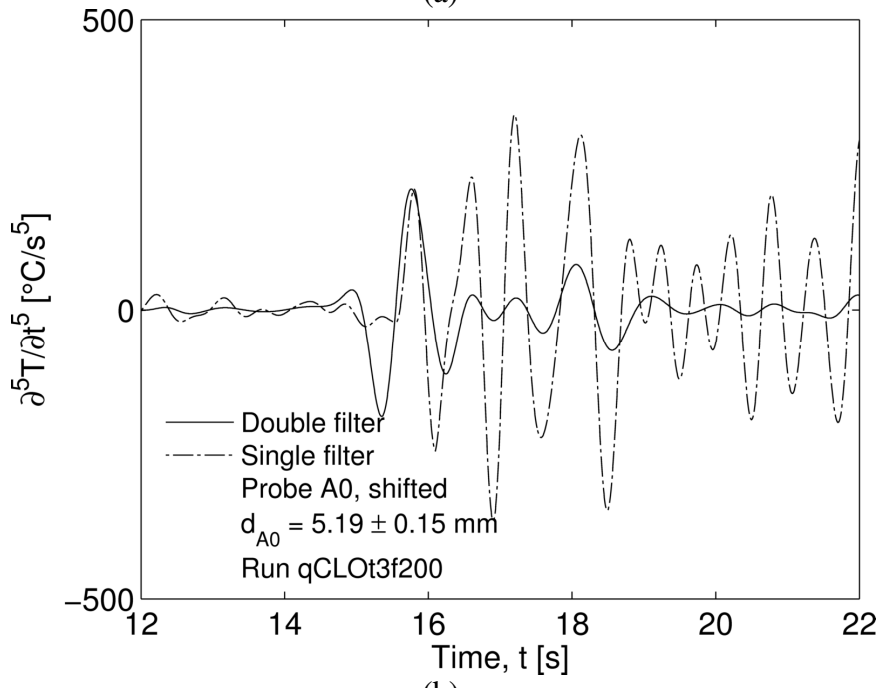

(b)

Figure 7.14: (a) First and (b) fifth time derivative of shifted temperature data from run qCLOt3f200 with f_c = 0.9 Hz.

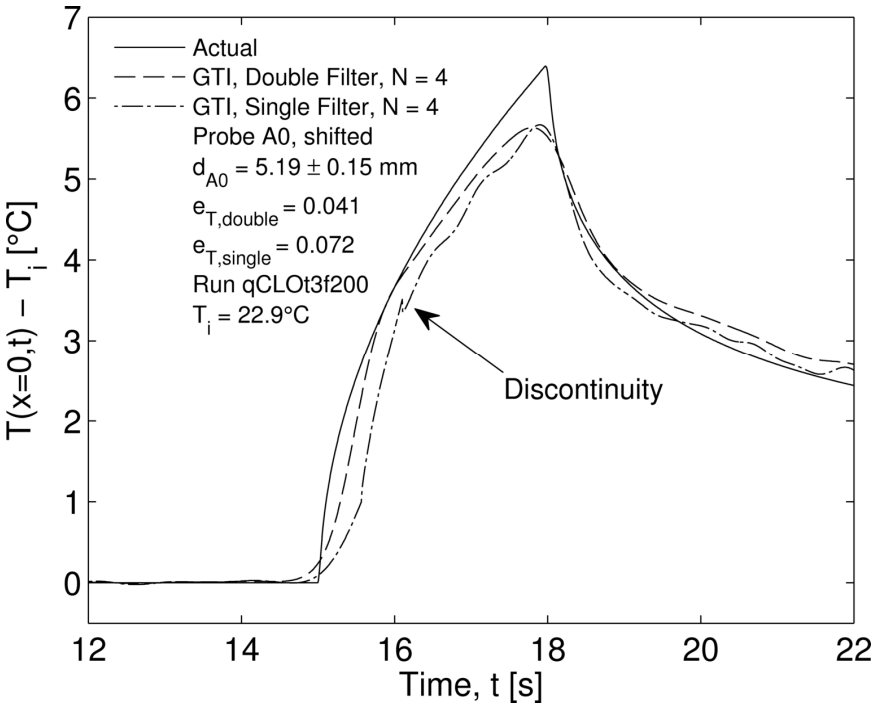

(a)

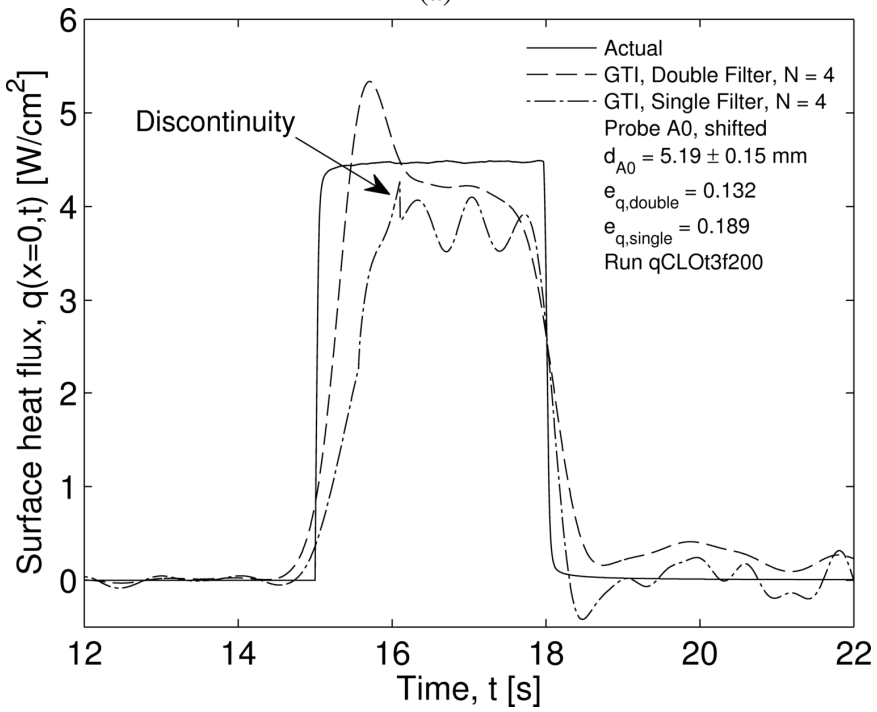

(b)

Figure 7.15: Global time inverse (a) temperature and (b) heat flux results using global time inverse method with $N = 4$ and $f_c = 0.9$ Hz for run qCLOt3f200. Discontinuity seen when single filter method of obtaining time derivatives is employed. The error norms were calculated over $12\text{s} \leq t \leq 22\text{s}$.

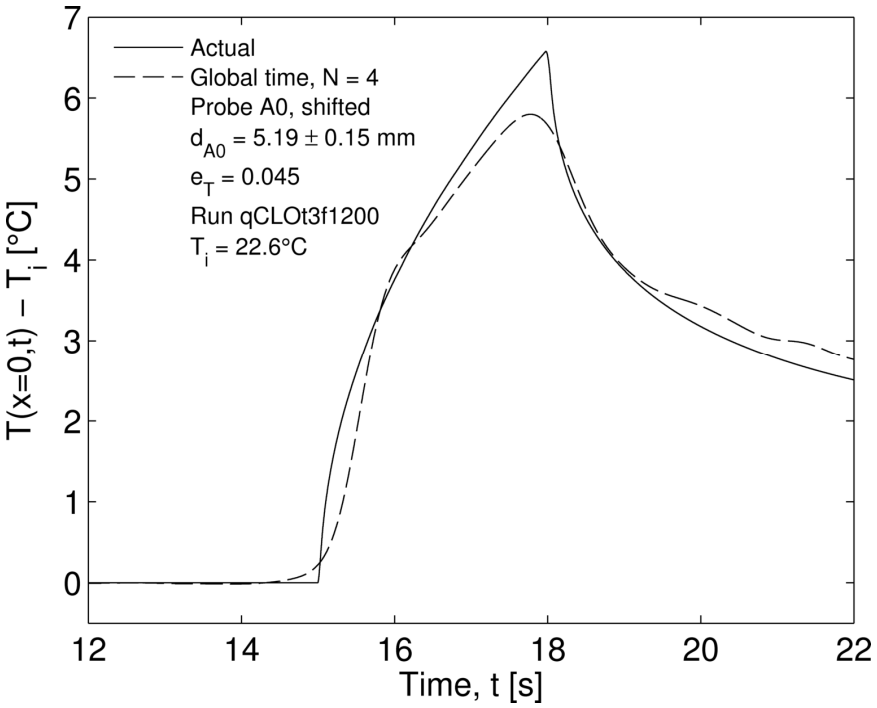

(a)

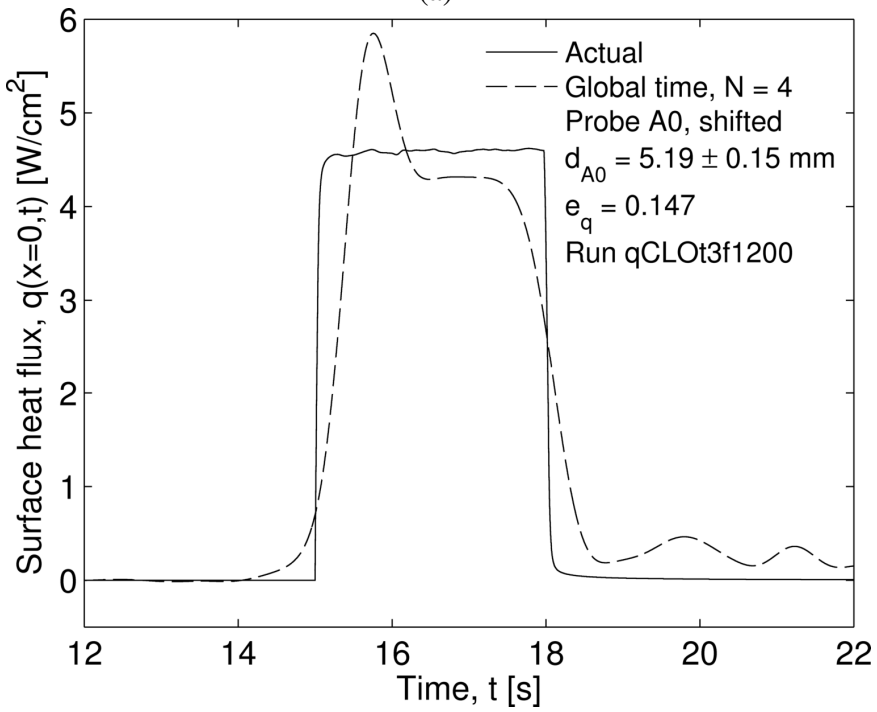

(b)

Figure 7.16: Effect of increased sampling rate on global time inverse method. Inverse (a) temperature and (b) heat flux results for run qCLOt3f1200 using global time inverse method with $N = 4$ and $f_c = 0.9$ Hz. The error norms were calculated over $12\text{s} \leq t \leq 22\text{s}$.

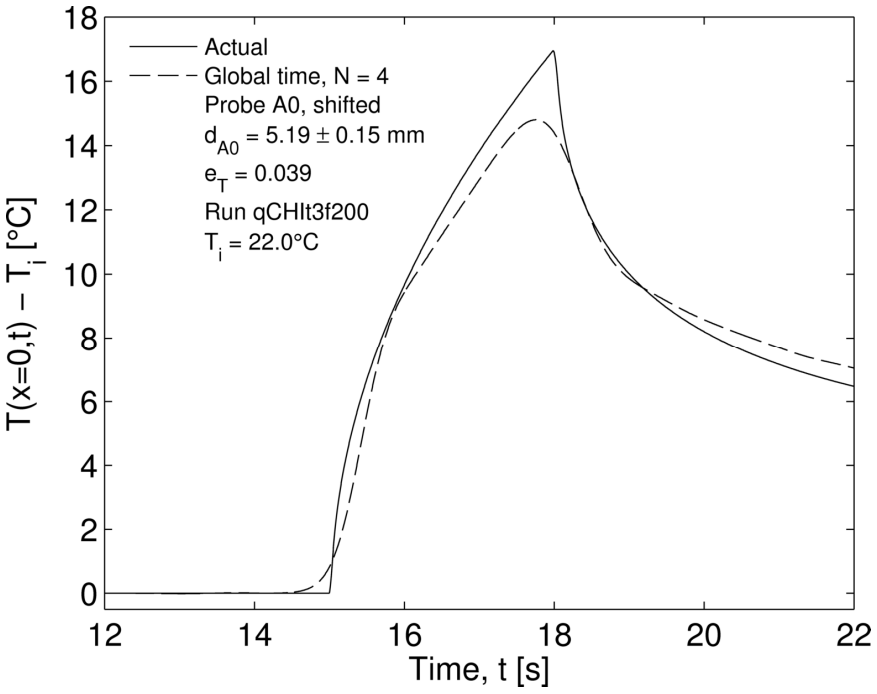

(a)

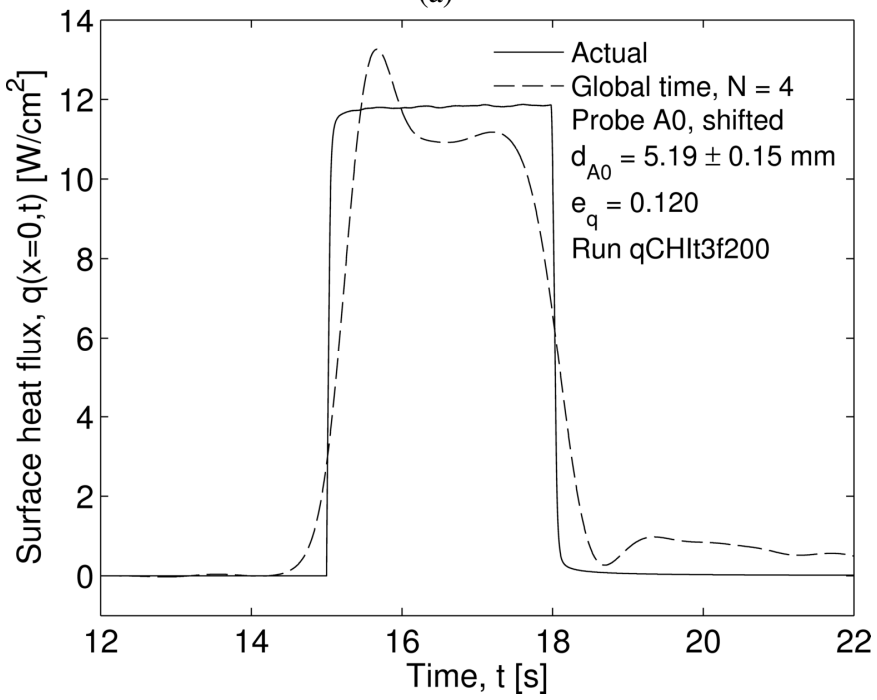

(b)

Figure 7.17: Global time inverse (a) temperature and (b) heat flux results using global time inverse method with $N = 4$ and $f_c = 0.9$ Hz for run qCHIt3f200. The error norms were calculated over $12\text{s} \leq t \leq 22\text{s}$.

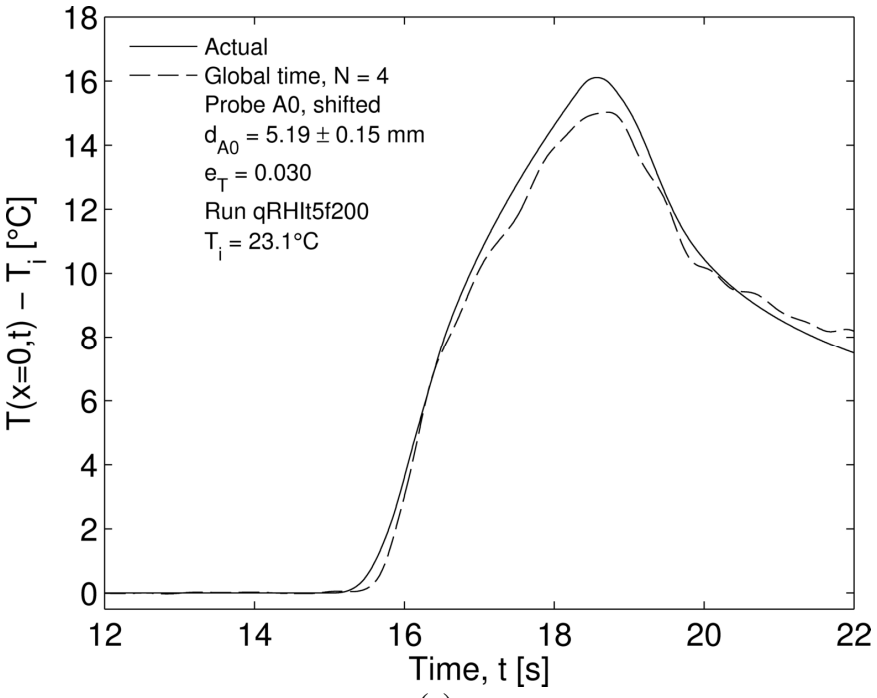

(a)

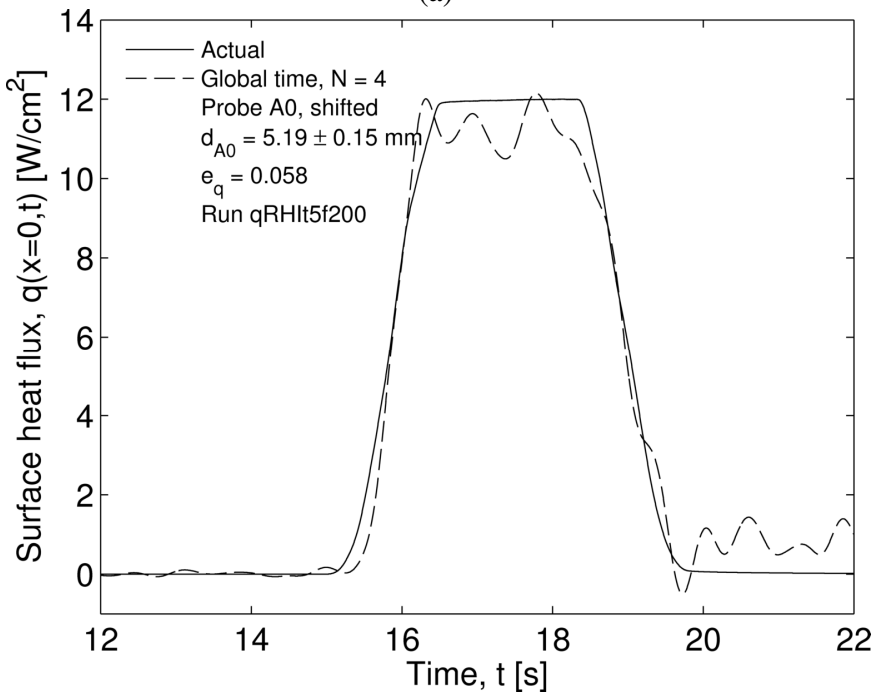

(b)

Figure 7.18: Global time inverse results for (a) temperature and (b) heat flux using data from run qRHIt3f200 with $N = 4$ and $f_c = 1.5$ Hz. The error norms were calculated over $12\text{s} \le t \le 22\text{s}$.

space-marching results with the global time results. This makes intuitive sense since both inverse methods are based on the same finite difference scheme in space. The advantage of the global time inverse method is that round-off can be avoided while increasing accuracy by using higher-time derivatives in the inverse projection. However, the accuracy and sampling rates of the measured temperatures with the available data acquisition system are not sufficient for extracting accurate higher-time derivatives that are needed. Table 7.2 shows that there is no gain in accuracy of the global time inverse method for $N>3$. Recall that in Chapter 3 it was demonstrated when accurate required higher-time derivatives of the data are available, an increase of N from 4 to 7 resulted in significant improvement of the inverse predictions.

In addition to the nominal value of the inverse predictions, it is also important to account for uncertainty in the inverse method. The Appendix outlines the derivation for the uncertainty in both the surface heat flux due to heater resistance, measured heat voltage, and surface area. The Appendix also outlines the derivation for uncertainty in the global time inverse method due to sensor depth, material properties, sensor depth, temperature data and its temporal derivatives, and heat flux data and its temporal derivatives. Figure 7.19 shows the inverse results with uncertainty for run qRHIt5f200. The actual surface temperature is seen to nearly lie inside the uncertainty band of the global time method over the entire time domain. However, significant differences are still seen near power on and peak temperature. The uncertainty band of the actual surface heat flux is seen to overlap the uncertainty band of the global time method for a significant amount of time. During the time of peak flux, the global time uncertainty band oscillates around the actual surface flux. However, significant differences between actual and inverse are still seen after the source is deactivated.

Table 7.2: Global time inverse method error norms for run qCLOt3f200

N	e_T	e_q
1	0.04813	0.18475
2	0.03709	0.10150
3	0.03530	0.10028
4	0.03475	0.09996
5	0.03451	0.09983
6	0.03439	0.09977
7	0.03431	0.09973
8	0.03427	0.09971
9	0.03423	0.09970
10	0.03421	0.09969
11	0.03421	0.09969
12	0.03418	0.09968

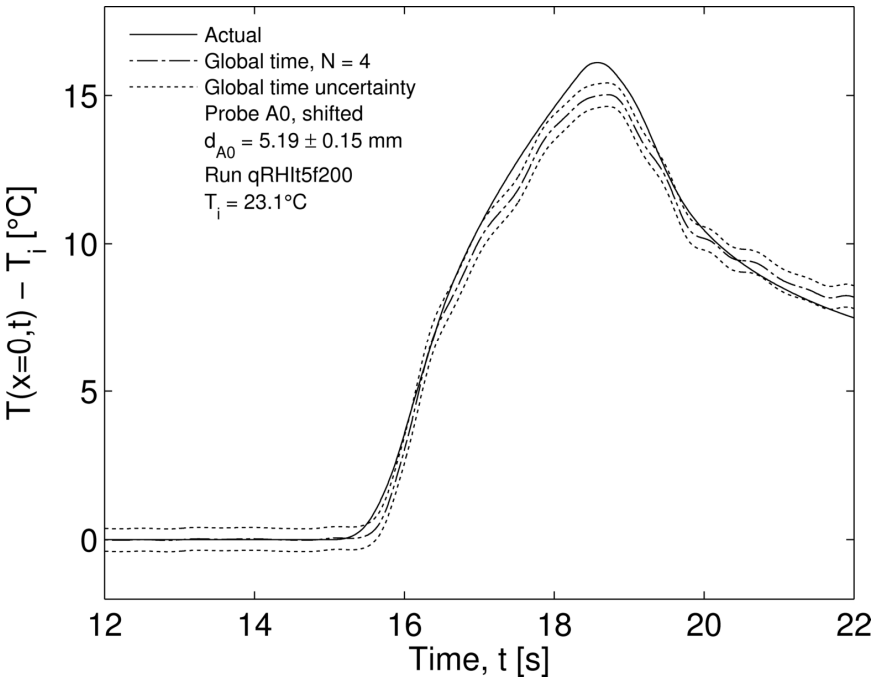

(a)

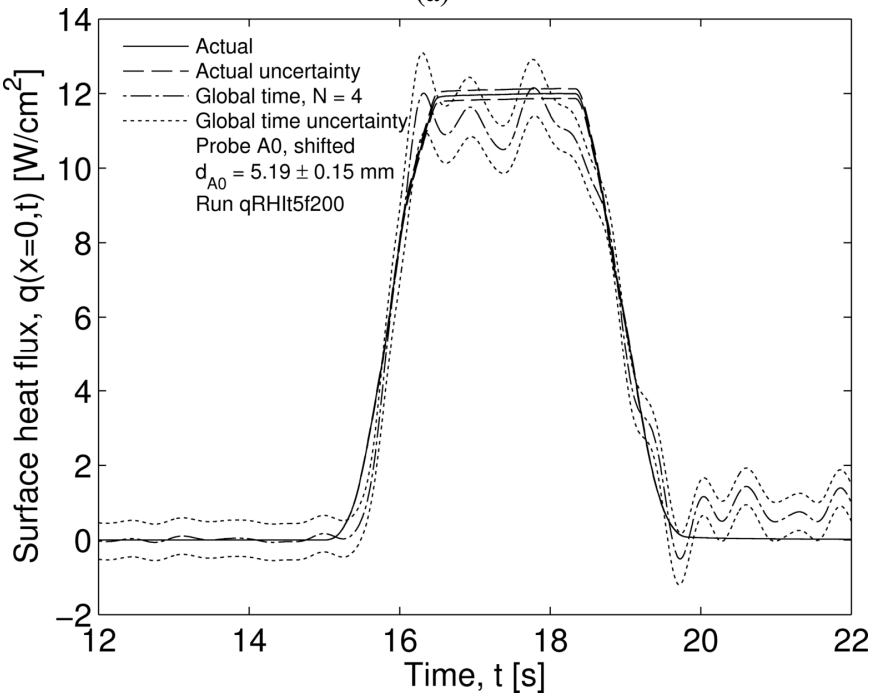

(b)

Figure 7.19: Uncertainty in global time inverse results for (a) temperature and (b) heat flux using data from run qRHIt3f200 with $N = 4$ and $f_c = 1.5$ Hz. The error norms were calculated over 12s $\leq t \leq$ 22s.

Calibration Integral Inverse Method

In addition to the inverse methods presented in Chapters 2 and 3, the recently developed calibration integral method presented in [22] will also be investigated herein. The novel result of the calibration integral method is the Volterra equation of the first kind

$$\int_{u=0}^{t} q_{run}(0,u)T_{cal}(d,t-u)du = \int_{u=0}^{t} q_{cal}(0,u)T_{run}(d,t-u)du, \tag{7.14}$$

where $q_{cal}(0,t)$ and $T_{cal}(d,t)$ are the known surface heat flux and measured in-depth temperature response for a calibration run, and $q_{run}(0,t)$ and $T_{run}(d,t)$ are the surface heat flux and measured in-depth temperature response for a second "real run." Eq. (7.15) is valid for the case of one-dimensional conduction into a semi-infinite medium where the sample is initially at some uniform temperature. Frankel et al. also showed that Eq. (7.15) is still valid for thermocouple data, T_{cal} and T_{run}, without accounting for the thermocouple sensor characteristics.

It should be noted that temperatures in Eq. (7.15) should be viewed as excess temperature above the initial condition – i.e., a trivial initial condition of $T(x, t=0) = 0$ is assumed. The unknown in Eq. (7.15) is $q_{run}(0,t)$. Therefore, Eq. (7.15) can be cast in a more familiar form such that

$$\int_{u=0}^{t} q_{run}(0,u)K(d,t-u)du = f(t), \tag{7.15}$$

where

$$K(d,t) = T_{cal}(d,t), \tag{7.16}$$

$$f(t) = \int_{u=0}^{t} q_{cal}(0,u)T_{run}(d,t-u)du. \tag{7.17}$$

Despite the elegant presentation, Eq. (7.16) is very difficult to solve. This is because Volterra integrals of the first kind are well-known to be ill-posed [68]. Therefore, some form of regularization must be utilized. For the results presented herein, the Gaussian low-pass filter of Eq. (7.3) will be utilized. Additionally, classical quadrature methods for Volterra integrals of the first kind rely on the assumption that $K(d,0) \neq 0$. However, the physics of conduction dictate that excess temperature $T(d,t) = 0$ for $d > 0$ and $t < t_p$. Therefore, $q_{run}(0,t)$ must be solved for at $t + t_p$. This is made clear by numerically integrating Eq. (7.16) such that

$$\sum_{j=0}^{m} w_j q_{run}(0,t_j) K(d,t_m - t_j) = f(t_m), \quad m = 0,1,2,...,M, \tag{7.18}$$

where w_j are the quadrature weights. The time step Δt and p^* are now defined such that $t_p = p^* \Delta t$ and write Eq. (7.19) for $m = p^*$ such that

$$w_0 q_{run}(0,0) K(d,t_p) + \sum_{j=1}^{p^*} w_j q_{run}(0,t_j) K(d,t_p - t_j) = f(t_p), \tag{7.19}$$

which reduces to

$$q_{run}(0,0) = \frac{f(t_p)}{w_0 K(d,t_p)}. \tag{7.20}$$

Therefore, a straightforward calculation of $q_{run}(0,t)$ can be made such that

$$q_{run}(0,t_m - t_p) = \frac{f(t_m) - \sum_{j=0}^{m-p^*-1} w_j q_{run}(0,t_j) K(d,t_m - t_j)}{w_{m-p^*} K(d,t_p)}, \qquad m = p^*, p^*+1,...,M, \tag{7.21}$$

where a negative integer in the summation limit sets the summation to zero. This leads to a solution procedure where $q_{run}(0,t)$ can be found one time step at a time, and this technique will be compared to the space-marching and global time methods previously discussed.

One additional note here is that Eq. (7.15) can be differentiated in time to yield (via Leibniz' rule [67])

$$\int_{u=0}^{t} q_{run}(0,u)\frac{dT_{cal}}{dt}(d,t-u)du = \int_{u=0}^{t} q_{cal}(0,u)\frac{dT_{run}}{dt}(d,t-u)du \tag{7.22}$$

Higher time derivatives of Eq. (7.15) are also possible. Since the higher-time derivatives of temperature have been shown to contain physical information for diffusion, it is possible that using the time derivatives of temperature for surface heat flux prediction, rather than temperature itself, might be advantageous. The resulting numerical technique is identical to Eq. (7.22), except that the definition of $f(t)$ and the kernel is changed to reflect the derivatives. Therefore, the effect of using the time derivatives of temperature will also be investigated below.

One of the main advantages to using the calibration integral method is that the user is not required to have knowledge of thermal properties. However, if the thermal properties are known, the surface temperature history can be obtained via [2]

$$T(x=0,t) = \sqrt{\frac{1}{\rho Ck\pi}}\int_{u=0}^{t} q(0,u)\frac{du}{\sqrt{t-u}}. \tag{7.23}$$

For the sake of comparison with the space-marching and global time methods, Eq. (7.24) is used below to obtain the surface temperature.

In preliminary analysis, a constant heat flux at the highest possible power level was found to provide the best calibration data. Therefore, run qCHIt10f200 was used as the calibration run for all "real" runs using a sampling rate of 200 Hz. As a first investigation, data from run qCLOt3f200 was used as the real run. Figure 7.20(a) shows actual surface flux for both the calibration and real runs. Figure 7.20(b) shows the unshifted thermocouple temperature histories for both the calibration and real runs. Figure 7.21 shows the first and second temporal

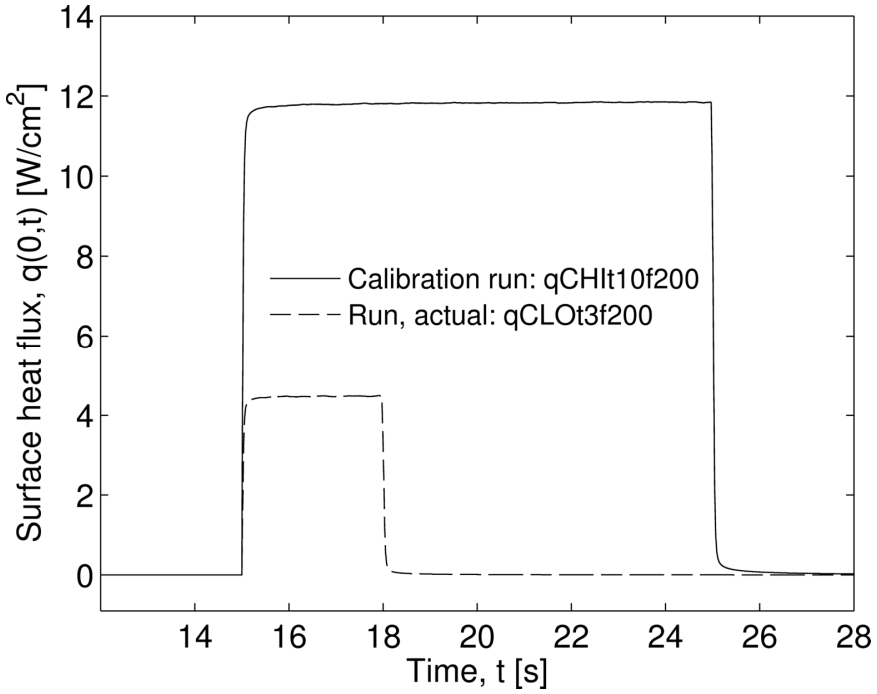

(a)

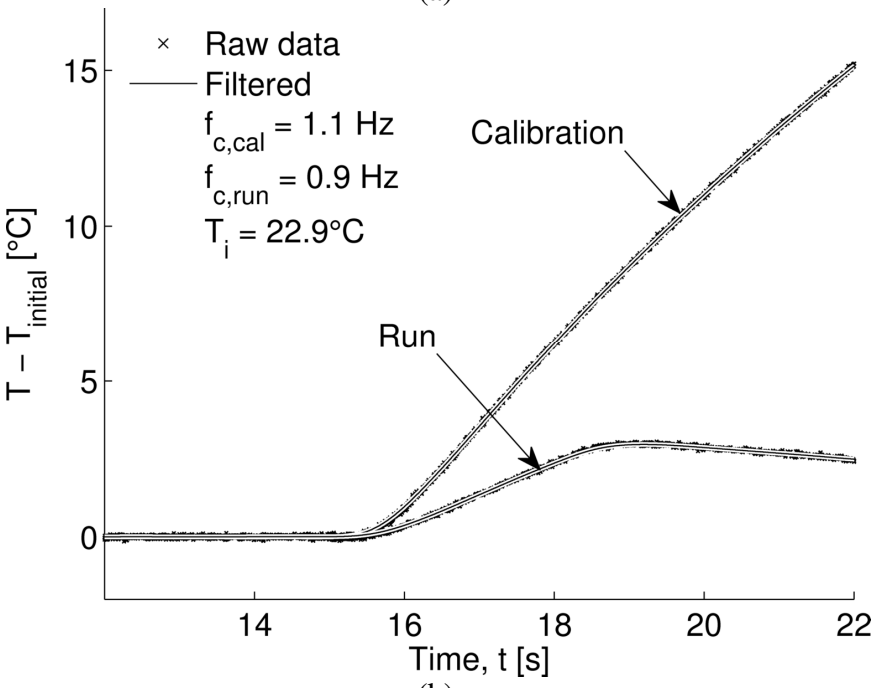

(b)

Figure 7.20: Calibration integral method data for calibration qCHIt10f200 and real run qCLOt3f200. (a) Actual calibration and real run heat flux and (b) calibration and real run temperature histories.

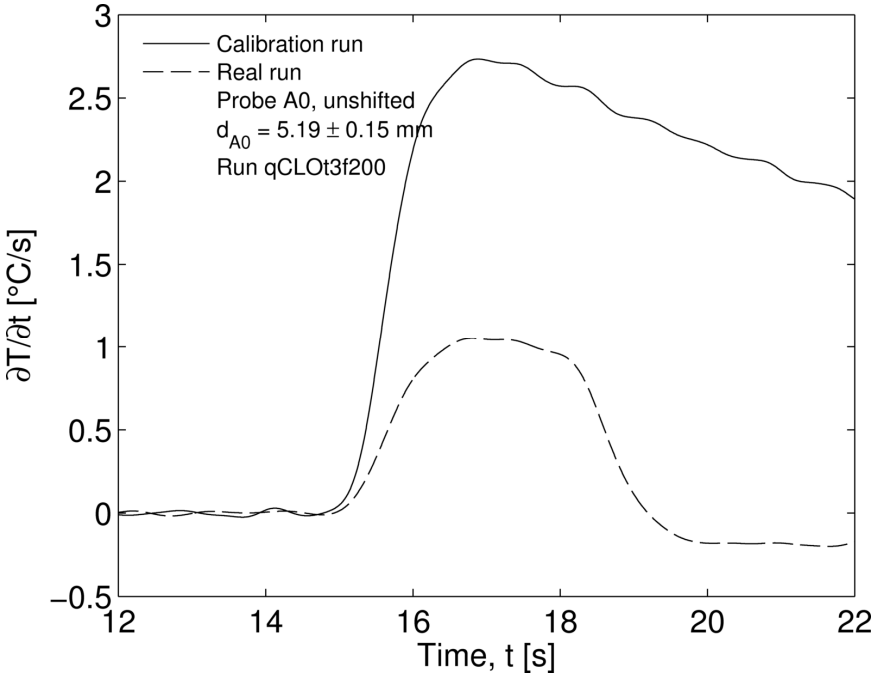

(a)

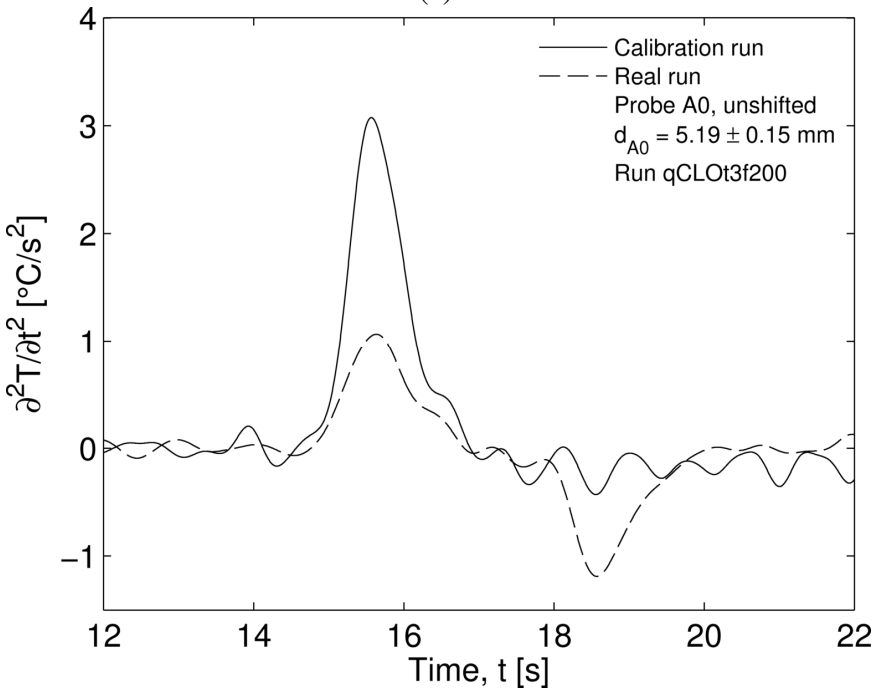

(b)

Figure 7.21: (a) First and (b) second temporal derivative of temperature data from calibration run qCHIt10f200 and real run qCLOt3f200. Derivatives were taken using Gaussian filter function.

derivatives (using the Gaussian filter function) for both the unshifted calibration and real run data. The resulting inverse predictions for the surface temperature and heat flux can be seen in Figure 7.22.

A strong case was made in Chapter 4 for the amount of physical information contained in higher time derivatives of temperature. Therefore, one might expect the highest meaningful temporal derivative of temperature to produce the best inverse results. However, this is not the case. In reality, the second derivative produced highly inaccurate results. The inverse results using temperature and heating rate were similar in accuracy and better than those using the second derivative. It is suspected that the reason for this is similar to the reason why the global time method was limited to $N = 4$. Namely, as the higher temporal derivatives of the Gaussian filter function are taken, the signal-to-noise ratio degrades. This is seen to be the case in Figure 7.20(b) and Figure 7.21. The SNR of the temperature data is strong. The SNR of the heating rate is seen to be perhaps slightly less than for temperature. However, the SNR of the second derivative of temperature is significantly lower than temperature or heating rate. Therefore, it is not surprising that the resulting inverse predictions made exclusively with the second derivative data are less accurate than inverse predictions made with temperature or heating rate data.

In order to compare the accuracy of the calibration integral method with that of the space-marching and global time techniques, analysis was conducted on the same four runs: qCLOt3f200 (discussed above), qCLOt3f1200, qCHIt3f200, and qCLOt5f200. The inverse results can be seen in Figures 7.23 – 7.25, and the corresponding error norms are tabulated in Table 7.1 for using temperature data as the kernel. In contrast to the global time and space-marching methods, the accuracy of the calibration integral method slightly *improved* as the

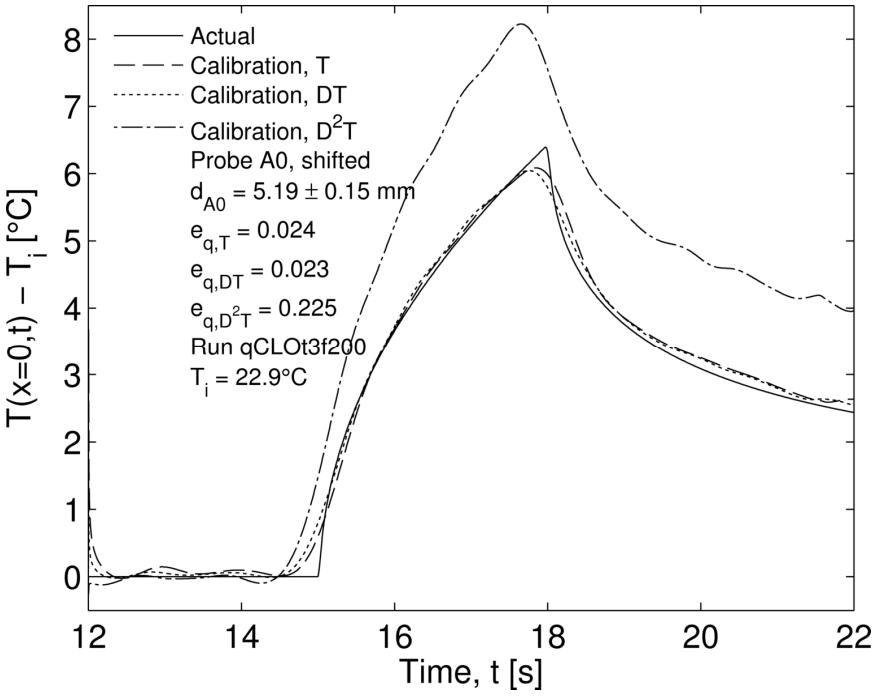

(a)

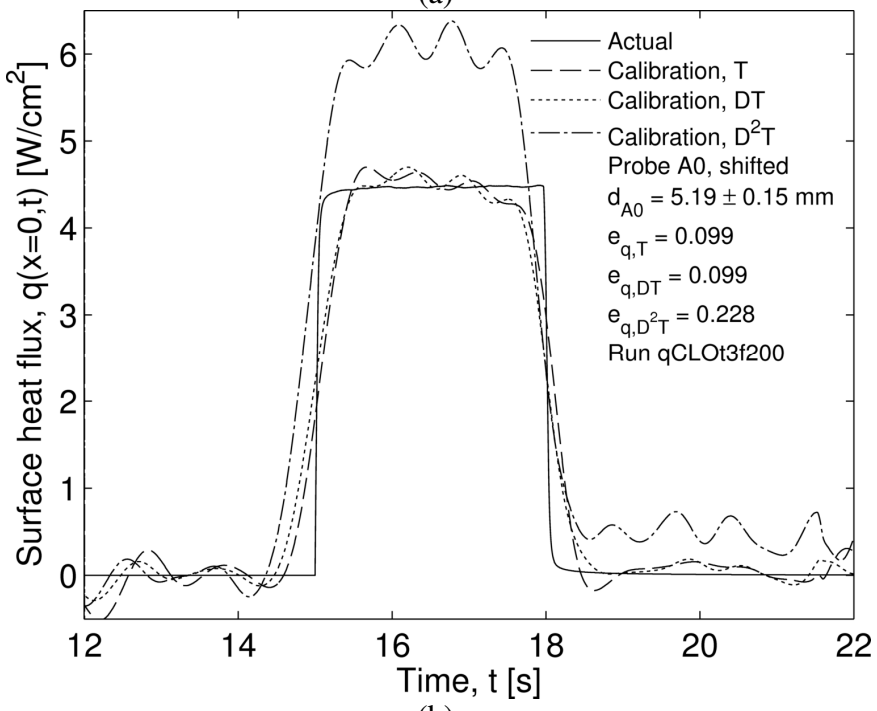

(b)

Figure 7.22: Calibration integral method inverse results for (a) temperature and (b) heat flux using calibration run qCHIt10f200 (f_c = 1.1 Hz) and real run qCLOt3f200 (f_c = 0.9 Hz). The error norms were calculated over 12s ≤ t ≤ 22s.

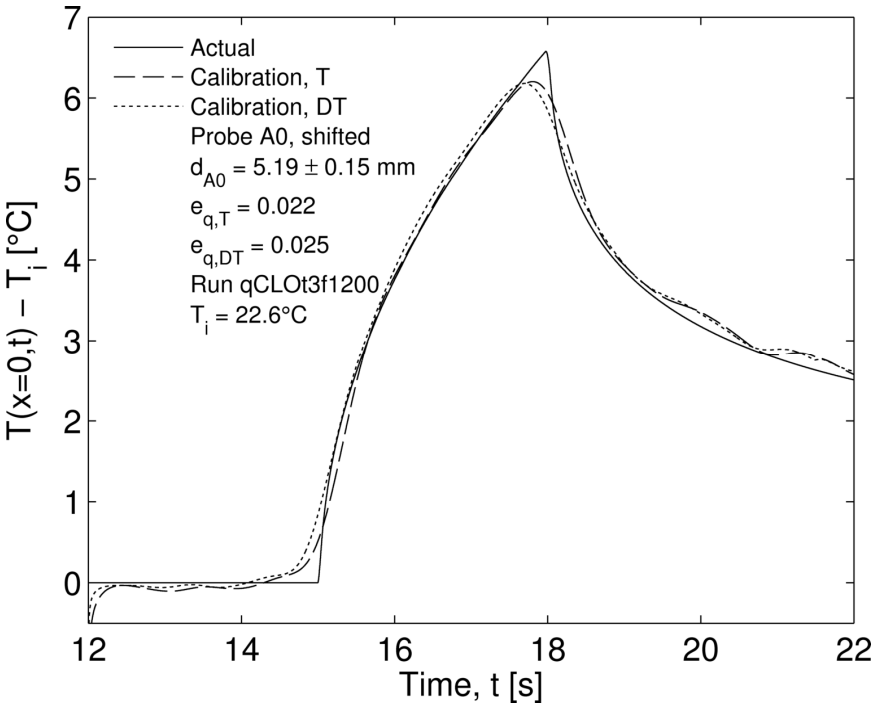

(a)

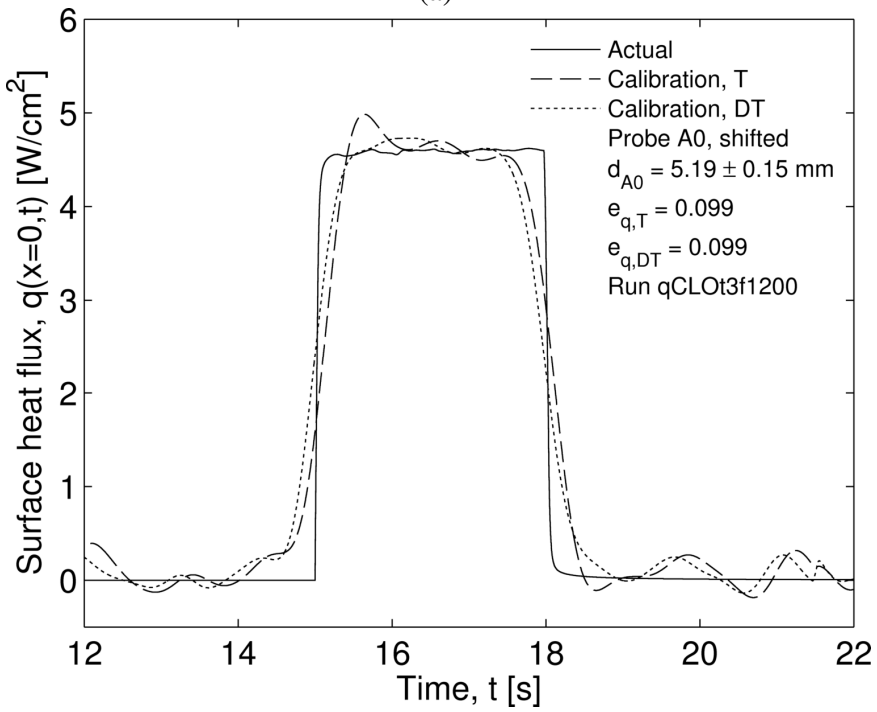

(b)

Figure 7.23: Calibration integral method inverse results for (a) temperature and (b) heat flux using calibration run qCHIt10f1200 (f_c = 0.9 Hz) and real run qCLOt3f1200 (f_c = 0.9 Hz). The error norms were calculated over 12s ≤ t ≤ 22s.

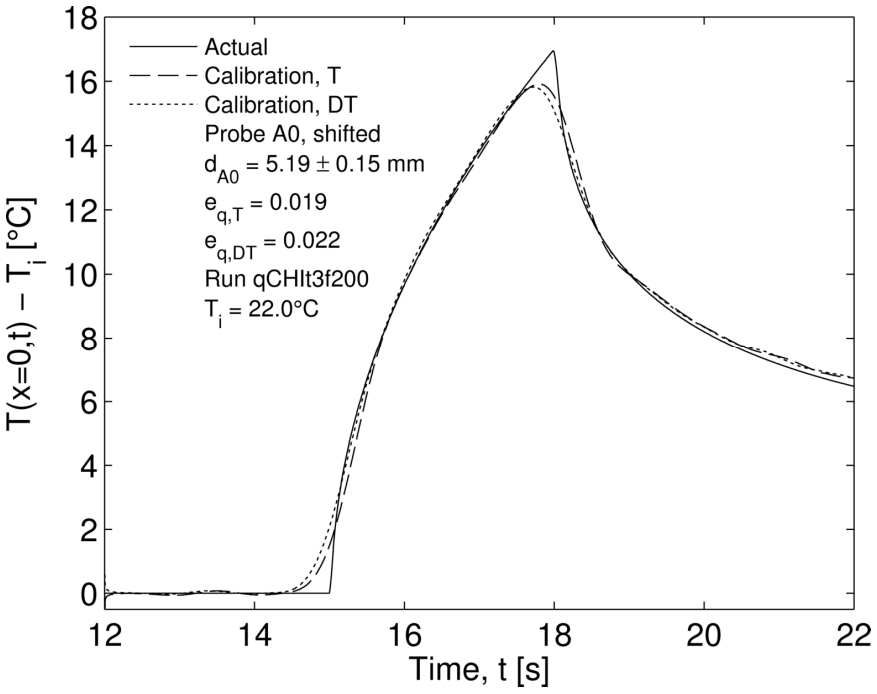

(a)

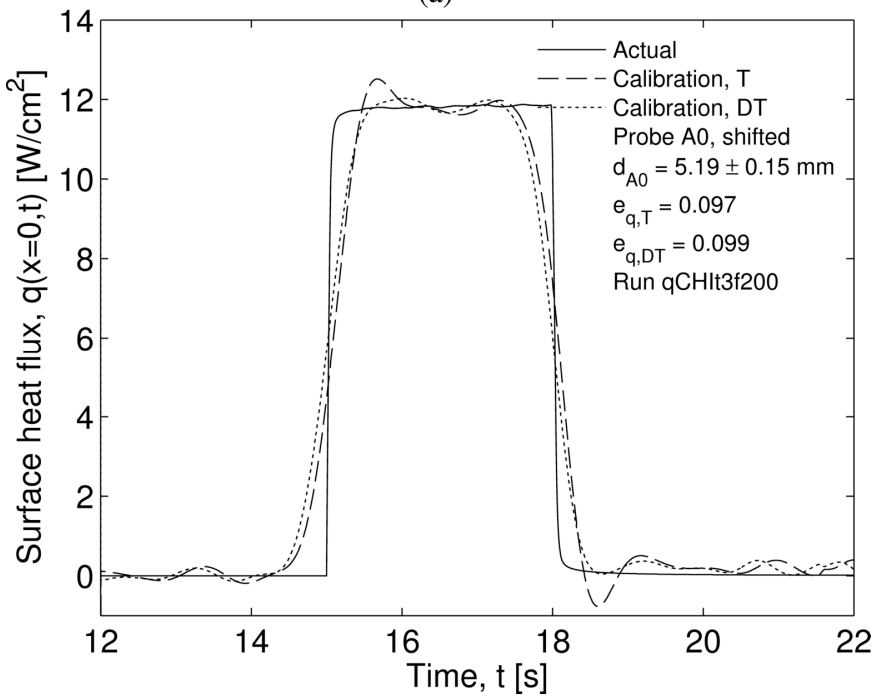

(b)

Figure 7.24: Calibration integral method inverse results for (a) temperature and (b) heat flux using calibration run qCHIt10f200 (f_c = 1.1 Hz) and real run qCHIt3f200 (f_c = 0.9 Hz). The error norms were calculated over 12s $\leq t \leq$ 22s.

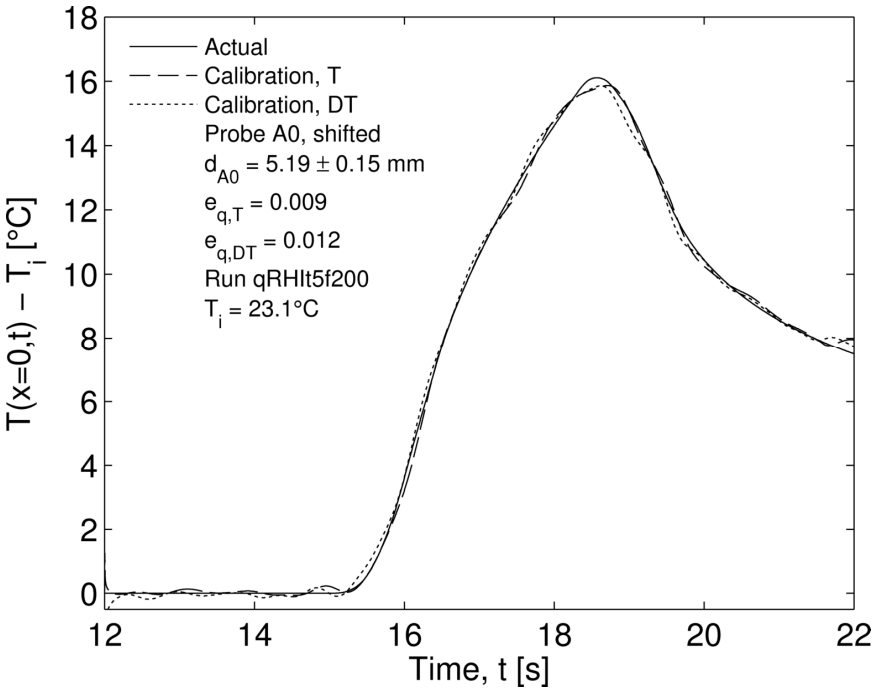

(a)

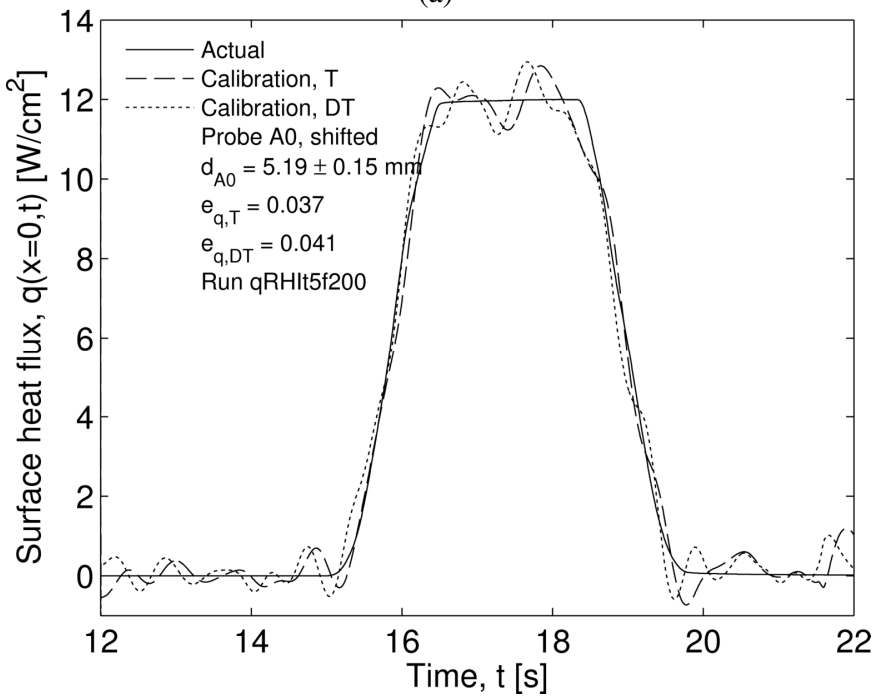

(b)

Figure 7.25: Calibration integral method inverse results for (a) temperature and (b) heat flux using calibration run qCHIt10f200 (f_c = 1.1 Hz) and real run qCHIt3f200 (f_c = 1.5 Hz). The error norms were calculated over 12s ≤ t ≤ 22s.

sampling rate was increased (run qCLOt3f1200). This significant result suggests a well-posed procedure. It should also be noted that the error norms decreased by almost one half from when the surface flux boundary condition was switched from a step change to a linear increase/decrease.

In all runs investigated, the calibration integral approach was much more accurate than either the space-marching or the global-time method. Additionally, the accuracy of the integral is heavily dependent on the numerical algorithm employed to evaluate it. The technique employed herein was a crude numerical procedure which solves for the surface flux using physical insight and numerical "brute force." A more elegant method of numerically evaluating the calibration integral could improve the already impressive accuracy of this approach.

7.3 Chapter Summary

This chapter provided experimental validation using one-probe analysis for the space-marching and global time inverse methods presented in Chapters 2 and 3, respectively, as well as for the newly developed calibration integral method. The space-marching and global time methods approach the inverse problem with a traditional point of view; they require accurate knowledge of the sensor depth, thermal properties, and sensor characteristics. In contrast, the calibration integral method does not require this information, but instead uses a preliminary experimental run as calibration data. Both the space-marching and global time methods predicted the surface temperature and heat flux with similar accuracy. The global time method could be improved if more accurate higher-time derivatives could be obtained. The calibration integral method produces surface temperature error norms that are an astounding 41% - 70% more accurate the space-marching and global time methods; heat flux results are 19%-36% more

accurate. These results are highly encouraging and suggest future efforts should be dedicated to the further development of more generalized (i.e., finite width, higher dimensions, etc.) calibration integral inverse techniques.

Chapter 8: Experimental Results with Two-Probe Analysis

The goal of this chapter is to experimentally validate the inverse heat conduction methods discussed in Chapters 2 and 3 using data from two probes at different depths. The inverse predictions presented in Chapter 7 relied on the assumption of a semi-infinite medium and used data from one probe to project to the surface. By using data from two probes at different depths, the approach used in this chapter no longer requires the semi-infinite medium assumption and is valid for finite width domains. At the time of this writing, a finite width domain parallel to the semi-infinite calibration integral method presented in Chapter 7 is still under development. Therefore, the space-marching and global time methods are the only inverse methods presented herein.

8.1 Two-Probe Data Analysis Procedure

As noted in Chapter 7, the global time and space-marching inverse methods require both embedded temperature and heat flux measurements in order to project to the surface. The sandwich experiment presented in Chapter 5 can be used to generate embedded temperature data, but heat flux data must be obtained through some form of post-processing. Chapter 7 utilized an integral relationship between the embedded heating rate and heat flux. However, this relationship is only valid for the case of a semi-infinite medium – i.e., until the thermal front reaches the back wall of the sample. While this is useful, inverse predictions for the sandwich experiment were limited to $t - t_{on} \leq 7$s. Therefore, an alternative method of calculating the embedded heat flux is required if inverse predictions are desired for $t - t_{on} > 7$s.

This chapter utilizes data from two embedded probes at different depths to calculate the embedded heat flux histories. A flow chart of the preprocessing used with the two-probe analysis can be seen in Figure 8.1. Using the procedure outlined in Chapters 4 and 7, embedded temperature data was shifted in time for the corresponding sensor characteristics. The shifted temperature data were then passed to a direct, finite difference code between the two embedded probes to calculate the embedded heat flux at both probe sites. The implicit-in-time approach of Patankar [50] was used to construct the code. Higher-time derivatives of temperature and heat flux data were obtained as in Chapter 7 using the Gaussian filter. Finally, the shifted temperature data and calculated embedded heat flux (with corresponding derivatives) from the "A" probe (closest to the surface) was passed to both the space-marching and global time inverse methods.

8.2 Two-Probe Analysis of Experimental Data

Chapter 7 demonstrated the inverse methods produced the best results using data with the highest signal-to-noise ratio. It was also demonstrated that a linearly increased (ramped) surface heat flux was more accurately predicted than the case of a step change in flux. The two experimental runs investigated in Chapter 7 which corresponded to these conditions were qCHIt3f200 and qRHIt5f200. To facilitate comparison of the two-probe analysis with the one-probe analysis, data from these two runs will first be analyzed with the two-probe technique.

Demonstration of Two-Probe Analysis Technique

Figure 8.2(a) shows the raw, filtered, and shifted temperature data for probes A0 and B0 for run qCHIt3f200. Probe B0 was chosen as the second probe since it is healthy and it is along the centerline of the sample. Using the technique and logic outlined in Chapter 7, the cutoff frequencies used here were $f_{c,A0}$ = 0.9 Hz and $f_{c,B0}$ = 1.1 Hz. The filtered, shifted temperature

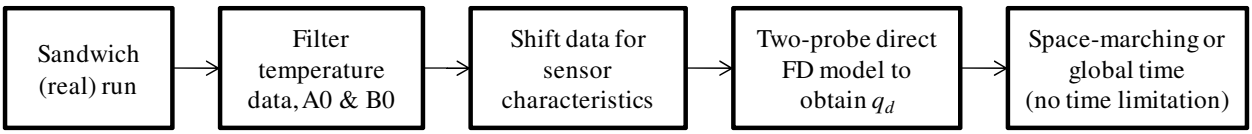

Figure 8.1: Flow chart for preprocessing of data for use in two-probe inverse analysis.

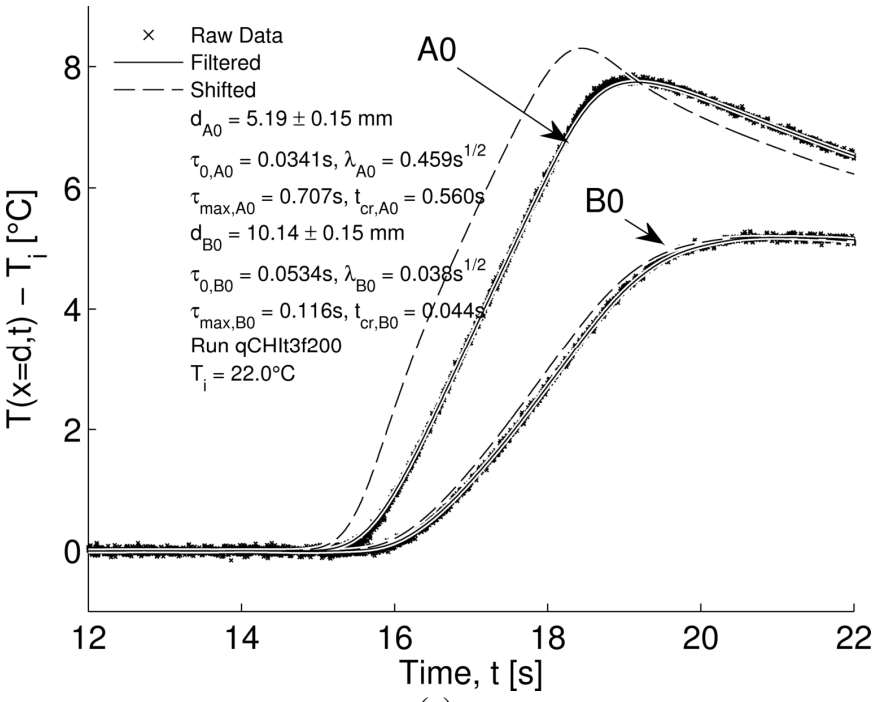

(a)

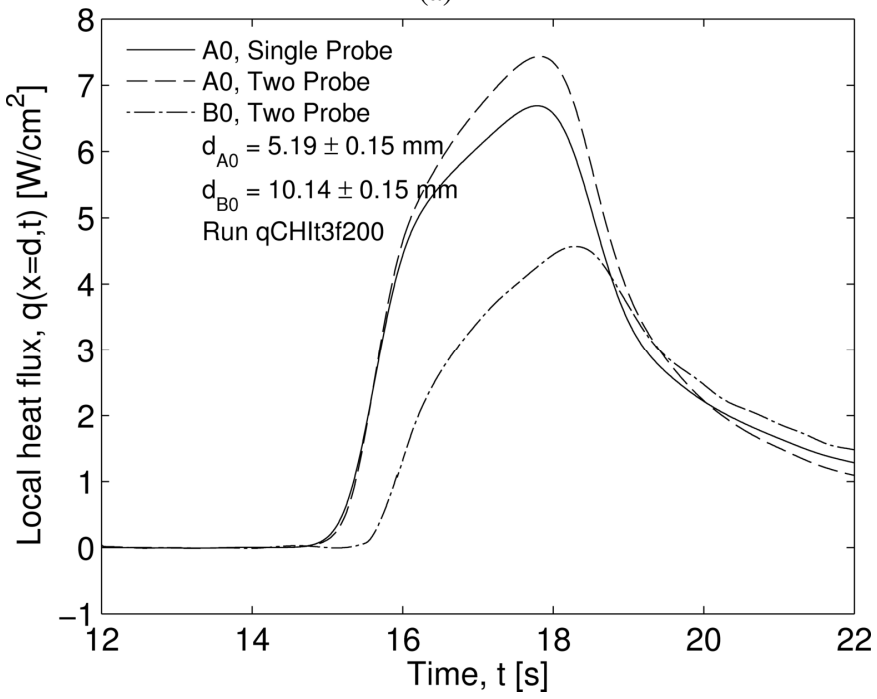

(b)

Figure 8.2: Inputs for inverse problem using data from run qCHIt3f200. (a) Raw, filtered, and shifted temperature data for both probes and (b) local heat flux at both probe sites using the single- and two-probe approach. Cutoff frequencies used were $f_{c,A0}$ = 0.9 Hz and $f_{c,B0}$ = 1.1 Hz.

data from both probes were then passed to the direct FD model, and the embedded heat flux histories were calculated at both probe sites shown in Figure 8.2(b), and the resulting inverse surface temperature and heat flux predictions can be seen in Figure 8.3. As in Chapter 7, the space-marching and global time inverse methods produce graphically identical results. Again, this is counter-intuitive. Chapter 3 demonstrated the high level of accuracy achievable with the global time method. If it were possible to resolve the needed higher-order time derivatives of the data accurately, then the global time method would be more accurate than the space-marching method. Nevertheless, both the space-marching and global time inverse methods produce excellent results; after the initial Gibbs' spike in the predicted heat flux, the nominal value of peak flux is predicted ± 2% of the actual surface flux.

The second experimental run investigated with the two-probe analysis was run qRHIt5f200. The embedded temperature and heat flux data can be seen in Figure 8.4, and the resulting inverse projections can be seen in Figure 8.5. Cutoff frequencies used for this run were $f_{c,A0}$ = 1.5 Hz and $f_{c,B0}$ = 1.1 Hz. Both the space-marching and global time inverse methods are seen to capture the transient behavior of the surface temperature and heat flux. Excellent agreement is seen between the actual surface condition and the inverse predicted history. As in the one-probe analysis, the two-probe inverse methods are seen to be much more accurate when predicting linear changes in heat flux rather than a step change. Comparing the ramped surface heat flux to the step change in flux, the error norm for the global time surface temperature decreased by 50% (0.030 to 0.015), and the surface heat flux error norm decreased by 62% (0.117 to 0.045). This behavior is mainly attributed to the Gaussian filter which smooths out

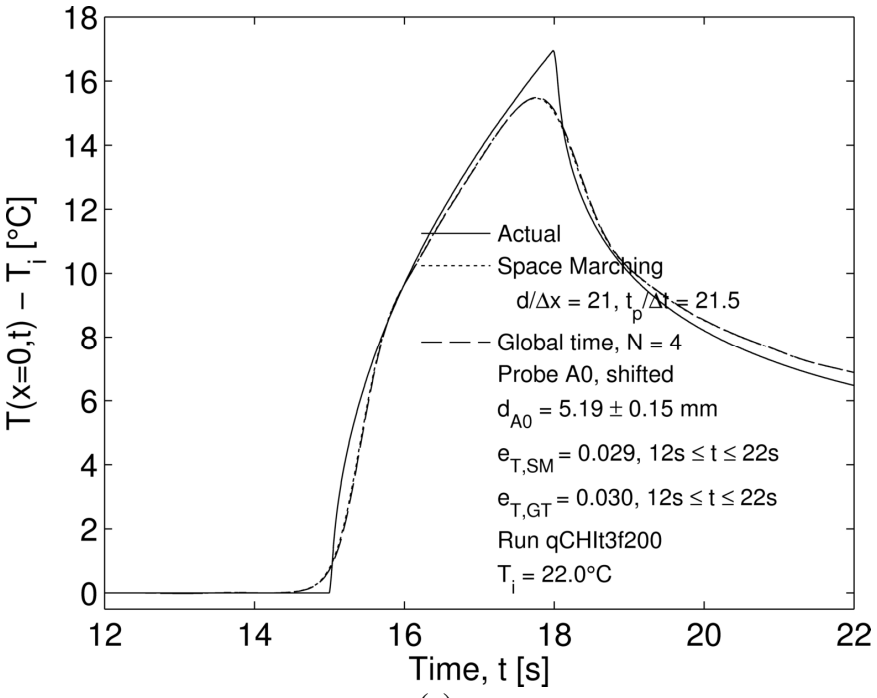

(a)

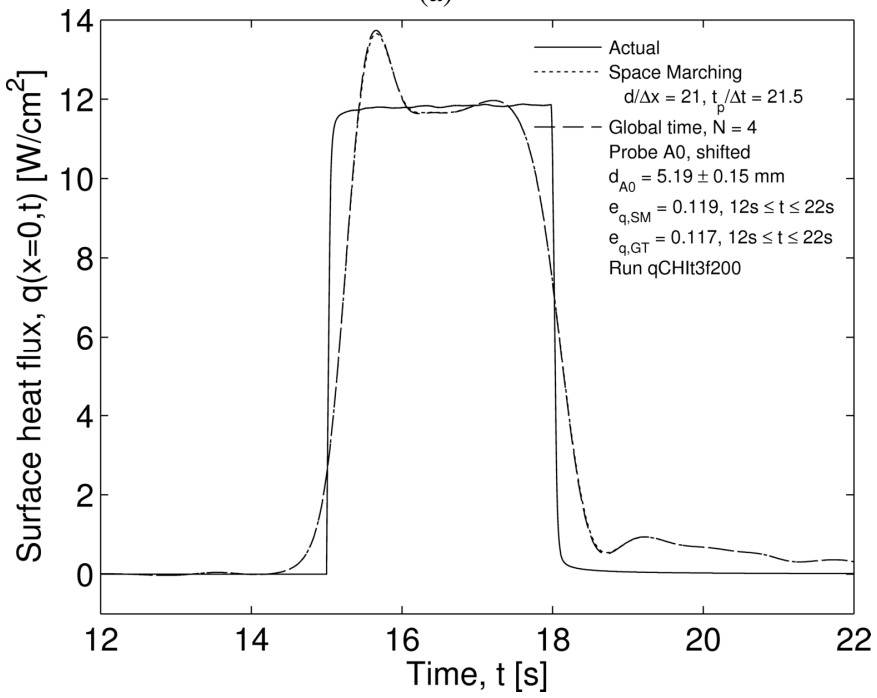

(b)

Figure 8.3: Two-probe inverse results for surface (a) temperature and (b) heat flux. Data used from run qCHIt3f200 seen in Figure 8.2.

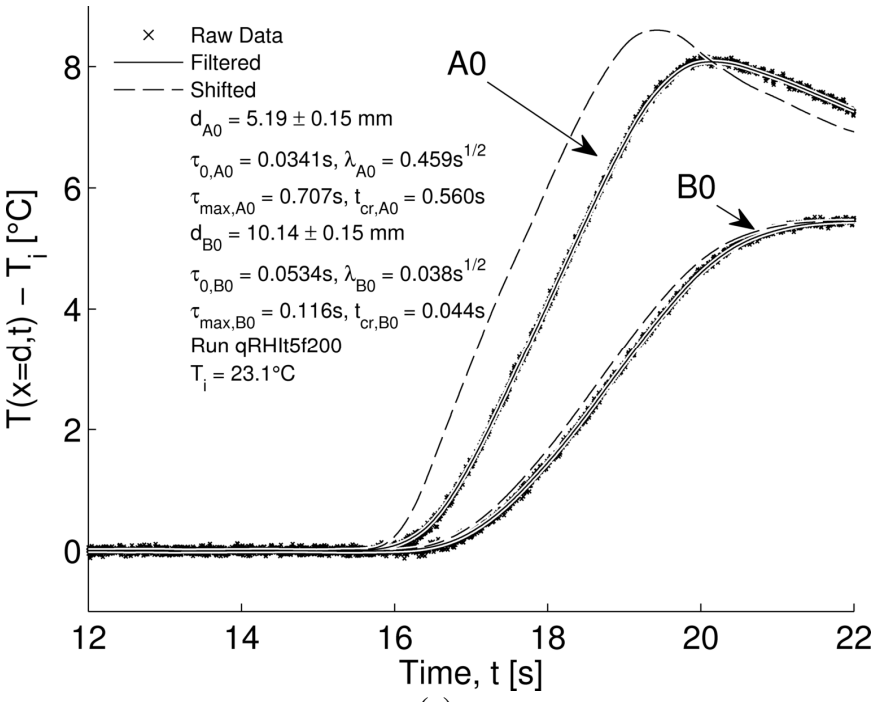

(a)

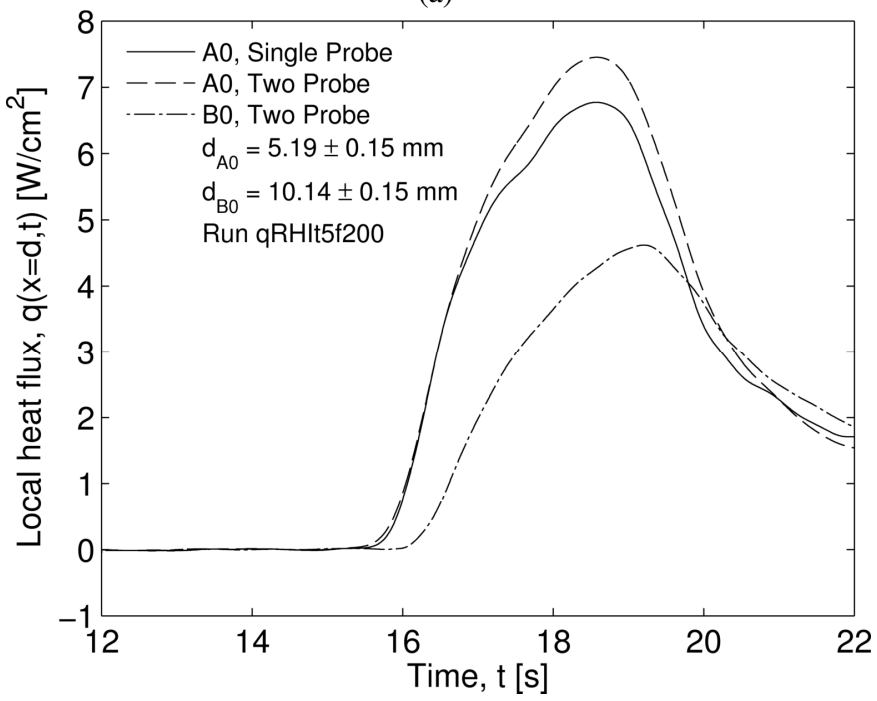

(b)

Figure 8.4: Inputs for inverse problem using data from run qRHIt5f200. (a) Raw, filtered, and shifted temperature data for both probes and (b) local heat flux at both probe sites using the single- and two-probe approach. Cutoff frequencies used were $f_{c,A0}$ = 1.5 Hz and $f_{c,B0}$ = 1.1 Hz.

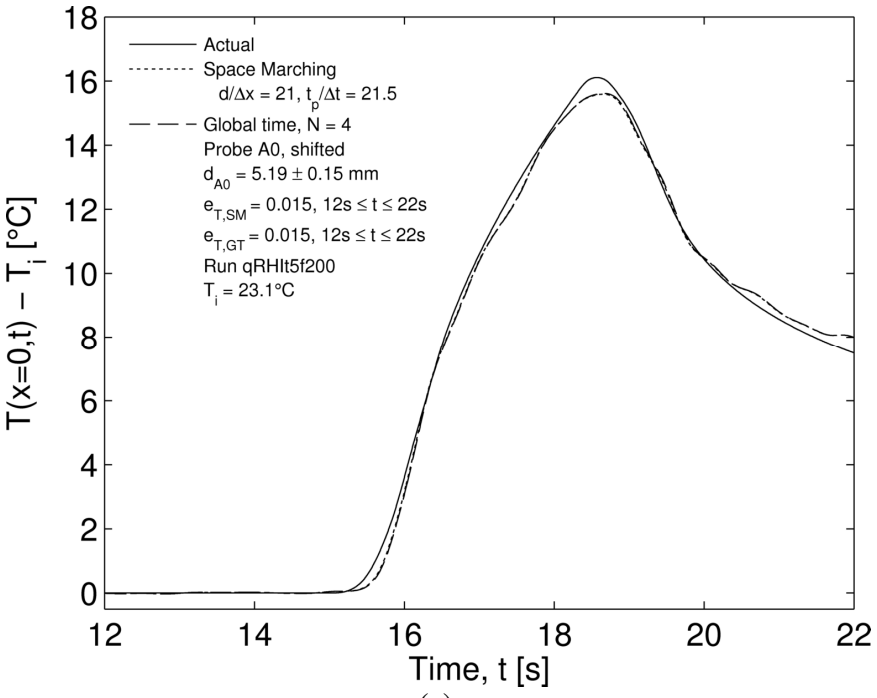

(a)

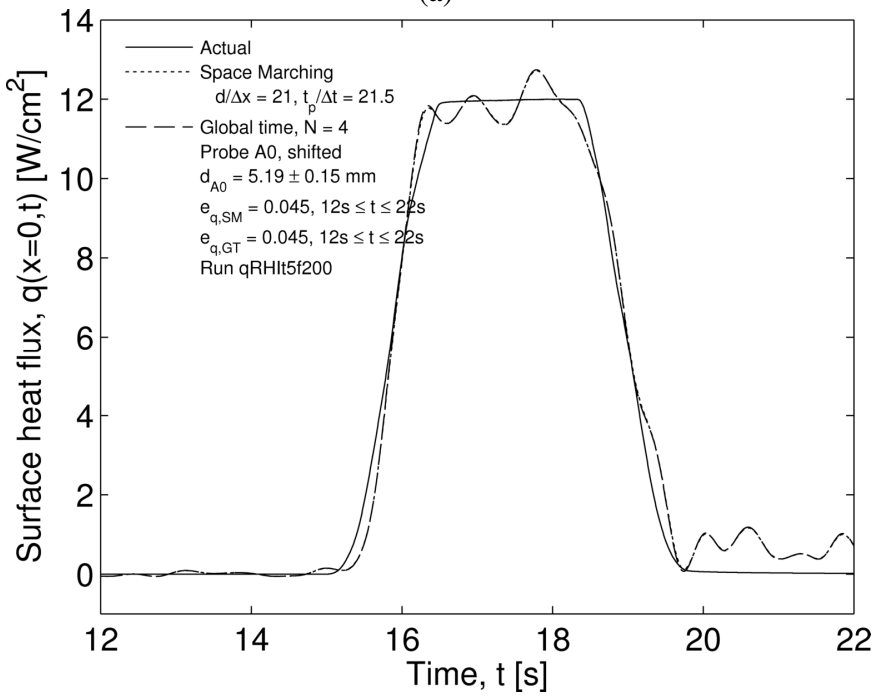

(b)

Figure 8.5: Two-probe inverse results for surface (a) temperature and (b) heat flux. Data used from run qRHIt5f200 seen in Figure 8.4.

sharp changes in the data, hence limiting the degree of accuracy which a step change in the surface can be recreated.

It should also be noted that the space-marching and global time methods are again seen to produce graphically identical results. Since the global time method lends itself to uncertainty analysis more easily than the space-marching method, the global time method is used to compare the one-probe and two-probe results and is employed in analysis of subsequent datasets. Henceforth, reference to the two-probe analysis refers to the global time inverse prediction using heat flux from the two-probe FD model.

Comparison of Two-Probe and One-Probe Analyses

The results for one-probe and two-probe analyses may be compared up to t=22s without violating the semi-infinite thermal condition. For both runs qCHIt3f200 and qRHIt5f200, a higher local heat flux was calculated for probe A0 using the two-probe FD model than for the one-probe analysis (see Figures 8.2(b) and 8.4(b)). Therefore, it is expected that a higher surface heat flux will be predicted using the global time two-probe method (GTTP) than for the single-probe global time method (GTSP). Figures 8.6 and 8.7 compare the two-probe inverse results with the one-probe global time and calibration integral inverse results, and the corresponding error norms are shown in Table 8.1.

As expected, for both runs GTTP predicted a higher surface temperature and heat flux than GTSP. Additionally, the accuracy of the global time method appears to be improved for both runs by employing data from two probes. For run qCHIt3f200 (Figure 8.6), employing GTTP as compared to GTSP resulted in a 23% improved in the surface temperature error norm and a 2.5% decrease in the surface heat flux error norm. However, this small reduction of e_q is

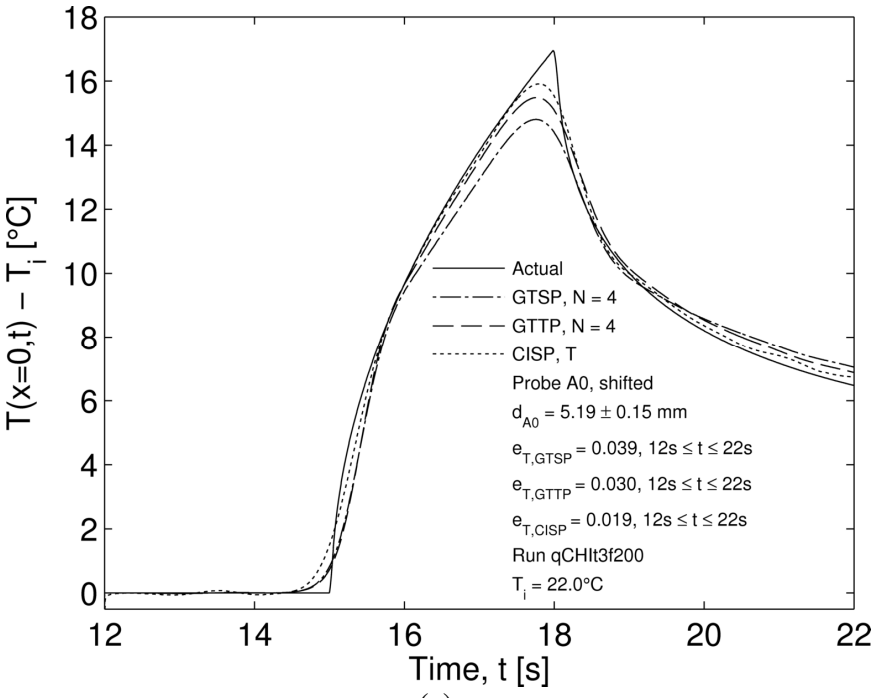

(a)

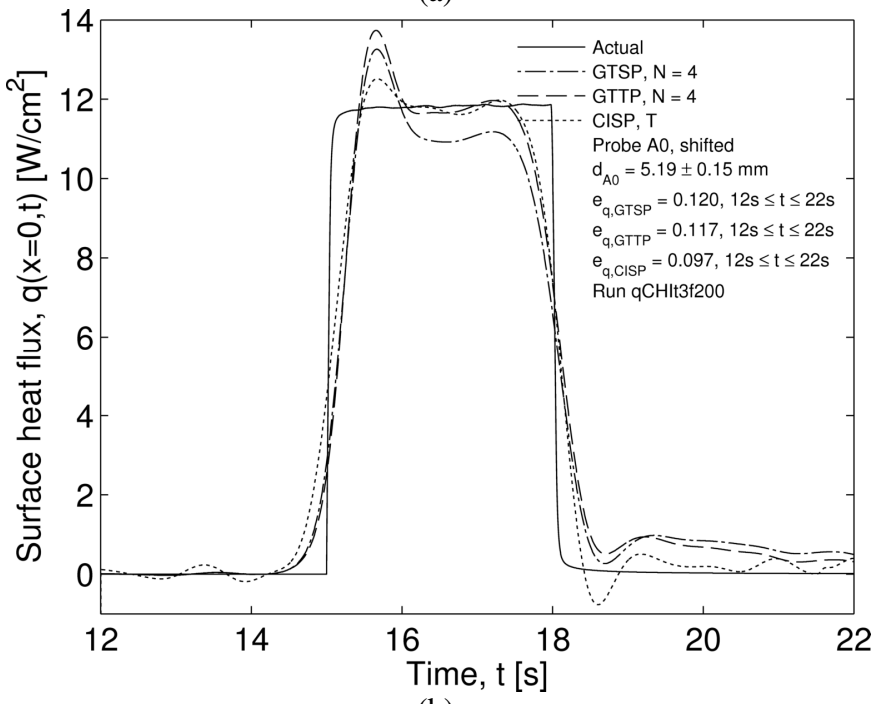

(b)

Figure 8.6: Comparison of two-probe inverse results with single-probe global time and calibration integral method for surface (a) temperature and (b) heat flux. Data used from run qCHIt3f200 seen in Figure 8.2.

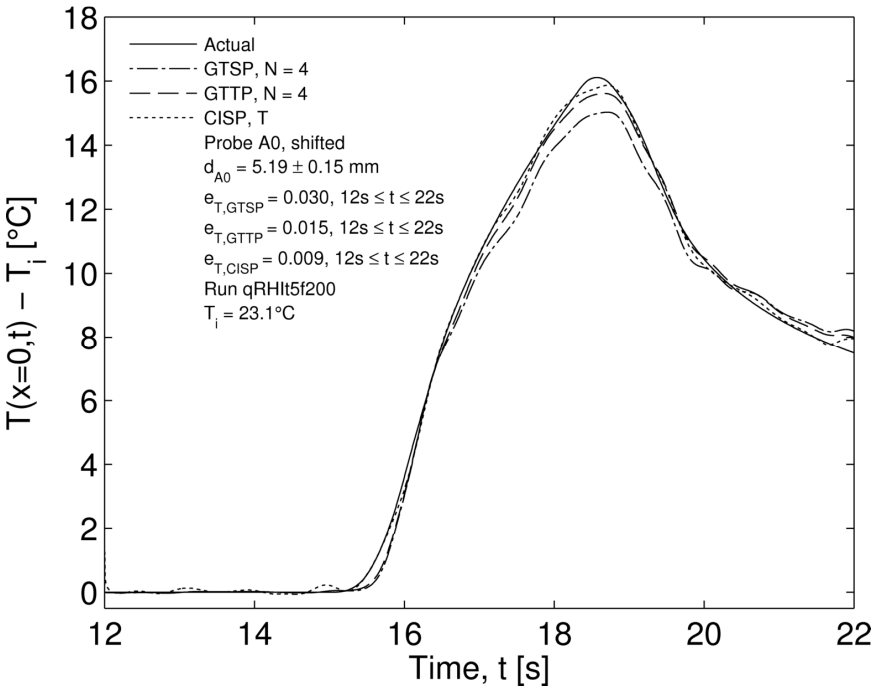

(a)

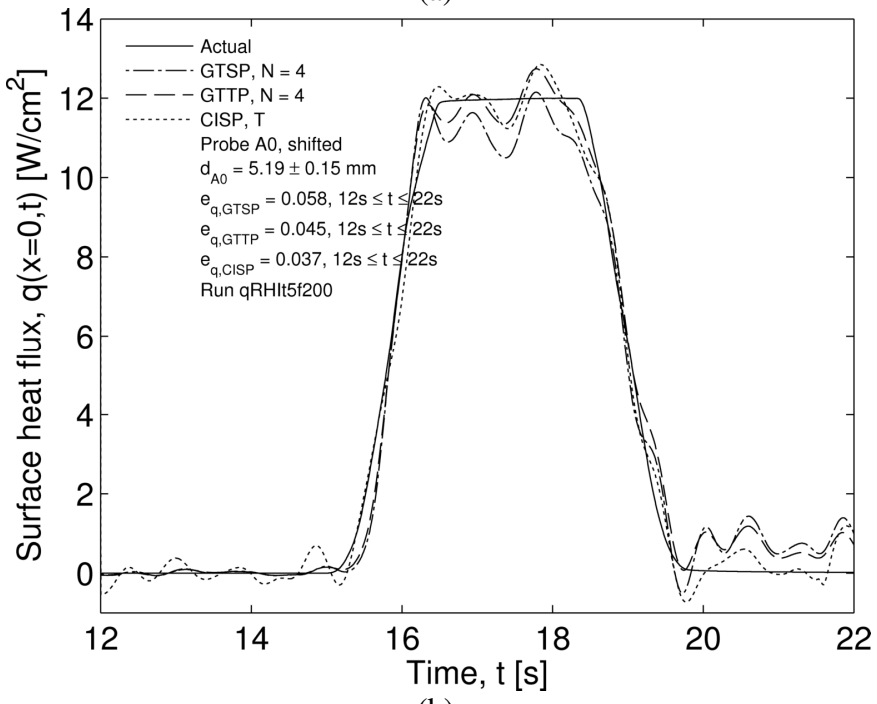

(b)

Figure 8.7: Comparison of two-probe inverse results with single-probe global time and calibration integral method for surface (a) temperature and (b) heat flux. Data used from run qRHIt3f200 seen in Figure 8.4.

Table 8.1: Inverse error norms for temperature and heat flux using both the one- and two-probe approaches. Calibration Integral uses the thermocouple temperature as the kernel (rather than the heating rate). The time range indicates the domain used to calculate the error norms.

		One-Probe				Two-Probe	
		Global Time		Calibration Integral		Global Time	
Run Name	Time Range	eT	eq	eT	eq	eT	eq
qCHIt3f200	$12s \leq t \leq 22s$	0.039	0.120	0.019	0.097	0.030	0.117
qRHIt5f200	$12s \leq t \leq 22s$	0.030	0.058	0.009	0.037	0.015	0.045
qCHIt10f200	$12s \leq t \leq 28s$	---	---	---	---	0.020	0.095
qCHIt10f1200	$12s \leq t \leq 28s$	---	---	---	---	0.022	0.102

not indicative of the improved accuracy. After the initial Gibbs' spike in the inverse predicted heat flux, GTTP is seen to oscillate around the actual surface heat flux. In contrast, GTSP is seen to have a bias of approximately -10% in the surface flux prediction. For the ramped surface heat flux (run qRHIt5f200, Figure 8.7), employing GTTP as compared to GTSP resulted in an amazing 50% improvement in e_T and 22.4% improvement in e_q (see Table 8.1). As in the step change boundary condition, GTTP was seen to oscillate around the actual surface heat flux while GTSP showed a negative bias in its predicted surface heat flux. In both runs (qCHIt3f200 and qRHIt5f200), both the single- and two-probe global time methods have a bias in predicting the power-off surface heat flux.

Despite the increased accuracy in the global time method by employing the two-probe approach, the calibration integral method was still seen to be more accurate than GTTP. For run qCHIt3f200 (Figure 8.6), employing CISP as compared to GTTP resulted in a 37% decrease in e_T and a 17% decrease in e_q. The initial Gibbs' spike was significantly improved for CISP; additionally, the bias in the power-off surface heat flux prediction was dramatically reduced. For run qRHIt5f200 (Figure 8.7), employing CISP as compared to GTTP resulted in a 53% decrease in e_T and an 18% decrease in e_q (see Table 8.1). While both CISP and GTTP are seen to be similarly accurate during heating, the bias in the power-off GTTP prediction was not visible in the CISP prediction. In all aspects of these two representative runs, the single-probe calibration integral method (CISP) was seen to be more accurate than GTTP. Future development of a two-probe calibration integral method should further increase accuracy of the inverse prediction.

Two-Probe Analysis with Finite Width Sample

As demonstrated above, the accuracy of the global time inverse method is improved by using the two-probe approach. The other major benefit to using two probes is the ability to perform inverse calculations after the semi-infinite condition is violated. As demonstrated in Chapter 5, this occurs for $t - t_{on} > 7$s. Run qCHIt10f200 provides a test case where the effect of violating the semi-infinite condition on the two-probe analysis can be investigated. Figure 8.8 shows the filtered ($f_{c,A0} = 1.1$ Hz, $f_{c,B0} = 1.3$ Hz), shifted temperature data and local heat flux histories. Figure 8.9 shows the corresponding inverse surface temperature and heat flux predictions, with error norms tabulated in Table 8.1. The error norms for this run were calculated over $12\text{s} \leq t \leq 28\text{s}$. A small bias is seen in the inverse prediction during heating and a larger bias is seen after the source was turned off. Despite this bias, the GTTP has excellent agreement with the actual surface heat flux. When comparing error norms for GTTP between a three second heating cycle and ten second heating cycle (runs qCHIt3f200 and qCHIt10f200), the surface temperature error norm is reduced by 33%, and the heat flux error norm is reduced by 19%.

Chapter 3 demonstrated that employing a higher data density with numerically simulated improved inverse results. A higher sampling rate can affect both the Gaussian filter and the two-probe direct FD model used to generate heat flux data. In contrast to the results of Chapter 3, Chapter 7 showed that increasing the data density using experimental data with the one-probe inverse results (using the Gaussian filter) was seen to decrease accuracy. This is because the noise level in the DAQ increases as the sampling rate is increased. Therefore, the negative effect of increasing the noise level outweighed the positive benefit of increasing the data density. We

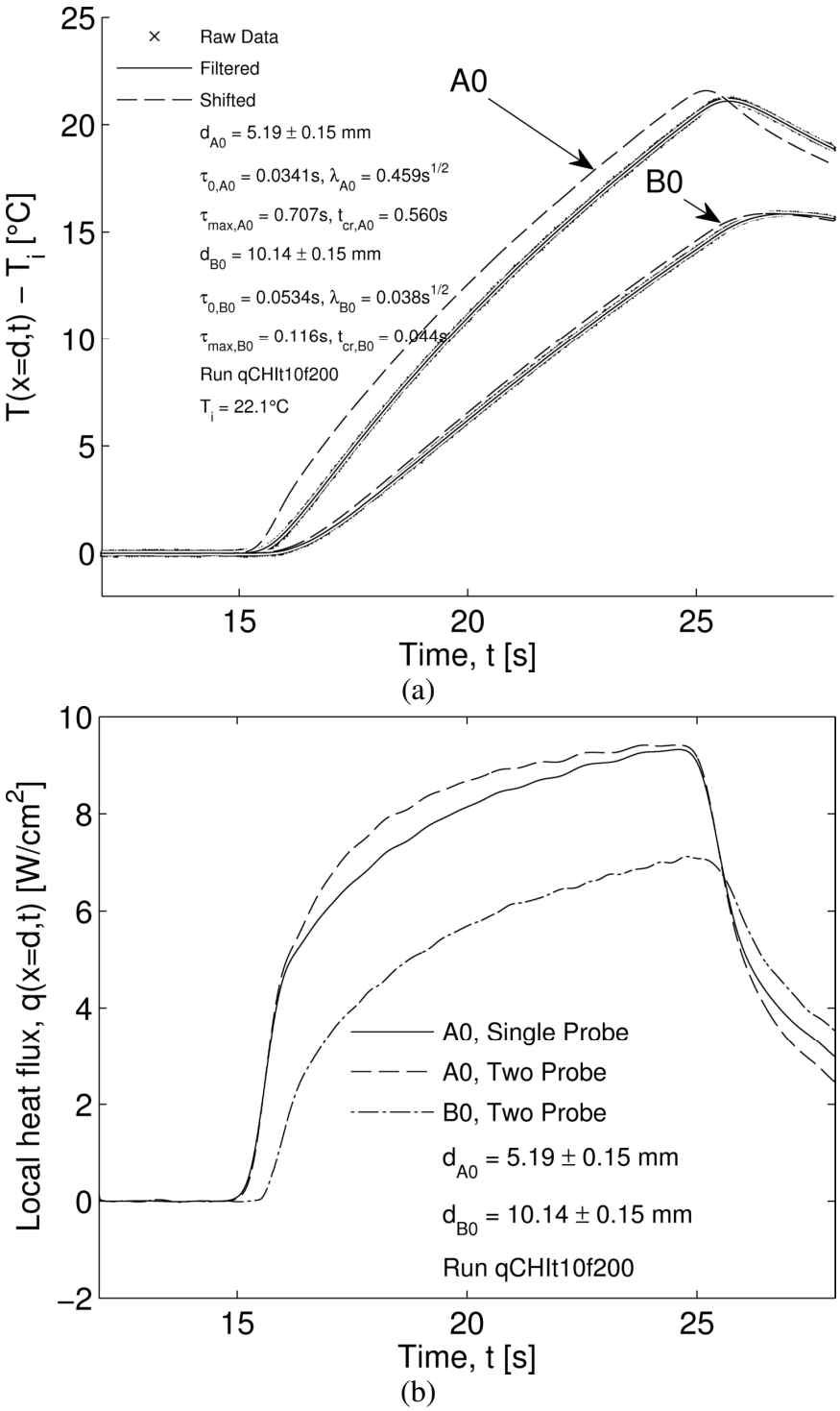

Figure 8.8: Inputs for inverse problem using data from run qCHIt10f200. (a) Raw, filtered, and shifted temperature data for both probes and (b) local heat flux at both probe sites using the single- and two-probe approach. Cutoff frequencies used were $f_{c,A0}$ = 1.1 Hz and $f_{c,B0}$ = 1.3 Hz. Note semi-infinite medium condition is violated at t = 22s.

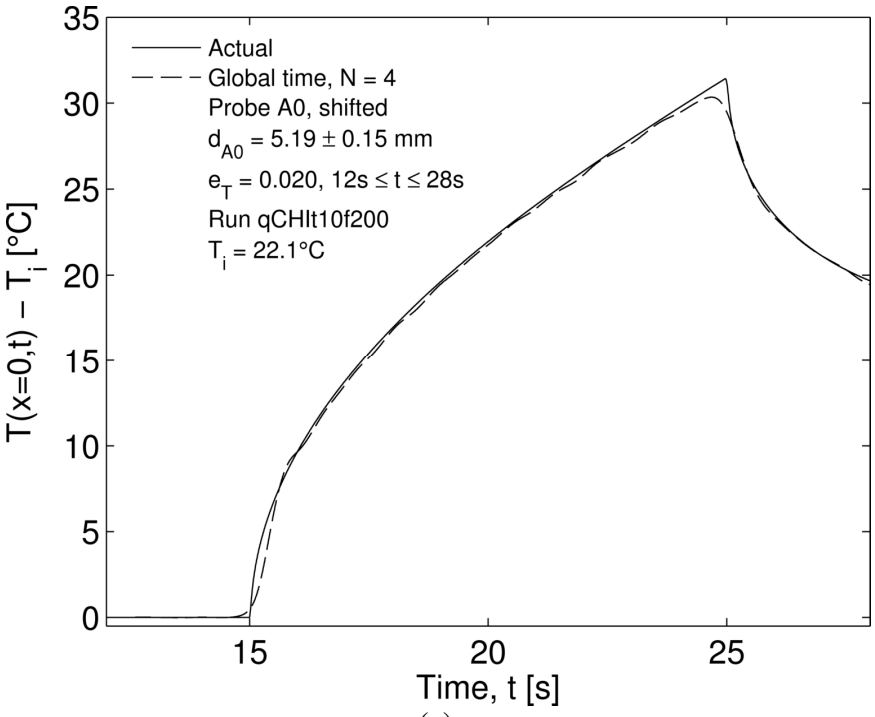

(a)

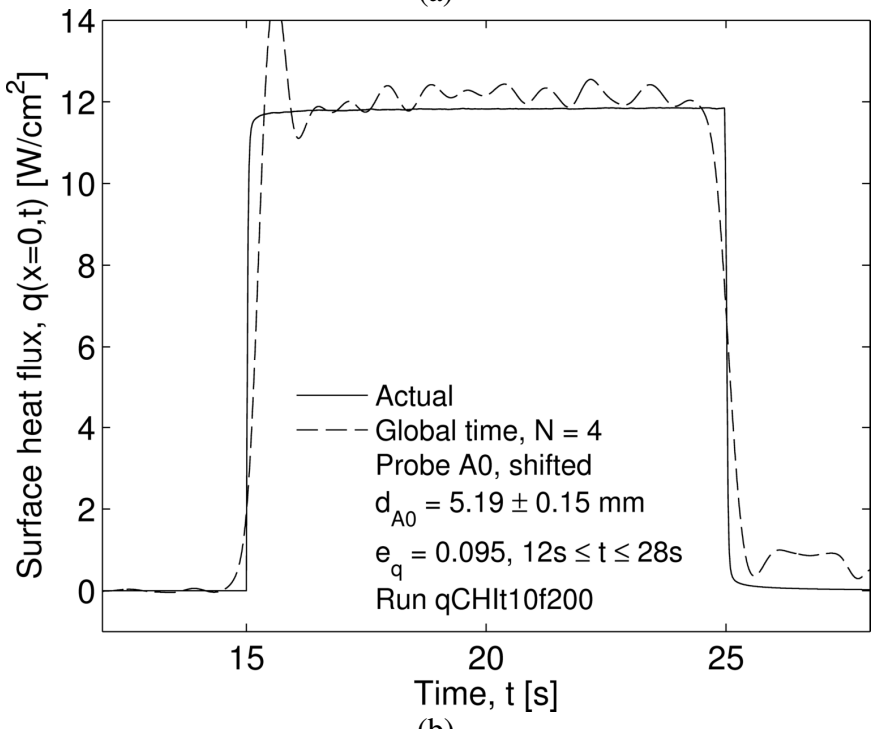

(b)

Figure 8.9: Two-probe inverse results for surface (a) temperature and (b) heat flux. Data used from run qCHIt10f200 seen in Figure 8.8. Note semi-infinite medium condition is violated at t = 22s.

now seek to investigate the effect of increasing the data density on two-probe analysis which includes not only the Gaussian filter, but also the two-probe direct FD model. Temperature and heat flux data for run qCHIt10f1200 can be seen in Figure 8.10 with $f_{c,A0}$ = 1.0 Hz and $f_{c,B0}$ = 1.3 Hz. Inverse surface temperature and heat flux results can be seen in Figure 8.11, with error norms tabulated in Table 8.1. Similar to the one-probe analysis, increasing the sampling rate is seen to increase the error norms by 10% for surface temperature and 7% for surface heat flux. This is for the same reason as noted above for the one-probe analysis. It is suspected, however, that if the higher-time derivatives of temperature were directly measured as in Chapter 4, the accuracy of the global time method could improve with increased data density provided the noise levels were controlled.

Two-Probe Analysis Uncertainty

As discussed in Chapter 7, all measurements and calculations are subject to uncertainty. The actual surface heat flux is subject to uncertainties (see the Appendix) in a) the heater resistance, b) the measured heater voltage, c) dimensions of the heater. The global time inverse predictions are subject to uncertainties in a) input thermophysical properties, b) sensor depth, c) temperature and higher-time derivatives of temperature data and d) heat flux and higher-time derivatives of heat flux data. Using the uncertainty derivation outlined in the Appendix, Figure 8.12 shows the uncertainty in the two-probe global time method inverse prediction and the uncertainty in the surface condition for a representative run qCHIt10f200. The uncertainty bands of the inverse prediction and actual surface temperature and heat flux are seen to overlap. Since this is the case for all four runs discussed in this chapter, the plots are superfluous, and only the results from one run are shown.

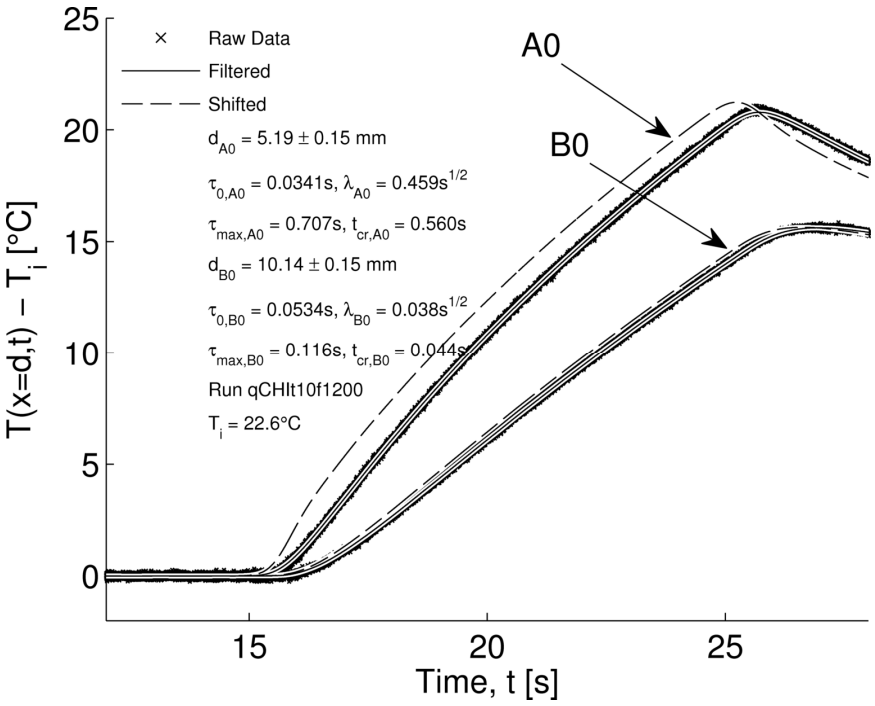

(a)

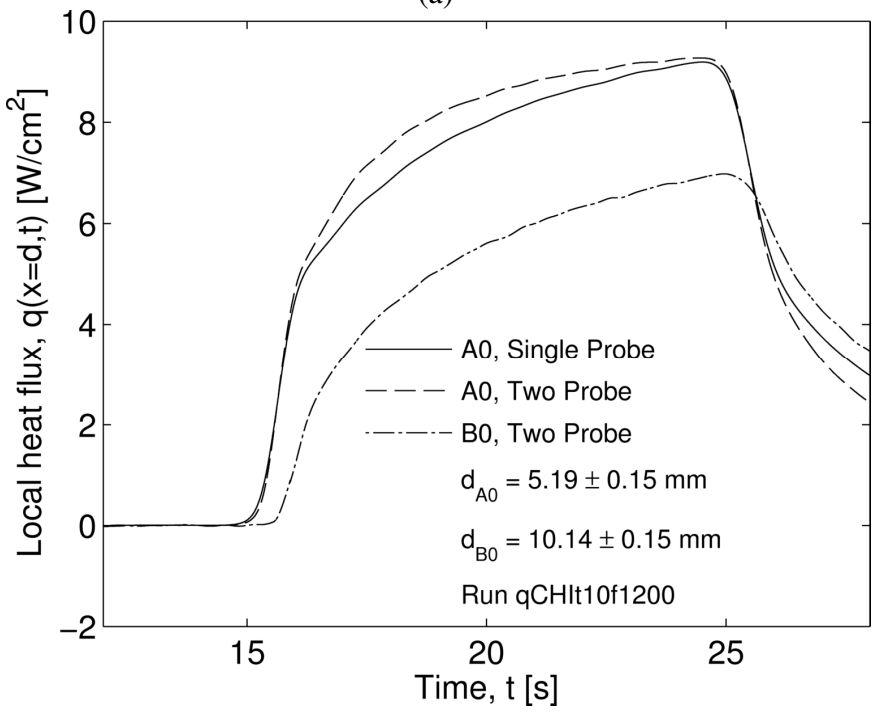

(b)

Figure 8.10: Inputs for inverse problem using data from run qCH10t10f1200. (a) Raw, filtered, and shifted temperature data for both probes and (b) local heat flux at both probe sites using the single- and two-probe approach. Cutoff frequencies used were $f_{c,A0}$ = 1.0 Hz and $f_{c,B0}$ = 1.3 Hz.

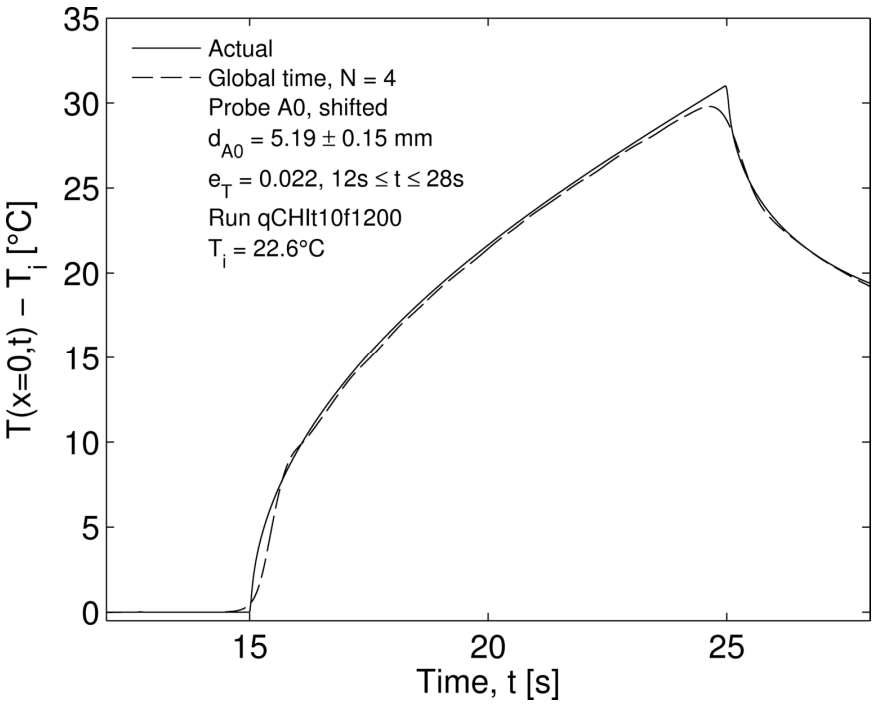

(a)

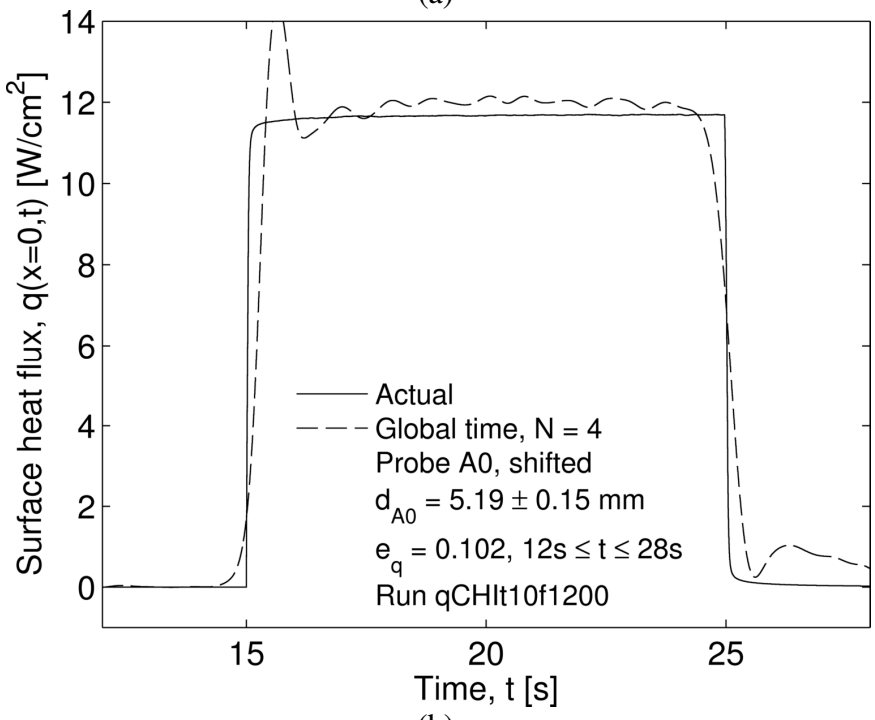

(b)

Figure 8.11: Effect of increasing the data density on the two-probe global time inverse results for surface (a) temperature and (b) heat flux. Data used from run qCHIt10f1200 seen in Figure 8.10.

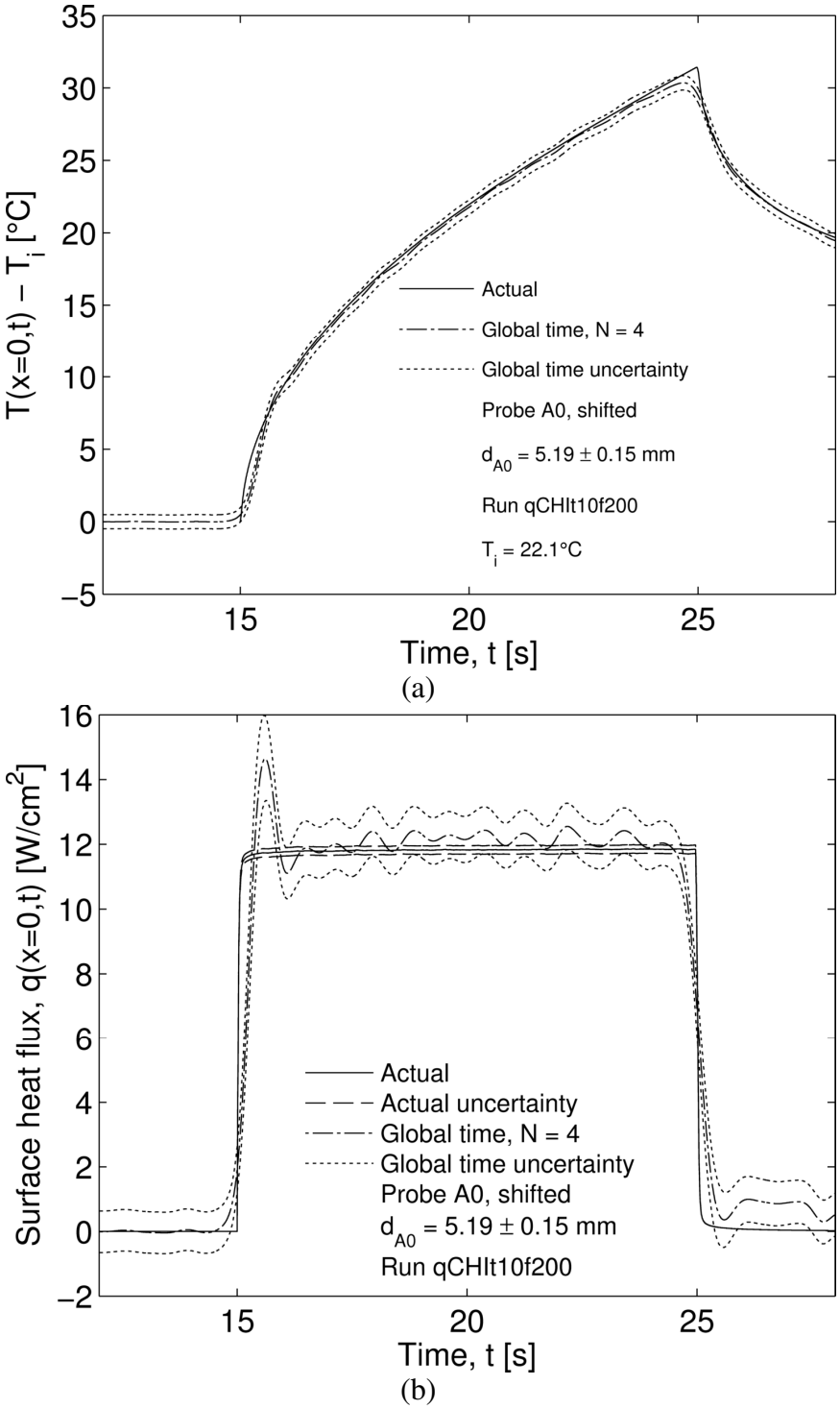

Figure 8.12: Uncertainty bands for actual and inverse predicted surface (a) temperature and (b) heat flux. Data used from run qCHIt10f200 seen in Figure 8.8.

8.3 Chapter Summary

This chapter validated the two-probe approach for the space-marching and global time inverse methods of Chapters 2 and 3 using sandwich experiment data. The accuracy of the one-probe results of Chapter 7 were improved in this chapter by using data from two-probes at different depths. Perhaps the most significant feature of the two-probe analysis is the ability to make inverse predictions without the assumption of a semi-infinite medium. Two experimental runs which violated this assumption were conducted, and it was shown that indeed the accuracy of the two-probe method was not degraded. Further, it was demonstrated that the uncertainty band of the two-probe inverse approach overlapped the uncertainty band in the actual surface condition.

Chapter 9: Conclusions and Future Work

9.1 Conclusions

The overall goal of this work was to provide a systematic methodology by which the noted difficulties associated with the inverse heat conduction problem can be resolved. To this end, two inverse heat conduction methods were presented in Chapters 2 and 3. First, a space-marching IHCP method (discrete space, discrete time) utilizing a Gaussian low-pass filter for regularization was studied. One key observation from Chapter 2 was that the stability and accuracy of the inverse prediction was more sensitive to the temporal mesh than the spatial mesh. Therefore, the goal of Chapter 3 was to eliminate this feature by employing a global time, discrete space inverse solution methodology. This was accomplished by assuming that the higher-time derivatives of temperature were available, and the time-derivative of the heat equation was not finite differenced. The novel treatment of the temporal derivative in the heat equation, combined with the global time Gaussian low-pass filter provided the regularization required for stable, accurate results. The numerical investigation of the global time method in Chapter 3 showed that in stark contrast to traditional inverse methods (including the space-marching method), increasing the data density did not compromise stability of the inverse prediction. Indeed, the global time inverse numerical results improved with faster data sampling.

Chapter 4 presented some preliminary work in obtaining higher-time derivatives of temperature from a voltage-rate interface used in conjunction with the thermocouple calibration curve. Significant motivation for the development of this sensor was discussed including use in the global time inverse heat conduction method; estimating local heat flux; detection of sudden jumps in surface heat flux from embedded sites; and, accurately predicting the future temperature

based on analytic continuation. A thermocouple drop tower experiment was used to validate the sensor, and two temporal derivatives were demonstrated.

Chapter 5 presented the setup of a physical experiment which was used as a test bed for validation of the numerical methods described in Chapters 2 and 3. Thermocouples were installed at specific distances from a heated surface. Careful design of this sandwich experiment ensured that the actual surface heat flux could be measured for comparison with the inverse techniques investigated. A detailed description of this setup was presented in Chapter 5.

Chapter 6 outlined the physics of installed thermocouple sensors, and presented two techniques by which the delay and attenuation characteristics of the sensors could be measured. The experimentally determined characteristics of each sensor were used to correct the measured thermocouple data of the sandwich experiment. The first technique, loop-current step response, provides a way to characterize in-situ sensors independently from the main experiment (i.e., the sandwich experiment). A new technique for the analysis of the LCSR data was presented, and excellent agreement was observed between this model and the data. The second technique, the Two-Probe Taylor Series (TPTS) method, was unable to characterize the probes of the sandwich experiment. The reason for this is in the underlying assumptions of the TPTS method; namely, this technique assumes the thermocouples have a constant τ. Since the thermocouples in the sandwich experiment have non-negligible conduction lead losses, the TPTS technique is an inappropriate characterization technique for the sandwich experiment. However, the Two-Probe Taylor Series method is promising for the case where leads are oriented parallel to the isotherm.

Chapter 7 presented experimental results and inverse projections using an analysis procedure with data from only one probe and limited to the case of a semi-infinite medium. The

space-marching method, global time method, and a new calibration integral method were all employed to analyze data from the sandwich experiment. The space-marching and global time methods approach the inverse problem with a traditional point of view; they require accurate knowledge of the sensor depth, thermal properties, and sensor characteristics. In contrast, the calibration integral method does not require this information, but instead uses a preliminary experimental run as calibration data. Excellent agreement was found between the actual surface heat flux and the inverse predictions. It was also found that the space-marching and global time methods produced inverse predictions which were graphically identical. This is because both techniques are based on the same spatial finite difference approach, and resolution of the higher-time derivatives of the temperature data was limited which hampered the global time method. The global time method could be improved if more accurate higher-time derivatives could be obtained. The calibration integral method produces surface temperature error norms that were an astounding 41% to 70% more accurate than the one-probe space-marching and global time methods; heat flux results were 19% to 36% more accurate. These results are highly encouraging and suggest future efforts should be dedicated to the further development of more generalized (i.e., finite width, higher dimensions, etc.) calibration integral inverse techniques.

Chapter 8 presented a more generalized approach to the inverse problem where data from two probes at different depths were used. In contrast to the one-probe analysis, the two-probe inverse approach was not restricted to the case of a semi-infinite medium. Data from the sandwich experiment was used for both the space-marching and global time inverse techniques. As in the one-probe analysis, it was found that these inverse methods produced graphically identical results due to limited resolution of the higher-time derivatives of the data. The two-

probe global time method was seen to significantly improve accuracy of the surface temperature predictions by as much as 50%, while surface heat flux prediction improved up to 10% over the single-probe global time method. The two-probe global time method was still seen to be significantly less accurate than the one-probe calibration integral method (up to 40% for surface temperature and 37% for surface heat flux). However, the uncertainty band of the two-probe global time inverse method was seen to significantly overlap the uncertainty band of the actual surface heat flux for nearly all time.

9.2 Future Work

Further Development of Higher-Time Derivative Sensor for Use in Inverse Analysis

Chapter 4 of this work demonstrated the accuracy that could be achieved with the higher-time derivative sensors. Additionally, Chapters 7 and 8 presented experimental data using the global time inverse method without the use of these sensors. For both one-probe and two-probe analysis, analytical derivatives of the Gaussian filter function were used, and the global time method was found to perform no more accurately than the space-marching method. It is suspected that this is due to the smoothing nature of the Gaussian filter – i.e., significant information is lost due to the filtering. It is the opinion of the author that the use of the voltage-rate sensors for measurement of the higher-time derivatives of temperature would significantly improve the ensuing inverse results using the global time method.

Further, Chapter 7 discussed the use of temperature derivatives in the calibration integral method. However, it was demonstrated that using the Gaussian filter to obtain the derivatives, inverse predictions using the calibration integral approach were more accurate using temperature directly rather than its derivatives. It is strongly suspected that this may not be the case if the

voltage-rate sensor was employed to measure the temperature derivative instead of relying on the analytical derivative of the Gaussian filter.

Sensor Characterization

The new analysis procedure of the LCSR data provided excellent results when applied to the sandwich experiment data in both Chapters 7 and 8. However, a "band aid" was required in the shifting procedure to prevent discontinuities from occurring in the higher-time derivatives. One way this could be remedied would be to use a smooth function to fit the LCSR data. Rather than a square root in time modeling of the sensor characteristics given by Eq. (6.25) perhaps a smooth function such as the error function would provide a smooth $\tau(t)$ and temporal derivatives.

The goal of the LCSR testing was to obtain the parameters τ and λ. An alternative way to finding these parameters independently of LCSR would be to directly use sandwich experimental data to calibrate the sensor. A direct FD model of this experiment is readily available, and the positional temperature from the FD model could be compared with the unshifted thermocouple data. Using Eq. (6.8), a least-squares algorithm could be employed to determine τ_0 and λ where $T_\infty(t)$ is the positional temperature from the FD model. This approach is similar to the calibration integral method in that it would require at least one calibration run before a "real run" could be performed. In contrast to the calibration integral method, however, actual values of the sensor characteristics would be determined.

The Two-Probe Taylor Series method of probe characterization showed excellent promise with numerical simulations. However, the sandwich experiment presented herein has probes where the leads wires are oriented perpendicular to the isotherms. A new experiment should be

constructed with lead wires oriented parallel to the isotherms, and the Two-Probe Taylor Series method should be experimentally validated with data from this experiment.

Further Development of the Calibration Integral Method

In Chapters 7 and 8, it was demonstrated that the new calibration integral method produced inverse results which were more accurate than either the space-marching or global time inverse methods. However, the calibration integral method is currently limited to the case of a semi-infinite medium. This is a significant limitation. Given the high promise of this method, significant effort should be dedicated to the further development of this approach to produce a calibration technique that is extendable to multi-material finite width domains, anisotropic materials, and higher dimensions.

List of References

[1] Beck, J. V., Blackwell, B., St. Clair, C. R., Jr., 1985, Inverse Heat Conduction, Wiley, New York.

[2] Frankel, J., 2007, "Regularization of inverse heat conduction by combination of rate sensor analysis and analytic continuation," Journal of Engineering Mathematics, 57(2), pp. 181-198.

[3] Monte, F. d., Beck, J. V., and Amos, D. E., 2008, "Diffusion of thermal disturbances in two-dimensional Cartesian transient heat conduction," International Journal of Heat and Mass Transfer, 51(25-26), pp. 5931-5941.

[4] Burggraf, O. R., 1964, "An exact solution of the inverse problem in heat conduction theory and application," Journal of Heat Transfer, 86, pp. 373-382.

[5] Beck, J. V., 1962, "Calculation of surface heat flux from an internal temperature history," ASME Paper 62-HT-46.

[6] Kurpisz, K., and Nowak, A. J., 1995, Inverse Thermal Problems, Computational Mechanics Publications, Southampton, UK.

[7] Beck, J. V., Blackwell, B., and Haji-Sheikh, A., 1996, "Comparison of some inverse heat conduction methods using experimental data," International Journal of Heat and Mass Transfer, 39(17), pp. 3649-3657.

[8] Beck, J. V., 2008, "Filter solutions for the nonlinear inverse heat conduction problem," Inverse Problems in Science & Engineering, 16(1), pp. 3-20.

[9] Tikhonov, A. N., and Arsenin, V. Y., 1977, Solutions of Ill-Posed Problems, V. H. Winston & Sons, Washington, D.C.

[10] D'Souza, N., 1974, "Numerical solution of one-dimensional inverse transient heat conduction by finite difference method," Winter Annual Meeting, ASME Paper no. 75-WA/HT-81, Houston, TX.

[11] Al-Khalidy, N., 1999, "Analysis of boundary inverse heat conduction problems using space marching with Savitzky-Gollay digital filter," International Communications in Heat and Mass Transfer, 26(2), pp. 199-208.

[12] Taler, J., 1999, "A new space marching method for solving inverse heat conduction problems," Forschung im Ingenieurwesen, 64(11), pp. 296-306.

[13] Frankel, J. I., Keyhani, M., and Taira, K., 2004, "In-phase error estimation of experimental data and optimal first derivatives," AIAA Journal, 42(5), pp. 1017-1024.

[14] Guo, L., Murio, D. A., and Roth, C., 1990, "A mollified space marching finite differences algorithm for the inverse heat conduction problem with slab symmetry," Computers & Mathematics with Applications, 19(7), pp. 75-89.

[15] Murio, D. A., 1988, "Parameter selection by discrete mollification and the numerical solution of the inverse heat conduction problem," Journal of Computational and Applied Mathematics, 22(1), pp. 25-34.

[16] Murio, D. A., and Hinestroza, D., 1993, "The space marching solution of the inverse heat conduction problem and the identification of the initial temperature distribution," Computers & Mathematics with Applications, 25(4), pp. 55-63.

[17] Carasso, A. S., 1992, "Space marching difference schemes in the nonlinear inverse heat conduction problem," Inverse Problems, 8(1), p. 25.

[18] Carasso, A. S., 1993, "Slowly divergent space marching schemes in the inverse heat conduction problem," Numerical Heat Transfer, Part B Fundamentals, 23(1), pp. 111 - 126.

[19] Battaglia, J. L., Cois, O., Puigsegur, L., and Oustaloup, A., 2001, "Solving an inverse heat conduction problem using a non-integer identified model," International Journal of Heat and Mass Transfer, 44(14), pp. 2671-2680.

[20] Lohle, S., Battaglia, J. L., Batsale, J. C., Bourserau, F., Conte, D., Jullien, P., van Ootegem, B., Couzi, J., and Lasserre, J. P., "Estimation of High Heat Flux in Supersonic Plasma Flows," Proc. IEEE Industrial Electronics, IECON 2006, pp. 5366-5373.

[21] Lohle, S., Battaglia, J. L., Batsale, J. C., Enouf, O., Dubard, J., and Filtz, J. R., 2007, "Characterization of a heat flux sensor using short pulse laser calibration," Rev. Sci. Instrum., 78(5), p. 6.

[22] Frankel, J. I., Keyhani, M., and Elkins, B. S., 2012, "Surface heat flux prediction through physics-based calibration part 1: theory," 50th AIAA Aerospace Sciences Meeting, AIAA, Nashville, TN.

[23] Taler, J., 1996, "A semi-numerical method for solving inverse heat conduction problems," Heat and Mass Transfer, 31(3), pp. 105-111.

[24] Al-Khalidy, N., 1998, "Application of stochastic method for solving inverse heat conduction problems," Numerical Heat Transfer, Part A: Applications, 34(3), pp. 331 - 342.

[25] Kim, S. K., and Lee, W. I., 2002, "Solution of inverse heat conduction problems using maximum entropy method," International Journal of Heat and Mass Transfer, 45(2), pp. 381-391.

[26] Özisik, M. N., and Orlande, H. R. B., 2000, Inverse Heat Transfer, Taylor & Francis, New York.

[27] Shen, S.-Y., 1999, "A numerical study of inverse heat conduction problems," Computers and Mathematics with Applications, 38(7-8), pp. 173-188.

[28] Deng, S., and Hwang, Y., 2006, "Applying neural networks to the solution of forward and inverse heat conduction problems," International Journal of Heat and Mass Transfer, 49(25-26), pp. 4732-4750.

[29] Raudenský, M., Horský, J., and Krejsa, J., 1995, "Usage of neural network for coupled parameter and function specification inverse heat conduction problem," International Communications in Heat and Mass Transfer, 22(5), pp. 661-670.

[30] Reginska, T., and Elden, L., 1997, "Solving the sideways heat equation by a wavelet - Galerkin method," Inverse Problems, 13(4), p. 1093.

[31] Frankel, J. I., 1996, "Residual-minimization least-squares method for inverse heat conduction," Computers and Mathematics with Applications, 32(4), pp. 117-130.

[32] Elden, L., 1995, "Numerical solution of the sideways heat equation by difference approximation in time," Inverse Problems, 11(4), p. 913.

[33] Beck, J. V., 1970, "Nonlinear estimation applied to the nonlinear inverse heat conduction problem," International Journal of Heat and Mass Transfer, 13(4), pp. 703-716.

[34] Joseph, D. D., and Preziosi, L., 1989, "Heat waves," Reviews of Modern Physics, 61(1), p. 41.

[35] Taitel, Y., 1972, "On the parabolic, hyperbolic and discrete formulation of the heat conduction equation," International Journal of Heat and Mass Transfer, 15(2), pp. 369-371.

[36] Özisik, M. N., and Vick, B., 1984, "Propagation and reflection of thermal waves in a finite medium," International Journal of Heat and Mass Transfer, 27(10), pp. 1845-1854.

[37] Özisik, M. N., 1980, Heat Conduction, Wiley, New York.

[38] Woodbury, K. A., 1990, "Effect of thermocouple sensor dynamics on surface heat flux predictions obtained via inverse heat transfer analysis," International Journal of Heat and Mass Transfer, 33(12), pp. 2641-2649.

[39] Woolley, J. W., 2008, "Accounting for Transient Temperature Measurement Error with a High Fidelity Thermocouple Model and Application to Metal/Mold Interfacial Heat Flux Estimation," Ph.D. Dissertation, The University of Alabama, Tuscaloosa, Alabama.

[40] Beck, J. V., 1968, "Determination of undisturbed temperatures from thermocouple measurements using correction kernels," Nuclear Engineering and Design, 7, pp. 9-12.

[41] Hashemian, H. M., Petersen, K. M., Mitchell, D. W., Hashemian, M., and Beverly, D. D., 1990, "In situ response time testing of thermocouples," ISA Transactions, 29(4), pp. 97-104.

[42] Kerlin, T. W., Shepard, R. L., Hashemian, H. M., Petersen, and M., K., 1982, "Response of Installed Temperature Sensors," Temperature Its Measurement and Control in Science and Industry, 5.

[43] Frankel, J. I., and Keyhani, M., 1997, "A Global Time Treatment for Inverse Heat Conduction Problems," Journal of Heat Transfer, 119(4), pp. 673-683.

[44] Frankel, J. I., Arimilli, R. V., Keyhani, M., and Wu, J., 2008, "Heating rate dT/dt measurements developed from in-situ thermocouples using a voltage-rate interface," International Communications in Heat and Mass Transfer, 35(8), pp. 885-891.

[45] Taler, J., and Zima, W., 1999, "Solution of inverse heat conduction problems using control volume approach," International Journal of Heat and Mass Transfer, 42(6), pp. 1123-1140.

[46] Ji, C.-C., and Jang, H.-Y., 1998, "Experimental investigation in inverse heat conduction problem," Numerical Heat Transfer, Part A: Applications, 34(1), pp. 75 - 91.

[47] Incropera, F. P., and DeWitt, D. P., 2002, Fundamentals of Heat and Mass Transfer, John Wiley & Soncs, Inc., New York.

[48] de Monte, F., Beck, J. V., and Amos, D. E., 2008, "Diffusion of thermal disturbances in two-dimensional Cartesian transient heat conduction," International Journal of Heat and Mass Transfer, 51, pp. 5931-5941.

[49] Figliola, 2000, Theory and Design for Mechanical Measurements, Wiley.

[50] Patankar, S. V., 1980, Numerical Heat Transfer and Fluid Flow, Hemishpere Publishing Corp., Washington, D.C.

[51] Frankel, J. I., Osborne, G., and Taira, K., 2006, "Stabilization of ill-posed problems through thermal rate sensors," Journal of Thermophysics and Heat Transfer, 20(2), pp. 238-246.

[52] Abramowitz, M., and Stegun, I. A., 1965, Handbook of Mathematical Functions, Dover, New York.

[53] Park, H. M., and Jung, W. S., 2001, "On the solution of multidimensional inverse heat conduction problems using an efficient sequential method," Journal of Heat Transfer, 123, pp. 1021-1029.

[54] Press, W. H., Flannery, B. P., Teukolsky, S. A., and Verrterling, W. T., 1986, Numerical Recipes, Cambridge, New York.

[55] Frankel, J. I., and Arimilli, R. V., 2007, "Inferring convective and radiative heating loads from transient surface temperature measurements in the half-space," Inverse Problems in Science and Engineering, 15, pp. 463-488.

[56] Frankel, J. I., 2007, "In-depth and surface, transient flux predictions using heating/cooling rate sensors and advanced engineering analysis for aerospace applications," International Society for Air Breathing Engines 2007, Beijing, PRC.

[57] Murio, D., 2002, "Mollification and space marching," Inverse Engineering Handbook, CRC Press.

[58] Hardy, R. L., 1990, "Theory and applications of the multiquadric-biharmonic method," Computers & Mathematics with Applications, 8, pp. 163-208.

[59] Frankel, J. I., Keyhani, M., Arimilli, R. V., and Wu, J., 2008, "Locating sudden changes in heat flux using higher-temporal derivatives of temperature," AIAA Journal of Spacecraft and Rockets, 45(3), pp. 631-635.

[60] Frankel, J. I., Keyhani, M., Arimilli, R. V., and Wu, J., 2008, "A new multidimensional integral relationship between heat flux and temperature for direct internal assessment of heat flux," Zeitschrift für angewandte Mathematik und Physik (ZAMP), 59(5), pp. 569-888.

[61] Frankel, J. I., Keyhani, M., and Arimilli, R. V., 2010, "A new three-dimensional heat flux-temperature integral relationship for half-space transient diffusion," Journal of the Franklin Institute, 347(9), pp. 1681-1688.

[62] Frankel, J. I., 2009, "A new asymptotic temperature-heat flux integral relationship in cylindrical coordinates," Journal of Thermophysics and Heat Transfer, 23(1), pp. 191-197.

[63] Frankel, J. I., Keyhani, M., and Arimilli, R. V., 2010, "New, orthotropic, two-dimensional, transient heat-flux/temperature integral relationship for half-space diffusion," Journal of Thermophysics and Heat Transfer, 24(1), pp. 212-215.

[64] NIST, 1995, "ITS-90 Thermocouple Database," http://srdata.nist.gov/its90/download/download.html.

[65] Semiconductor, N., 1969, "An applications guide for op amps," Application Note 20.

[66] Wing, G. M., 1991, A Primer on Integral Equations of the First Kind, SIAM, Philadelphia, PA.

[67] Greenberg, M. D., 1988, Advanced Engineering Mathematics, Prentice Hall, Englewood Cliffs, NJ.

[68] Linz, P., 1985, Analytical and Numerical Methods for Volterra Equations, Siam, Philadelphia.

Appendix

A.1 Uncertainty in Actual Surface Heat Flux

The actual surface heat flux of the slab is obtained via a finite difference (FD) code (see Section 5.4). The geometry used for the FD code is three layers: 1) nichrome heater with volumetric generation 2) electrical insulator (mica) and 3) instrumented sample (bronze). Chapter 7 shows that the surface heat flux reported by the FD model asymptotically approaches the direct flux model. Therefore, for ease of manipulation, we obtain the uncertainty in the surface heat flux from the approximation

$$q_S(t) = \frac{V_{RMS}^2(t)}{2A_{heat}R_{heat}}. \tag{A.1}$$

where V_{RMS} is the RMS of the AC voltage applied to the heater, A_{heat} is the surface area of one of the bronze plates, and R_{heat} is the resistance of the heater. For the derivations presented herein, U_ϕ denotes uncertainty such that $\phi = \phi_{av} \pm U_\phi$. The uncertainty in the surface heat flux via Kline-McClintock's [49] equation is given by

$$U_{qS} = \sqrt{\left(U_{V\,RMS}\frac{\partial q_S}{\partial V_{RMS}}\right)^2 + \left(U_{R\,heat}\frac{\partial q_S}{\partial R_{heat}}\right)^2 + \left(U_{A\,heat}\frac{\partial q_S}{\partial A_{heat}}\right)^2}. \tag{A.2}$$

The uncertainty in the area is negligible as compared to the uncertainty in the power measurement. Therefore, Eq. (A.2) simplifies to

$$U_{qS} = \sqrt{\left(U_{V\,RMS}\frac{\partial q_S}{\partial V_{RMS}}\right)^2 + \left(U_{R\,heat}\frac{\partial q_S}{\partial R_{heat}}\right)^2}. \tag{A.3}$$

The required partial derivatives of Eq. (A.3) are given by

$$\frac{\partial q_S}{\partial V_{RMS}} = \frac{V_{RMS}(t)}{A_{heat}R_{heat}} \tag{A.4}$$

$$\frac{\partial q_S}{\partial V_{RMS}} = -\frac{V_{RMS}^2(t)}{2A_{heat}R_{heat}^2} \tag{A.5}$$

Substituting Eqs. (A.4-A.5) into Eq. (A.3) and dividing both sides of Eq. (A.3) by Eq. (A.1) yields

$$\frac{U_{qS}}{q_S} = \sqrt{\left(2\frac{U_{V\,RMS}}{V_{RMS}}\right)^2 + \left(\frac{U_{R\,heat}}{R_{heat}}\right)^2}. \tag{A.6}$$

All that remains is to find the uncertainties in the heater voltage and resistance.

Uncertainty in Heater Voltage

The transient voltage of the heater was passed through a voltage divider, and then measured via a DT9806 data acquisition board with a gain of 1. The equation for the heater voltage is then given by

$$V_{RMS} = \left(1 + \frac{R_{h2}}{R_{h1}}\right)V_{h,DAQ} \tag{A.7}$$

where R_{h1} and R_{h2} are the individual resistances in the voltage divider and $V_{h,DAQ}$ is the RMS of the voltage recorded by the data acquisition system. Depending on the power level desired, two different values of R_{h2} were used as seen in Table A.1. The equation for the overall uncertainty in the heater voltage is given by Kline-McClintock's method as

$$U_{V\,RMS} = \pm\sqrt{\left(U_{Rh1}\frac{\partial V_h}{\partial R_{h1}}\right)^2 + \left(U_{Rh2}\frac{\partial V_h}{\partial R_{h2}}\right)^2 + \left(U_{Vh,DAQ}\frac{\partial V_h}{\partial V_{h,DAQ}}\right)^2} \tag{A.8}$$

The required partial derivatives are given by

Table A.1: Uncertainty parameters for actual surface heat flux calculation.

Parameter	Value	
Run	qCLOt3f200	qCHIt3f200
Resistance		
R_h	4.326 Ω	
FSO_{Rh}	100 Ω	
LSD_{Rh}	0.001 Ω	
U_{Rh}	± 0.005 Ω	
R_{h1}	2.7178 kΩ	
FSO_{Rh1}	10 kΩ	
LSD_{Rh1}	0.1 Ω	
U_{Rh1}	± 0.4 Ω	
R_{h2}	50.992 kΩ	75.215 kΩ
FSO_{Rh2}	100 kΩ	
LSD_{Rh2}	1 Ω	
U_{Rh2}	± 6 Ω	± 7 Ω
Voltage		
V_{RMS}	82.0 V_{RMS}	133.3 V_{RMS}
$V_{h,DAQ}$	4.15 V_{RMS}	4.65 V_{RMS}
$FSO_{h,DAQ}$	± 10V	
$LSB_{h,DAQ}$	305 µV	
E_{system}	± 0.01% $FSO_{h,DAQ}$	
$E_{accuracy}$	± 0.01% $FSO_{h,DAQ}$	
$E_{linearity}$	± 1.2 $LSB_{h,DAQ}$	
E_{drift}	± 25 µV	
$U_{Vh,OIE}$	± 0.0021 V_{RMS}	
$t_{\infty,95\%}$	1.96	
σ_h	0.012 V	0.012 V
$U_{Vh,\sigma}$	± 0.023 V	± 0.024 V
$U_{Vh,DAQ}$	± 0.023 V_{RMS}	± 0.024 V_{RMS}
U_{VRMS}	± 0.46 V_{RMS}	± 0.69 V_{RMS}
U_{VRMS}/V_{RMS}	0.0056	0.0056
U_{Rh}/R_h	0.0012	
U_{qS}/q_S	0.011	0.011

$$\frac{\partial V_{RMS}}{\partial R_{h1}} = -\frac{R_{h2}}{R_{h1}^2} V_{h,DAQ} \tag{A.9}$$

$$\frac{\partial V_{RMS}}{\partial R_{h2}} = \frac{1}{R_{h1}} V_{h,DAQ} \tag{A.10}$$

$$\frac{\partial V_{RMS}}{\partial V_{h,DAQ}} = 1 + \frac{R_{h2}}{R_{h1}} \tag{A.11}$$

The voltage divider resistances were assumed to be constant and were measured with a Data Precision 3500 multimeter. The specifications of this device state that the uncertainties in R_{h1} and R_{h2} are given by

$$U_{Rhi} = \pm\left(0.007\% R_{hi} + 0.001\% FSO_{Rhi} + 1 LSD_{Rhi}\right), \qquad i = 1,2 \tag{A.12}$$

The overall uncertainty in the measured heater voltage is given by

$$U_{Vh,DAQ} = \pm\sqrt{U_{Vh,\sigma}^2 + U_{Vh,OIE}^2} \tag{A.13}$$

where $U_{Vh,\sigma}$ is the uncertainty in the voltage due to the noise level of the data and $U_{Vh,OIE}$ is the overall instrument (DT9806) uncertainty. These uncertainties are given by

$$U_{Vh,\sigma} = \pm t_{\infty,95\%} \sigma_h \tag{A.14}$$

$$U_{Vh,OIE} = \pm\sqrt{E_{system}^2 + E_{accuracy}^2 + E_{linearity}^2 + E_{drift}^2} \tag{A.15}$$

where σ_h is the standard deviation of the lead voltage data, $t_{\infty,95\%}$ is the Student's t-distribution value [49], and all "E" terms in Eq. (A.15) are manufacturer's specifications. The parameters needed to compute Eqs. (A.12-A.15) can be found in Table A.1 which details the uncertainty calculation for a low power run (qCLOt3f200) and a high power run (qCHIt3f200). Interestingly, the resulting ratio of V_{RMS}/U_{VRMS} was found to be 0.0056 for both the low and high powered runs. Indeed, this was found to be the case for all experimental runs.

Uncertainty in Heater Resistance

The resistance of the heater was measured with the Data Precision 3500 instrument using the lowest range (100 Ω). The equation for the uncertainty in the heater resistance is given by

$$U_{Rh} = \pm\left(0.008\%R_h + 0.004\%FSO_{Rh} + 1LSD_{Rh}\right) \tag{A.16}$$

where the required parameters can be seen in Table A.1. The overall uncertainty in the heater resistance was found to be 4.326 ± 0.005 Ω.

Overall Uncertainty in Actual Surface Heat Flux

Using the results above for the uncertainties in the heater voltage and resistance, the overall uncertainty in the actual surface heat flux was found to be

$$\frac{U_{qS}}{q_S} = 0.011 \tag{A.17}$$

It was found that the overall uncertainty in the actual surface heat flux is dominated by the uncertainty in the heater voltage. This was in turn dominated by $U_{Vh,DAQ}$, which was dominated by $U_{Vh,\sigma}$. Therefore, in order to reduce the uncertainty in the actual surface heat flux, the standard deviation of the lead voltage data should be reduced. Indeed, this is a nontrivial task considering the high sampling rate of 7500 Hz (required for resolution of the RMS function), and reduction is unnecessary for most applications since the overall uncertainty is only 1.1%.

A.2 Uncertainty in Global Time Inverse Method

It is desirable to quantify the uncertainty in the global time inverse method. In Chapter 3, the projection equations were written in compact form. In order to quantify the uncertainty in the inverse projection, it is recommended that the compact notation first be expanded. For N = 1, 2, …, 7, the surface temperature equations are given by

$$T_{N=1} = \frac{C_1}{2} D T_d + T_d + C_2 q_d \tag{A.18}$$

$$T_{N=2} = \left[\frac{C_1^2}{2} D^2 + 2C_1 D + 1 \right] T_d + C_2 \left[C_1 D + 2 \right] q_d \tag{A.19}$$

$$T_{N=3} = \left[\frac{C_1^3}{2} D^3 + 3C_1^2 D^2 + \frac{9}{2} C_1 D + 1 \right] T_d + C_2 \left[C_1^2 D^2 + 4C_1 D + 3 \right] q_d \tag{A.20}$$

$$\begin{aligned} T_{N=4} = &\left[\frac{C_1^4}{2} D^4 + 4C_1^3 D^3 + 10C_1^2 D^2 + 8C_1 D + 1 \right] T_d + \\ &C_2 \left[C_1^3 D^3 + 6C_1^2 D^2 + 10C_1 D + 4 \right] q_d \end{aligned} \tag{A.21}$$

$$\begin{aligned} T_{N=5} = &\left[\frac{C_1^5}{2} D^5 + 5C_1^4 D^4 + \frac{35}{2} C_1^3 D^3 + 25C_1^2 D^2 + \frac{25}{2} C_1 D + 1 \right] T_d + \\ &C_2 \left[C_1^4 D^4 + 8C_1^3 D^3 + 21C_1^2 D^2 + 20C_1 D + 5 \right] q_d \end{aligned} \tag{A.22}$$

$$\begin{aligned} T_{N=6} = &\left[\frac{C_1^6}{2} D^6 + 6C_1^5 D^5 + 27C_1^4 D^4 + 56C_1^3 D^3 + \frac{105}{2} C_1^2 D^2 + 18C_1 D + 1 \right] T_d + \\ &C_2 \left[C_1^5 D^5 + 10C_1^4 D^4 + 36C_1^3 D^3 + 56C_1^2 D^2 + 35C_1 D + 6 \right] q_d \end{aligned} \tag{A.23}$$

$$\begin{aligned} T_{N=7} = &\left[\frac{C_1^7}{2} D^7 + 7C_1^6 D^6 + \frac{77}{2} C_1^5 D^5 + 105C_1^4 D^4 + 147C_1^3 D^3 + 98C_1^2 D^2 + \right. \\ &\left. \frac{49}{2} C_1 D + 1 \right] T_d \\ &C_2 \left[C_1^6 D^6 + 12C_1^5 D^5 + 55C_1^4 D^4 + 120C_1^3 D^3 + 126C_1^2 D^2 + \right. \\ &\left. 56C_1 D + 7 \right] q_d \end{aligned} \tag{A.24}$$

where

$$C_1 = \frac{d^2}{N^2 \alpha} \tag{A.25}$$

$$C_2 = \frac{d}{Nk} \tag{A.26}$$

$$D = \frac{d}{dt} \tag{A.27}$$

The corresponding expansions for surface heat flux are given by

q at the surface is given by

$$q_{N=1} = \frac{1}{C_2}\left[\frac{C_1^2}{4}D^2 + C_1 D\right]T_d + \left[\frac{C_1}{2}D + 1\right]q_d \tag{A.28}$$

$$q_{N=2} = \frac{1}{C_2}\left[\frac{C_1^3}{4}D^3 + \frac{3}{2}C_1^2 D^2 + 2C_1 D\right]T_d + \left[\frac{C_1^2}{2}D^2 + 2C_1 D + 1\right]q_d \tag{A.29}$$

$$\begin{aligned} q_{N=3} = \frac{1}{C_2}\left[\frac{C_1^4}{4}D^4 + 2C_1^3 D^3 + \frac{19}{4}C_1^2 D^2 + 3C_1 D\right]T_d + \\ \left[\frac{C_1^3}{2}D^2 + 3C_1^2 D^2 + \frac{9}{2}C_1 D + 1\right]q_d \end{aligned} \tag{A.30}$$

$$\begin{aligned} q_{N=4} = \frac{1}{C_2}\left[\frac{C_1^5}{4}D^5 + \frac{5}{2}C_1^4 D^4 + \frac{17}{2}C_1^3 D^3 + 11C_1^2 D^2 + 4C_1 D\right]T_d + \\ \left[\frac{C_1^4}{2}D^4 + 4C_1^3 D^3 + 10C_1^2 D^2 + 8C_1 D + 1\right]q_d \end{aligned} \tag{A.31}$$

$$\begin{aligned} q_{N=5} = \frac{1}{C_2}\left[\frac{C_1^6}{4}D^6 + 3C_1^5 D^5 + \frac{53}{4}C_1^4 D^4 + 26C_1^3 D^3 + \frac{85}{4}C_1^2 D^2 + 5C_1 D\right]T_d + \\ \left[\frac{C_1^5}{2}D^5 + 5C_1^4 D^4 + \frac{35}{2}C_1^3 D^3 + 25C_1^2 D^2 + \frac{25}{2}C_1 D + 1\right]q_d \end{aligned} \tag{A.32}$$

$$\begin{aligned} q_{N=6} = \frac{1}{C_2}\left[\frac{C_1^7}{4}D^7 + \frac{7}{2}C_1^6 D^6 + 19C_1^5 D^5 + 50C_1^4 D^4 + \frac{259}{4}C_1^3 D^3 + \right. \\ \left. \frac{73}{2}C_1^2 D^2 + 6C_1 D\right]T_d + \\ \left[\frac{C_1^6}{2}D^6 + 6C_1^5 D^5 + 27C_1^4 D^4 + 56C_1^3 D^3 + \frac{105}{2}C_1^2 D^2 + 18C_1 D + 1\right]q_d \end{aligned} \tag{A.33}$$

$$q_{N=7} = \frac{1}{C_2}\left[\frac{C_1^8}{4}D^8 + 4C_1^7D^7 + \frac{103}{4}C_1^6D^6 + 85C_1^5D^5 + \frac{303}{2}C_1^4D^4 + 140C_1^3D^3 + \frac{231}{4}C_1^2D^2 + 7C_1D\right]T_d + \left[\frac{C_1^7}{2}D^7 + 7C_1^6D^6 + \frac{77}{2}C_1^5D^5 + 105C_1^4D^4 + 147C_1^3D^3 + 98C_1^2D^2 + \frac{49}{2}C_1D + 1\right]q_d \tag{A.34}$$

Next, we define the overall uncertainty in the surface temperature projection with the aid of Kline-McClintock's method [49] as

$$U_{TN} = \left[\left(U_k\frac{\partial T_N}{\partial k}\right)^2 + \left(U_{\rho C}\frac{\partial T_N}{\partial \rho C}\right)^2 + \left(U_d\frac{\partial T_N}{\partial d}\right)^2 + \sum_{i=0}^{N}\left(\varpi_{T,T^{(i)}}\right)^2 + \sum_{i=0}^{N-1}\left(\varpi_{T,q^{(i)}}\right)^2\right]^{1/2} \tag{A.35}$$

where

$$\frac{\partial T_N}{\partial k} = \frac{\partial T_N}{\partial C_1}\frac{\partial C_1}{\partial k} + \frac{\partial T_N}{\partial C_2}\frac{\partial C_2}{\partial k} \tag{A.36}$$

$$\frac{\partial T_N}{\partial \rho C} = \frac{\partial T_N}{\partial C_1}\frac{\partial C_1}{\partial \rho C} \tag{A.37}$$

$$\frac{\partial T_N}{\partial k} = \frac{\partial T_N}{\partial C_1}\frac{\partial C_1}{\partial d} + \frac{\partial T_N}{\partial C_2}\frac{\partial C_2}{\partial d} \tag{A.38}$$

$$\varpi_{T,T^{(i)}} \equiv U_{T_d^{(i)}}\frac{\partial T_N}{\partial T_d^{(i)}} \tag{A.39}$$

$$\varpi_{T,q^{(i)}} \equiv U_{q_d^{(i)}}\frac{\partial T_N}{\partial q_d^{(i)}} \tag{A.40}$$

Similarly, the uncertainty in the surface heat flux projection is defined as

$$U_{qN} = \left[\left(U_k\frac{\partial q_N}{\partial k}\right)^2 + \left(U_{\rho C}\frac{\partial q_N}{\partial \rho C}\right)^2 + \left(U_d\frac{\partial q_N}{\partial d}\right)^2 + \sum_{i=0}^{N+1}\left(\varpi_{q,T^{(i)}}\right)^2 + \sum_{i=0}^{N}\left(\varpi_{q,q^{(i)}}\right)^2\right]^{1/2} \tag{A.41}$$

where

$$\frac{\partial q_N}{\partial k} = \frac{\partial q_N}{\partial C_1}\frac{\partial C_1}{\partial k} + \frac{\partial q_N}{\partial C_2}\frac{\partial C_2}{\partial k} \tag{A.42}$$

$$\frac{\partial q_N}{\partial \rho C} = \frac{\partial q_N}{\partial C_1}\frac{\partial C_1}{\partial \rho C} \tag{A.43}$$

$$\frac{\partial q_N}{\partial k} = \frac{\partial q_N}{\partial C_1}\frac{\partial C_1}{\partial d} + \frac{\partial q_N}{\partial C_2}\frac{\partial C_2}{\partial d} \tag{A.44}$$

$$\varpi_{q,T^{(i)}} \equiv U_{T_d^{(i)}}\frac{\partial q_N}{\partial T_d^{(i)}} \tag{A.45}$$

$$\varpi_{q,q^{(i)}} \equiv U_{q_d^{(i)}}\frac{\partial q_N}{\partial q_d^{(i)}} \tag{A.46}$$

Before proceeding, it is necessary to obtain an estimate of the uncertainty in probe depth and in material properties.

Uncertainty in probe depth

The holes in which the probes have been installed were drilled with small diameter (0.040 in.) drill bits. A diagram of representative resulting hole can be seen in Figure A.1. The depth of each hole was measured as the distance from the heated surface to the tip of the hole. The installation technique used yields good confidence that the thermocouple bead is in contact with the bottom of the hole somewhere along the slope. The depths of the holes were measured with Microval, a coordinate measuring machine manufactured by Browne and Sharpe. The accuracy of the machine was found to be ± 0.000 16 in. This was verified with DoALL gage blocks set 86S which had a tolerance of ± 0.000 002 in. Therefore, the uncertainty in the measurement was negligible as compared to the uncertainty due to the hole bottom slope. The equation for the uncertainty in the hole depth is then

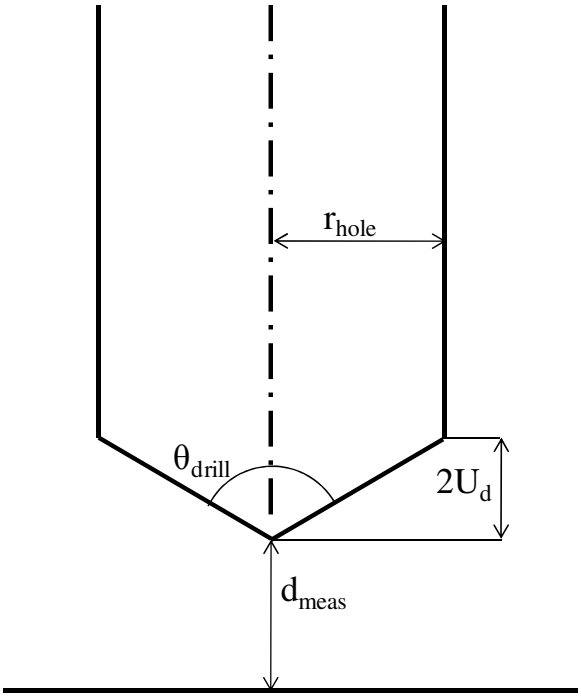

Figure A.1: Sketch of drilled hole geometry and uncertainty of hole depth.

$$U_d = \frac{r_{hole}}{2}\tan\left(90^o - \frac{\theta_{drill}}{2}\right) \tag{A.47}$$

where values for bronze samples can be found in Table A.2. The probe depth is then given by

$$d = \left(d_{meas} + U_d\right) \pm U_d \tag{A.48}$$

Uncertainty in Material Properties

The manufacturer of the bronze (Atlas Bronze) was contacted to determine the uncertainty in the material properties. At the present time, they have not responded. Therefore, based on uncertainties reported in the literature for other materials, a 5% uncertainty was assumed in the product ρC as well as a 5% uncertainty in the nominal value of k.

Overall Uncertainty in the Global Time Inverse Method

Tables A.2-A.6 show the resulting uncertainty in the inverse projection for $1 \le N \le 4$. As defined above, an uncertainty of ± 0.15 mm was assumed for d, 5% uncertainty in the nominal value of the product of ρC was assumed, and 5% uncertainty in k was also assumed. An uncertainty of ± 0.2°C was assumed for T_d, and 5% of the maximum value was assumed for the uncertainty in the temporal derivatives of T_d as well as q_d and its temporal derivatives. Data from probe A0, run qCHIt3f200 was used with f_c = 0.9 Hz, τ_o =0.0338s, τ_{max} = 0.701s, λ = 0.460s$^{1/2}$ to populate Table A.2-A.6. The one-probe analysis technique outlined in Chapter 7 was used to calculate the in-situ heat flux.

The uncertainty in the surface temperature due to probe depth and material properties is seen to converge to a plateau value as the number of spatial nodes is increased (see Table A.2). Likewise, the uncertainty in the surface temperature prediction due to uncertainties in temperature data (Table A.3) and heat flux data (Table A.4) converges to a plateau value. This is

Table A.2: Contribution of uncertainty in k, ρ, C, and d to the overall uncertainty in the inverse predicted surface temperature and heat flux for different values of N. Temperature uncertainty is in °C and heat flux uncertainty is in W/cm^2. Data used from run qCHIt3f200.

N	$U_k \left.\frac{\partial T_N}{\partial k}\right\|_{max}$	$U_{\rho C} \left.\frac{\partial T_N}{\partial \rho C}\right\|_{max}$	$U_d \left.\frac{\partial T_N}{\partial d}\right\|_{max}$	$U_k \left.\frac{\partial q_N}{\partial k}\right\|_{max}$	$U_{\rho C} \left.\frac{\partial q_N}{\partial \rho C}\right\|_{max}$	$U_d \left.\frac{\partial q_N}{\partial d}\right\|_{max}$
1	0.113	0.113	0.131	0.487	0.487	0.564
2	0.142	0.142	0.165	0.435	0.435	0.503
3	0.147	0.147	0.170	0.423	0.423	0.489
4	0.148	0.148	0.171	0.419	0.419	0.485

Table A.3: Contribution of uncertainty in temperature data and its temporal derivatives to the overall uncertainty in the inverse predicted surface temperature for different values of N in °C. Data used from run qCHIt3f200.

N	$\varpi_{T,T^{(0)}}$	$\varpi_{T,T^{(1)}}$	$\varpi_{T,T^{(2)}}$	$\varpi_{T,T^{(3)}}$	$\varpi_{T,T^{(4)}}$	$\left[\sum_{i=0}^{N}\left(\omega_{T,T^{(i)}}\right)^2\right]^{1/2}$
1	0.200	0.0971	---	---	---	0.22231
2	0.200	0.0971	0.00805	---	---	0.22246
3	0.200	0.0971	0.00954	0.00390	---	0.22252
4	0.200	0.0971	0.0101	0.00548	$2.96\text{x}10^{-5}$	0.22254

Table A.4: Contribution of uncertainty in heat flux data and its temporal derivatives to the overall uncertainty in the inverse predicted surface temperature for different values of N in °C. Data used from run qCHIt3f200.

N	$\varpi_{T,q^{(0)}}$	$\varpi_{T,q^{(1)}}$	$\varpi_{T,q^{(2)}}$	$\varpi_{T,q^{(3)}}$	$\left[\sum_{i=0}^{N}\left(\omega_{T,q^{(i)}}\right)^2\right]^{1/2}$
1	0.267	---	---	---	0.26684
2	0.267	0.0228	---	---	0.26782
3	0.267	0.0271	0.00110	---	0.26821
4	0.267	0.0286	0.00157	$5.16\text{x}10^{-5}$	0.26837

Table A.5: Contribution of uncertainty in temperature data and its temporal derivatives to the overall uncertainty in the inverse predicted surface heat flux for different values of N in W/cm^2. Data used from run qCHIt3f200.

N	$\varpi_{q,T^{(0)}}$	$\varpi_{q,T^{(1)}}$	$\varpi_{q,T^{(2)}}$	$\varpi_{q,T^{(3)}}$	$\varpi_{q,T^{(4)}}$	$\varpi_{q,T^{(5)}}$	$\left[\sum_{i=0}^{N}\left(\omega_{q,T^{(i)}}\right)^2\right]^{1/2}$
1	0	0.220	0.0728	---	---	---	0.23143
2	0	0.220	0.0546	0.00502	---	---	0.22641
3	0	0.220	0.0513	0.00529	0.000502	---	0.22563
4	0	0.220	0.0501	0.00534	0.000671	$2.71\text{x}10^{-5}$	0.22536

Table A.6: Contribution of uncertainty in heat flux data and its temporal derivatives to the overall uncertainty in the inverse predicted surface heat flux for different values of N in W/cm^2. Data used from run qCHIt3f200.

N	$\varpi_{q,q^{(0)}}$	$\varpi_{q,q^{(1)}}$	$\varpi_{q,q^{(2)}}$	$\varpi_{q,q^{(3)}}$	$\varpi_{q,q^{(3)}}$	$\left[\sum_{i=0}^{N}\left(\omega_{q,q^{(i)}}\right)^2\right]^{1/2}$
1	0.302	0.103	---	---	---	0.31911
2	0.302	0.103	0.00948	---	---	0.31926
3	0.302	0.103	0.0103	0.0112	---	0.31931
4	0.302	0.103	0.0119	0.0119	$3.22\text{x}10^{-5}$	0.31934

a desirable characteristic since the accuracy of the global time method was demonstrated in Chapter 3 to improve as the number of spatial nodes is increased.

The uncertainty in the surface heat flux due to uncertainties in probe depth (Table A.2), material properties (Table A.2), temperature data (Table A.5), and heat flux data (Table A.6) is seen in to decrease to a converged value as more spatial nodes are used. Again, this is highly desirable since the accuracy of the global time method improves as N is increased.

In summary, for the example run of qCHIt3f200, the maximum overall uncertainty in the surface temperature due to material properties, sensor depth, temperature data and heat flux data was ± 0.96 °C. The maximum observed surface temperature was 16.9 °C; therefore, the ratio of maximum uncertainty to maximum temperature was 5.7%. Similarly, the maximum overall uncertainty in surface heat flux was ± 1.87 W/cm^2, and the maximum surface heat flux was 11.9 W/cm^2. Therefore, the ratio of maximum uncertainty to maximum surface heat flux was 16%. These ratios of uncertainty to maximum value were similar for different experimental runs.

Vita

Bryan Elkins is a doctoral student in Aerospace Engineering. His research interests include experimental and numerical methods in thermal fluid sciences with a focus on the inverse heat conduction problem, thermophysical properties for aerospace materials, sensitivity analysis and real-time sensors.